SUDAAR No. 481

STANFORD UNIVERSITY

CENTER FOR SYSTEMS RESEARCH

Error Modeling of Precision Orientation Sensors in a Fixed Base Simulation

by

David L. Klinger

Guidance and Control Laboratory

July 1974

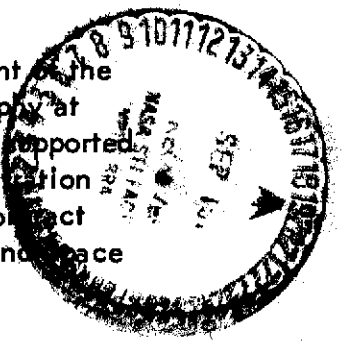

This research was performed in partial fulfillment of the requirements for the degree of doctor of philosophy at Stanford University. The research was partially supported by the National Aeronautics and Space Administration under Grant NGR-05-020-019, by Air Force Contract F33615-72-C-1297, and by Lockheed Missiles and Space Co. independent development funding.

Department of Aeronautics and Astronautics
Guidance and Control Laboratory
Stanford University
Stanford, California 94305

W. W. HANSEN LABORATORIES OF PHYSICS
STANFORD UNIVERSITY
STANFORD, CALIFORNIA 94305

Microwave Laboratory
High Energy Physics Laboratory
Stanford Synchrotron Radiation Facility

Telephone (415) 497-1389
497-0286

September 4, 1974

Gentlemen,

Dr. Everitt asked me to send you a copy of the enclosed Ph.D. thesis by D. Klinger, performed under Professor DeBra's direction. We expect to apply the techniques developed here in precision gyro testing during the coming year.

Sincerely,

Irene Pereira

Mrs. Irene Pereira
Secretary to Dr. C. W. F. Everitt

Distribution:
R. A. Potter
R. Decher
H. D. Calahan
N. Roman
NASA Headquarters Gravitational Physics Office
NASA Scientific and Technical Information Facility

ERROR MODELING OF PRECISION ORIENTATION SENSORS IN A FIXED BASE SIMULATION

by

David L. Klinger

July 1974

SUDAAR No. 481

This research was performed in partial fulfillment of the requirements for the degree of doctor of philosophy at Stanford University. The research was partially supported by the National Aeronautics and Space Administration under Grant NGR-05-020-019, by Air Force Contract F33615-72-C-1297, and by Lockheed Missiles and Space Co. independent development funding.

Department of Aeronautics and Astronautics
Guidance and Control Laboratory
Stanford University
Stanford, California 94305

ABSTRACT

Models of noise and dynamic characteristics of a gyro and autocollimator for very small signal levels are presented. Measurements have been evaluated using spectral techniques for identifying noise from base motion. The techniques have been developed to enable the sensors for a relativity experiment to be evaiuated in spite of the fact their accuracy will exceed any reference standards available.

Conventional tests of gyroscopes, telescopes, and other precise orientation sensors normally rely on more accurate standards to provide a reference. These standards are used in an absolute sense, in that all errors are attributed to the instruments being tested, including those of the calibration equipment. When the precision of the instruments under test surpasses that of available laboratory calibration equipment, different methods are needed. This situation exists in a test of general relativity theory being developed at Stanford University.

The experiment is constructed to measure the precession, due to relativistic effects, of an extremely precise earth-orbiting gyroscope. The design goal for non-relativistic gyro drift is 0.001 arcsec per year. A telescope, used to maintain the experiment satellite in an inertially fixed orientation, has similar extreme precision. A laboratory test is desired which accounts for environmental effects, especially gravity, and isolates inherent sensor errors.

Developing appropriate test methods using the actual relativity sensors was impractical due to the expense and unavailability of prototypes. Consequently, an analogous, though less accurate fixed base simulator was developed. This simulator was used in developing methods of instrument error modeling and performance evaluation applicable to the relativity experiment sensors and other precision pointing instruments.

Two Atlas missile gyros, integrated into a Minuteman I guidance assembly, and two specially designed autocollimators serve as analogs to

the relativity experiment sensors. A three-axis Minuteman I stable platform provides a movable mount for the sensors. The sensors are used to stabilize the platform with less than 1 arcsec jitter. The noise equivalent angle of the primary autocollimator is 0.1 arcsec.

A spectral approach is used in analyzing the fixed base simulator signals and developing error models for the sensors. A review of spectral theory and practical considerations in computing spectral functions introduces a discussion of experimental results. Comparisons are made of gyro and autocollimator spectra taken with the instruments both resting on quiet test beds and serving as feedback sensors in platform stabilization loops. Coherency between signals is used to indicate mutual instrument error sources and to provide confidence in the estimation of system transfer functions.

Analysis of autocollimator spectra uncovered the presence of a platform gimbal resonance. The source of resonance was isolated to gimbal bearing elastic restraint properties most apparent at very small levels of motion (< 100 μrad). A model of these properties which include both elastic and coulomb friction characteristics is discussed, and a describing function developed.

ACKNOWLEDGMENTS

The author wishes to thank Professor Daniel B. DeBra, under whose direction this research was conducted. His support, interest, and encouragement are deeply appreciated. The author is also grateful to Professors J. David Powell and John V. Breakwell for their careful review and helpful criticisms of the manuscript.

The efforts of Dr. Walter Pondrom, Jr., who greatly aided the experimental development, were an inspiration to the author and are gratefully acknowledged.

Working with the staff of the Guidance and Control Laboratory: Robert Clappier, Howard Frosch, Russell Hacker, Geoffrey Jones, John Nikirk, and Richard Van Patten, was a rewarding and pleasurable experience. Their support is appreciated.

The many suggestions and assistance of friends and associates at Stanford University and Lockheed Missiles and Space Co. have been helpful. The comments and perspective provided by Dr. Vance Coffman were invaluable.

Special thanks go to Connie Calica, Inga Lof and Ida Lee for their assistance in preparing the manuscript, and to Steve Beach for his logistical support.

For sharing the years of this research, for the constant support, encouragement, and understanding provided by my wife, Judy, the deepest appreciation is expressed.

This research was partially supported by NASA Grant NGR-05-020-019, by Air Force Contract F33615-72-C-1297, and by the Lockheed Missiles and Space Co. independent development program and is gratefully acknowledged.

CONTENTS

CONTENTS (Cont'd)

CONTENTS (Cont'd)

ILLUSTRATIONS

ILLUSTRATIONS (Cont'd)

ILLUSTRATIONS (Cont'd)

TABLES

LIST OF SYMBOLS

a	width of aperture image on autocollimator photodetector
a_n	Fourier series coefficients
A	matrix of powers of W
A_1	autocollimator stabilization closed loop gain
c	gyro viscous damping coefficient
c_1, c_2	constants
C	gyro caging amplifier feedback capacitance
$C(S)$	platform compensation network transfer function
C, $C(t)$	output (measurement) matrix
C_1, C_2	caging amplifier feedback control gains
d	distance from autocollimator aperture and photodetector to center of beamsplitter
D_o, D_i	gyro flotation fluid [outer, inner] viscous friction coefficients
E	platform gimbal motor back EMF
f	frequency
f	autocollimator objective lens focal length (Ch. II)
f_s	sampling frequency
F, $F(t)$	state matrix
g	gap between autocollimator photodetector quadrants
G, $G(t)$	input transformation matrix
h	magnitude of gyro rotor spin angular momentum
$\bar{h}_w$	gyro rotor spin angular momentum vector
$h(t,\tau)$, $h(\tau)$	filter impulse response (Ch. IV)
$\bar{H}_f$, $\bar{H}_g$	total angular momentum of gyro [float, gimbal]

$H(f)$	transfer function
i	platform gimbal motor armature current
i_1, i_2, i_3, i_4	autocollimator photodetector quadrant currents
i_{1_d}, i_{2_d}, i_{3_d}, i_{4_d}	autocollimator photodetector quadrant dark currents
I	identity matrix ($N \times N$) (Ch. IV)
I	platform gimbal moment of inertia
$\bar{\bar{I}}_p$	platform effective moment of inertia matrix
$\bar{\bar{I}}_f$, $\bar{\bar{I}}_g$	moment of inertia tensor of gyro [float, gimbal]
I_{f_s}, I_{f_t}	combined gyro wheel and float [spin, transverse] moment of inertia
I_{g_s}, I_{g_t}	gyro gimbal [spin, transverse] moment of inertia
I_{xx}, I_{yy}, I_{zz}	on-diagonal elements of platform inertia matrix
$\widehat{IA}_c$, $\widehat{IA}_f$, $\widehat{IA}_g$	inner axis of gyro [case, float, gimbal] reference frame
j	$\sqrt{-1}$
k	gyro elastic restraint coefficient
k	time index (Ch. IV)
k_i	autocollimator photodetector quadrant current scale factor (Ch. II)
k_o, k_i	gyro support wire [outer, inner] rotational elastic restraint coefficients
k_x, k_y	autocollimator preamplifier scale factors
K	simplified autocollimator supervision loop gain (Ch. II)
K, K_{ss}	Kalman filter gain matrix (Ch. IV)
K_{AC}, K_{AI}	autocollimator [control, instrumentation] channel scale factors

K_b	platform gimbal motor back EMF scale factor
K_d	platform control amplifier command torque gain
K_g	gyro pickoff scale factor
K_L	autocollimator stabilization closed loop gain
K_m	platform gimbal motor torque gain
K_p	platform control power amplifier gain
K_s	platform gimbal bearing elastic restraint coefficient
K_T	gyro torquer overall caging input to torque rate scale factor
K_{T_B}	gyro torquer bias voltage input to current gain
K_{T_C}	gyro torquer caging voltage input to current gain
K_{T_o}	gyro torquer output voltage to torquer rate scale factor
L_a	platform gimbal motor armature inductance
m	correlation index
$\bar{M}_b$	platform gimbal bearing torque
$\bar{M}_d$	platform gimbal disturbance torque
$\bar{M}_f$, $\bar{M}_g$	resultant moment applied to gyro [float, gimbal]
$M^c_{f_o}$, $M^c_{f_i}$	gyro torquer moment about [outer, inner] axis
$M^d_{f_o}$, $M^d_{f_i}$	gyro float disturbance moment about [outer, inner] axis
$M^{d'}_{f_o}$, $M^{d'}_{f_i}$	zero-mean gyro float disturbance moment about [outer, inner] axis
$M^d_{g_o}$, $M^d_{g_i}$	gyro gimbal disturbance moment about [outer, inner] axis

$\bar{M}_{gr}$	gyro reaction torque
M_{gr_o}, M_{gr_i}	gyro reaction torque about [outer, inner] axis
M_{gr_x}, M_{gr_y}, M_{gr_z}	combined gyro reaction torque about platform [X, Y, Z] axis
$\bar{M}_m$	platform gimbal motor torque
n	frequency index (Ch. IV)
n, n(t)	measurement noise
n_A	autocollimator noise
n_G	gyro gimbal disturbance torque noise
n_p	gyro pickoff noise
n_x, n_y	autocollimator pickoff noise voltages
n_1, n_2, n_3, n_4	autocollimator photodetector quadrant noise currents
N	number of data points
$\widehat{OA}_c$, $\widehat{OA}_f$, $\widehat{OA}_g$	outer axis of gyro [case, float, gimbal] reference frame
P(f), $P_{xx}(f)$, $P_{yy}(f)$	power spectral density function
$P_{xy}(f)$	cross-spectral density function
Q, Q(t)	process noise covariance matrix (Ch. IV)
Q(S)	autocollimator stabilization loop characteristicc equation
Q_1, Q_2, Q_3, Q_4	autocollimator photodetector quadrant designations
R, R(t)	measurement noise covariance matrix
$R_{xx}(t,\tau)$, $R_{xx}(\tau)$	autocorrelation function
$R^c_{xx}(m)$	circular discrete autocorrelation function
$R_{xy}(\tau)$	cross-correlation function

$R_{xy}^{c}(m)$	circular discrete cross-correlation function
R_a	platform gimbal motor armature resistance
R_f, R_i	gyro caging amplifier [feedback, input] resistance
s	signal
S	Laplace operator
$\widehat{SA}_c$, $\widehat{SA}_f$, $\widehat{SA}_g$	spin axis of gyro [case, float, gimbal] reference frame
t	time
T	length of data record (Ch. IV)
T, T(t)	process and measurement noise cross-covariance matrix
T, $\overline{T}$	[actual, normalized] frictional torque (Ch. V)
T_o, $\overline{T}_D$	[actual, normalized] frictional torque describing function amplitude
T_m, $\overline{T}_m$	[actual, normalized] sinusoidal frictional torque amplitude
T_o	maximum (running) frictional torque (Ch. V)
T_o, T_i	gyro support wire [outer, inner] axis tension coefficients (Ch. III)
T_x	gyro viscous friction torque
V_c	platform compensation network output voltage
V_F	gyro caging amplifier feedback voltage
V_g	gyro pickoff voltage
V_I	gyro caging amplifier integral control voltage
V_{in}	platform compensation network input voltage
V_p	platform control amplifier output voltage
V_{T_d}	platform control amplifier command torque voltage

V_x, V_y	autocollimator preamplifier pickoff voltages
V_{x_d}, V_{y_d}	autocollimator dark current pickoff voltages
V_1, V_2, V_3, V_4	autocollimator preamplifier output voltages
w	width of autocollimator photodetector quadrants (Ch. II)
w, w(t)	process noise (Ch. IV)
W	$e^{-j2\ /N}$
x, y, x', y'	pitch transformation resolver [input, output] voltages (Ch. II)
x, y	displacement from null of centroid of autocollimator aperture image on photodetector (Ch. II)
x(t), y(t)	time functions
$\bar{X}$, $\bar{Y}$	E[x(t)], E[y(t)]
$\hat{x}_o(t)$	least squares estimate of x(t)
X(f), $\hat{X}$(f)	Fourier transform of x(t), x(k)
X, Y, Z	platform reference axes
X_{RD}	X-Z gyro redundant axis
y(t)	output vector
z(t)	state vector

γ	dummy variable of integration
γ_{AC}, γ_{AI}	autocollimator [control, instrumentation] output signals
γ_c	autocollimator stabilization loop command voltage
γ_g	gyro pickoff signal
$\gamma^2_{xy}(f)$	coherence function

$\delta(t-\tau)$	Dirac delta function
Δf	frequency interval (1/T)
Δt	elapsed time (Ch. II)
Δt	sample interval (Ch. IV)
ΔV_g	change in gyro pickoff voltage
ΔV_T	change in gyro torquer amplifier output voltage
ζ, ζ_p, $\bar{\zeta}_p$, ζ_{AC}, $\bar{\zeta}_{AC}$	damping ratios
η	platform gimbal bearing model parameter
θ	angle
θ, $\bar{\theta}$	[actual, normalized] frictional torque angle (Ch. V)
θ_c	platform gimbal command angle (Ch. III)
$\bar{\theta}_g$	vector of gyro gimbal angles
θ_{g_o}, θ_{g_i}, θ_{g_s}	[outer, inner, spin] axis components of $\bar{\theta}_g$
θ_o, $\bar{\theta}_o$	[actual, normalized] friction torque angle amplitude
θ_p, $\bar{\theta}_p$, θ_{p_1}, θ_{p_2}	platform gimbal angles
θ_x, θ_y	angles between autocollimator optical axis and normal to reference mirror
τ	correlation time (Ch. IV)
τ	lead compensation time constant (Ch. III)
τ	dummy variable of integration
σ	dummy variable of integration
$\bar{\sigma}$	gyro float angle relative to case
σ_o, σ_i, σ_s	gyro float angles about [outer, inner, spin] reference axis
σ_x^2	variance of X, $[E(x-\bar{x})^2]$
Σ	mean square error $E\lvert\hat{x} - x\rvert^2$

Σ	covariance matrix
φ	frictional torque describing function angle
$\Phi(t)$	state transition matrix
ω^c	gyro command rate
ω^d	gyro drift rate
ω^i	inertial angular rate of gyro case
ω_{AC}, ω_{AI_1}, ω_{AI_2}	autocollimator filter break frequencies
$\bar{\omega}_{AC}$, $\bar{\omega}_{c_1}$, $\bar{\omega}_{c_4}$, $\bar{\omega}_p$	stabilization closed loop break frequencies
ω_{c_1}, ω_{c_2}, ω_{c_3} ω_{c_4}, ω_{c_5}, ω_{c_6}	platform compensation network break frequencies
ω_m	platform gimbal motor break frequency
ω_n	gyro caging loop natural frequency
ω_n	gyro nutation frequency
ω_p	platform gimbal bearing/inertia resonant frequency
ω_1, ω_2	gyro characteristic equation roots

Frames of Reference

c	gyro case
f	gyro float
g	gyro gimbal
i	inertial
p	platform

Special Notation

$\times$	vector cross product
$\bar{\omega}^{u-v}$	angular velocity of reference frame u with respect to reference frame v
$(\overset{u}{\ })$	first derivative of vector ( ) with respect to time in u reference frame
$(\overset{uu}{\ })$	second derivative of vector ( ) with respect to time in u reference frame
$(\dot{\ })$	first derivative of scalar ( ) with respect to time
$(\ddot{\ })$	second derivative of scalar ( ) with respect to time
$\hat{(\ )}$	approximate or estimated value of ( )
$\bar{(\ )}$	vector
$(\ )_u$	vector or tensor ( ) coordinatized in u reference frame
$(\ )_o$, $(\ )_i$, $(\ )_s$	outer, inner, spin axis component of ( )
$(\ )_x$, $(\ )_y$, $(\ )_z$	[x,y,z] component of ( )
E[ ]	expected value of [ ]
$(\ )^*$	complex conjugate of ( )
$(\ )^{-1}$	matrix inverse
$(\ )^T$	matrix transpose
$\lvert(\ )\rvert$	magnitude of ( )
$\angle(\ )$	angle of ( )
$\hat{(\ )}$	unit vector

I. INTRODUCTION

A. Problem Statement

Reliable prelaunch testing and evaluation of extremely precise satellite orientation sensors has become an important concern. As the accuracy of both optical and inertial sensors has improved, it often equals or surpasses that of conventional reference instruments.

In conventional testing, where a precise reference exists, differences in output between the test sensor and the reference instruments are usually attributed to errors in the test instruments. When a more precise reference does not exist, the best source of information about the orientation is often the sensor itself. The purpose of this research is to demonstrate the effectiveness of a frequency domain approach to orientation sensor error modeling and performance evaluation when a precise reference is not available. The demonstration is accomplished through experiments on a pair of gyros and autocollimators mounted on a stabilized three-axis platform.

B. The Stanford Relativity Experiment

The motivation for this study was a requirement to verify in the laboratory the design and fabrication of the extremely precise gyros and telescope of the Stanford Relativity Experiment. This experiment, first proposed in 1960 [S1], is designed to measure the precession of a gyroscope predicted by the general theory of relativity. The accuracy will be sufficient to distinguish between Einstein's theory and other theories which have been proposed.

Precession is measured relative to a telescope pointed at a star. As outlined in [B11], two general relativistic precession effects are of interest. The first, known as geodetic precession, is due to motion of the gyros through a gravitational field. For a 500 nautical mile altitude earth polar orbit, the predicted precession is 6.9 arcsec per year. An even smaller effect, called motional drift, is due to rotation of the gravity field. The secular portion of this effect for the same orbit is 0.05 arcsec per year. This experiment differs from all other proposed

relativity experiments in that it is the only one which can measure the effects of a gravity field produced by a rotating body. In order to observe the latter precession to 2% accuracy, a design goal of 0.001 arcsec per year of drift due to Newtonian torques has been established.

In addition to the extreme accuracy required of the gyros, the null stability of the telescope must also be held to 0.001 arcsec. To meet this requirement, the telescope is limited to a linear dynamic range of 0.1 arcsec and is of special construction.

Achieving such accuracies, more than six orders of magnitude better than existing instruments in the case of the gyros, obviously requires special techniques. The two principal aids are the low g orbital environment and use of liquid helium temperatures. The environment is provided by placing the sensor package inside a dewar filled with superfluid helium. At these temperatures creep is virtually nonexistent, providing excellent mechanical stability, and the superfluid helium is a perfect heat conductor which minimizes temperature gradients. A superconducting niobium shield around the experiment package eliminates magnetic interaction torques between the gyro and the earth's magnetic field. Superconducting electronics are also used in the essentially torque-free gyro pickoff, and helium boiloff is used in linear differential thrusters [B12] to provide attitude control to within 0.05 arcsec rms.

The gyro rotors are made of fused quartz covered with thin metallic superconducting layers. The rotors are electrostatically suspended with a nominal orbital preload of 1×10^{-6} g to prevent satellite disturbances from causing contact with the gyro. Gravity-gradient drift torques are reduced to acceptable levels by producing the rotors spherical and homogeneous to within 10^{-6}. Details of the design and mission can be found in [E2], [B1], and [B11].

C. Fixed Base Simulator

Although the precision just indicated for an orbital environment cannot be obtained in the laboratory, primarily due to the one-g environment, it is nevertheless important to have measures of performance to ensure that the instruments have been properly fabricated and assembled.

Proper operation of the instruments requires that they be in a liquid helium dewar, where they have poor accessibility. It may not be possible to keep the instruments within their linear range due to mechanical shifts and thermal distortion without some means of sensor output feedback. Further, since drift due to gravity will be the dominant effect seen in the laboratory, it is desirable to be able to change the orientation of the sensor package relative to the local vertical in order to separate various error terms.

For these reasons, a fixed base simulation using a gimballed dewar mount and an artificial star assembly to provide a reference target for the telescope is being constructed to test the experiment sensors.

The complexity, inflexibility, and expense of working with the Relativity Experiment package in its helium environment made a preliminary study using similar but less sensitive hardware desirable. Consequently, a relatively low cost and considerably more flexible analogous fixed base simulator was constructed. It contains a pair of Atlas missile two-degree-of-freedom floated gyros which provide an analog to the Relativity Experiment free-rotor gyros. A small specially built autocollimator and reference mirror are similar in behavior to the telescope and artificial star of the main experiment. The dewar mount is replaced in the fixed base simulator by a three-axis gimballed platform on which are mounted the gyros and autocollimator. A detailed description of the simulator hardware is given in Chapter II. It has been used to develop and demonstrate test methods which can be applied to the Relativity Experiment and other fine-pointing experiments.

D. Related Work

1. Isolation Platform

The problem of providing a quiet, stable test bed to evaluate precise motion sensors has received considerable attention. Concrete piers in seismically quiet areas, passive isolation using pneumatic or mechanical spring supports, and active servo-controlled test platforms have all been tried.

The Martin Company [M1] has constructed a large (23 ft $\times$ 39 ft $\times$ 8 ft) concrete block resting on bedrock for testing inertial guidance

components. Its location, just outside Denver, Colorado, was selected after extensive seismic studies because of its relative quietness. Flack and Dickie [F1] studied the effects of ground noise on accelerometer and gyro testing when the Singer-Kearfott Company decided to construct a dynamic test facility in close proximity to an existing inertial test facility. Of particular interest was the noise transmission characteristics between the facilities.

Numerous passively sprung isolation platforms have also been constructed. These platforms are effective in attenuating high frequency disturbances, but move with the underlying structure at low frequencies. A six-degree-of-freedom isolation platform which is suspended by a pendulum from an isolating suspension system has been used for precision testing at the Aerospace Guidance and Metrology Center at Heath, Ohio [P3]. The Seiler Laboratory at the Air Force Academy has also developed an isolation platform, described by Wittry [W6], which is supported by twenty pneumatic isolators. Tsutsumi [T2] reviews these and other isolation platforms in a geokinetics review paper.

When greater precision and low frequency isolation has been required, actively servo-controlled platforms have been developed. Tsutsumi [T3] developed a ground tilt isolation platform which used electronic tilt sensors and hydraulic actuators to provide isolation from low frequency floor motion. Weinstock [W1] improved this system by using a gyro for higher frequency sensing and control with a tilt sensor eliminating gyro drift errors. DeBra, Mathieson and Van Patten [D2] developed a two-degree-of-freedom table leveling system employing direct electromagnetic force actuators for low frequency attenutation. These augment the primary support and high frequency attenuation afforded by Belleville type springs. A temperature controlled level senses the local vertical. Lorenzini [L2] describes improvements to the Seiler Laboratory platform which control the platform actively in all six degrees-of-freedom. A combination of pneumatic cylinders and electromagnetic shakers provide control forces, while tiltmeters, angular accelerometers, seismometers, and a gyrocompass sense the platform motion. Another tilt isolation platform has been constructed at the Newark Air Force Station, Ohio [P2].

2. Simulation

The primary purpose of all isolation platforms is to reduce instrument output signals caused by test base motion to levels substantially lower than those created by instrument errors. Other applications require accurately known base motion in order to calibrate the motion sensing instruments and to perform system checkouts. Such fixed-base and moving-base simulations have become an integral part of the development of nearly all aerospace vehicle and transportation systems. Reinel [R1] describes a typical satellite fixed base simulation used in testing the European Symphonie satellite. The sensors were mounted on a gimballed platform whose orientation is continuously controlled by servo loops in response to angle and angular velocity or rate commands from an analog computer. Platform angles are sensed by potentiometers or encoders while rates are sensed by tachometers. Differences between these signals and the commands are nulled by accelerating the platform gimbals with electro-hydraulic actuators and an electric motor.

Davis [C8] describes a precision satellite attitude determination system called SPARS which uses strapdown gyros for short term control and discrete star sightings to correct for gyro drift. The laboratory test of this combined optical-inertial system is described by Hvoschinsky and Horiuchi [H2]. A sophisticated six-degree-of-freedom hybrid simulation is also discussed by Hogan and Welch [H1]. A salient feature of all these simulations is that primary orientation sensing is provided by test fixture transducers and not by the instruments under test. This feature is not present in the Fixed Base Simulator described in this dissertation.

In very accurate pointing systems, the components under test may far exceed the accuracy of available test fixture transducers. Hence there is no absolute laboratory standard for comparison and calibration. Since typical operating signals of these systems are less than 1 arcsec, it is necessary to do modeling and testing with signals of comparable amplitude to obtain realistic results. Even though larger signals are easier to measure accurately, the increased motion can alter significantly the physical characteristics of the hardware components.

A fairly recent branch of the simulation field known as "model-following" is concerned with accurate simulation of systems by means of

other possibly dissimilar systems. Tyler [T4] discusses an optimal control approach to the problem. Other interesting aspects of this area have been studied by Erzberger [E1], Asseo [A1], Curran [C6], and Winsor and Roy [W5].

3. Data Analysis

Analysis of orientation sensor signals using spectral techniques to determine instrument errors is quite recent although the theory has been available for several decades [W4], [J1], [N1]. Earlier efforts to do so were limited by the expense of computing the spectra, a situation which has been remedied by the development of high speed computers and efficient algorithms. An interesting application of the modern digital spectral techniques used in this dissertation, is the analysis of the voices of killer whales discussed by Singleton and Poulter [S2]. Their paper gives an extensive discussion of the methods used in obtaining the voice spectra. Continuous recordings taken from underwater microphones were broken into short segments and the spectra computed. By comparing the spectra, speech patterns could be discerned. To name a few other applications, spectral techniques have been used in the study of electrocardiograms, ocean waves, atmospheric radio propagation, and seismic events.

More closely related to the present study is an analysis of the effects of vibration on gyro testing performed by Crowly and Ossing [C5]. Vibration of the test platform was measured by pendulous seismometers and the sensed angles subtracted from the gyro output. The coherence between the gyro and sesimometer signals indicated the relative contribution of vibration to the test gyro signal.

Another closely related experimental study of the spectral characteristics of gyro drift was conducted by Truncale, Koenigsberg and Harris [T1]. A gyro with low mid-frequency noise (0.01 to 100 Hz) was desired for use in the Orbiting Astronomical Observatory. Gyros from several different manufacturers were tested. Analyzing the frequency distribution of drift noise proved powerful in selecting a suitable gyro. A source of concern in the tests which was discussed extensively was the uncertainty in the amount of output due to base motion.

Although many other spectral studies of inertial instruments are known to have been performed, there remains a paucity of experimental results available in the open literature particularly for small signal levels.

E. Summary of Research

The principal contributions of this research are

- the construction of a fixed base simulator to aid in developing methods of testing precise optical and inertial orientation sensors.
- fabrication and design of a precise autocollimator linearity better than 0.1% and noise equivalent angle of 0.5 μrad.
- the analysis of spectra of the precise autocollimator and an Atlas missile two-degree-of-freedom gyro and the development of noise models for each.
- the measurement of small motion behavior of ball bearings and the development of a describing function.
- the demonstration of an approach to develop error models of optical and inertial sensors.
- the establishment of a method for evaluating the Relativity Experiment instruments. Programs for numerically carrying this out have been written and verified using this fixed base simulator.

Chapter II

FIXED BASE SIMULATOR

In this chapter, the Fixed Base Simulator developed as an analog to the Stanford Relativity Experiment laboratory test is described. An overview of the system is first presented. Since the configuration of the simulator was heavily influenced by hardware constraints, a discussion of its development follows. The subsystems introduced in the development section are then discussed in detail. Finally, the modes in which the simulator can be operated are described.

A. Overview

The Fixed Base Simulator consists of a three-axis stable platform assembly, motion sensing instruments, and electronics, Fig. 1. The platform is a modified government surplus Minuteman I stable platform on which are mounted two Atlas missile gyros and a specially designed two axis autocollimator. The platform and an autocollimator reference mirror are installed on a 24 in. rotary table, which serves as an earth orientation reference. A second miniature autocollimator, necessary to give the third optical measurement of orientation, is attached to the rotary table and uses a reference mirror mounted on the gimballed platform. The platform and sensors are shown in Fig. 2.

Minuteman I electronics used in the simulator are located in their original guidance assembly chassis, Fig. 3, while newly developed electronics are integrated into a separate control console. Since the gyros and autocollimators are not Minuteman I equipment, extensive electronic and mechanical modification and new development was required to make them compatible with the gimballed platform. Original Minuteman electronics used are (1) various power supplies, (2) gyro pickoff preamplifiers, (3) pickoff excitation amplifier, (4) pitch transformation resolver, and (5) control amplifiers, consisting of demodulators, compensation networks, and power amplifiers. New equipment consists of (1) gyro torquer and caging amplifiers, (2) heaters, (3) preamplifiers, and (4) torquer magnet excitation; (5) autocollimator circuitry, (6) several dc and ac precision power supplies, (7) mode switching logic and relays, (8) interconnect cabling,

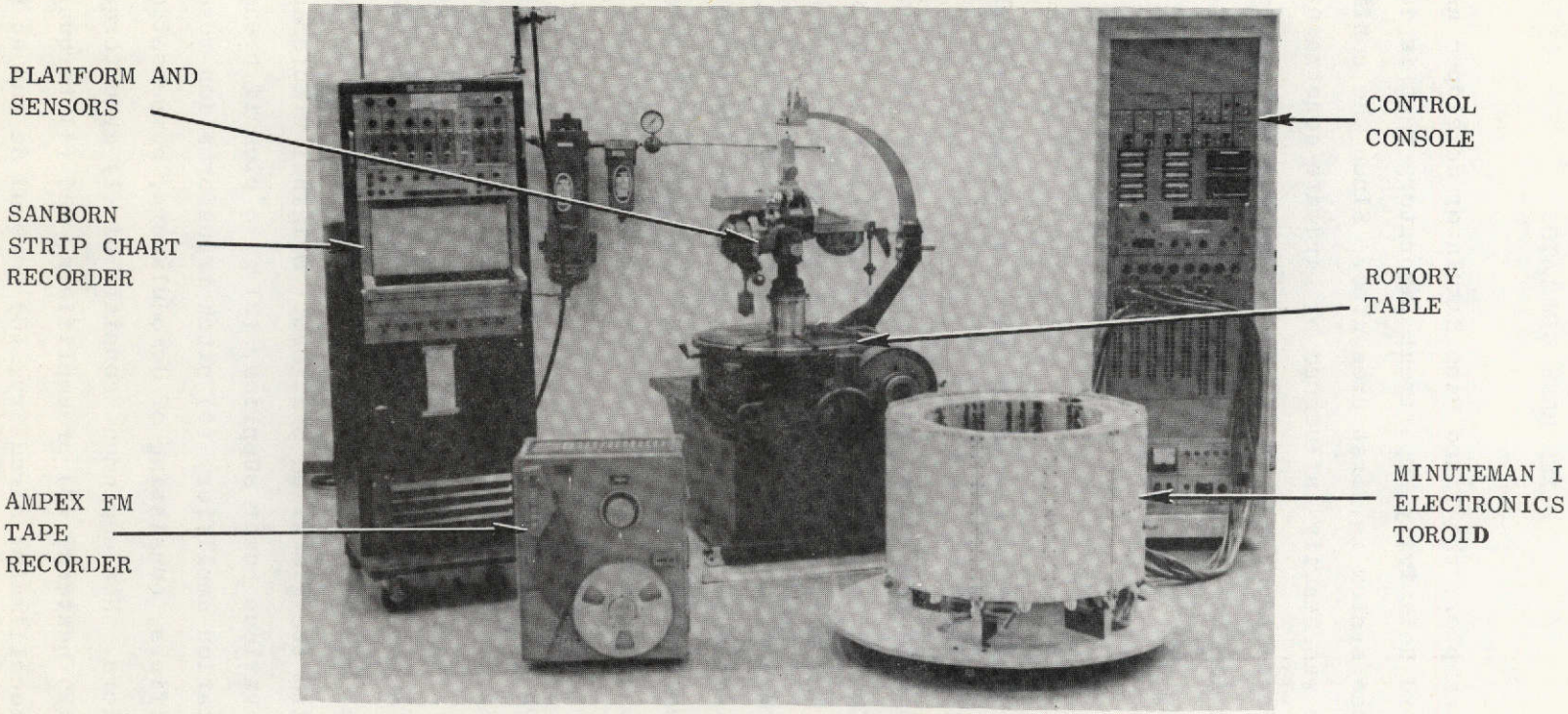

FIG. 1 FIXED BASE SIMULATOR. The control console and Minuteman I electronics support and control the platform and sensors. Analog recorded data is digitized before processing.

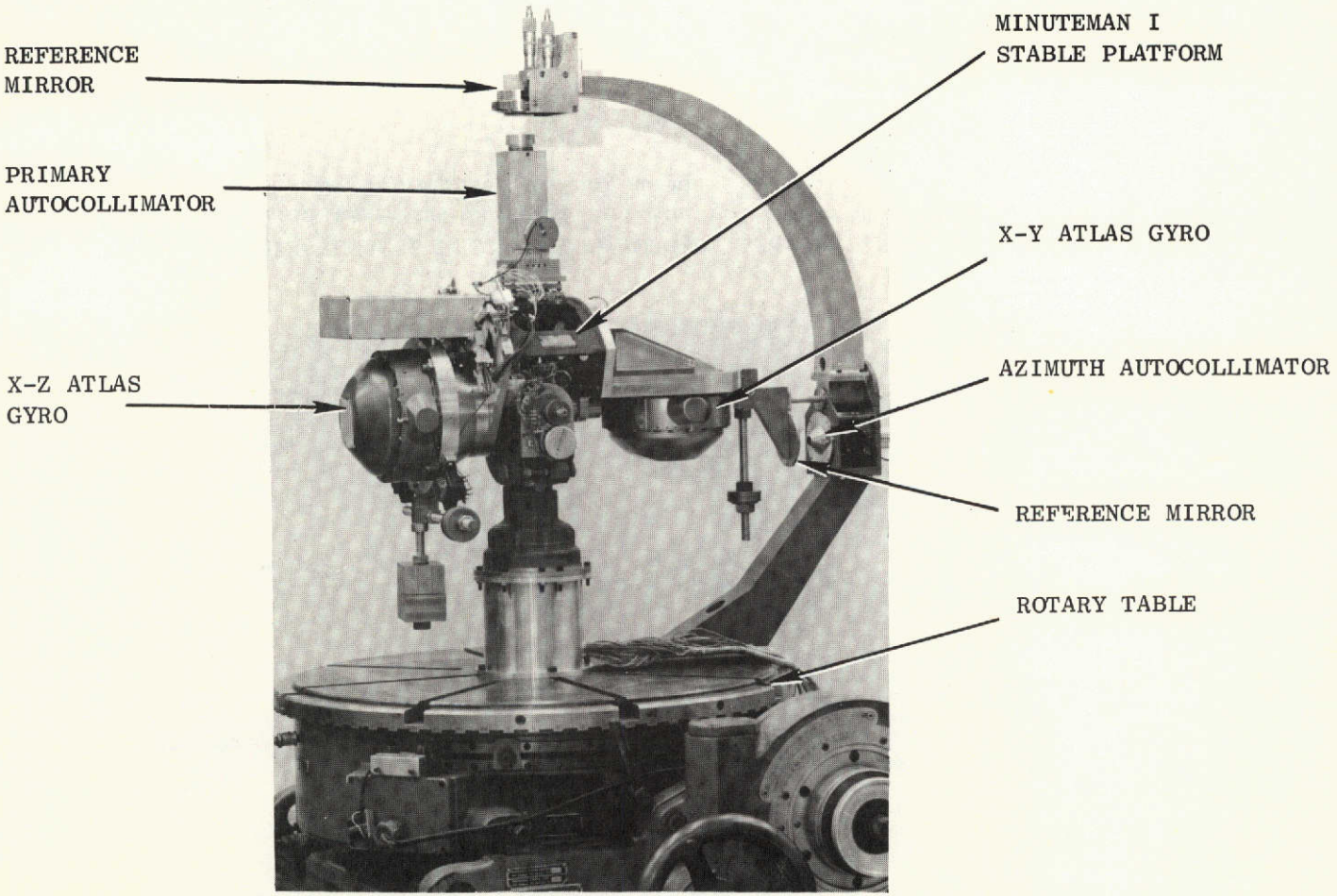

FIG. 2 PLATFORM AND SENSORS ASSEMBLY. The two autocollimators or the two gyros provide the reference required for stabilization.

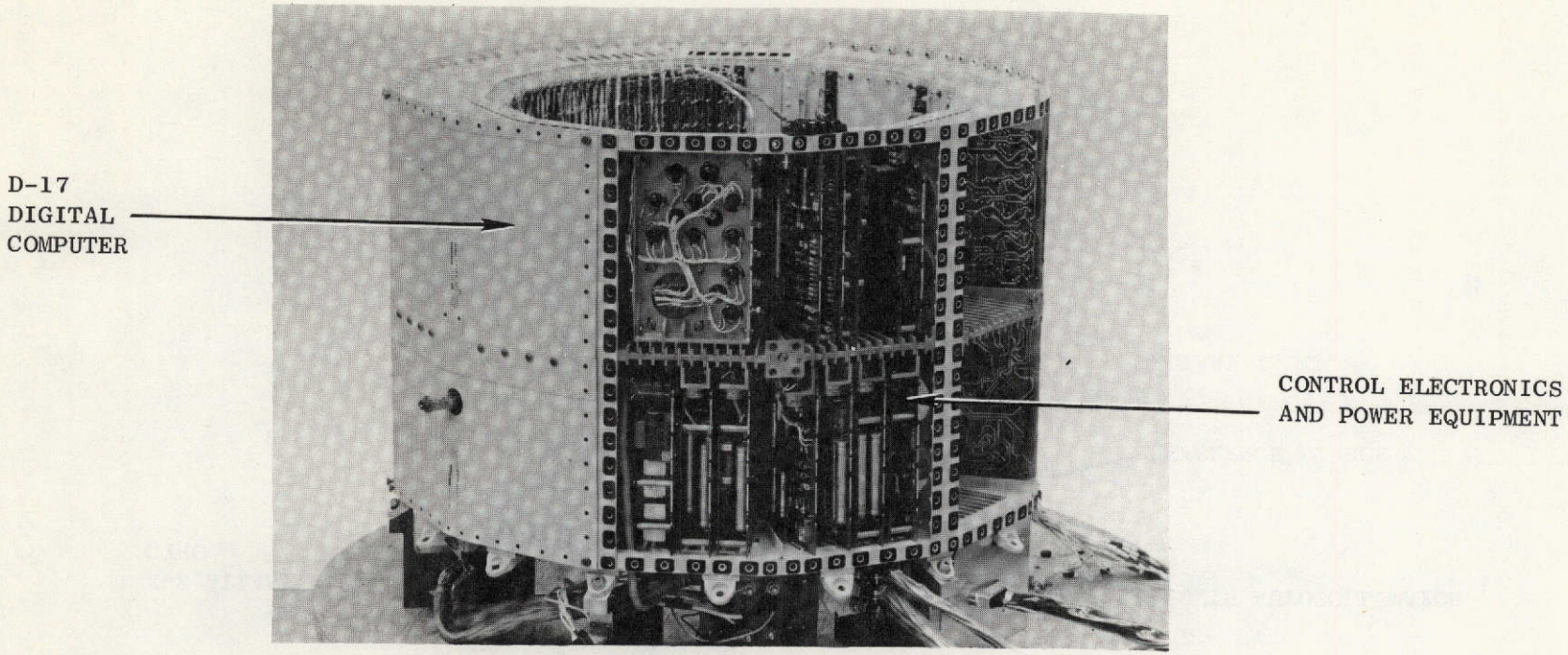

FIG. 3 MINUTEMAN I ELECTRONICS TOROID. Several modules are used to provide power and control platform motion. The D-17 computer is not used.

and (9) instrumentation. These are all discussed in greater detail later in this chapter.

In all modes of operation, the platform is stabilized using either the gyro or the autocollimator signals. Figure 4 shows the basic operation of the Fixed Base Simulator.

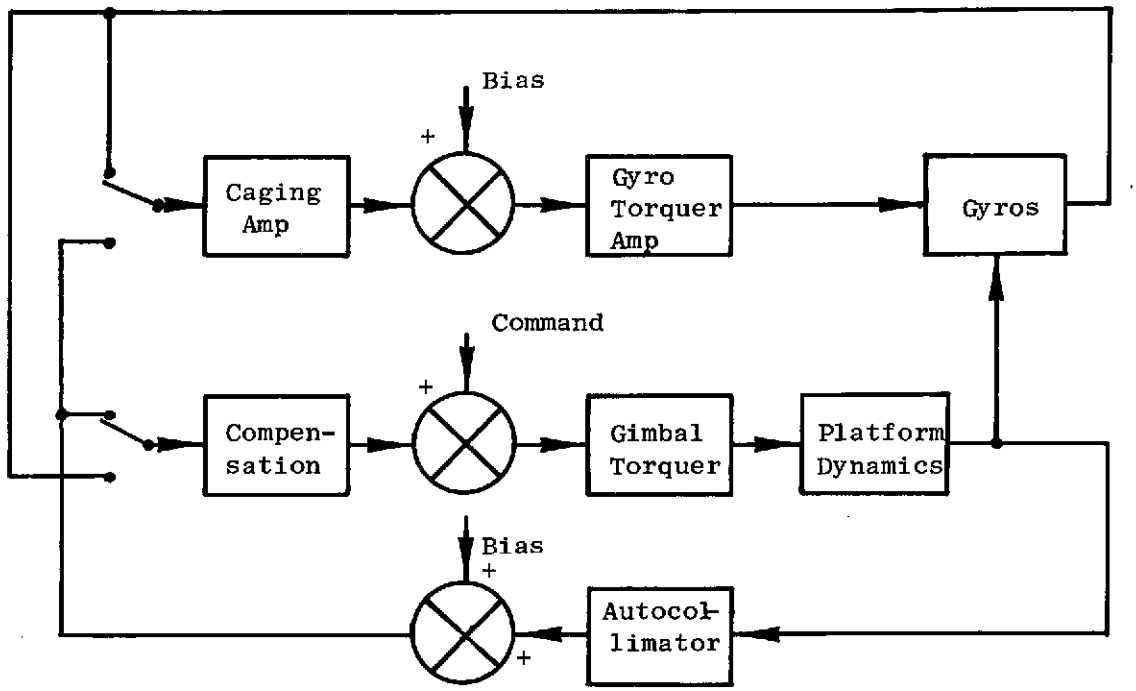

Fig. 4. FIXED BASE SIMULATOR FUNCTIONAL DIAGRAM.

Motion of the platform is sensed by the gyros and the autocollimators, producing ac signals proportional to angular displacement. The instrument signals are amplified and demodulated and then sent to the instrumentation equipment. Also, depending on the mode of operation, either the gyro signals or the autocollimator signals are passed through compensation networks and amplified to drive the platform gimbal torque motors. The direction of torque is that required to null the controlling sensor output. Simultaneously, signals from the noncontrolling sensors are used as inputs to the gyro caging amplifiers, required to keep the gyro pickoff in the small linear region about null, or to maintain optical reference.

Command inputs are introduced in three different ways. First, the outputs of the autocollimators can be biased directly. Second, bias torque levels can be applied to the gyros through the torquer amplifiers. Finally, command torque signals can be added to the compensated error signals at the inputs to the gimbal torquer power amplifiers.

Several modes of operation allow selection of the controlling sensors, on and off switching of gyro spin motor power, and inhibiting of caging amplifier outputs.

B. Simulator Development

Before giving a more detailed discussion of the system, the evolution and development of the Fixed Base Simulator is described both as a matter of interest and to give a better understanding of the final configuration. This description is basically chronological in order, and attempts to outline the rationale and constraints which affected the course of development.

1. Platform Selection

The first basic requirement of a fixed base simulator was a movable platform to which motion and attitude sensors could be mounted. To speed development, existing hardware was sought. It was found that several aircraft and missile stable platforms were available either as government surplus or commercially. Of these platforms, the ten-year-old Minuteman I was selected for several reasons. The primary advantage of this system is its "inside-out" gimbal arrangement, in which the motion sensors are physically located outside of the gimbal bearings and no gimbal rings are required. This arrangement allows mounting of test instruments to the control element without volume constraints. The direct drive dc gimbal motors do not inherently limit pointing accuracy, and the precision gimbal bearings do not present a serious stiction problem. Furthermore, two complete guidance electronics packages and several stable platforms were available as surplus equipment, eliminating any spare parts concern.

The major disadvantage of the Minuteman I system was the unavailability of the gyros and velocity meters due to their security classification.

The Minuteman I two-degree-of-freedom air bearing gyros would have been ideally suited for use with the simulator, but it was felt unlikely that the instruments would be declassified in time to be of use.

It was further felt that other gyros could be made compatible with the Minuteman system, and consequently, an order was placed for the equipment.

2. Sensor Selection

The second basic requirement of the simulator was sensors closely analogous to those of the Relativity Experiment; i.e., free rotor gyros and a telescope. Consideration was first given to the gyros.

a. Gyro

A search for gyros revealed no suitably priced free rotor, or gimballed two-degree-of-freedom gyros other than several fifteen year vintage Atlas missile instrument gyros already possessed by the Stanford Guidance and Control Laboratory. The gyros are large (4.6 kg), two-degree-of-freedom, floated instruments.

Available documentation on these instruments consisted solely of a brief familiarization manual. No wiring diagrams, mechanical drawings, detailed performance specifications, or operating manual were found. Nevertheless, since the gyros were immediately available, and were reasonably analogous to the Relativity Experiment gyros, it was decided to attempt to integrate them into the Minuteman I system.

b. Autocollimator

Before proceeding with the gyro modification, however, the question of a suitable analog to the Relativity Experiment telescope had to be resolved. Use of a telescope would have required development of an artificial star, and made the system subject to angular errors arising

from translations of the telescope and artificial star. An autocollimator, which provides its own light reference, has neither of these disadvantages, yet is sufficiently similar to a telescope to make meaningful studies. A survey showed that no autocollimator meeting the simulator requirements was commercially available. Since an in-house capability existed to design and build a suitable model, it was decided to develop one rather than compromise simulator design goals. Design and fabrication of the instrument was postponed until the rest of the system was near completion, since no major development problems were anticipated.

3. Minuteman I Guidance Assembly

Delivery of the Minuteman I guidance assemblies ushered in an extremely interesting and enlightening phase of the system development. The assemblies arrived just as they were taken from the missile, with the exception that the inertial instrument, fan, battery, and ordnance switching unit had been removed and the hermetic seal broken.

Each cylindrical assembly is covered by a reflective surface to prevent excessive thermal radiation to internal parts and to provide a hermetic seal. Inside the cover is a hollow, twelve-sided, cylindrical structure, referred to as the toroid, in which the guidance computer and stable platform electronics are located. The stable platform rests on a heat exchanger surrounded by the toroid. The toroid is separable into two parts: the D17 guidance computer, and the platform electronics. Although functional, the computer is not employed in the simulator because of the amount of supporting equipment and software which would have been required.

Mounted on the stable platform is an alignment unit consisting of bubble levels for vertical reference and a mirror for use as an optical azimuth reference.

A period of hardware familiarization followed, in which the physical layout, external connectors, and internal wiring were studied.

Before power could be applied to the system, cooling requirements had to be evaluated. The original Minuteman I ground cooling system was complex and required pumping refrigerated water through the

assembly in addition to circulating pressurized helium by means of a vaneaxial fan.

Laboratory cooling requirements were judged not as severe since a hermetic seal is not necessary. However, the amount of cooling required was difficult to analyze. Furthermore, a decision on whether or not to use the guidance computer had not yet been made. To ensure adequate cooling, design of an air blower ducting system was therefore conducted in parallel with other tasks.

The toroid was removed from the missile mounting structure and bolted to a circular plywood frame equipped with casters to provide mobility. A blower was attached to the "bonnet" on top of the toroid which originally held the vaneaxial fan. Sheet metal skirts were placed around the toroid base to cover the gap between the bottom of the toroid and the plywood frame. In this configuration, air was forced down through the center of the hollow toroid, deflected by the plywood and sheet metal skirts, and circulated back up past the electronics modules mounted in the vented toroid walls. Later, after deciding not to use the computer, it was found that operating temperatures were acceptable without using the cooling system. As a consequence, the blower was removed from the toroid in the final configuration.

4. Power

Concurrent with the cooling system development, a power source for the platform electronics was sought. The Minuteman system requires 28 VDC, but current requirements without the computer were not accurately known. Estimates ranged from 10 to 30 A. A reasonably priced ($25) power supply meeting the maximum requirements was procured. The unit is a well-regulated, safeguarded, Autonetics surplus supply which had originally been a part of the Minuteman I ground equipment. The sole drawback of this power supply was that it required 115 V, 3Ø, 400 Hz input power which was not available. To provide 400 Hz power, a pair of 60 Hz to 400 Hz motor-generator sets, U.S. Marine Corps surplus, were reclaimed from Stanford University storage. The required input power to the motor-generators, 115 V, 3Ø, 60 Hz, rather than the 208 V, 3Ø power available

in the laboratory, was provided by three large power transformers again found in storage. Connecting these transformers in a Wye configuration provided the necessary voltage stepdown. All of the components were cabled together and satisfactory power was established.

With adequate power available, studies were made of the platform electronics voltage levels, waveforms, and other characteristics. These studies were necessary since only module schematics and no detailed performance specifications were available. The primary objective was to determine the interface with the rest of the simulator.

5. Gyro Operation

At the same time, work began on determining the operating characteristics of the Atlas gyros. The work was severely hampered by the lack of documentation. It is imperative to note that the professional assistance of Dr. W. G. Pondrom was crucial in the successful completion of this task.

After extracting two gyros from an Atlas stable platform, it was first necessary to determine the function of each connecting wire. A gyro wiring schematic was eventually deduced from ohmic measurements. A gyro test breadboard was then constructed which allowed activation of the pickoffs and torquers and application of power to the spin motor.

a. Pickoff and Torquer Coupling

It was soon deduced that the pickoff and torquer coils were imbedded in a common magnetic structure. This implies that non-cancelling ac currents in the pickoff coils, which occur when the pickoff is off-null, will induce currents in the torquer coil, thereby loading the pickoff circuit. The result is poor off-null pickoff performance. In the intended application, this characteristic was not important since the gyro was held at null by the servo control loop.

However, simulator requirements demanded good off-null performance, so equivalent current source torquers were needed to eliminate pickoff loading. Design of torquer amplifiers was postponed while other characteristics were determined.

b. Pickoff Modification

It was necessary to make the gyro pickoffs compatible with the Minuteman electronics. Atlas pickoff excitation frequency is 400 Hz while the Minuteman I frequency is 4800 Hz. In addition, the Atlas excitation requires 4.65 VDC power for the torquer electromagnet with one side grounded, while the Minuteman gyro has no dc excitation and is capacitively coupled. Finally, Minuteman excitation amplifier voltage is 100 V rms, while the Atlas originally used 8 V. (The 8 V amplitude was later changed to 30 V to increase pickoff gain.) Extensive modifications were clearly required. Detailed documentation of these modifications is presented in the subsystems section later in this chapter.

c. Spin Motor Power

The next design step was to provide spin motor power to the gyro. Available Minuteman power was 400 Hz, 22 V, 3Ø quasi-square wave (+,0,-,0,+,...). Required Atlas power is 24 V, 3Ø sine wave with one side grounded. Isolation and voltage stepup to achieve the appropriate rms power were accomplished by hand winding three bifilar coils on ferrite cores. These transformers were placed in a custom box and potted in beeswax.

d. Breadboard Test

At this point the gyro test breadboard was sufficiently complete to fully operate the gyro, with the exception of the heater. The Minuteman caging amplifier, used in controlling the redundant fourth gyro axis, was taken from each of the two guidance assemblies. The gyro pickoffs were connected to the amplifier inputs and the torquers to the outputs through isolation transformers. The caging amplifier outputs are very nearly current sources so pickoff loading was not a problem. The gyros were then successfully operated closed loop, with the pickoff outputs held at null. Keeping one gyro axis caged, rough estimates of the pickoff and torquer scale factors were made using earth rate as a reference. These estimates were used in the torquer amplifier design

and also indicated the need for pickoff preamplifiers to achieve sufficient platform stabilization loop gain.

Enough information had been gained at this time to proceed with the electronics design. Mechanical design of two adapter brackets to hold the gyros on the platform was also begun.

6. System Configuration

While this work was going on, system layout design was initiated. Connector pin assignment, cabling requirements, grounding, shielding, switching, and monitoring were each planned in detail prior to system assembly.

7. Autocollimator Design

As system layout and electronics design proceeded, and after the gyro mounts had been completed, design of an autocollimator was started. Once the optics and light source had been selected, detailed mechanical drawings were made. An adjustable reference mirror mount also was designed.

8. Rotary Table Platform Mount

Questions about where to mount the platform and how to orient it to locally vertical and polar positions were resolved when a 24 in. rotary table with base was made available by the Stanford Physics Department. A steel plate with bolt brackets was fabricated to adjust the table base in azimuth and to level the table. The table and plate were positioned at a point where theodolite sightings of Polaris could be made through a special window in the laboratory ceiling.

9. Platform Stabilization

Upon completion of the electronics design and system wiring, but before the autocollimator was completed, the platform was stabilized using the gyros. At first, the system was only marginally stable due to the decrease in loop gain caused by the increased moments of inertia of

the modified platform. Stability of the system was improved by increasing the gain of the pickoff preamplifiers from 10 to 40. Bandwidth of the servo loops was observed to be approximately 15 Hz.

The autocollimator was completed several weeks after the initial gyro stabilization. This autocollimator and a second unit designed on another Stanford project were incorporated into the system. Initial attempts to stabilize the platform using autocollimator signals failed due to instability induced by flexibility in the primary autocollimator mount. The instability was eliminated by filtering, reducing the bandwidth of the autocollimator signal below the dominant bending frequency.

10. System Verification

The temporary autocollimator reference mirror mount which had been used up to this point was replaced by a newly designed unit. The new assembly was attached to the rotary table and aligned. After aligning the mirror and bringing autocollimator and gyro axes into coincidence, basic data on scale factors, drift rates, and noise levels were taken.

A peculiar anomaly appeared in the gyro and autocollimator output signals upon close inspection of the data. It was discovered that large, very low frequency disturbances were appearing in the instrument signals. In particular, when the platform was stabilized using either the autocollimator or gyro signals, the offset in the noncontrolling instrument varied approximately as a square wave with 20 arcsec amplitudes and 40 to 400 sec periods.

The cause of the disturbance was eventually isolated to an interaction between the 400 Hz quasi-square wave power source for gyro spin and the 1.2 MHz crystal oscillator, used in modulating power to the autocollimator light source. The two separate ac sources would lock together for many seconds and then slip relative to each other. When this happened there was a sudden large change in offset in the autocollimator output.

A variable frequency generator was substituted for the 1.2 MHz crystal and was varied from 0.9 to 1.5 MHz. The noise output of the instrument increased rapidly as the drive frequency approached 1.2 MHz in either direction, but just as it reached 1.2 MHz, the random noise disappeared and the low frequency square wave offsets appeared. The 1.2 MHz

crystal oscillator, which had been selected at random, had the ideally wrong operating frequency. By varying the frequency, a noise minimum was found at 1.32 MHz, and a new crystal at this frequency was installed.

New measurements were made of gyro bias, torquer scale factor, and gyro pickoff scale factor. The bias and torquer scale factor were deduced by turning the rotary table about a vertical axis while under autocollimator control, and measuring the torquer amplifier voltages required to keep the gyro pickoffs at null. Gyro pickoff scale factors were found by putting known step changes into the torquers and measuring the time required for the pickoff voltage to change a known amount. Excellent consistency of results indicated the system was operating properly.

C. Subsystems

All of the major components of the Fixed Base Simulator have been introduced above in the discussion of system development. Since an intimate knowledge of most of these components is necessary to interpret the results presented later in this dissertation, details on their construction and operation are now provided. Circuit schematics of newly developed electronic modules are included in the Appendices.

1. Sensors

The sensor subsystem consists of the two gyros, and the primary and azimuth orientation autocollimators.

a. Gyros

The ARMA Atlas missile gyros used in the simulator, and pictured in Fig. 5, are two-degree-of-freedom, floated inertial grade instruments. Angular momentum is 10×10^6 gm-cm^2/sec.

A spherical float is centered inside the housing by means of two orthogonal sets of flexible wires, which also serve as power leads. One set connects the float to an intermediate gimbal ring; the other set,

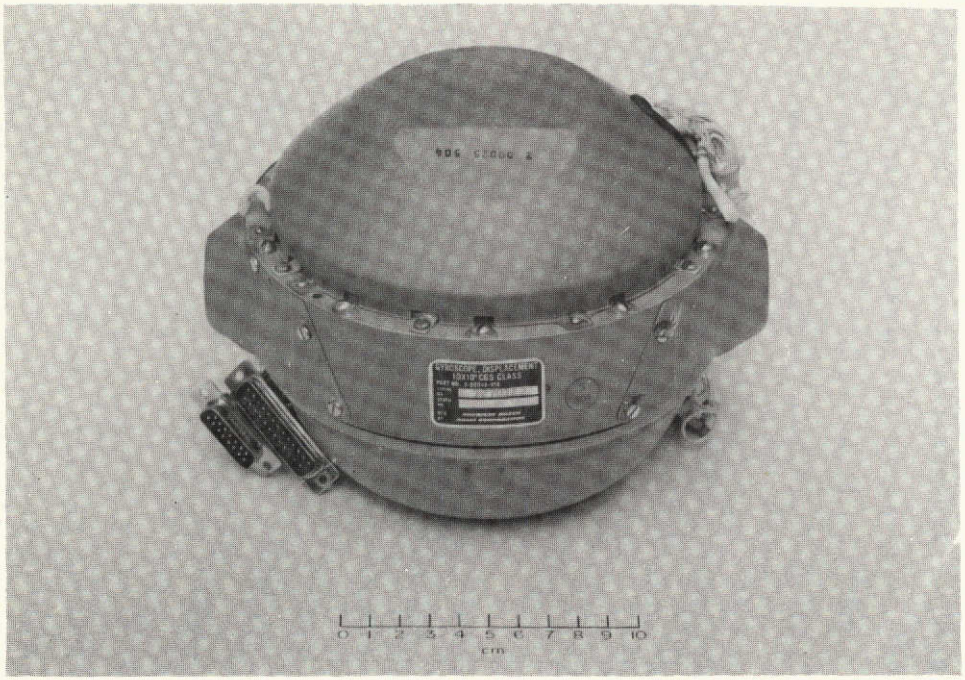

FIG. 5 ARMA ATLAS MISSILE TWO-DEGREE-OF-FREEDOM GYROSCOPE. Viscosity of the flotation fluid creates low frequency cross-axis coupling. Except for this, the gyroscopes are closely analogous to the free rotor gyros of the Stanford Relativity experiment.

oriented 90° away, connects the gimbal ring to the housing. A rotational degree of freedom exists about each set of wires. Within the float, a pair of flywheels are driven by two 400 Hz, 4 pole induction motors. Also contained in the float are a pair of electromagnets, one at each end of the spin axis, which are excited by both ac and dc voltages. A pair of coils are mounted on the housing directly across from the electromagnets to provide two axis pickoff and torquing functions. Direct current through the torquer coils sets up a magnetic field which reacts with the dc electromagnet field to produce precessional torques. AC excitation of the electromagnets induces currents in the pickoff coils, wound in the form of figure eights. When the float is off null, these coils develop voltages proportional to the relative angular displacement of the float.

Heating coils and temperature sensing resistors are mounted on the housing to keep the flotation fluid at the neutrally buoyant temperature. The Atlas platform was temperature controlled as a unit so there were no gyro heater electronics. Thus, new temperature control circuits were designed.

Measurements were made of the viscous friction and elastic restraint parameters. This was accomplished by torquing the float with the wheel turned off. Observing changes in steady state pickoff voltage with known small changes in torque yielded estimates of the elastic restraint coefficient h/k. Measured values are 424, 708, 1072, and 515 sec for the X, Y, Z, and X_{RD} (redundant) gyro axes, respectively. Similarly, observing the time rate of change of pickoff voltage with large changes in torque, gave measurements for the dimensionless viscosity coefficient h/c. These are 1.96, 21.0, 35.7, and 2.43.

(1) Torquer Amplifiers. As discussed in the previous section, new torquer electronics had to be designed to overcome undesirable coupling between the pickoff and torquer. A broadband current source was initially contemplated to eliminate the coupling. However, after experiencing difficulty with amplifier oscillation, the amplifier was designed to have very high output impedance only at the critical 4800 Hz pickoff excitation frequency and moderate impedance elsewhere.

Each torquer amplifier consists of a high bandwidth, low drift, chopper-stabilized preamplifier feeding a high-current driver with a twin-T circuit in the driver's feedback path. The twin-T provides high loop gain at 4800 Hz. A current sensing resistor in series with the load provides the necessary feedback to make the combined circuit a high bandwidth (70 KHz) current amplifier with excellent performance at 4800 Hz.

The torquers provide extremely stable torquing current with drift rates less than 1 μA/day, thereby eliminating the torquer amplifiers as a significant source of gyro drift. They also have a 140,000:1 linear dynamic range with a maximum torquing capability of 3.5 times earth rate. This large dynamic range allows compensation of large biases while not masking the more interesting small changes in required torquing levels. Torquer amplifier output can be precisely biased by adjusting a ten turn potentiometer connected to a precision voltage regulator. The wiper voltage provides input to the torquer amplifier. Closing a control panel switch allows maximum torquer output for gyro slewing. Slewing capability is required to quickly reorient the platform without forcing the gyros into their stops.

When all four torquer amplifiers were initially connected to the same power supply, heavy oscillation resulted. The oscillation, caused by feedback through the small power supply impedance, was eliminated using four decoupling networks. A low pass input filter was also required to keep the Minuteman redundant axis caging amplifier from saturating.

Each amplifier has two inputs: one driven by a caging amplifier, the other by the biasing circuit. The two scale factors K_{T_C}, K_{T_B} are -6.04 and -10.00 mA/V, respectively. Another scale factor, which has proven to be more convenient is use, relates the induced gyro precession rate to the voltage across the 92.1 ohm torquer amplifier current sensing resistor. This parameter was deduced from a series of measurements of the torque voltage, taken at 30° azimuth increments with the spin axis vertical, required to hold the pickoff at null. Fixed and gravity sensitive drift effects are held constant in this way, leaving only the known horizontal component of earth rate in the gyro input axes as a variable. The values of this parameter, K_{T_o}, are 31.6, 33.4, 34.1,

32.0 μrad/sec-V for the X, Y, Z, and X_{RD} gyro channels, respectively. All other desired torquer scale factors are easily derived using the above values.

(2) Pickoff Excitation and Preamplifiers. In the discussion on system development earlier in this chapter, several problems in making the Atlas gyro pickoffs compatible with the Minuteman electronics were pointed out. The Atlas gyro requirements for both ac and dc electromagnet excitation, the phase shift due to a higher excitation frequency, and a lower excitation level were the primary concerns. New requirements of the pickoff, not related to incompatibility, were to reject noise and to establish the proper loop gain for system stability. Electronic modifications separated into two areas: alteration of the excitation signal and the development of a preamplifier. Each is discussed in turn.

The 100 V rms Minuteman pickoff excitation amplifier output is used to drive the primaries of two stepdown isolation transformers. One end of each secondary is connected to a 5 VDC power supply and the other end to a gyro excitation coil. This configuration simultaneously isolates the torquer magnet dc excitation from the amplifier and reduces the excitation voltage to a nonsaturating level. The amplifier is mounted at the base of the platform to isolate its high voltages from other electronics. The transformers are conveniently mounted on one of the gyro adaptors on the stable platform.

Compensation of the 40° phase lag could have been accomplished either in the excitation or in the pickoff output. However, uncertainties in the magnitude and stability of the Q of the excitation isolation transformer made it desirable to shift the phase at the input to the preamplifier. Each preamplifier, therefore, consists of a narrow passband filter centered at the 4800 Hz excitation frequency, followed by a unity gain phase lead network at the input to an amplifier with single ended input and differential output.

The gain of the three primary preamplifiers is 40, while the redundant channel is 10. An isolation transformer was also required at the output of the redundant channel preamplifier to make it compatible

with the Minuteman caging amplifier. To minimize noise pickup, the preamplifiers are located in a box atop one of the gyro brackets.

(3) Pickoff Postamplifiers. The amplified signals from the new pickoff preamplifiers are sent to the Minuteman electronics toroid via the control console. Inside the console the three primary channel signals are tapped so that each signal is sent to two separate Minuteman ac amplifiers. These amplifiers, which formerly were the gyro and velocity meter (VM) pickoff amplifiers, were renamed postamplifiers to distinguish them from the newly developed preamplifiers. The VM and gyro postamplifiers are all identical ac differential amplifiers with a gain of 220 and negligible phase shift.

(4) Pitch Transformation Resolver. Signals sent to the VM postamplifiers are amplified and immediately demodulated in the Minuteman VM control amplifiers. However, two of the three signals sent to the gyro postamplifiers pass through the platform pitch transformation resolver before being demodulated. The resolver couples the signals by the relationships

$$x' = x \cos \theta + y \sin \theta$$

$$y' = -x \sin \theta + y \cos \theta$$

where θ is the inner platform gimbal angle. When the angle θ is zero, both the VM and gyro demodulated signals are the same except for electronic errors. The transformed signals are required for platform stabilization when the gimbal axes are not orthogonal.

(5) Pickoff Demodulators. The outputs of the postamplifiers and the pitch transformation resolver are finally sent to the control amplifiers for demodulation. A 4800 Hz square wave signal, synchronous with the signal used by the pickoff excitation amplifier, provides the reference. Formerly, the demodulated signals went directly to the platform and VM servo compensation networks. In the Fixed Base Simulator,

however, the signals are sent to instrumentation jacks and to relays. The relays allow the signals to be opened selectively, transferred to the caging amplifiers, or sent back to the control amplifier compensation networks.

(6) Pickoff Scale Factors. Measurements of the overall pickoff scale factors are based on knowledge of the torquer scale factor, which in turn is based on earth rate as the primary reference. The procedure is as follows.

(1) The caging amplifier for the channel of interest is disabled and precession is manually nulled using the biasing potentiometer.

(2) Pickoff and torquer output voltages are recorded.

(3) A step change is introduced into the torquer through the biasing network and simultaneously a stopwatch is started.

(4) The new torquer output voltage is recorded.

(5) The time required for the pickoff voltage to increase to a value much larger than the initial is recorded.

With the precession rate known, the pickoff scale factor is computed as

$$K_g = \Delta V_g / \Delta t \Delta V_T K_{T_o}$$

where

K_g = pickoff scale factor (mV/μrad)

ΔV_g = change in pickoff voltage (mV)

Δt = elapsed time (sec)

ΔV_T = change in torquer amplifier output voltage (V)

K_{T_o} = torquer output scale factor (μrad/sec-V)

Several measurements of each scale factor were made and averaged. The scale factors for the X, Y, Z, and X_{RD} axes are 6.03, 6.70, 7.51, and 5.74 mV/μrad, respectively.

(7) Caging Amplifiers. It is necessary to keep the gyro floats near null to maintain linear pickoff performance and to prevent the floats from drifting into their stops. However, it is also necessary to keep caging loop dynamics from interfering with the primary function of sensing changes in attitude. To satisfy these needs, rebalance servo loops were designed with bandwidths less than the lowest signal frequency of interest (0.1 rad/sec). In addition, the original Minuteman caging amplifier was kept to control the noncritical redundant axis.

It was further desired to have the caging amplifiers be able to cancel out earth rate without requiring a large position offset. For this reason, a proportional plus integral control law was employed for the three primary channels. The proportional feedback of the redundant axis amplifier was not altered.

(8) Caging Amplifier Gyro Supervision. At low frequencies, the motion of float relative to the housing can be adequately modeled as

$$\dot{\sigma} = \omega^{i} + \omega^{c} + \omega^{d}$$

where

$\dot{\sigma}$ = pickoff rate

ω^{i} = inertial angular rate of the housing about the pickoff axis

ω^{c} = commanded rate

ω^{d} = drift rate

In steady state, $\omega^{c} = -(\omega^{i} + \omega^{d})$. With the pickoff providing a voltage $V_g = K_g \sigma$, and letting V_I be the integral of V_g, the feedback control law becomes $V_F = -C_1 V_g - C_2 V_I$, with arbitrary gains C_1 and C_2. This voltage is then put into the torquer amplifier which precesses the float at a rate

$$\omega^c = K_T V_F$$

where

K_T = overall torquer scale factor

(The scale factor K_T is related to the previously defined torquer scale factors K_{T_o} and K_{T_c} by $K_T = 92.1\ K_{T_o} K_{T_c}$, where 92.1 is the resistance in ohms of the amplifier current-sensing resistor.) Combining all of the above relations, Laplace transforming, and neglecting initial conditions results in the equation

$$S\sigma + K_T K_g C_1 \sigma + K_T K_g C_2 \frac{\sigma}{S} = \omega^i + \omega^d$$

Multiplying through by s or differentiating the original expressions yields

$$\left(s^2 + 2\zeta\omega_n + \omega_n^2\right) \sigma = s(\omega^i + \omega^d)$$

where

$\omega_n = \sqrt{K_T K_g C_2}$ = control loop natural frequency

$\zeta = \sqrt{K_T K_g C_1^2/4C_2}$ = control loop damping ratio

The gains C_1 and C_2 were selected to produce a natural frequency of 0.1 rad/sec and a damping ratio of 0.7.

The caging amplifiers were implemented using one operational amplifier in each circuit. Figure 6 is a simplified block diagram of the caging loop, while Fig. 7 shows a basic schematic of the caging amplifier.

An additional small resistor in series with a switch is tied between the summing junction and the output of the operational amplifier to allow manual inhibiting of the caging amplifier output.

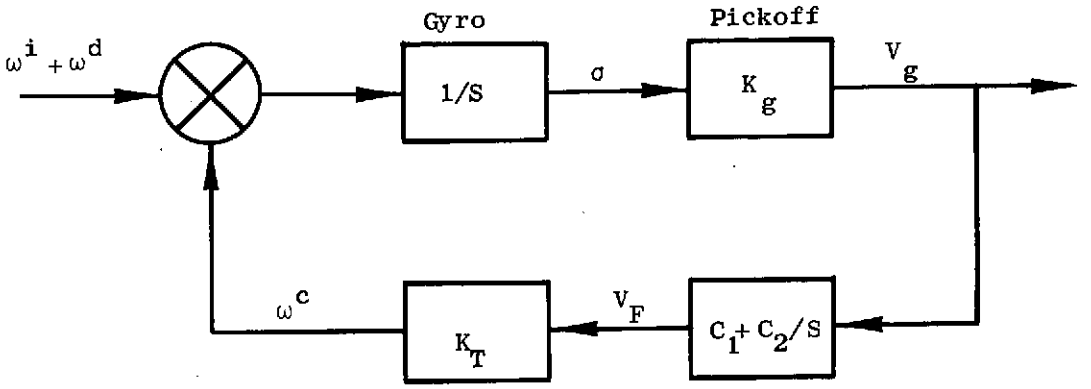

Fig. 6. GYRO CAGING LOOP. When the platform is autocollimator stabilized, the gyro pickoff signals can be fed back to the torquers to compensate for earth rate and gyro drift.

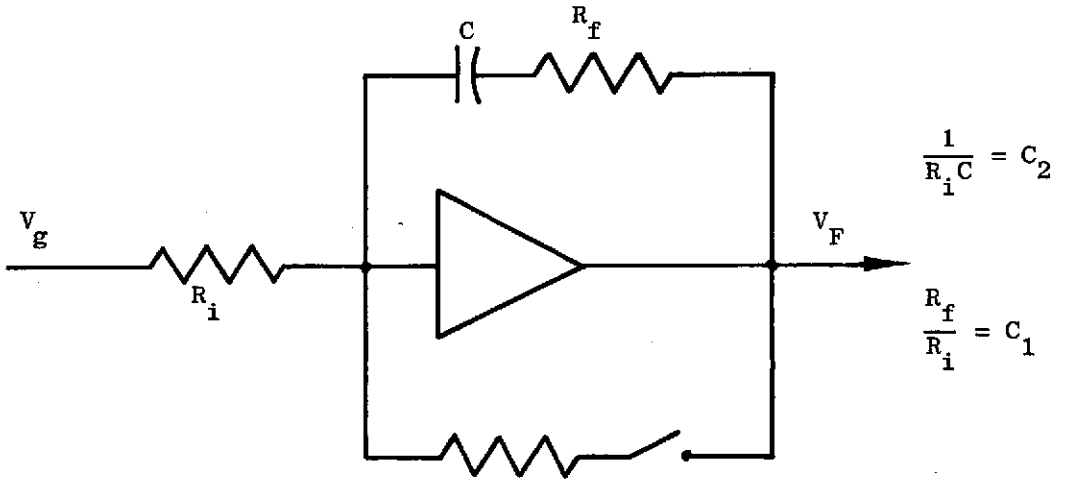

Fig. 7. BASIC CAGING AMPLIFIER MECHANIZATION. A single operational amplifier provides both proportional and integral control.

(9) Caging Amplifier Autocollimator Supervision. A second caging loop is required when the gyros provide the platform stabilization signals. In this case, the gyro pickoff signals are held at null by the servo. However, any error torques on the gyro float cause the entire platform to drift away from its original orientation. To maintain constant orientation, error signals from the autocollimators are used as inputs to the caging amplifiers. The caging amplifiers then cause the torquer amplifier to exactly cancel the drift torques in the steady state. Figure 8 shows a simplified autocollimator supervision loop.

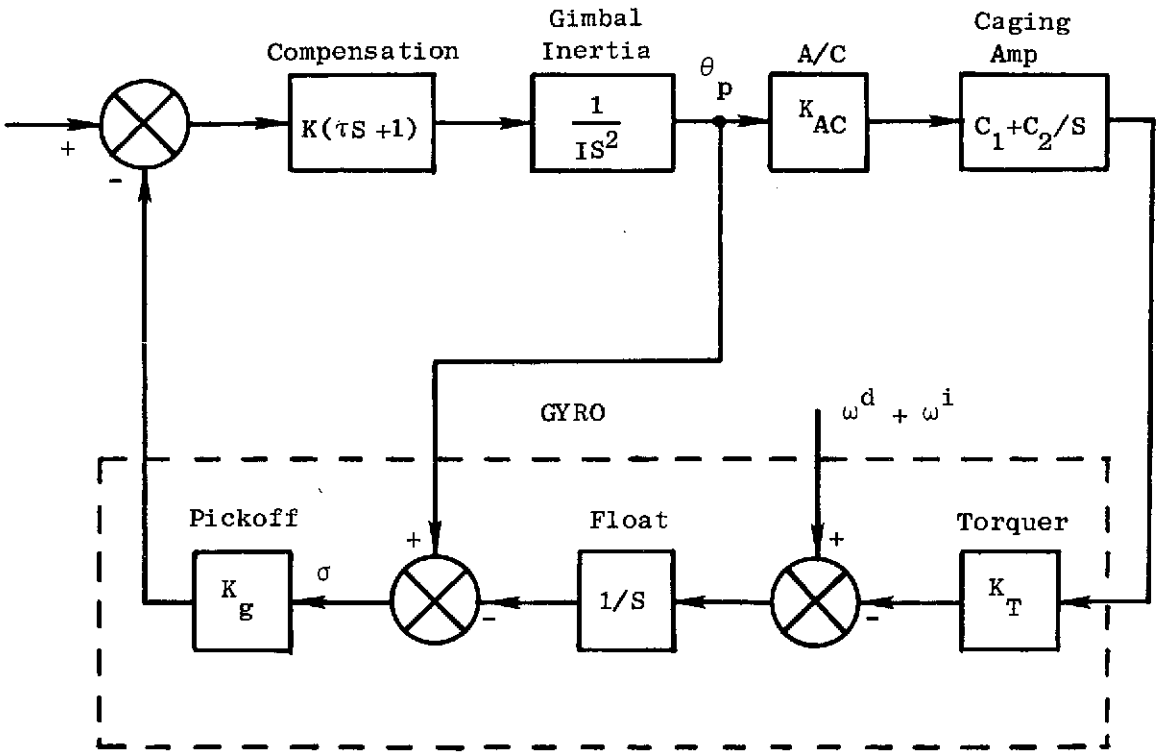

Fig. 8. AUTOCOLLIMATOR SUPERVISION LOOP. To maintain the orientation of the platform while under gyro control, autocollimator signals are used to torque the gyros.

(10) Heaters. It is essential to keep the flotation fluid at a temperature which makes the float neutrally buoyant in order to minimize drift torques. Tight temperature control is maintained by a new set of electronics using the temperature sensitive resistor mounted on each gyro as the sensor. This resistor is used in a bridge circuit, the output of which is compared to a precision reference voltage. An integrated circuit thyristor controller is used to switch a thyristor on and off, allowing a sufficient number of 60 Hz full and half waves to pass through the gyro heater coils to maintain temperature. High gain in a small linear region allow the temperature of each gyro to be held at 40°C ± 0.1°C. The heater circuits are completely isolated from the rest of the system, and are normally operated continuously to avoid long period thermal transients.

b. Autocollimators

Optical reference for the Fixed Base Simulator is provided by two different autocollimators: one for maintaining azimuth orientation, the other as the primary test sensor. The azimuth unit, which was used in a spining vehicle simulator constructed in the Stanford Guidance and Control Laboratory [L1], has good wideband performance and moderately low noise. Recent advances in solid state electronics, however, made possible significant improvements in noise levels and null stability. These advances were used advantageously in the design of the primary autocollimator, and resulted in an improved sensor described below.

(1) Primary Sensor Configuration. The newly developed autocollimator is pictured in Fig. 9. Visible externally are the main body, objective lens and mount, light source housing and heat sink, and preamplifier box. Also shown is the reference mirror and its adjustable mount.

(2) Primary Sensor Optical and Mechanical Arrangement. A functional diagram of the autocollimator, Fig. 10, shows the arrangement of the main mechanical and optical components.

The infrared emitting diode is switched on and off at 2.2 KHz. Radiated energy is collected by the field lens and passes through a 0.050 in. square aperture located at the focal plane of the objective lens. (A square rather than a circular aperture is used to enhance linearity.) A portion of the emerging energy is diverted 90° by a cubical beamsplitter, and passes through the objective lens, emerging as a collimated beam. The beam is then reflected off the reference mirror, and passes back through the objective lens forming a focused image of the square aperture on the four quadrant detector as indicated in Fig. 11.

(3) Primary Sensor Signal Conversion. The position of the aperture image on the photodetector is converted into measurements of the small angles θ_x and θ_y between the autocollimator optical axis and the reference mirror normal as discussed below. Each quadrant of the diffused barrier photodetector creates a small current proportional to

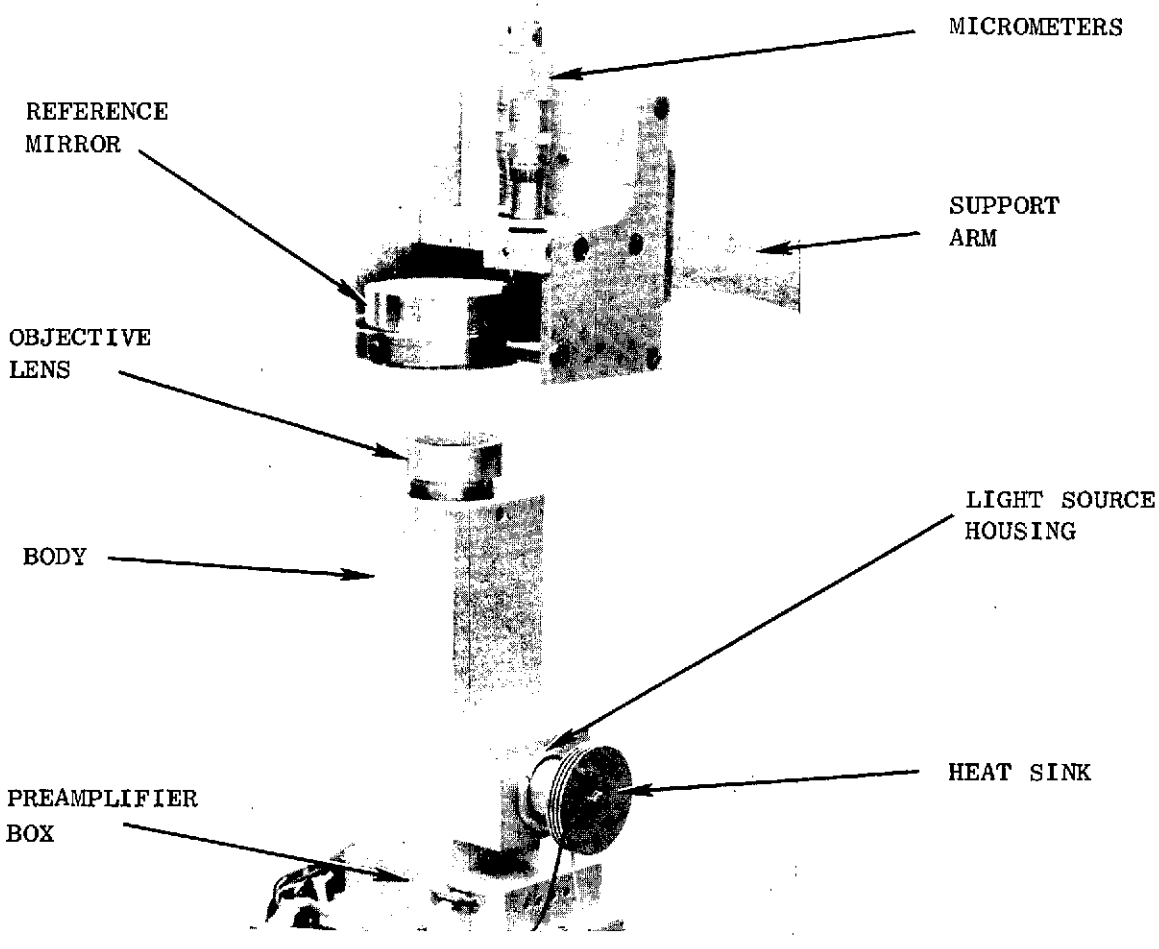

FIG. 9 PRIMARY AUTOCOLLIMATOR AND REFERENCE MIRROR ASSEMBLY. Signals from the autocollimator provide two axes of optical reference. A second similar autocollimator senses motion about the azimuth (vertical) axis.

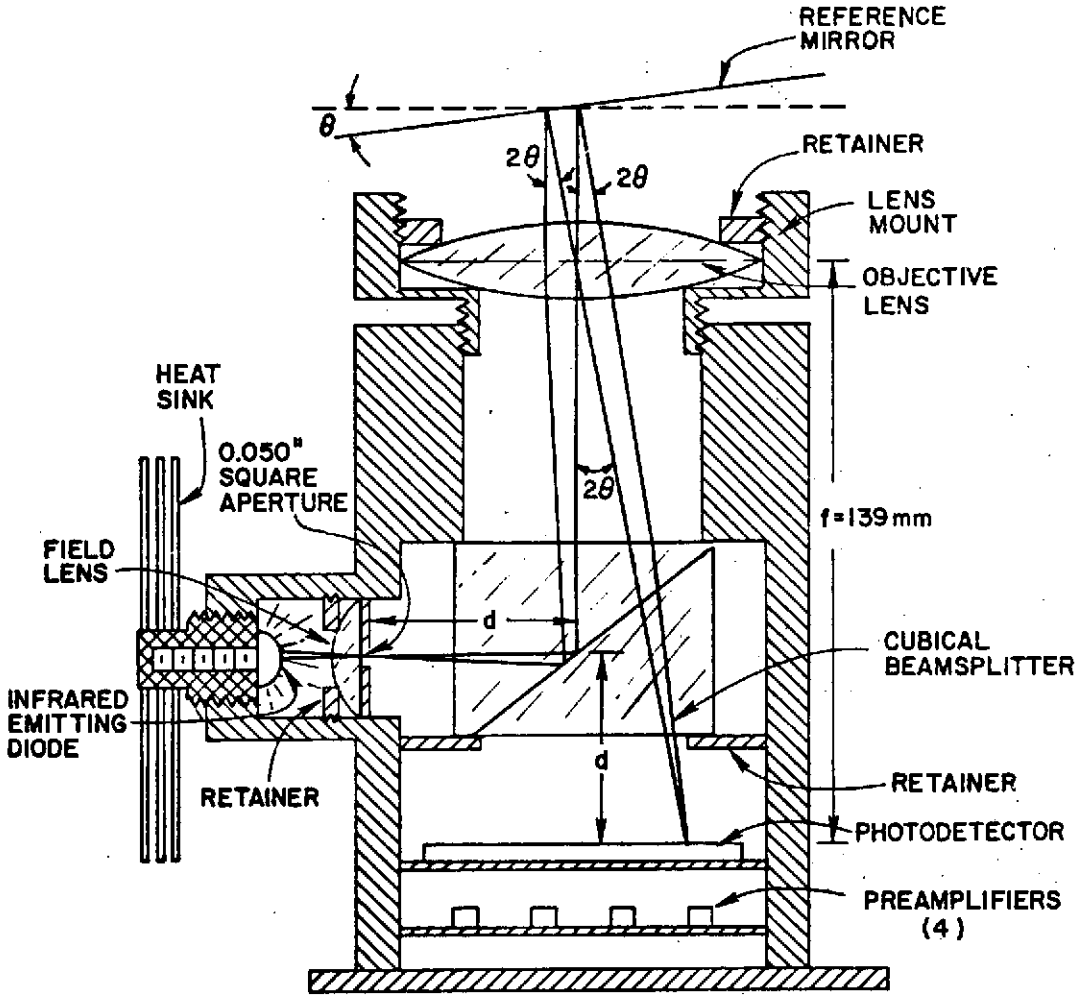

Fig. 10. PRIMARY AUTOCOLLIMATOR FUNCTIONAL DIAGRAM. Infra-red rays originating at the same point of the aperture emerge from the objective lens collimated (parallel). After being reflected through an angle twice that of the reference mirror, the rays are focused on a four-quadrant photodetector.

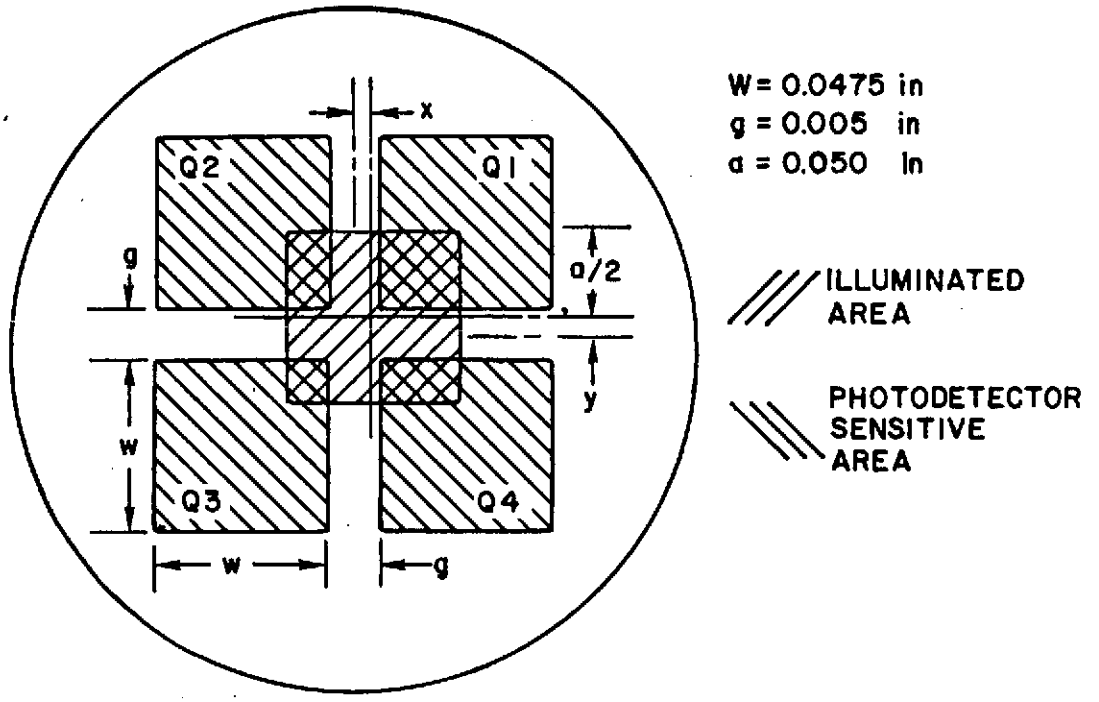

Fig. 11. GEOMETRY OF THE FOUR-QUADRANT PHOTODETECTOR AND APERTURE IMAGE. Displacement of the illuminated area from the center of the quadrants results in voltages proportional to the x and y distances.

the total energy flux into its surface. In addition, a dark current, similar to the saturation current of a transistor, is created independently of the external light. The level of dark current is subject to long term drifts. Finally, noise is produced whose power spectral density varies inversely with frequency (often called flicker or 1/f noise).

It is assumed that the energy flux density across the aperture image is constant, and therefore the total energy flux is proportional to the illuminated area. Referring to Fig. 11, the currents produced in the four quadrants are

$$i_1 = k_i\left(\frac{a - g}{2} + x\right)\left(\frac{a - g}{2} + y\right) + i_{1_d} + n_1$$

$$i_2 = k_i\left(\frac{a - g}{2} - x\right)\left(\frac{a - g}{2} + y\right) + i_{2_d} + n_2$$

$$i_3 = k_i\left(\frac{a - g}{2} - x\right)\left(\frac{a - g}{2} - y\right) + i_{3_d} + n_3$$

$$i_4 = k_i\left(\frac{a - g}{2} + x\right)\left(\frac{a - g}{2} - y\right) + i_{4_d} + n_4$$

$$\text{with} \quad |x|, |y| < w - \frac{a}{2} + \frac{g}{2}$$

where i_{m_d} and n_m, $m = 1,2,3,4$ are the individual dark currents and noise, respectively; and k_i is the constant of proportionality, assumed to be the same for all quadrants. Each current is converted to a voltage in a set of integrated circuit preamplifiers immediately adjacent to the photodetector and sent to the main electronics rack. Here, the individual voltages are first summed and differenced as follows:

$$V_x = (V_1 + V_4) - (V_2 + V_3) = k_x x + V_{x_d} + n_x$$

$$V_y = (V_1 + V_2) - (V_3 + V_4) = k_y y + V_{y_d} + n_y$$

where

V_m = preamplifier outputs $(m = 1,2,3,4)$

$k_x = k_y$ = proportionality constants

V_{x_d}, V_{y_d} = voltages due to dark current

n_x, n_y = noise voltages

The resulting voltages V_x and V_y are therefore direct linear indications of the displacement of the centroid of the aperture image. This displacement is further related to angular rotations of the mirror relative to the autocollimator by the linearized expressions

$$\theta_x = y/2f$$

$$\theta_y = -x/2f$$

as can be deduced from the geometry of Figs. 10 and 11.

The signals V_x and V_y are further amplified and demodulated. Since the power spectral densities of the dark current and the 1/f noise are greatest at low frequencies, and the signal occurs at 2.2 KHz, demodulation effectively eliminates these two error sources. Also eliminated are any biases in the amplifiers. The demodulated signal is then amplified and actively filtered above 40 Hz to attenuate 2.2 KHz ripple and high frequency noise, and to prevent autocollimator mount resonances from destabilizing the platform. The demodulated signal is also amplified and filtered above 120 Hz for high bandwidth instrumentation purposes. An automatic gain control loop provides additional gain stability and linearity by adjusting the output of the IR diode to keep the sum of the four quadrant preamplifier outputs at a constant level.

(4) Primary Sensor Alignment and Collimation. The autocollimator was aligned and collimated using the following procedure. A Wild T2 theodolite was first sharply focused at infinity by converting it to an autocollimator, pointing it at a mirror, and bringing the reflected image of the projected reticle into focus. The mirror was then replaced by the autocollimator and positioned such that the theodolite could look into the autocollimator through the objective lens. An external lamp was placed near the objective lens to illuminate the interior of the autocollimator. The detector face was then placed at the focal plane of the autocollimator objective lens by adjusting the threaded lens mount until a sharply focused image of the detector face appeared in the theodolite eyepiece. At this position the image distance of the detector face is infinity, enabling the theodolite to focus the detector image.

The IR beam was similarly collimated by bringing the image of the square aperture into focus by sliding the aperture plate in and out by means of a differential screw assembly. It was necessary to replace the IR emitting diode by a similar diode emitting in the red spectrum in order to make the aperture visible. The degree of collimation required made unnecessary a correction for the different wavelength of the IR and visible red emitting diodes.

Alignment of the detector to the aperture, to center the aperture image and make their sides parallel, was accomplished by observing the detector and aperture images in the theodolite, and rotating and translating the detector in the focal plane with adjusting screws. The IR diode was reinstalled and the detector mounting plate, objective lens, and aperture plate were locked in place by set screws.

During the original assembly, the IR diode was defocused to ensure uniform illumination of the detector across the aperture image. Defocusing was accomplished by adjusting the distance between the diode and the field lens so that the image of the diode was focused on the objective lens.

(5) Primary Sensor Performance. Scale factor, linearity, noise, and null stability measurements were made using a Davidson D-707 autocollimator, which has a resolution of 0.1 arcsec. A precision, adjustable, two-sided mirror was placed between the two autocollimators such that both were in their linear range. By introducing small changes in the orientation of the mirror and recording the outputs of both instruments, scale factor and linearity information was obtained. Noise estimates were made using the data recording and processing procedures described in Chapter IV. Twenty-four hour null stability was determined by continuously displaying the autocollimator outputs on a Sanborn strip chart recorder. Results of all these tests are summarized in Table 1. Also included are the characteristics of the useful channel of the azimuth autocollimator.

(6) Azimuth Orientation Sensor. The second autocollimator, which provides the necessary information to stabilize the platform in rotation about the boresight of the precision autocollimator, is also a two-axis device; however, one channel is not used. Mechanical arrangement of the unit is essentially the same as the primary sensor. Basic differences of the secondary sensor are:

(a) incadescent bulb light source

(b) dc electronics

Table 1

AUTOCOLLIMATOR PERFORMANCE CHARACTERISTICS

	θ_x (Control)	θ_y (Control)	θ_x (Instrumentation)	θ_y (Instrumentation)	θ_z (Azimuth)
Scale Factor (mV/μrad)	5.70	5.99	5.63	5.92	7.36
Linearity Error (%)	<0.1	<0.1	<0.1	<0.1	1 (±2.5 mrad) 2.5 (±5 mrad)
Linear Range (mrad)	±2.3	±2.3	±2.3	±2.3	±5
Standard Deviation of Noise Equivalent Angle (μrad) (0.1 to 100 Hz)	0.451	0.506	0.610	0.550	2.78
24 Hour Null Stability (μrad)	<5	<5	<5	<5	No Data
Power Required (W)	4.5				5.0

(3) four phototransistor detector

(4) ground glass image focusing surface with four light pipes leading to phototransistors

(5) partially silvered mirror beam splitter

(6) circular aperture

Performance of this sensor is shown above in Table 1. For more details see [L1].

2. Control Console

During system layout design, the need for a control center became evident. As a result, a large mobile 19 in. panel console, pictured in Fig. 12 , was employed to provide front panel space and storage. Front panels consist of:

(1) control

(2) meters--analog and digital

(3) switchable instrumentation

(4) hardwired instrumentation

(5) toroid to platform connectors

(6) 28 VDC power supply control

Storage is provided for the following items:

(1) electronics rack

(2) 28 VDC power supply

(3) ±15 VDC power supplies

(4) gyro spin power isolation transformers

(5) heater isolation transformers

(6) relay panel

(7) wire interconnect panel

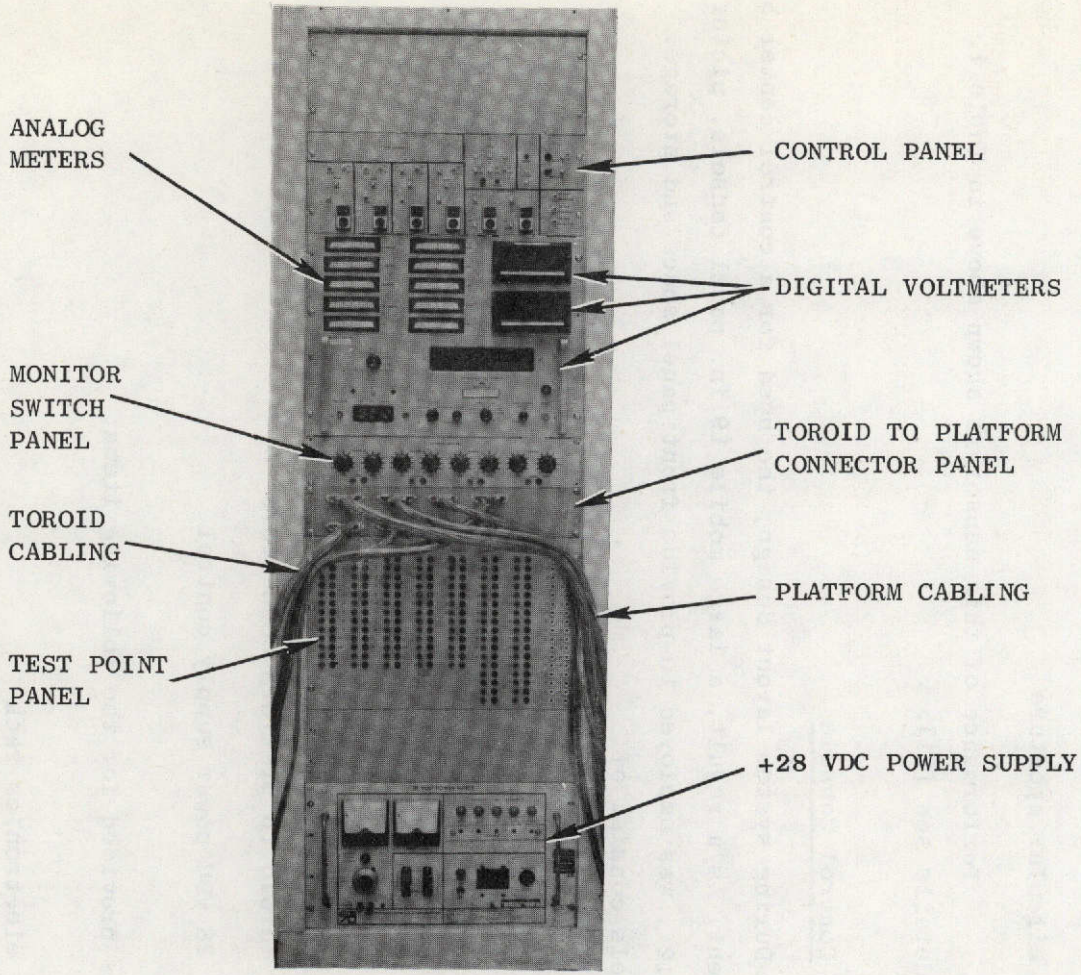

FIG. 12 CONTROL CONSOLE. All control, switching, and system monitoring functions are conveniently handled with this unit.

a. Electronics Rack

All of the electronic circuit cards developed for the system, with the exceptions of the gyro and autocollimator preamplifiers, are contained in an electronics rack inside the control console, Fig. 13 . Each removable circuit card plugs into a connector. The connectors are interwired and also linked to the rest of the system through two large wire bundles terminating in 50-pin connectors at the interconnect panel. A separate cable connects directly to the external autocollimator cable. Table 2 provides a list of the cards and their individual functions.

Table 2

ELECTRONIC CARD RACK FUNCTIONAL DESCRIPTION

Card	Description
1	X and Y gyro torquer amplifiers
2	Torquer amplifier decoupling networks
3	Z and X_{RD} gyro torquer amplifiers
4	Gyro caging (torque rebalance) amplifiers; ±6.2 VDC precision voltage regulator
5	Mode switching logic and relay drivers; 1.32 MHz crystal controlled clock
6	Gyro magnet excitation 5 VDC power supply; mode switching logic 5 VDC power supply
7	5 VDC, 1000 ma autocollimator LED power supply; gyro temperature controller
8	Primary autocollimator electronics
9	Azimuth autocollimator electronics
10	Autocollimator instrumentation output filters; ±12 VDC power supply

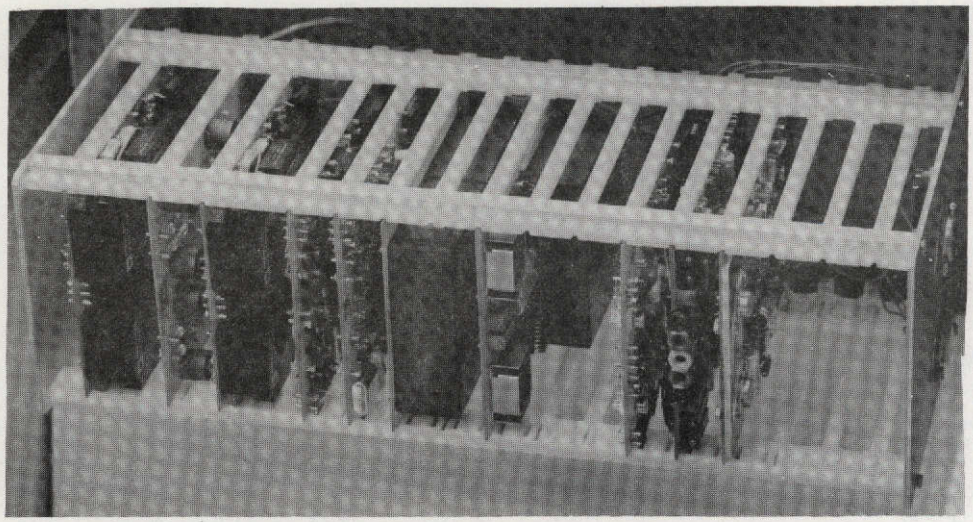

FIG. 13 ELECTRONICS RACK. Most of the new electronics required by simulator are mounted on cards which plug into this rack. The rack is interwired to provide power and signal distribution.

b. Control Panel

(1) Arrangement. The simulator is operated from a control panel near the top of the control console. As shown in Fig. 14, the panel is divided into several areas:

(1) power switches and display lamps

(2) mode select switches and display lamps

(3) caging amplifier inhibit switches

(4) gyro torquer biasing switches and potentiometers

(5) autocollimator output biasing switches and potentiometers

All of these controls except item (2) are self-explanatory or have been previously described.

(2) Mode Switching. The mechanics of switching modes is included here; however, discussion of the various modes is deferred until the next section. Selection of modes 1 through 6 is accomplished by depressing the "hold" momentary switch, setting the three mode select switches arranged in binary order, and then releasing the "hold" switch. Three lamps indicate if the select switches are on.

Each select switch controls one logic level input to a clocked three-bit register. A 1.32 MHz oscillator provides continuous clocking unless inhibited either by the selection of disallowed modes 0 and 7, or by depressing the "hold" switch. A panel alarm light also indicates if the select switches are in mode 0 or 7. The "hold" switch allows the operator to set all switches before releasing into the next mode and prevents incorrect modes from being entered during switching. The oscillator is included so that if a power surge or other anomaly falsely switches the register, the register will be reset to the desired mode before the mode-switching relays can change state.

The three bit register output is decoded in a logic circuit, which then controls current to the various relay coils through a set of transistor relay drivers. The 1.32 MHz oscillator output is also counted down to 2.2 KHz in the autocollimator electronics.

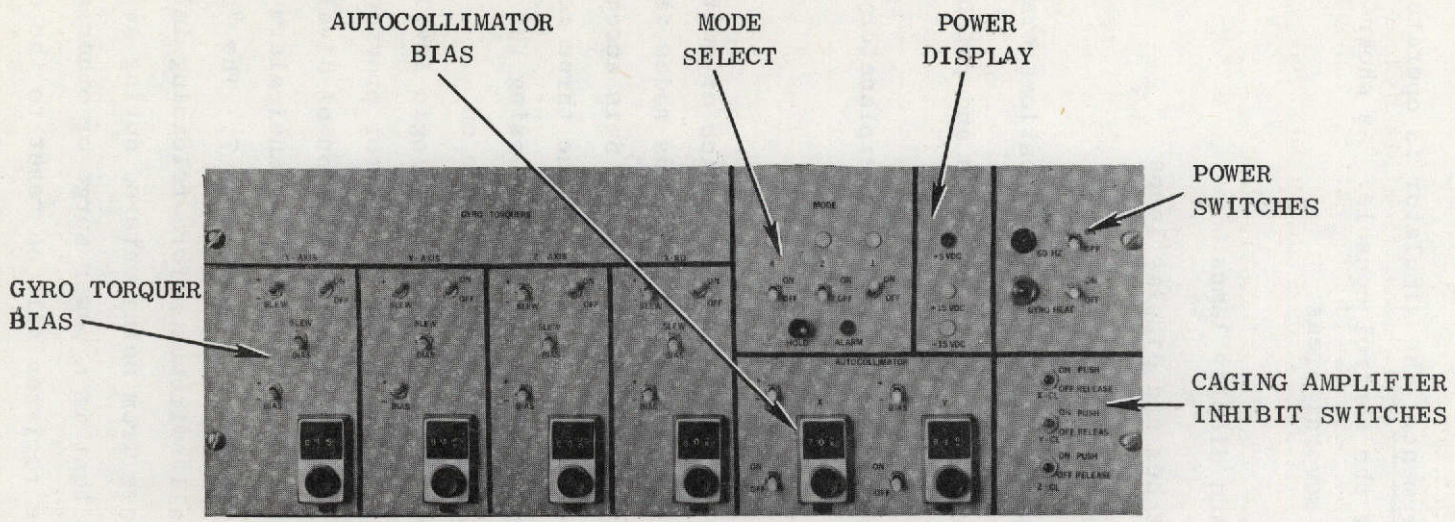

FIG. 14 CONTROL PANEL. Except for primary +28Vd-c power switching, all control functions are accomplished on this panel.

c. System Monitoring

A desire for convenient and flexible system monitoring strongly influenced the configuration of the control console. Figure 15 displays the arrangement of the system components and cabling and emphasizes the advantages of a central monitoring area.

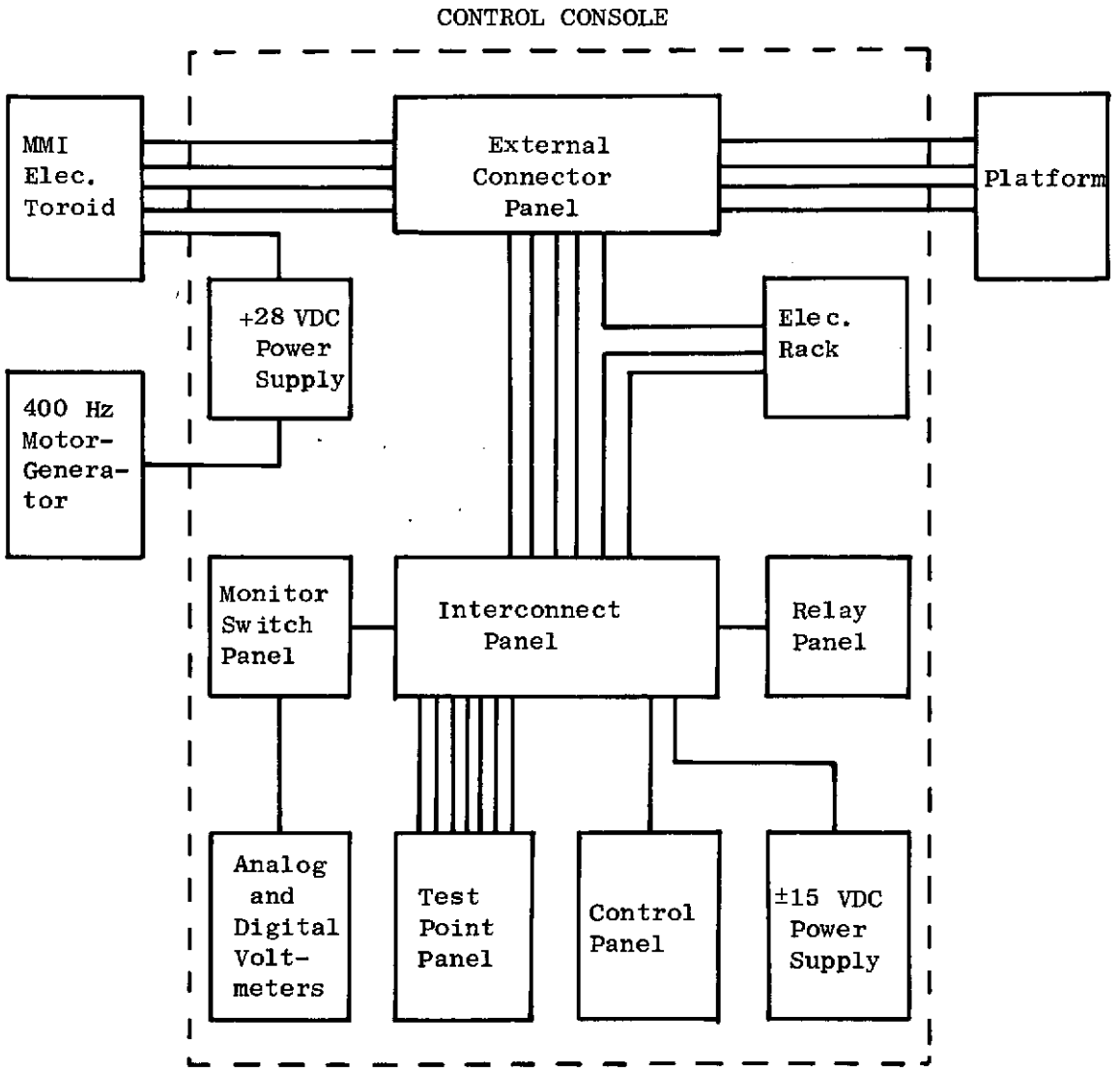

Fig. 15. SYSTEM INTERCONNECT DIAGRAM. In addition to providing control and monitoring functions, the control console serves as an interface between the Minuteman I electronics and the platform.

The test point panel consists of 31 connected pairs of jacks: one side tied to a signal, the other to ground. The purpose of this panel is to provide multiple outputs so that several channels of data may be recorded simultaneously. External command signals are also introduced to the system through these jacks.

The monitor switch panel consists of four sets of two rotary switches with output jacks, enabling any of 61 signals to be monitored. This panel allows rapid selection of signals to be displayed on up to four instruments; e.g., an oscilloscope. All signals appearing at the breakout panel are also sent to the monitor switch panel. Channel 4 of the monitor switch panel is permanently connected to two digital dc voltmeters on the meter panel; one with a range of ±2 VDC, the other ±100 VDC.

Ten signals were selected for permanent display via analog dc voltmeters, also mounted on the meter panel. They are: all four gyro pickoff demodulator outputs, all four gyro torque amplifier output voltages, and two control channel autocollimator outputs, θ_x and θ_y. These meters are useful indicators of system status during autocollimator acquisition and gyro spin-up and caging transients.

3. Minuteman Electronics

To minimize modification of existing equipment, all Minuteman I electronics used were left in the toroid except the pickoff excitation amplifier, which was left in its original location mounted at the base of the stable platform.

Other modules not needed by the simulator were either removed or disabled. The computer was completely removed from the system by unplugging several connectors. The computer power supplies were disabled by removing the dc to dc converter. Also no longer needed was the power discrete switch used by the Minuteman in switching from ground to airborne power sources. Level detection, originally used to erect the platform, was not needed on the simulator so the level detector converter was removed from the toroid, and the level detecting bubble levels were not mounted on the modified platform. Since the gyro torquing arrangement was drastically altered, the gyro tuning network and torque converter

were eliminated. The final components removed from the toroid, which potentially could be used in future work with the simulator, are the digital resolver converters used to indicate the platform gimbal angles. To use the resolver converter output, however, would require the development of digital accumulators. Since the resolvers were not immediately needed, no effort was made to use them.

The following toroid modules are used in the simulator.

(1) Platform Control Amplifiers (3)

(2) Velocity Meter Control Amplifiers (3)

(3) Gyro Pickoff Postamplifiers (3)

(4) Velocity Meter Postamplifiers (3)

(5) Hybrid Circuit

(6) Direct Current Filter

(7) Caging Amplifier

(8) -28 VDC Power Supply

(9) 4.8 kHz Power Supply

(10) 400 Hz Precision Power Supply

(11) 400 Hz Audio Frequency Amplifier

(12) Signal Generator

Power from the 28 VDC supply in the control console is delivered to the Minuteman electronics through a special cable which eventually terminates at a glass-epoxy board installed at the base of toroid. Communication between the toroid and the control console is through four cables with connectors at both ends. Three connectors on the toroid, originally for the stable platform, already had many of the desired signals and were used. A fourth new cable brings out many other signals needed by the simulator. Additional coaxial wiring was required inside the toroid for this purpose.

4. Platform Assembly

The primary purpose of the platform assembly is to provide controlled motion for the sensors. The platform assembly, consisting of the stable platform, rotary table, and mirror mount, has already been pictured in Fig. 2 at the beginning of this chapter. The rotary table provides flexible and convenient orientation of the platform control axes relative to the directions of gravity and the earth's spin axis. Optical reference is provided by the mirror mount, which is rigidly attached to the rotary table head.

a. Stable Platform

The "inside-out" gimbal arrangement of the Minuteman I stable platform proved to be quite amenable to modifications. The gimbal arrangement and axes convention are shown in Fig. 16. All three gimbal

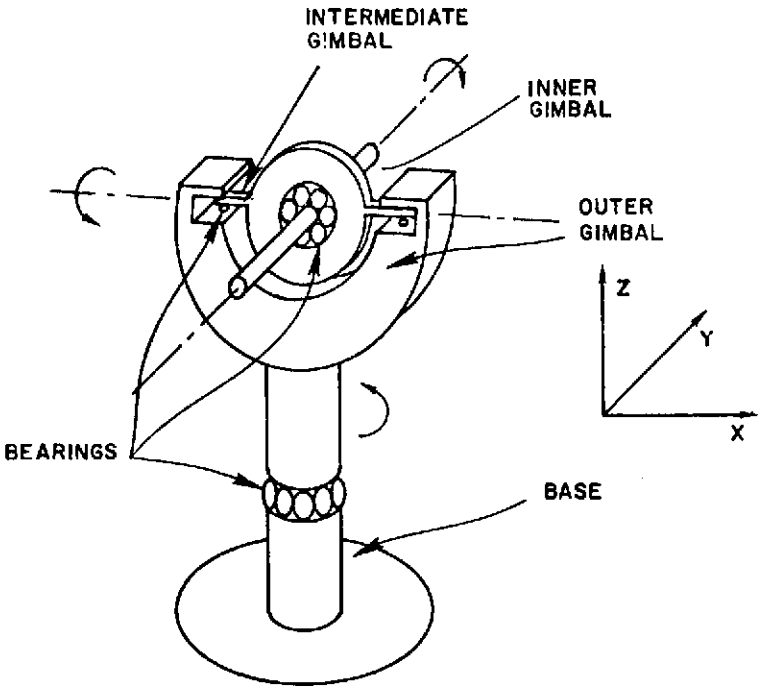

Fig. 16. PLATOFRM GIMBAL CONFIGURATION. The orientation sensors are clamped rigidly to the inner gimbal shaft.

shafts are supported by ball bearings. Torques between gimbals are applied by permanent magnet dc motors whose static gains are 0.027 N-m/V. The motor input voltages are provided by the power amplifier stages of the platform control amplifiers. The gains of these power amplifiers are 302, 164, and 333 for the X, Y, and Z axes, respectively. Command voltage inputs to the power amplifier may be applied through dropping resistors, giving gains of 2.26, 1.23, and 2.49.

The original gyro and velocity meter mounting brackets were replaced by new mounts for the Atlas gyros and autocollimator. The alignment unit, consisting of bubble levels and mirror mounted on a quartz block, and supporting electronic components were removed with the original brackets. The two gyro brackets are rigidly clamped to the inner gimbal shaft and are tied together by the autocollimator and connector mounting bracket as pictured in Fig. 17. Several additional brackets were fabricated to mount the azimuth reference mirror, primary autocollimator, balancing weights, and isolation transformers. Three digital gimbal angle resolvers were left in place on the platform, although not used because of their inferior small angle accuracy.

Mechanical stops prevent the outer and intermediate gimbals (Z and X) from rotating more than ±110° and ±25°, respectively. Inner gimbal travel must be held to within ±90° to avoid pinching wire cables.

b. Rotary Table

The platform base is rigidly attached to a 24 in. tilting rotary table by means of a special adaptor. This hollow, cylindrical fixture allows passage of external cabling into the platforms and also provides room for the pickoff excitation amplifier suspended from the platform base.

Elevation angles about an East-West axis between 0 and 90° can be set by cranking the tilting handwheel. A vernier scale allows reading of the elevation angle to 1 arcmin. The platform may also be rotated by crank through any angle about the spindle axis perpendicular to the rotary table face. This angle can be repeatedly read out to an accuracy of 2 arcsec. With these two-degrees-of-freedom, the outer (Z)

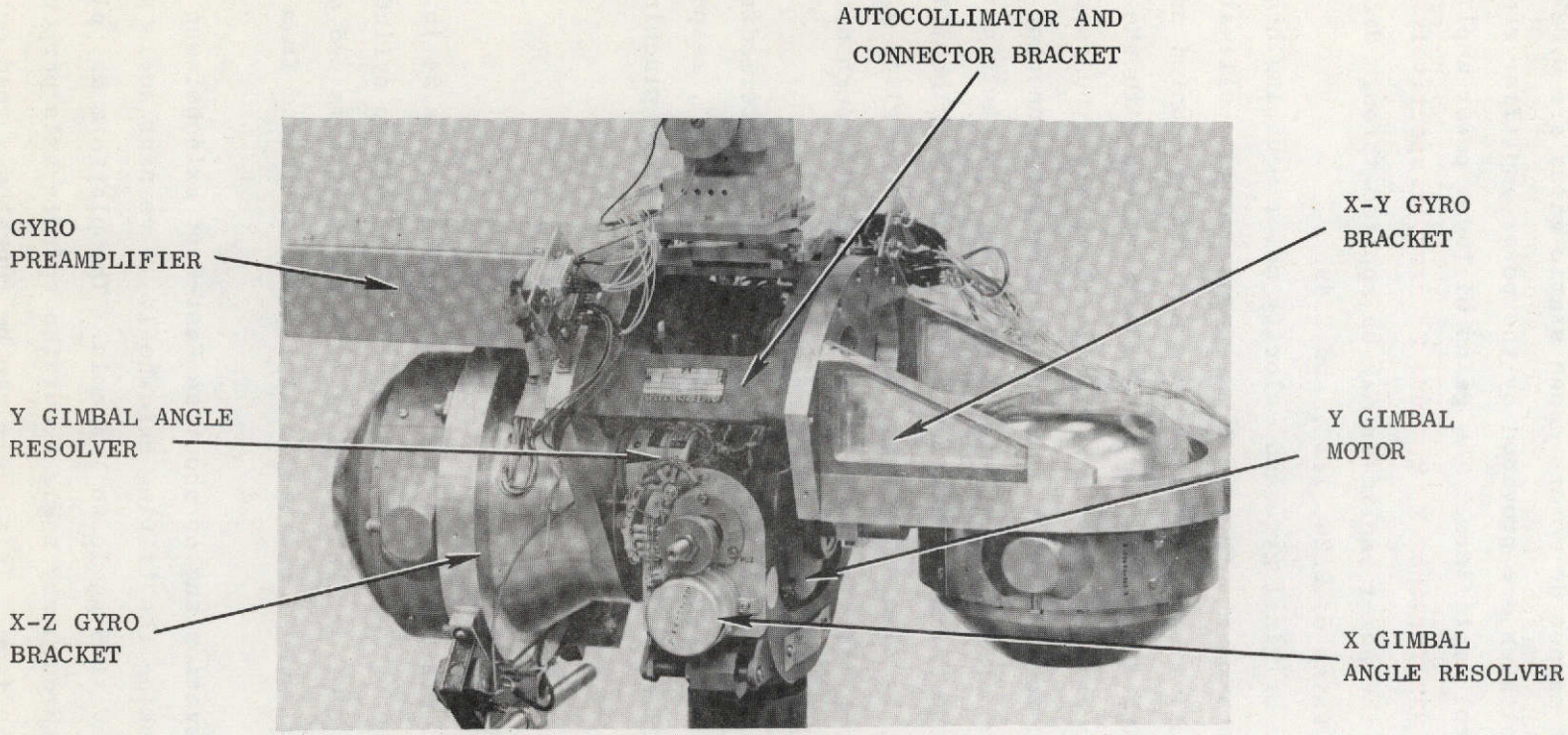

FIG. 17 SENSOR MOUNTING CONFIGURATION. New gyro brackets are mated to the original cross (autocollimator) bracket and are clamped to the inner (Y) gimbal shaft. This arrangement provides rigidity and reduces deflections due to the cantilevered gyros.

gimbal axis can be oriented quickly to any position between vertical and horizontal, including earth polar; and the sensors then rotated about this axis.

The table base rests on three adjustable bolts so that the table can be leveled. There are also four brackets holding bolts located at the bottom corners of the base. These bolts push against the base and may be adjusted in various combinations to rotate the table in azimuth. Tightening all bolts locks the table base to the floor plate.

c. Mirror Mount

A special mount was built to hold the primary autocollimator reference mirror and the azimuth autocollimator. The crescent shaped arm, which is pivoted at the midpoint, curves up and around the stable platform to hold the reference mirror directly above the primary autocollimator. Although normally locked in the unpivoted position, the arm can also be rotated and locked at angles of 10° and 57°. These positions allow the platform to be operated with the gimbals nonorthogonal, while still maintaining an optical reference.

The azimuth autocollimator is installed in a hole in the arm below the pivot point thereby remaining permanently fixed relative to the rotary table head. This autocollimator reflects off a mirror mounted on a compensating weight bracket attached to one end of the inner (Y) gimbal structure. It therefore senses platform motion about the intermediate and outer (X and Z) gimbal axes, although the X axis sensing is redundant and is not used.

The primary mirror mount is cantilevered from the upper end of the arm. The mirror is suspended in a two-axis gimbal and is adjusted by two micrometers.

d. Alignment

Alignment of the gyros and autocollimators involved several stages of adjustments. The sequence of relative alignments used is as follows.

- The rotary table was leveled.

- The two sided primary mirror was made parallel to the rotary table head. A Wild T2 theodolite, used as an autocollimator, was pointed at the back side of the primary mirror. The table head was elevated about 60° for this purpose. The table head (and thereby the mirror) was then rotated and the motion of the reflected reticle image observed. (The origin of the reticle image describes a circle if the mirror is not perpendicular to the rotation axis.) The micrometers were then adjusted to minimize the diameter of the described circle. The procedure was iterated until no apparent motion of the reticle image was observed.

- The rotary table tilt shaft was oriented East-West by referring to the star Polaris, again using the theodolite. The rotary table, which had already been oriented approximately East-West under a door through which Polaris could be observed, was elevated to the local latitude. The theodolite was then positioned along the line from the primary reference mirror to Polaris which was precisely centered in the theodolite. Corrections to true North from Polaris were computed from American Ephemeris and Nautical Almanac Pole Star tables, and the theodolite moved to the true Polar position. The theodolite was then plunged 180° about its elevation axis, which brought it to an orientation looking at the approximately polar oriented mirror. The theodolite was converted to an autocollimator, and the vertical lines of the actual and the image reticle were brought into coincidence by adjusting the table base plate bolts. The horizontal lines were brought together by cranking the table elevation control wheel. At this point the reference mirror was very precisely (error <50 μrad) perpendicular to the earth's spin axis and the elevation shaft horizontal East-West.

- The primary autocollimator optical axis was made parallel to the X-Y gyro spin reference axis. The platform was oscillated about the Z axis while under autocollimator stabilization control by driving the Z gimbal motor power amplifier with a 1 Hz sine wave from a low frequency function generator. Since the X and Y autocollimator outputs were held at null by the servo loop, sinusoidal outputs from the X-Y gyro indicated that the spin axis was not parallel to the autocollimator optical axis. Screws on the autocollimator mount were then adjusted to minimize the gyro outputs.

Attempts to align precisely the X-Y gyro and autocollimator about the Z axis were thwarted by the viscosity of the gyro flotation fluid. A rotation about the X axis, for example, is accompanied by a rotation of the float about the Y axis. This is easily shown by the following simplified analysis:

$$T_x = c_x \dot{\sigma}_x$$

$$h\dot{\sigma}_y = T_x$$

$$\dot{\sigma}_y = \frac{c_x}{h} \dot{\sigma}_x$$

where

c_x = viscous friction coefficient

T_x = viscous friction torque

h = gyro angular momentum

$\dot{\sigma}_x, \dot{\sigma}_y$ = float angular rates

Values for h/c are presented in Section C.1.a.

The gyro outputs are clearly coupled. Since careful attention had been paid to the original mechanical alignment, it was felt that the existing accuracy was adequate. By the same reasoning, no attempt was made to improve the alignment of the noncritical X-Z gyro and the azimuth autocollimator.

In summary, orienting the reference mirror and azimuth autocollimator using the rotary table controls provides the basic laboratory and inertial reference. The servo loops then hold the sensor axes to this reference.

5. Power

Eleven power supplies, four regulators, two crystal oscillators, and a motor generator supply power to the system. These in turn receive their power from both single-phase and three-phase laboratory 60 Hz lines. Power distribution is indicated in Figs. 18a and 18b.

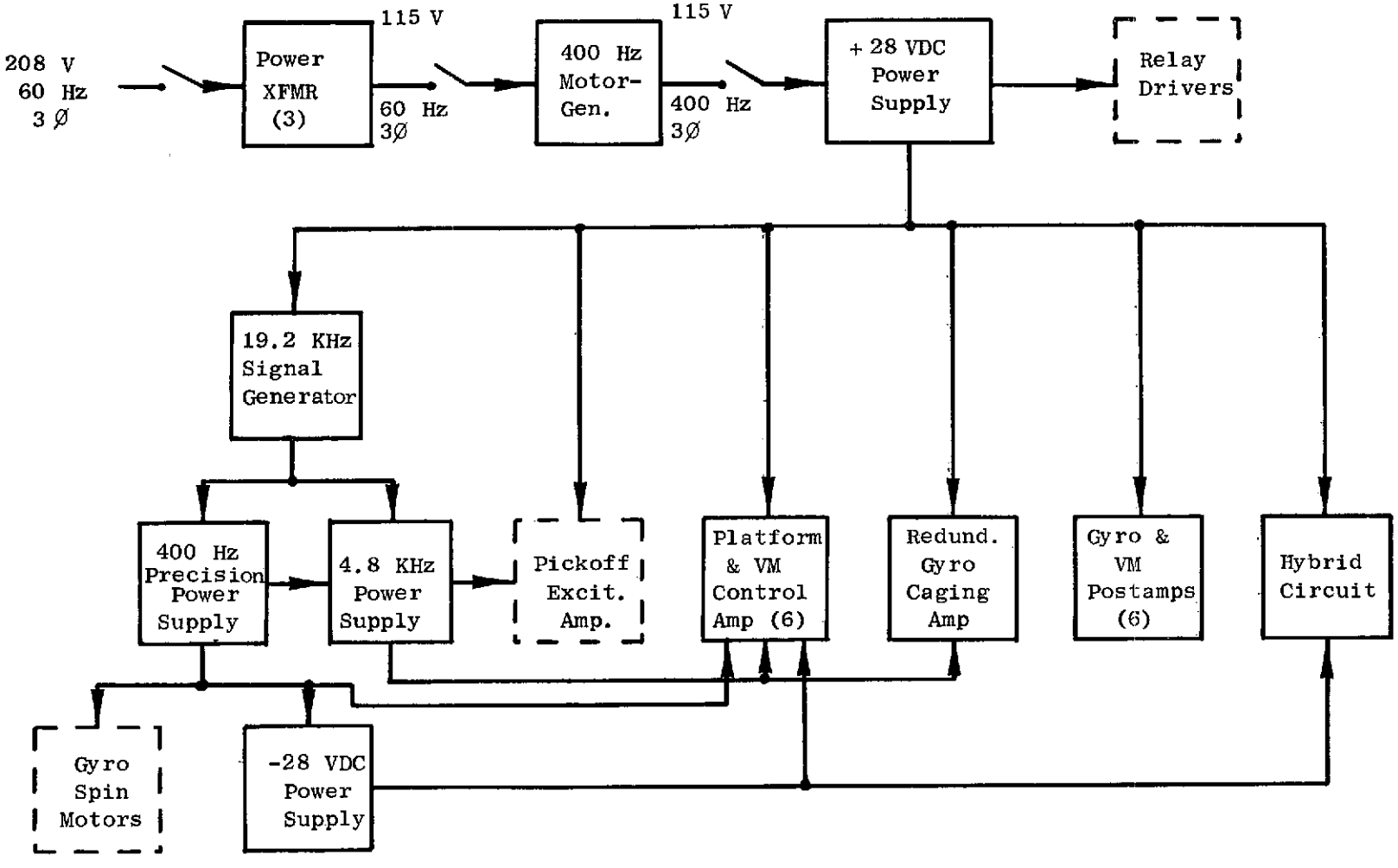

Fig. 18a. MINUTEMAN I ELECTRONICS TOROID POWER DISTRIBUTION. Components located outside the toroid are distinguished by dashed boxes.

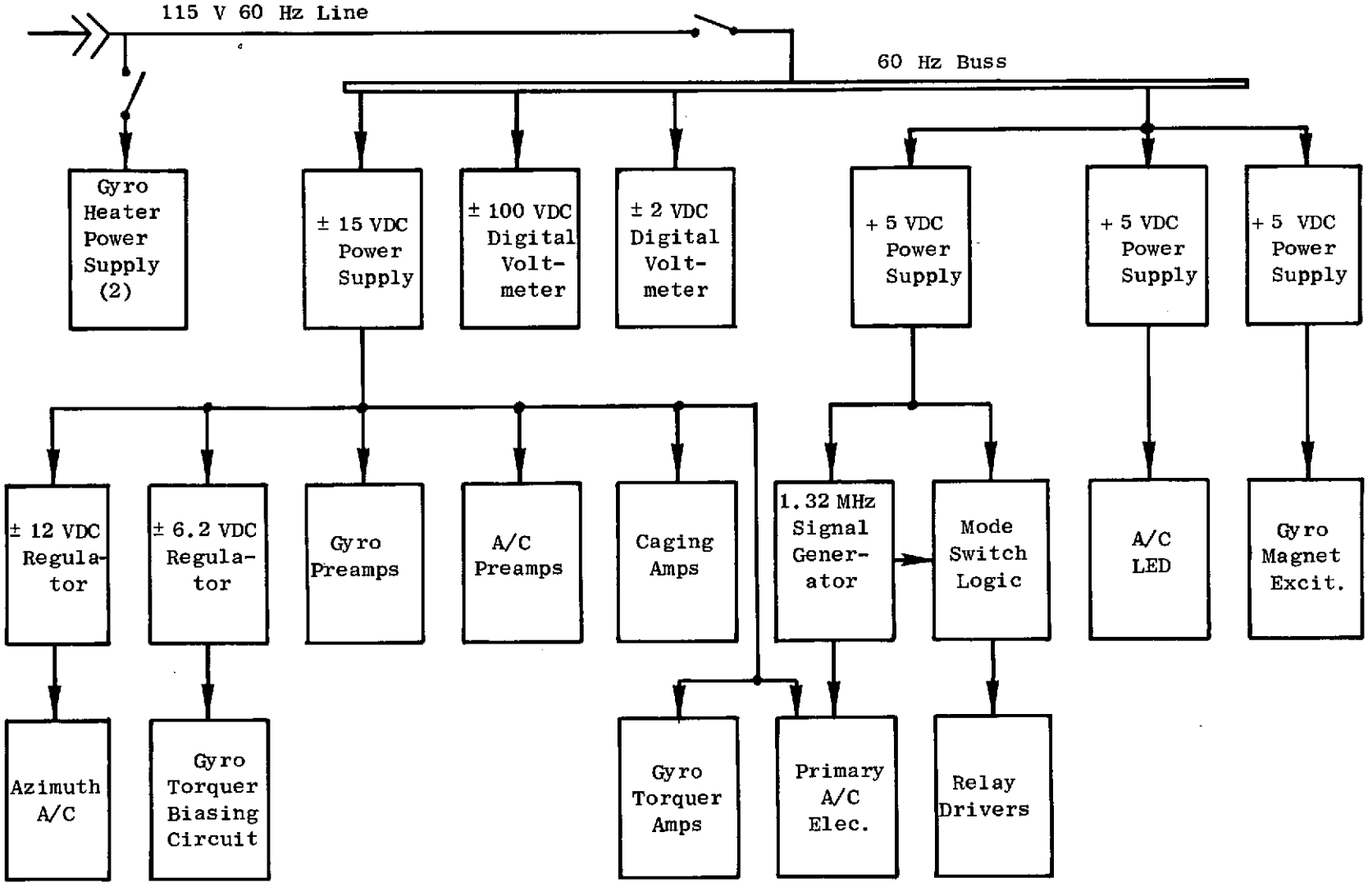

Fig. 18b. CONTROL CONSOLE AND PLATFORM POWER DISTRIBUTION.

As can be seen from these two figures, the original Minuteman toroid and the new electronics have essentially separate power distribution systems. They are tied to each other only through the ground buss in the control console and through the relay drivers which control the flow of 28 VDC power through the relay coils.

6. Data Acquisition

a. Strip Chart Recording

Permanent records of both analog and digital data are made using a variety of equipment. An eight channel Sanborn strip chart recorder is used to display analog signals directly. This instrument is primarily used in obtaining qualitative information, since it is inherently limited to about 1 percent accuracy by the resolution of grid paper. More precise data in a form suitable for digital processing is obtained by a procedure illustrated in Fig. 19.

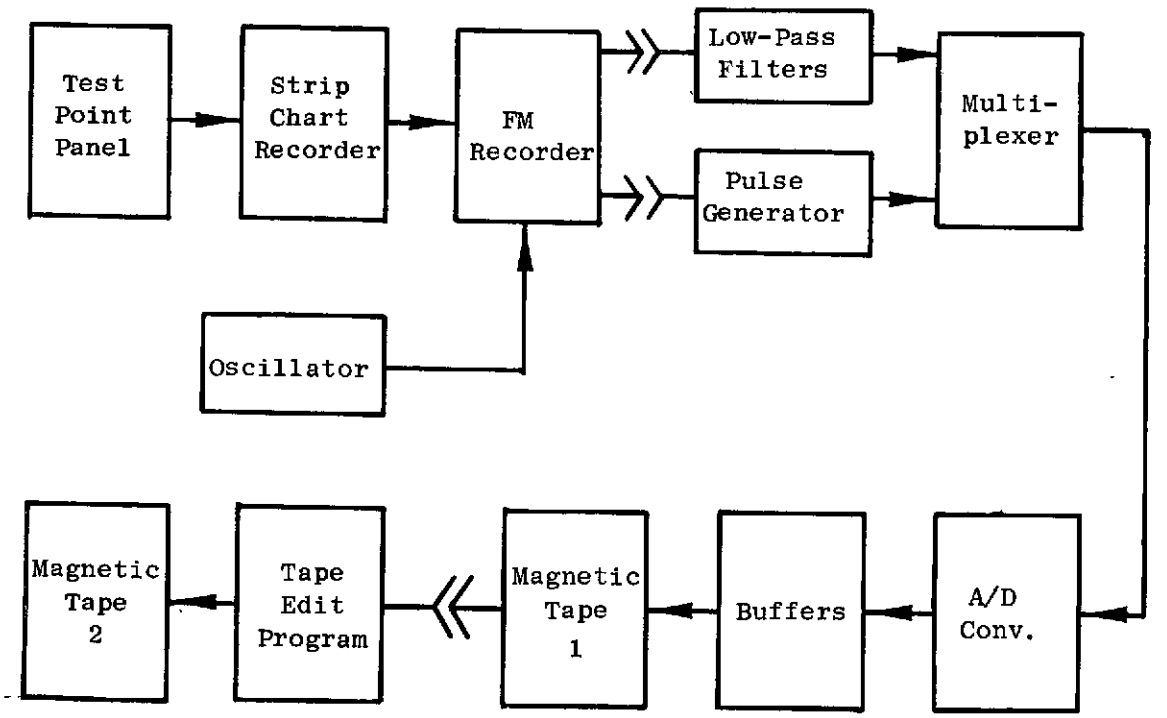

Fig. 19. DATA ACQUISITION PROCEDURE. Three stages of data acquisition and editing are required to put data in a form suitable for digital processing.

b. FM Analog Recording

Up to eight signals of interest are tapped at the control console test point panel and sent to the strip chart recorder for amplification and display. The amplified signals are then recorded on magnetic tape by a high fidelity Ampex FR-1300 FM recorder/reproducer. The amount of amplification is selectable and is usually chosen so that the maximum output voltages are approximately ±1 V. Amplification is necessary to maximize the signal-to-noise ratio in the recorder, which has a maximum input level of ±2 V. Since the recorded signals are to be digitized, it is necessary to simultaneously record a sine wave from an oscillator set at the desired sampling frequency. Recording length is determined by the desired number of sampled data points and the sampling frequency.

c. Digitization and Storage

After the test run is completed, the recorder and tape are moved from the laboratory to an XDS Sigma 5 computer facility located in the same building. The appropriate signal playback channels are connected to three-pole active low-pass filters to attenuate signal components at frequencies greater than approximately 30 percent of the sampling frequency. This is necessary to prevent high frequencies being aliased into the low frequency spectrum. The analog data is normally recorded at a tape speed of 3 3/4 ips, but is played back at either 15 or 30 ips, resulting in digitization time savings of factors of 4 or 8. The increased speed requires, however, that the anti-aliasing filter cutoff frequency be increased by the same factor.

The oscillator channel is connected directly to a pulse shaping circuit that generates a 1 μsec square pulse at every positive zero crossing of the input sine wave. This pulse is then used to trigger a multiplexed input analog-to-digital converter (ADC). The advantage of triggering from a frequency signal recorded simultaneously with the data signals is the elimination of frequency distortions caused by variations in tape speed during playback.

Upon receipt of the triggering pulse, the input channels are sampled and digitized at a 140 kHz repetition rate, resulting in a 14 bit plus sign word for each sampled channel to be stored sequentially

in a double buffer. Buffer length is set such that n channels of 256 words per channel fill each buffer. The number of input channels n is variable. Once one buffer is filled, the other buffer is used. While the second buffer is being filled, the first buffer is written as a record onto magnetic tape. The buffer roles are then alternately swapped until a preset number of digital tape records have been written.

The format of the digital tape is not convenient for processing since channel data are interlaced. To make the tape format more compatible, an editing program is executed which passes through the data record by record, selecting points from one channel only, and writing out 256 word records until the desired number of records have been written. A file mark is then placed on the tape. This is repeated for a preselected number of original channels.

D. Operation

The simulator can be operated in any of six modes. As discussed previously, the modes are selected on the console control panel through twelve triple-pole, double-throw relays. A functional description of each of the modes is given below. Diagrams of the relay connections are contained in Appendix B.

Mode 0: Not allowed.

Mode 1: Gyro Off

a. Autocollimator stabilization
b. No gyro spin power
c. Caging amplifiers inhibited
d. Gyro torquer biasing

Mode 2: Gyro Spin-up

a. Autocollimator stabilization
b. Gyro spin power
c. Caging amplifiers inhibited
d. Gyro torquer biasing

Mode 3: Autocollimator Control

a. Autocollimator Stabilization
b. Gyro spin power

c. Gyro caging via gyro pickoff
d. Gyro torquer biasing

Mode 4: Gyro Control with 4-Channel Caging

a. Gyro stabilization
b. Gyro spin power
c. Gyro caging via autocollimator (4 axes)
d. Gyro torquer biasing

Mode 5: Gyro Control with 3-Channel Caging

a. Gyro stabilization
b. Gyro spin power
c. Gyro caging via autocollimator (no z channel)
d. Gyro torquer biasing

Mode 6: External Stabilization

a. Stabilization by external compensation
b. Gyro spin power
c. Gyro caging via external signals
d. No gyro torquer biasing

The simulator can be started in modes 1, 2, 3, or 6. The gyro controlled modes 4 and 5 require that the gyros be at operating speed and caged before entering. Mode 5 is primarily used to keep the platform inertially fixed in the polar orientation while maintaining optical reference in the polar direction. Mode 6 is to be used when external compensation is available from a computer or other network which combines the gyro and autocollimator error signals.

Chapter III

SIMULATOR MODEL

A mathematical model of the Fixed Base Simulator is now developed. Major system components are first analysed and then combined to evaluate the responses of the autocollimator and gyro stabilization loops. This model is used in Chapter V to help interpret experimental data obtained from the orientation sensors and to develop refined models of the system.

A. Gyro Model

The two-degree-of-freedom Atlas missile gyros can be represented as in Fig. 20. The two flywheels of the gyro are treated as one combined wheel.

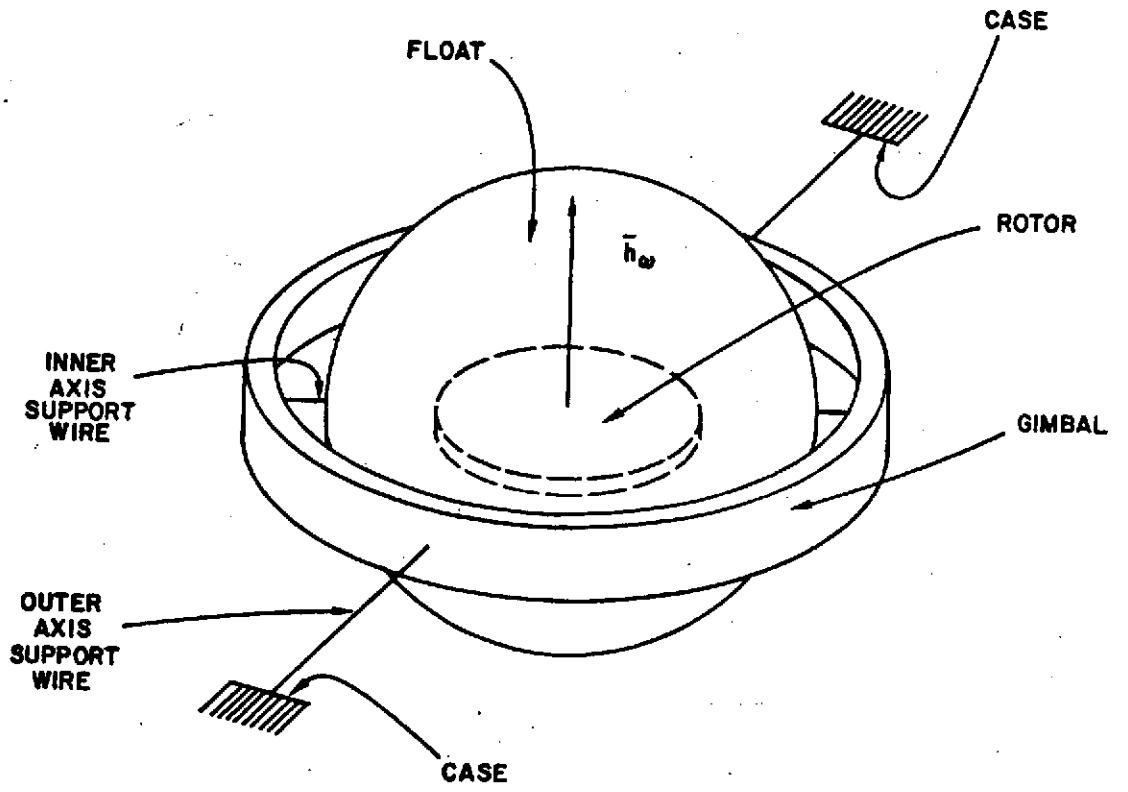

Fig. 20. FUNCTIONAL ARRANGEMENT OF ATLAS MISSILE TWO-DEGREE-OF-FREEDOM GYRO. The spherical float and the gimbal are floated inside the case. Support wires center the float.

The float and gimbal are restricted to small angles about their null position and are oriented as in Fig. 21a and b.

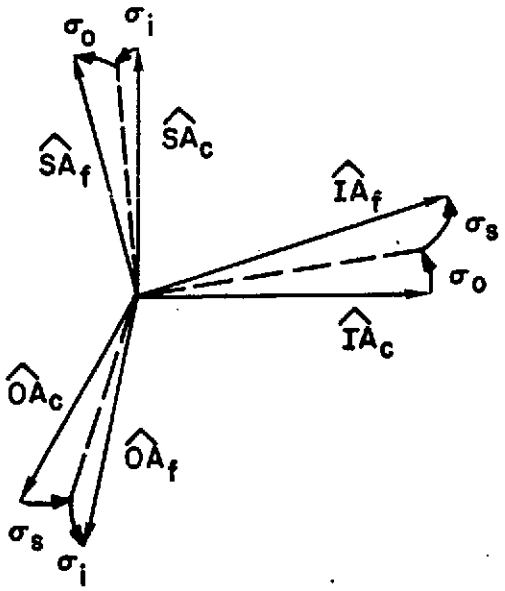

Fig. 21a. GYRO FLOAT SMALL ANGLE ORIENTATION.

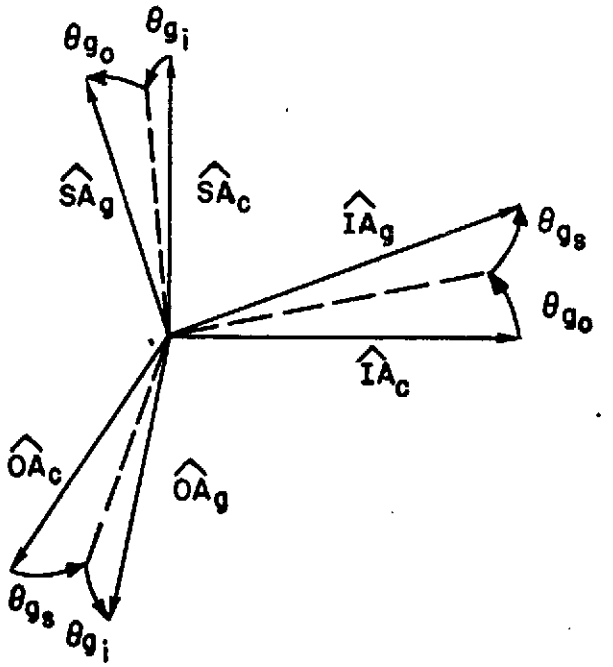

Fig. 21b. GYRO GIMBAL SMALL ANGLE ORIENTATION.

The subscripts i, o, s refer to the inner, outer and spin axes respectively, and the subscripts c, f, g denote case, float, and gimbal.

The total angular momentum of the float is

$$\bar{H}_f = \bar{\bar{I}}_f \bar{\omega}^{f-i} + \bar{h}_w \tag{3.1}$$

where $\bar{\bar{I}}_f$ is the combined moment of inertia of the float and wheel, and $\bar{h}_w$ is the angular momentum of the wheel with respect to the float. (Notation is defined in the List of Symbols, p. xiv.) Taking the time derivative of (3.1) in the inertial reference frame yields

$$\frac{i}{H_f} = \bar{\bar{I}}_f \frac{f}{\omega}^{f-i} + \bar{\omega}^{f-i} \times \bar{H}_f \ , \tag{3.2}$$

where it is assumed that the wheel speed is constant; i.e.

$$\frac{f}{h_w} = 0 \tag{3.3}$$

Since the float angles are small,

$$\bar{\omega}^{f-i} = \frac{f}{\sigma} + \bar{\omega}^{c-i} \tag{3.4}$$

where

$$\bar{\sigma} = \begin{bmatrix} \sigma_o \\ \sigma_i \\ \sigma_s \end{bmatrix}$$

Expanding (3.2) using (3.4)

$$\frac{i}{H_f} = \bar{\bar{I}}_f \left[\frac{ff}{\sigma} + \frac{c}{\omega}^{c-i} + (\bar{\omega}^{c-f} \times \bar{\omega}^{c-i}) \right] + (\frac{f}{\sigma} + \bar{\omega}^{c-i}) \times \left[\bar{\bar{I}}_f (\frac{f}{\sigma} + \bar{\omega}^{c-i}) + \bar{h}_w \right] \tag{3.5}$$

Equation (3.5) may now be linearized by assuming that products of angular velocities are negligibly small.

$$\frac{i}{H_f} = \bar{\bar{I}}_f \frac{ff}{\sigma} + \frac{f}{\sigma} \times \bar{h}_w + \bar{\bar{I}}_f \frac{c}{\omega}^{c-i} + \bar{\omega}^{c-i} \times \bar{h}_w \tag{3.6}$$

Coordinatizing (3.6) in the float reference frame yields

$$\frac{i}{H_{ff}} = \begin{bmatrix} I_{f_t} \ddot{\sigma}_o + \dot{\sigma}_i h \\ I_{f_t} \ddot{\sigma}_i - \dot{\sigma}_o h \\ I_{f_s} \ddot{\sigma}_s \end{bmatrix} + \begin{bmatrix} I_{f_t} (\dot{\omega}_o^{c-i} + \sigma_s \dot{\omega}_i^{c-i} - \sigma_i \dot{\omega}_s^{c-i}) \\ I_{f_t} (\dot{\omega}_i^{c-i} - \sigma_s \dot{\omega}_o^{c-i} + \sigma_o \dot{\omega}_s^{c-i}) \\ I_{f_s} (\dot{\omega}_s^{c-i} + \sigma_i \dot{\omega}_o^{c-i} - \sigma_o \dot{\omega}_i^{c-i}) \end{bmatrix} + \begin{bmatrix} (\omega_i^{c-i} - \dot{\sigma}_s \omega_o^{c-i} + \sigma_o \omega_s^{c-i}) h \\ -(\omega_o^{c-i} + \sigma_s \omega_i^{c-i} - \sigma_i \omega_s^{c-i}) h \\ 0 \end{bmatrix} \tag{3.7}$$

where

I_{f_t} = combined wheel and float transverse moment of inertia

I_{f_s} = combined wheel and float spin axis moment of inertia

h = magnitude of wheel angular momentum

and

$$\underset{c}{\omega}^{c-i} = \begin{bmatrix} \omega_o^{c-i} \\ \omega_i^{c-i} \\ \omega_s^{c-i} \end{bmatrix}$$

Considering all products of float angles and case angular velocities and accelerations as negligibly small, (3.7) may be simplified as

$$\underset{f}{\overset{i}{H}}_f = \begin{bmatrix} I_{f_t}(\ddot{\sigma}_o + \dot{\omega}_o^{c-i}) + (\dot{\sigma}_i + \omega_i^{c-i})h \\ I_{f_t}(\ddot{\sigma}_i + \dot{\omega}_i^{c-i}) - (\dot{\sigma}_o + \omega_o^{c-i})h \\ I_{f_s}(\ddot{\sigma}_s + \dot{\omega}_s^{c-i}) \end{bmatrix} \tag{3.8}$$

With the small angle assumption, the spin axis equation is uncoupled from the two transverse axes equations.

In a similar manner, the gimbal angular momentum is

$$\overline{H}_g = \overline{\overline{I}}_g \overline{\omega}^{g-i} \tag{3.9}$$

Again, taking the time derivative in the inertial reference frame,

$$\overset{i}{\overline{H}}_g = \overline{\overline{I}}_g \overset{g}{\overline{\omega}}^{g-i} + \overline{\omega}^{g-i} \times \overline{\overline{I}}_g \overline{\omega}^{g-i} \tag{3.10}$$

Assuming the gimbal angles to be small allows the gimbal angular velocity to be written as

$$\overline{\omega}^{g-i} = \overset{g}{\overline{\theta}}_g + \overline{\omega}^{c-i} \tag{3.11}$$

where

$$\overline{\theta}_{g_g} = \begin{bmatrix} \theta_{g_o} \\ \theta_{g_i} \\ \theta_{g_s} \end{bmatrix}$$

Expanding (3.10) using (3.11) results in

$$\overline{\overset{i}{H}}_g = \overline{\overline{I}}_g \left[\ddot{\overline{\theta}}_g + \overline{\omega}^{c-i} + \overline{\omega}^{c-g} \times \overline{\omega}^{c-i} \right] \tag{3.12}$$

Neglecting the products of gimbal angles, case angular velocities and their derivatives, and coordinatizing in the gimbal reference frame yields

$$\overline{\overset{i}{H}}_{g_g} = \begin{bmatrix} I_{g_t} (\ddot{\theta}_{g_o} + \dot{\omega}_o^{c-i}) \\ I_{g_t} (\ddot{\theta}_{g_i} + \dot{\omega}_i^{c-i}) \\ I_{g_s} (\ddot{\theta}_{g_s} + \dot{\omega}_s^{c-i}) \end{bmatrix} \tag{3.13}$$

From Newton's equations,

$$\overline{M}_f = \overline{\overset{i}{H}}_f \tag{3.14}$$

and

$$\overline{M}_g = \overline{\overset{i}{H}}_g \tag{3.15}$$

where $\overline{M}_f$ and $\overline{M}_g$ are the resultant moments applied to the float and gimbal, respectively. The moments applied to the float are due to the torque generator, flotation fluid viscosity, support wires, and other unspecified sources. Gimbal moments arise from the same sources except for the torquer. Expanding these moments into scalar form results in

$$M_{f_o} = M_{f_o}^c - D_i(\dot{\sigma}_o - \dot{\theta}_{g_o}) - T_i(\sigma_o - \theta_{g_o}) + M_{f_o}^d \tag{3.16a}$$

$$M_{f_i} = M^c_{f_i} - D_i(\dot{\sigma}_i - \dot{\theta}_{g_i}) - k_i(\sigma_i - \theta_{g_i}) + M^d_{f_i} \qquad (3.16b)$$

and

$$M_{g_o} = -D_o\dot{\theta}_{g_o} + D_i\dot{\sigma}_o - T_i(\theta_{g_o} - \sigma_o) - k_o\theta_{g_o} + M^d_{g_o} \qquad (3.17a)$$

$$M_{g_i} = -D_o\dot{\theta}_{g_i} + D_i\dot{\sigma}_i - T_o\theta_{g_i} - k_i(\theta_{g_i} - \sigma_i) + M^d_{g_i} \qquad (3.17b)$$

where

$M^c_{f_o}$, $M^c_{f_i}$ = torque generator command moments

D_o, D_i = flotation fluid viscous friction coefficients

k_o, k_i = support wire rotational elastic restraint coefficients

T_o, T_i = support wire tension coefficients

$M^d_{f_o}$, $M^d_{f_i}$ = float disturbance moments

$M^d_{g_o}$, $M^d_{g_i}$ = gimbal disturbance moments

Expanding (3.14) and (3.15), and Laplace transforming results in

$$\begin{bmatrix} I_{f_t}S^2+D_iS+T_i & hS & -(D_iS+T_i) & 0 \\ -hS & I_{f_t}S^2+D_iS+k_i & 0 & -(D_iS+k_i) \\ -(D_iS+T_i) & 0 & I_{g_t}S^2+D_oS+(T_i+k_o) & 0 \\ 0 & -(D_iS+k_i) & 0 & I_{g_t}S^2+D_oS+(T_o+k_i) \end{bmatrix} \begin{bmatrix} \sigma_o(S) \\ \sigma_i(S) \\ \theta_{g_o}(S) \\ \theta_{g_i}(S) \end{bmatrix} = \begin{bmatrix} M^c_{f_o}(S) \\ M^c_{f_i}(S) \\ 0 \\ 0 \end{bmatrix}$$

$$- \begin{bmatrix} I_{f_t}S & h \\ -h & I_{f_t}S \\ I_{g_t}S & 0 \\ 0 & I_{g_t}S \end{bmatrix} \begin{bmatrix} \omega^{c-i}_o(S) \\ \omega^{c-i}_i(S) \end{bmatrix} + \begin{bmatrix} M^d_{f_o}(S) \\ M^d_{f_i}(S) \\ M^d_{g_o}(S) \\ M^d_{g_i}(S) \end{bmatrix}. \qquad (3.18)$$

Initial conditions are neglected since only steady state response is desired.

Parameter values for the gyros are listed in Table 3.

Table 3

EXPERIMENTALLY EVALUATED GYRO PARAMETERS

Parameter	X-Y Gyro	X-Z Gyro	Units
h	1.0	1.0	$Kg\text{-}m^2/sec$
D_i	0.048	0.028	N-m-sec
D_o	0.51	0.41	N-m-sec
k_i	0.0014	0.00093	N-m/rad
k_o	0.0024	0.0019	N-m/rad
I_{f_t}	0.0016	0.0016	$Kg\text{-}m^2$
I_{g_t}	0.022	0.022	$Kg\text{-}m^2$
T_i	1.35	1.35	N-m/rad
T_o	1.35	1.35	N-m/rad

The design value for the angular momentum h is used since the wheel moment of inertia is unknown due to lack of documentation. Values for the viscous dampling coefficients D_i, D_o and support wire rotational elastic restraint coefficients k_i, k_o and the tests used to obtain them are discussed in Chapter II. These values are accurate to within 10%. The float and gimbal inertias and the support wire tension coefficients were derived from tests performed on the X-Y gyro with the spin power off. Sinusoidal torques at numerous frequencies were applied to each axis of the float and the pickoff voltages recorded. The transfer functions between the input torques and pickoff signals with zero angular momentum were derived and fit to the experimental frequency response. Large uncertainties, perhaps as high as 100%, exist in the inertia and tension estimates due to pickoff noise and variability of the experimental

data. However, it will be shown later that these parameters have an insignificant effect on overall system response, and as a result no effort was made to improve the estimates. Values of the inertias and support wire tension coefficients for the X-Z gyro are assumed to be equal to those of the X-Y gyro, since the gyros are of identical construction. These values also are of little consequence in the ensuing discussion.

Several additional approximations and assumptions will now be made in order to simplify (3.18).

1. k_o, k_i are negligibly small.
2. $D_o \gg D_i$
3. The inner gimbal equation is decoupled from the rest of the system due to smallness of the term $(D_i s + k_i)\ \sigma_i$. It will no longer be considered.
4. The case perturbations are limited to small angles θ_{c_o} and θ_{c_i}.
5. The command torques, M_f^c, derived from the caging amplifiers exactly cancel the constant earth rate term and any constant terms in the disturbance torques.
6. Caging amplifier dynamics are sufficiently low in frequency to be neglected.
7. The angular velocity of the case ω^{c-i} consists of a constant term due to rotation of the earth and a zero mean perturbation due to motion of the gyro mount relative to the earth.

With these assumptions (3.18) becomes

$$\begin{bmatrix} I_{f_t} S^2 + D_i S + T_i & hS & -(D_i S + T_i) \\ -hS & I_{f_t} S^2 + D_i S & 0 \\ -(D_i S + T_i) & 0 & I_{g_t} S^2 + D_o S + T_i \end{bmatrix} \begin{bmatrix} \sigma_o(S) \\ \sigma_i(S) \\ \theta_{g_o}(S) \end{bmatrix} = - \begin{bmatrix} I_{f_t} S^2 & hS \\ -hS & I_{f_t} S^2 \\ I_{g_t} S^2 & 0 \end{bmatrix} \begin{bmatrix} \theta_{o_c}(S) \\ \theta_{i_c}(S) \end{bmatrix} + \begin{bmatrix} M_{f_o}^{d'}(S) \\ M_{f_i}^{d'}(S) \\ M_{g_o}^{d}(S) \end{bmatrix} \tag{3.19}$$

where $M_{f_o}^{d'}$ and $M_{f_i}^{d'}$ are the residual float disturbance torques after the mean is removed.

The roots of the characteristic equation associated with (3.19) are well separated, and, as a result, the characteristic equation can be factored approximately into

$$h^2 T_i S^2 \left(\frac{S^2}{\omega_n^2} + 2\zeta \frac{S}{\omega_n} + 1\right)\left(\frac{S}{\omega_1} + 1\right)\left(\frac{S}{\omega_2} + 1\right) = 0 \qquad (3.20)$$

where

$$\omega_n^2 \cong \frac{h^2}{I_{f_T}^2} = (625 \text{ rad/sec})^2$$

$$\zeta \cong \frac{D_i}{h}\left(1 + \frac{I_{f_t} D_o}{2 I_{g_t} D_i}\right) = 0.07$$

$$\omega_1 \cong \frac{T_i}{D_o} = 2.6 \text{ rad/sec}$$

$$\omega_2 \cong \frac{D_o}{I_{g_t}} = 23 \text{ rad/sec}$$

The approximate transfer functions between the case angles θ_c and the pickoff angles σ are presented in Table 4.

From these transfer functions it can be seen that the only major departure of the Atlas gyro from direct angle indication is the large low frequency coupling of outer axis case motion into inner axis pickoff angle ($\sigma_i/\theta_{o_c} \cong 0.51$, $\omega < 1$). This coupling was acceptable in the original Atlas platform since the pickoff angles were held at null by the platform servo loops.

B. Autocollimator

As discussed in Chapter II, the primary autocollimator has two outputs, one for control and the other for instrumentation. The transfer function between base angle and control channel signal is

$$\frac{\gamma_{AC}}{\theta} = \frac{K_{AC}}{\frac{S^2}{\omega_{AC}^2} + 2\zeta \frac{S}{\omega_{AC}} + 1} \qquad (3.21)$$

Table 4

RESPONSE OF GYRO FLOAT AND GIMBAL TO CASE MOTION

Transfer Function	Parametric	Numerical (X-Y gyro)	Remarks
$\frac{\sigma_o}{\theta_{o_c}}$	$-1 - \frac{I_g D_1 T_1^2}{h^2} \frac{S\left[I_{f_T} S^2 + \left(\frac{I_{f_T}}{D_1} + \frac{D_1}{T_1}\right)S + 1\right]}{\left(\frac{S^2}{\omega_n^2} + \frac{2\zeta S}{\omega_n} + 1\right)\left(\frac{S}{\omega_1} + 1\right)\left(\frac{S}{\omega_2} + 1\right)}$	$-1 + \frac{0.0019\, S\left(\frac{S^2}{(25)^2} + \frac{2(0.86)S}{(25)} + 1\right)}{\left[\frac{S^2}{(625)^2} + \frac{2(0.07)S}{625} + 1\right]\left(\frac{S}{2.6} + 1\right)\left(\frac{S}{23} + 1\right)}$	$\cong 1$
$\frac{\sigma_o}{\theta_{i_c}}$	$-\frac{D_1}{h} \frac{1}{\left(\frac{S^2}{\omega_n^2} + \frac{2\zeta S}{\omega_n} + 1\right)}$	$-\frac{0.048}{\frac{S^2}{(625)^2} + \frac{2(0.07)S}{625} + 1}$	small
$\frac{\sigma_i}{\theta_{o_c}}$	$\frac{D_o}{h} \frac{\left(\frac{D_1}{D_o T_1 h} S + 1\right)}{\left(\frac{S^2}{\omega_n^2} + \frac{2\zeta S}{\omega_n} + 1\right)\left(\frac{S}{\omega_1} + 1\right)\left(\frac{S}{\omega_2} + 1\right)}$	$\frac{0.51\left(\frac{S}{14} + 1\right)}{\left[\frac{S^2}{(625)^2} + \frac{2(0.07)S}{625} + 1\right]\left(\frac{S}{2.6} + 1\right)\left(\frac{S}{23} + 1\right)}$	large cross-coupling $\lvert S\rvert \ll 3$
$\frac{\sigma_i}{\theta_{i_c}}$	$-1 + \frac{I_{f_t} T_1}{h^2} \frac{\left(\frac{D_1}{T_1} S + 1\right)^2}{\left(\frac{S^2}{\omega_n^2} + \frac{2\zeta S}{\omega_n} + 1\right)\left(\frac{S}{\omega_1} + 1\right)\left(\frac{S}{\omega_2} + 1\right)}$	$-1 + \frac{0.0019\left(\frac{S}{28} + 1\right)^2}{\left[\frac{S^2}{(625)^2} + \frac{2(0.07)S}{625} + 1\right]\left(\frac{S}{2.6} + 1\right)\left(\frac{S}{23} + 1\right)}$	$\cong 1$
$\frac{\theta_{g_o}}{\theta_{o_c}}$	$-\frac{\frac{I_{g_t}}{T_1} S^2 + D_1\left(\frac{I_{g_t}}{h^2} + \frac{1}{T_1}\right)S + 1}{\left(\frac{S}{\omega_1} + 1\right)\left(\frac{S}{\omega_2} + 1\right)}$	$-\frac{\left[\frac{S^2}{(7.8)^2} + \frac{2(0.14)S}{7.8} + 1\right]}{\left(\frac{S}{2.6} + 1\right)\left(\frac{S}{23} + 1\right)}$	$\cong 1$; $\frac{\lvert S\rvert}{7.8}\frac{\lvert S\rvert}{7.8} \ll 1$, $\frac{\lvert S\rvert}{7.8} \gg 1$
$\frac{\theta_{g_o}}{\theta_{i_c}}$	$\frac{D_1}{h} \frac{\left(\frac{D_1}{T_1} S + 1\right)}{\left(\frac{S^2}{\omega_n^2} + \frac{2\zeta S}{\omega_n} + 1\right)\left(\frac{S}{\omega_1} + 1\right)\left(\frac{S}{\omega_2} + 1\right)}$	$\frac{0.048\left(\frac{S}{28} + 1\right)}{\left(\frac{S^2}{(333)^2} + \frac{2(0.08)S}{333} + 1\right)\left(\frac{S}{2.6} + 1\right)\left(\frac{S}{23} + 1\right)}$	small
$\frac{\sigma_{g_i}}{\sigma_{o_c}}$	0	0	negligible
$\frac{\theta_{g_i}}{\theta_{i_c}}$	$-\frac{I_{g_t}}{T_o} \frac{S^2}{\left(\frac{S}{\omega_1} + 1\right)\left(\frac{S}{\omega_2} + 1\right)}$	$-0.016 \frac{S^2}{\left(\frac{S}{2.6} + 1\right)\left(\frac{S}{23} + 1\right)}$	$\cong 0$ $\lvert S\rvert \ll 2.6$ $\cong 1$ $\lvert S\rvert > 23$

where

γ_{AC_x}, γ_{AC_y} = autocollimator control output signals (V)

θ_x, θ_y = autocollimator base angles (rad)

K_{AC_x}, K_{AC_y} = 5700, 5990 V/rad

ω_{AC} = 264 rad/sec

ζ = 0.71

The transfer function for the instrumentation channel is

$$\frac{\gamma_{AI}}{\theta} = \frac{K_{AI}}{\left(\frac{S}{\omega_{AI_1}} + 1\right)\left(\frac{S^2}{\omega^2_{AI_2}} + 2\zeta\,\frac{S}{\omega_{AI_2}} + 1\right)} \tag{3.22}$$

where

γ_{AI_x}, γ_{AI_y} = autocollimator instrumentation output signals (V)

K_{AI_x}, K_{AI_y} = 5630, 5920 V/rad

ω_{AI_1} = 755 rad/sec

ω_{AI_2} = 1250 rad/sec

ζ = 0.71

Due to flexibility in the autocollimator mount, the base angle is composed of both the "rigid" displacement of the platform gimbals and the bending angle of the mount. The latter is considered a disturbance input to the autocollimator.

C. Platform

The Fixed Base Simulator is normally operated with the gimbals orthogonal, although it can be stabilized under gyro control with the gimbals non-orthogonal. Since all data were taken with the gimbals orthogonal, the platform model will be limited to this case. Derivations of the general non-orthogonal three-axis platform equations can be found in [W7] and [B9].

The linearized rotational equations of motion of the platform with orthogonal gimbals are

$$\bar{\bar{I}}_p \ddot{\bar{\theta}}_p = \bar{M}_m + \bar{M}_b + \bar{M}_{gr} + \bar{M}_d \tag{3.23}$$

where

$\bar{\theta}_p$ = angular acceleration of gimbals relative to base

$\bar{\bar{I}}_p$ = effective moment of inertia matrix

$\bar{M}_m$ = gimbal motor torque

$\bar{M}_b$ = gimbal bearing torque

$\bar{M}_{gr}$ = gyro reaction torque

$\bar{M}_d$ = disturbance torque

Values of the on-diagonal moments of inertia obtained from a closed loop frequency response of autocollimator output to command torque input are: $I_{xx} = 0.70$ Kg-m^2, $I_{yy} = 0.25$ Kg-m^2, $I_{zz} = 0.52$ Kg-m^2. The effects of off-diagonal terms are small and are treated as disturbances.

D. Motor Torque

The torque from each of the three permanent magnet gimbal motors is proportional to the armature current,

$$M_m = K_m i \tag{3.24}$$

where

K_m = motor torque gain (0.53 N-m/A)

i = armature current

The current, in turn, is related to the platform control amplifier output voltage and the back EMF of the motor by

$$i = \frac{(V_p - E)}{R_a\left(\frac{S}{\omega_m} + 1\right)} \tag{3.25}$$

where

R_a = armature resistance (23 Ω)

L_a = armature inductance (23 mH)

V_p = control amplifier output voltage

E = back EMF

$\omega_m = R_a/L_a$ = 1000 rad/sec

The motor torque gain was deduced from measurements of the torque required to balance motor torque at several values of input current. The torque was supplied by a calibrated spring balance acting through a known moment arm. Errors introduced from uncertainty in the moments arm and calibration of the spring balance were limited to less than 5%.

The back EMF of the motor is

$$E = K_b\dot{\theta}_p \tag{3.26}$$

where

K_b = back EMF proportionality factor (0.53 V-sec)

In order to satisfy the condition that input power must equal output power plus power lost, the back EMF coefficient must equal the motor torque gain. An independent check of the back EMF coefficient was made by oscillating the platform by hand and recording the voltage induced across the motor armature. This low accuracy experiment produced a value of $K_b = 0.6$, well within the limits of experimental error.

The output of each platform control amplifier is

$$V_p = K_p(V_c + K_d V_{T_d}) \tag{3.27}$$

where

V_c = output of compensation network

V_{T_d} = command torque voltage

K_p = platform control power amplifier gain

K_d = command torque gain

The values of the X, Y, and Z axes amplifier gain K_p are 302,164,333 V_{DC}/V_{DC}. All three command torque gains are 0.0075 V_{DC}/V_{DC}. Accuracy of these electronic measurements is approximately 1%.

E. Compensation Network

Each Minuteman I platform control amplifier has a passive compensation network. Its input is either an autocollimator output or a demodulated gyro pickoff signal. The output is amplified by a power stage to drive the gimbal motors.

The compensation can be separated into three main functions: lag-lead to increase low frequency gain, lead-lag to provide damping and stability margins, and high frequency noise attenuation. The transfer function, computed from a network schematic, is

$$\frac{V_c}{V_{i_n}} = C(S) = \frac{\left(\frac{S}{\omega_{c_2}} + 1\right)\left(\frac{S}{\omega_{c_3}} + 1\right)}{\left(\frac{S}{\omega_{c_1}} + 1\right)\left(\frac{S}{\omega_{c_4}} + 1\right)\left(\frac{S}{\omega_{c_5}} + 1\right)\left(\frac{S}{\omega_{c_6}} + 1\right)} \qquad (3.28)$$

where the break frequencies in rad/sec are

$\omega_{c_1} = 0.15$ $\quad \omega_{c_3} = 30$ $\quad \omega_{c_5} = 1200$

$\omega_{c_2} = 10$ $\quad \omega_{c_4} = 200$ $\quad \omega_{c_6} = 5000$

Fig. 22 is a Bode plot of the compensation network.

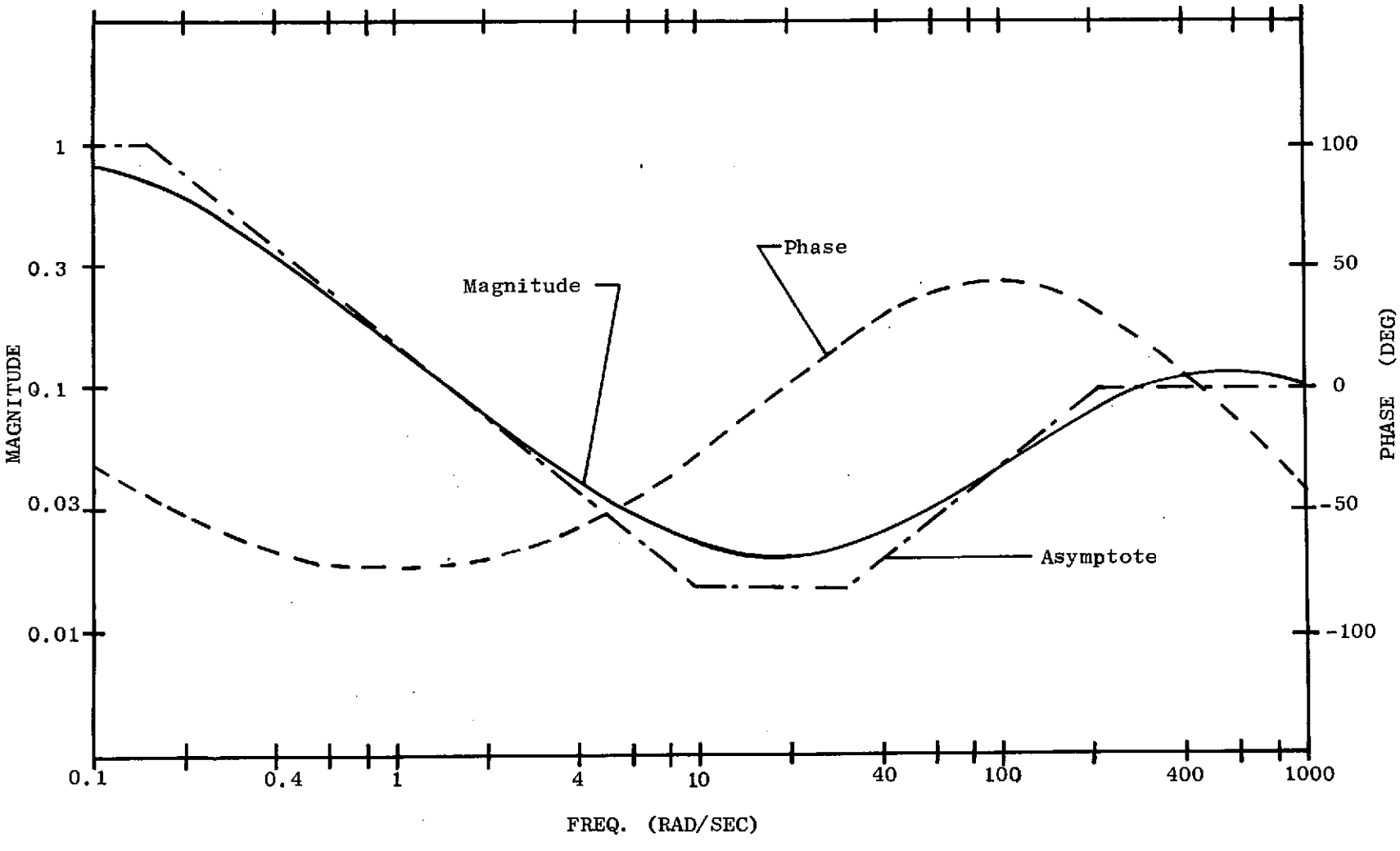

Fig. 22. COMPUTED COMPENSATION NETWORK FREQUENCY RESPONSE.

F. Gyro Reaction Torque

Motion of the platform gimbals is resisted by the two gyros through tension in the gimbal support wires and viscous coupling between the gyro gimbals and case. From (3.17), throwing out unnecessary or small terms, the torque applied by the gimbal to the case is

$$M_{g_{r_o}} = D_o \dot{\theta}_{g_o} \tag{3.29}$$

$$M_{g_{r_i}} = D_o \dot{\theta}_{g_i} + T_o \theta_{g_i} \tag{3.30}$$

The two gyros are oriented such that both the outer gimbal axes are directed along the platform X axis, Fig. 23. The inner gimbal axes of the X-Y and X-Z gyros are in the direction of the platform Y and Z axes, respectively.

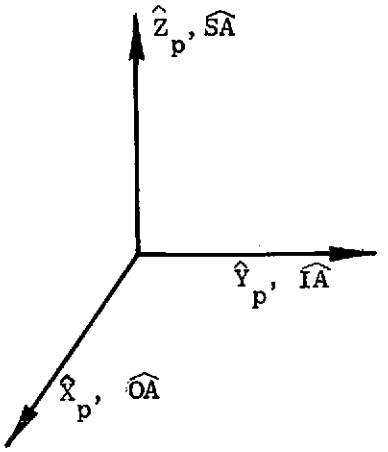

Fig. 23a. X-Y GYRO CASE ORIENTATION.

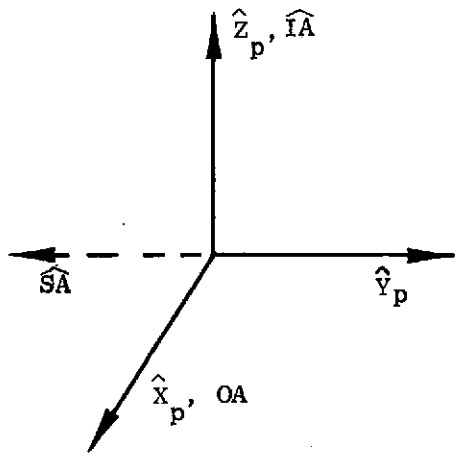

Fig. 23b. X-Z GYRO CASE ORIENTATION.

With this orientation the gyro reaction torques, expressed in platform axes, are

$$M_{g_{r_x}} = D_o(\dot{\theta}_{g_{o_1}} + \dot{\theta}_{g_{o_2}}) \tag{3.31}$$

$$M_{g_{r_y}} = D_o(\dot{\theta}_{g_{i_1}} + T_o \theta_{g_{i_1}}) \tag{3.32}$$

$$M_{g_{r_z}} = D_o \dot{\theta}_{g_{i_2}} + T_o \theta_{g_{i_2}} \tag{3.33}$$

where the subscripts 1 and 2 refer to the X-Y and X-Z gyros, respectively.

G. Gimbal Bearing Torque

The gimbal shafts are supported by ball bearings which provide close alignment and low friction between the shafts and their supports. The friction normally is considered to be caused by a combination of rolling and sliding resistance, and the level of friction to be independent of the relative velocity and displacement. However, for the small motion exhibited by the simulator it was found that a more descriptive model is a lightly damped rotational spring. The background and supporting evidence for this result is presented in Chapter V. It is an important example of how power spectral density results can be used in developing system models.

Nonlinearity of the friction in the restraint torque makes analysis of the system difficult. However, for small motion of the platform gimbals, the bearing coulomb friction is small compared to the viscous damping provided by the gyros and can be neglected. The gimbal bearing torque is therefore modeled as

$$M_b = -K_s \theta_p \tag{3.34}$$

Experimentally determined values of the X and Y axes elastic restraint coefficients are K_{s_x} = 410 N-m/rad and K_{s_y} = 380 N-m/rad. The Z axis coefficient was not measured since only the primary X and Y axes are considered in the experiments of Chapter V.

H. Closed Loop Dynamics

The equations describing the major system components are now combined so that the closed loop behavior of the system can be described.

The simulator can be stabilized using either the gyro or autocollimator error signals, and these two cases must be treated separately.

1. Autocollimator Stabilization

Using the autocollimators as the reference, the simulator stabilization loops separate into three independent channels. Products of inertia and the elastic restraint terms of the gyro reaction torques are small and are considered disturbances. Figure 24 shows the functional relationships of the major components.

The figure as shown represents only the Y platform axis. In the X axis, both gyro gimbals provide damping to the platform, and therefore a second parallel gyro gimbal feedback path around the platform block should be included. The transfer function of these blocks must also be changed to $\theta_{g_o}/\theta_{o_c}$ (Table 4). Gyro pickoff cross-coupling indicated at the bottom of the figure can be neglected for the X axis.

The Z axis block diagram is similar to the Y axis shown, except that the Z autocollimator does not have an instrumentation channel or noise filtering. The autocollimator block here is more appropriately modeled as a constant gain K_{AC}.

In all three channels, motor back EMF can be neglected. The motor lag and the two highest frequency lags in the compensation network can also be neglected when considering frequencies less than 15 Hz. Above this frequency, phase shifts from these elements become important.

Further noted in Fig. 24 are the sources of disturbance and command to the system. Starting at the upper left of the diagram, the autocollimator output can be biased by introducing a signal γ_c. Biased and unbiased autocollimator outputs are then physically available at the points denoted γ_{AC} and γ_{AI}, respectively. Platform torque commands are introduced by applying a voltage V_{T_d} to a divider circuit with gain K_d at the input to the platform motor power amplifier. Environmental and other unspecified torques M_d directly accelerate the platform gimbals. All gyro gimbal disturbances are included in the small additive term n_G. Autocollimator noise n_A is created primarily in the photodetector and in the flexible autocollimator mount. This noise is filtered in both the

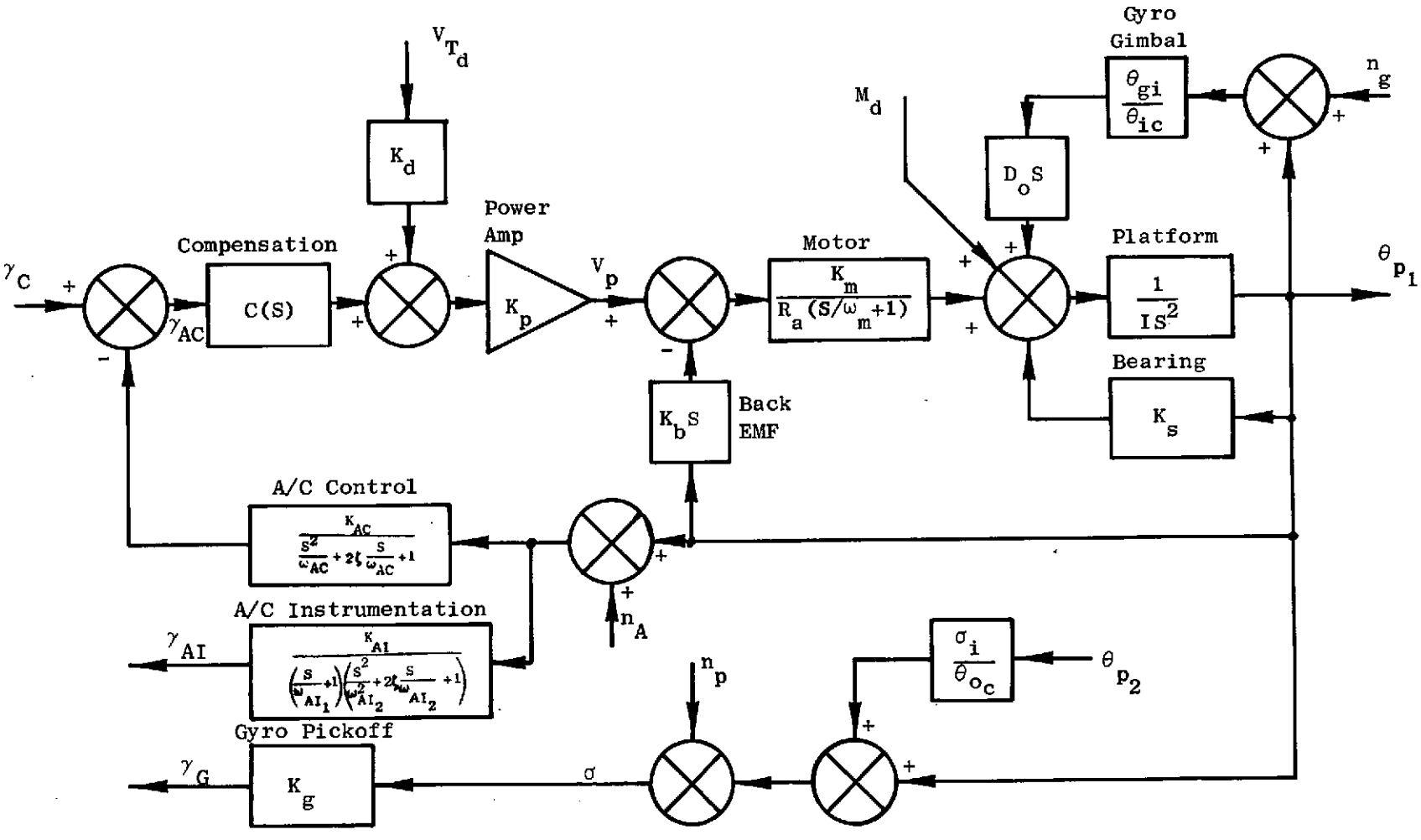

Fig. 24. SINGLE-AXIS AUTOCOLLIMATOR STABILIZATION LOOP. At mid-frequenices (0.1 to 100 Hz), back EMF, motor lag, and gyro gimbal dynamics have a negligible effect on the response of the loop.

control and instrumentation output channels of the primary X-Y autocollimator. Finally, gyro electronic noise and the effects of disturbance torques are combined in the additive input n_p.

It will be of later interest in evaluating experimental results to have expressions for the closed loop transfer functions between the sensor outputs and the various command and disturbance inputs. As a first step, a transfer function for the platform section is derived.

The transfer function between the motor torque M_m and the platform angle θ_p including the gyro gimbal dynamics is almost identical to the transfer function obtained by replacing the gyro dynamics with a gain of unity. In other words, the gyro gimbal dynamics are not important. The reduced transfer function for the Y axis is then simply

$$\frac{\theta_{p_y}}{M_{m_y}} \cong \frac{1}{I_{yy}S^2 + D_oS + K_{s_y}} \tag{3.35}$$

The X axis damping coefficient is twice as large since both gyros are viscously coupled.

$$\frac{\theta_{p_x}}{M_{m_x}} \cong \frac{1}{I_{xx}S^2 + 2D_oS + K_{s_x}} \tag{3.36}$$

Figure 25a is a root locus of the autocollimator stabilization loops as a function of autocollimator gain. The actual operating gain is sufficiently low that the poles of the closed loop are quite close to those of the open loop.

An enlarged view of the locus near the origin is shown for the X and Y axes in Fig. 25b and 25c. Note that the presence of the autocollimator filter poles at $(-180, \pm j180)$ sec^{-1} prevents the roots originating at the lower frequency platform gimbal/bearing poles [X = $(-0.8, \pm j24.2)$ sec^{-1} and Y = $(-1.1, \pm j39.0)$ sec^{-1}] from penetrating very far into the left half plane. As a consequence, the closed loop poles lying on this branch of the locus are lightly damped.

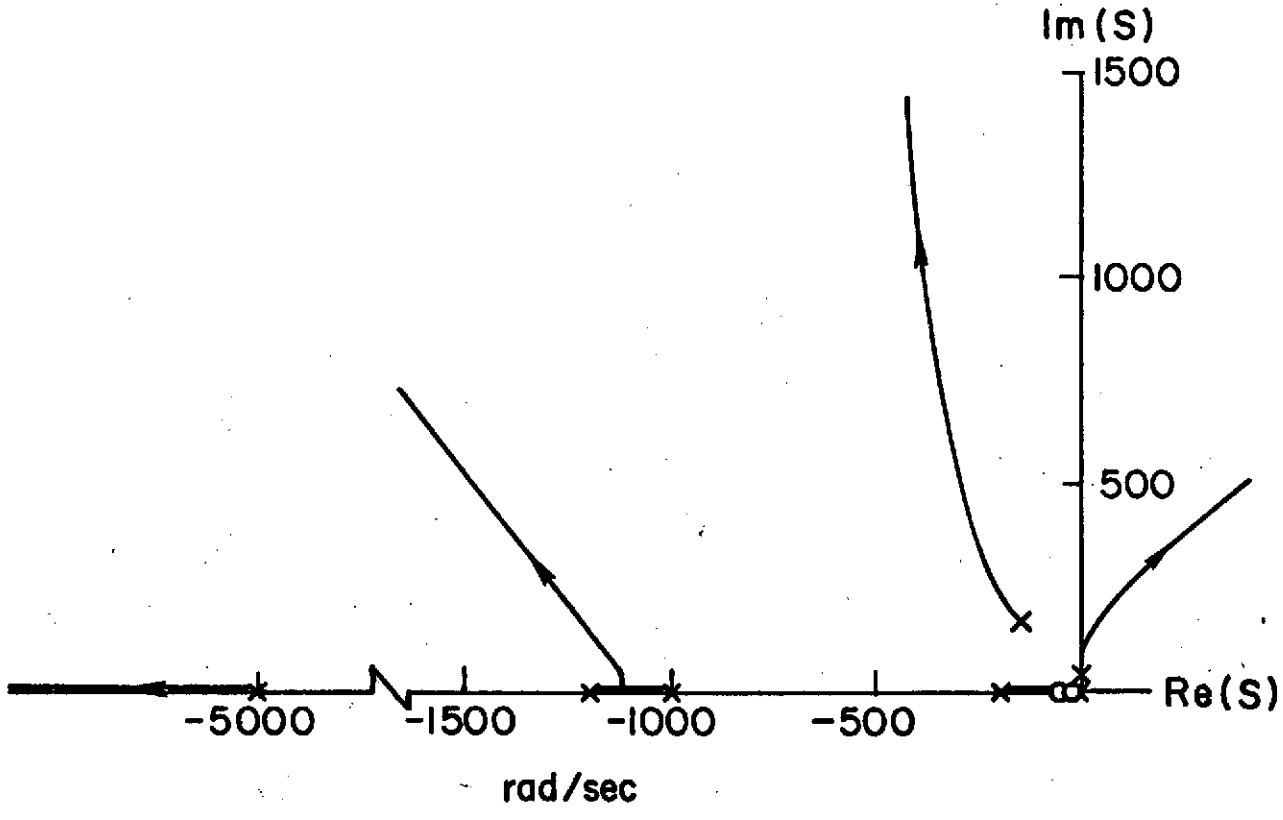

FIG. 25a AUTOCOLLIMATOR STABILIZATION LOOP OVERALL ROOT LOCUS

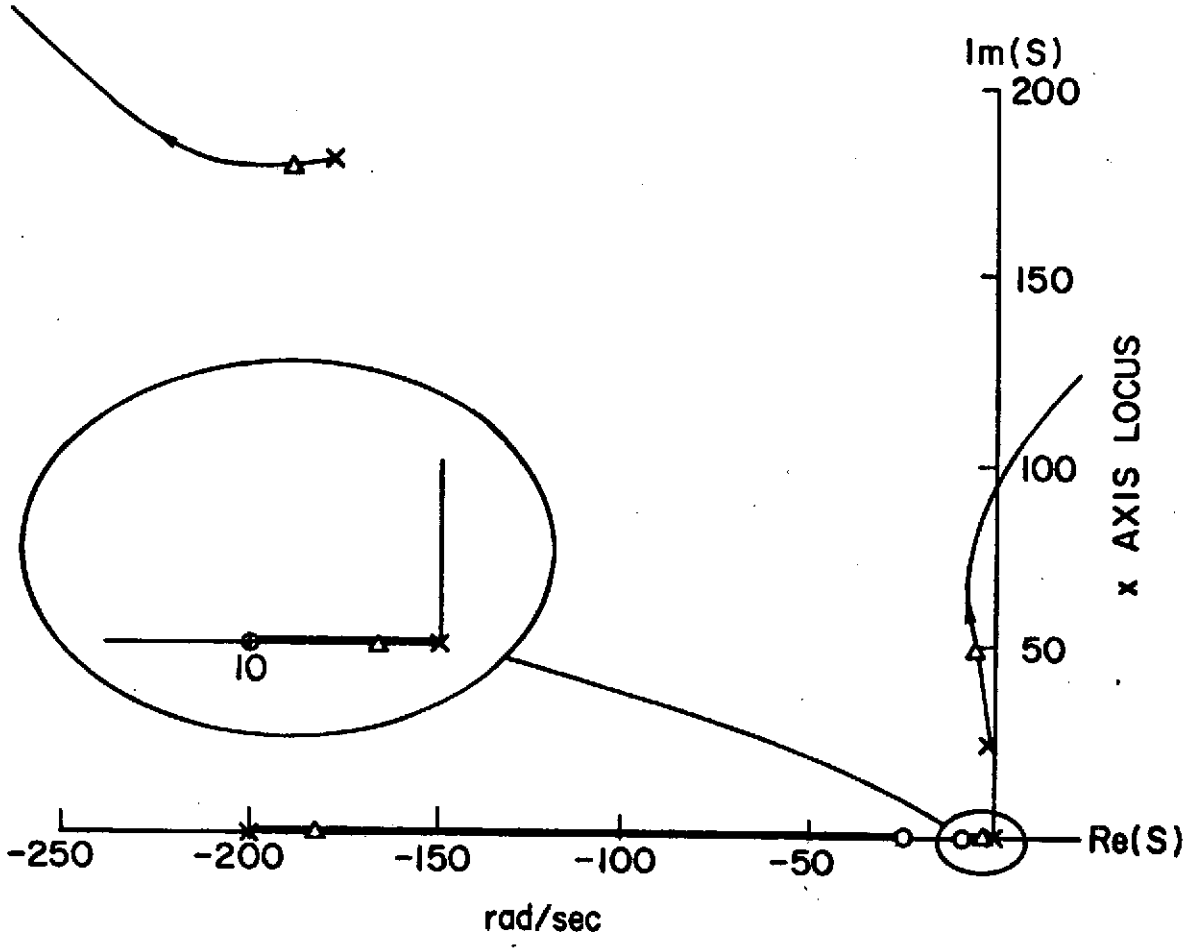

FIB. 25b X-AXIS AUTOCOLLIMATOR STABILIZATION LOOP LOW FREQUENCY ROOT LOCUS

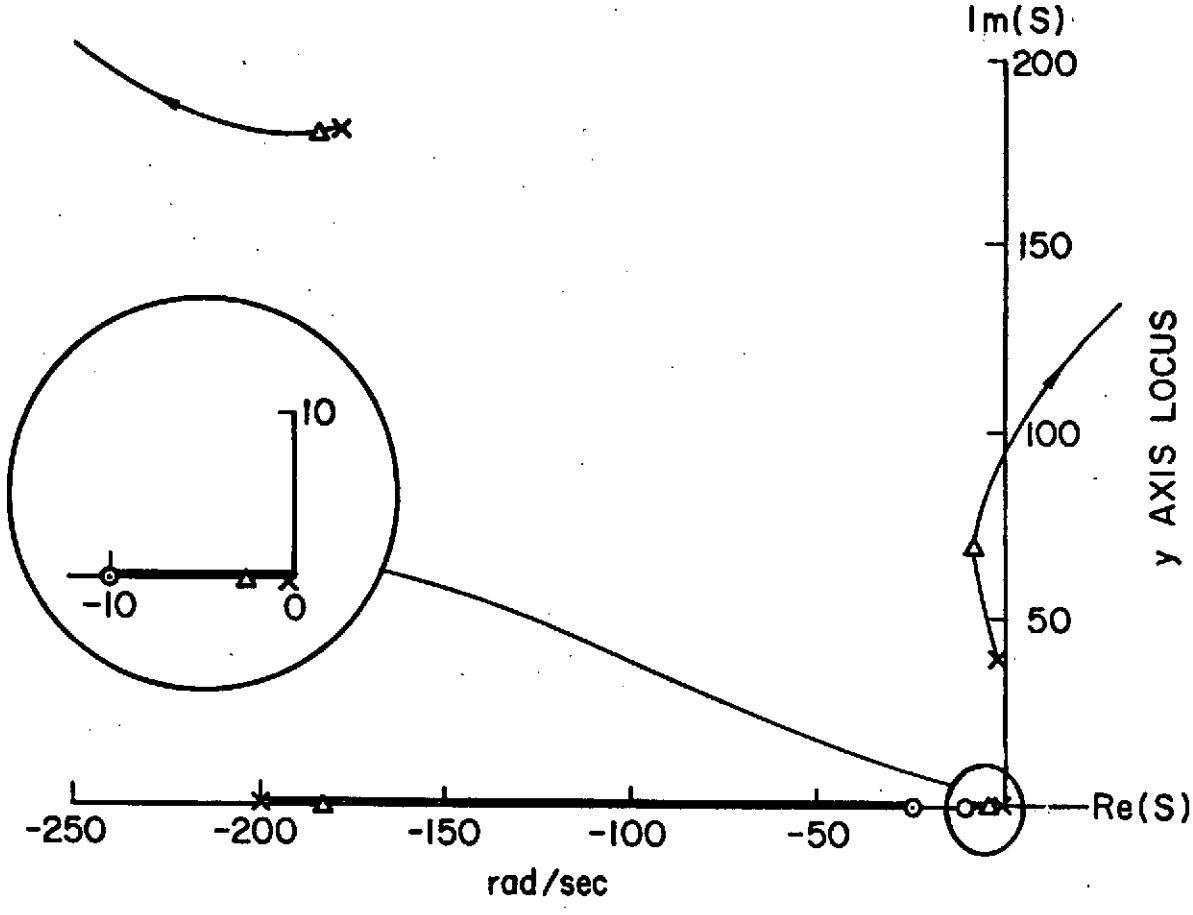

FIG. 25c Y-AXIS AUTOCOLLIMATOR STABILIZATION LOOP LOW FREQUENCY ROOT LOCUS

Closed loop transfer functions between most of the system inputs and outputs indicated in Fig. 24 are expressed in Table 5. Roots above 100 Hz are of little interest and are neglected for simplicity. The positions of the closed loop poles are indicated in the root loci of Fig. 25b and c.

The transfer functions between autocollimator noise n_A and the sensor outputs will be of particular interest in the discussion of experimental results in Chapter V. Magnitude plots of these transfer functions, based on the parameter estimates indicated in this chapter, are shown in Fig. 26.

2. Gyro Stabilization

Using the gyros as the reference, the simulator stabilization loops are coupled due to the gyro viscosity and cannot be treated as three independent channels except at higher frequencies. The coupling, however, is almost entirely from the X axis into the Y and Z axis and not in the reverse direction. Figure 27 is a block diagram of the coupled X and Y stabilization loops. The unidirectional coupling is indicated by the block $\sigma_i(S)/\theta_{o_c}(S)$ evaluated in Table 4. The magnitude of this transfer function is less than 0.1 above 20 r/sec falling off inversely with increasing frequency.

At higher frequencies, where coupling can be disregarded, the individual stabilization loops are nearly identical to the autocollimator stabilization loops except that the gyro does not have filtering. Filtering is not required in the gyros since their mounting brackets are sufficiently rigid to prevent instabilities.

The closed loop poles of the X-Y system in Fig. 27 factor, by inspection, into the poles of each individual axis and the poles of the coupling transfer function. Root loci can therefore be drawn for each axis; Fig. 28 shows the loci for the X and Y axes. The gyro loops are characterized by improved damping of the dominant oscillatory platform/bearing roots over the damping in the autocollimator loops, primarily due to the absence of the autocollimator filter.

The input-output relationships of the gyro stabilized system are quite similar to those of the autocollimator stabilized system and

Table 5

AUTOCOLLIMATOR STABILIZATION CONTROL LOOP RESPONSE

Output / Input	Transfer Function
$\frac{\gamma_{AC}}{\gamma_c}$; $\frac{1}{K_{AI}}\frac{\gamma_{AI}}{n_A}$	$A_1 \frac{\left(\frac{S}{\omega_{c_1}}+1\right)\left(\frac{S}{\omega_{c_4}}+1\right)\left[\left(\frac{S}{\omega_p}\right)^2+2\zeta_p\left(\frac{S}{\omega_p}\right)+1\right]\left[\left(\frac{S}{\omega_{AC}}\right)^2+2\zeta_{AC}\left(\frac{S}{\omega_{AC}}\right)+1\right]}{Q(S)}$
$\frac{1}{K_{AC}}\frac{\gamma_{AC}}{n_A}$;	$A_1 \frac{\left(\frac{S}{\omega_{c_1}}+1\right)\left(\frac{S}{\omega_{c_4}}+1\right)\left[\left(\frac{S}{\omega_p}\right)^2+2\zeta_p\left(\frac{S}{\omega_p}\right)+1\right]}{Q(S)}$
$\frac{K_{AC}}{K_{AI}}\frac{\gamma_{AI}}{\gamma_c}$; $\frac{K_{AC}}{K_g}\frac{\gamma_G}{\gamma_c}$	$K_L A_1 \frac{\left(\frac{S}{\omega_{c_2}}+1\right)\left(\frac{S}{\omega_{c_3}}+1\right)\left[\left(\frac{S}{\omega_{AC}}\right)^2+2\zeta_{AC}\left(\frac{S}{\omega_{AC}}\right)+1\right]}{}$
$\frac{1}{K_g}\frac{\gamma_G}{n_A}$	$K_L A_1 \frac{\left(\frac{S}{\omega_{c_2}}+1\right)\left(\frac{S}{\omega_{c_3}}+1\right)}{Q(S)}$
$\frac{\gamma_{AC}}{K_d V_{T_d}}$; $K_p K_m \frac{\gamma_{AC}}{N_d}$	$K_L A_1 \frac{\left(\frac{S}{\omega_{c_1}}+1\right)\left(\frac{S}{\omega_{c_4}}+1\right)}{Q(S)}$
$\frac{K_{AC}}{K_{AI}}\frac{\gamma_{AI}}{K_d V_{T_d}}$; $\frac{K_{AC}}{K_g}\frac{\gamma_G}{K_d V_{T_d}}$ $\frac{K_{AC}}{K_{AI}} K_p K_m \frac{\gamma_{AI}}{N_d}$; $\frac{K_{AC}}{K_g} K_p K_m \frac{\gamma_G}{N_d}$	$K_L A_1 \frac{\left(\frac{S}{\omega_{c_1}}+1\right)\left(\frac{S}{\omega_{c_4}}+1\right)\left[\left(\frac{S}{\omega_{AC}}\right)^2+2\zeta_{AC}\left(\frac{S}{\omega_{AC}}\right)+1\right]}{Q(S)}$
$\frac{1}{K_g}\frac{\gamma_G}{n_p}$; $\frac{1}{K_g}\frac{\theta_{o_c}}{\theta_i}\frac{\gamma_G}{U_{p_2}}$	1

$$Q(S) = \left(\frac{S}{\omega_{c_1}}+1\right)\left(\frac{S}{\omega_{c_4}}+1\right)\left[\left(\frac{S}{\omega_p}\right)^2+2\zeta_p\left(\frac{S}{\omega_p}\right)+1\right]\left[\left(\frac{S}{\omega_{AC}}\right)^2+2\zeta_{AC}\left(\frac{S}{\omega_{AC}}\right)+1\right]$$

$$A_1 = \frac{\omega_{c_1}\omega_{c_4}\omega_p^2\omega_{AC}^2}{\omega_{c_2}\omega_{c_3}\omega_p^2\omega_{AC}^2}$$

$$K_L = \frac{K_p K_m K_{AC}}{R K_S}$$

Parameters			
Symbol	X	Y	Units
ω_{c_1}	0.15	0.15	rad/sec
$\bar{\omega}_{c_1}$	5.6	4.5	rad/sec
ω_{c_2}	10	10	rad/sec
ω_{c_3}	30	30	rad/sec
ω_{c_4}	200	200	rad/sec
$\bar{\omega}_{c_4}$	123	98	rad/sec
ω_p	21.2	39.0	rad/sec
$\bar{\omega}_p$	46.0	70.4	rad/sec
ζ_p	0.03	0.03	---
$\bar{\zeta}_p$	0.13	0.09	---
ω_{AC}	264	264	rad/sec
$\bar{\omega}_{AC}$	275	288	rad/sec
ζ_{AC}	0.71	0.71	---
$\bar{\zeta}_{AC}$	0.76	0.77	---
K_p	302	164	---
K_m	0.53	0.53	N-m/A
R_a	23	23	Ω
K_S	410	380	N-m/rad
K_{AC}	5700	5990	V/rad
K_{AI}	5630	5920	V/rad
K_g	6030	6700	V/rad
A_1	0.011	0.018	---
K_L	86.8	59.8	---

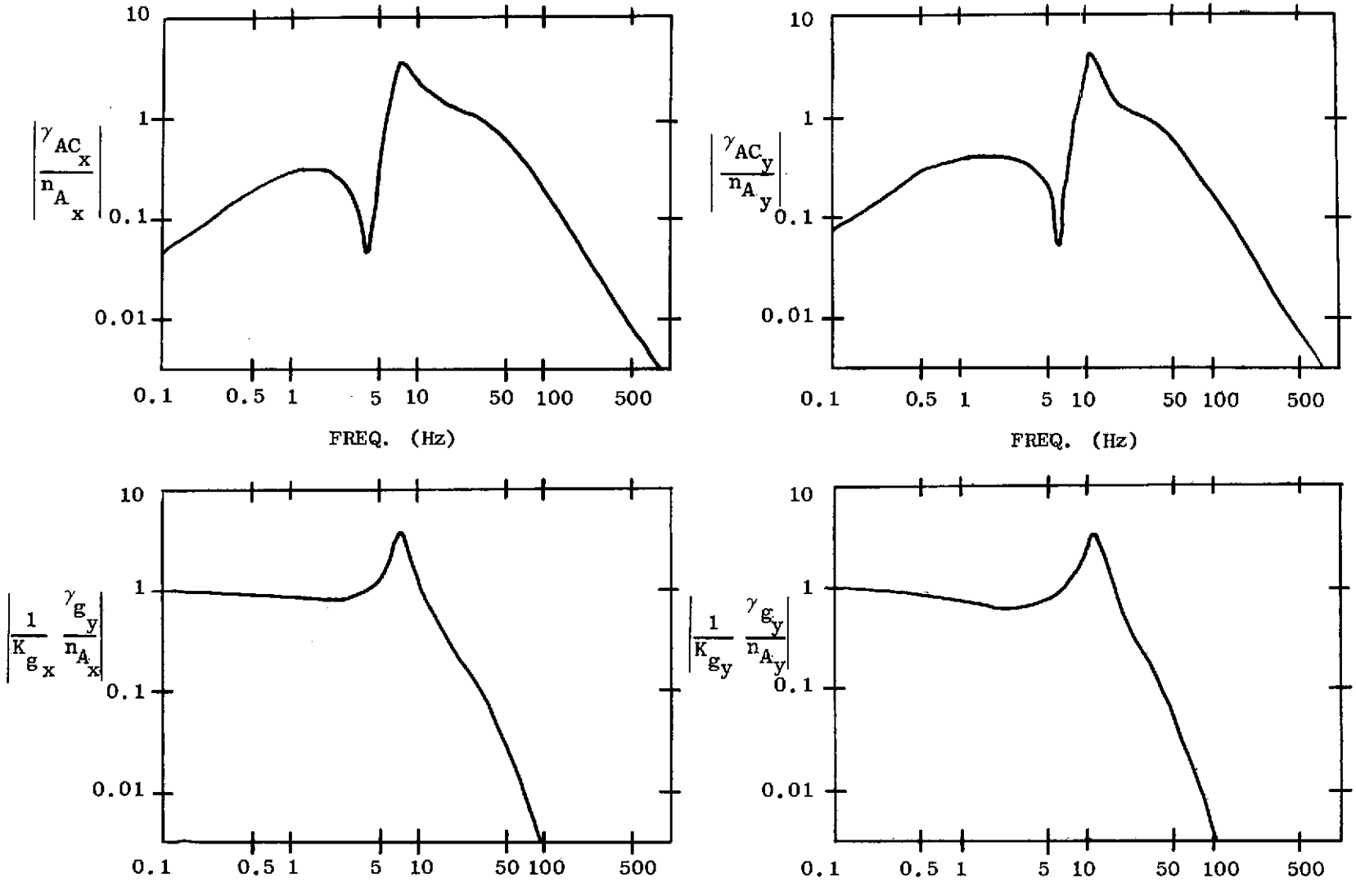

Fig. 26. MAGNITUDE OF SENSOR RESPONSE TO AUTOCOLLIMATOR NOISE n_A--AUTOCOLLIMATOR STABILIZATION.

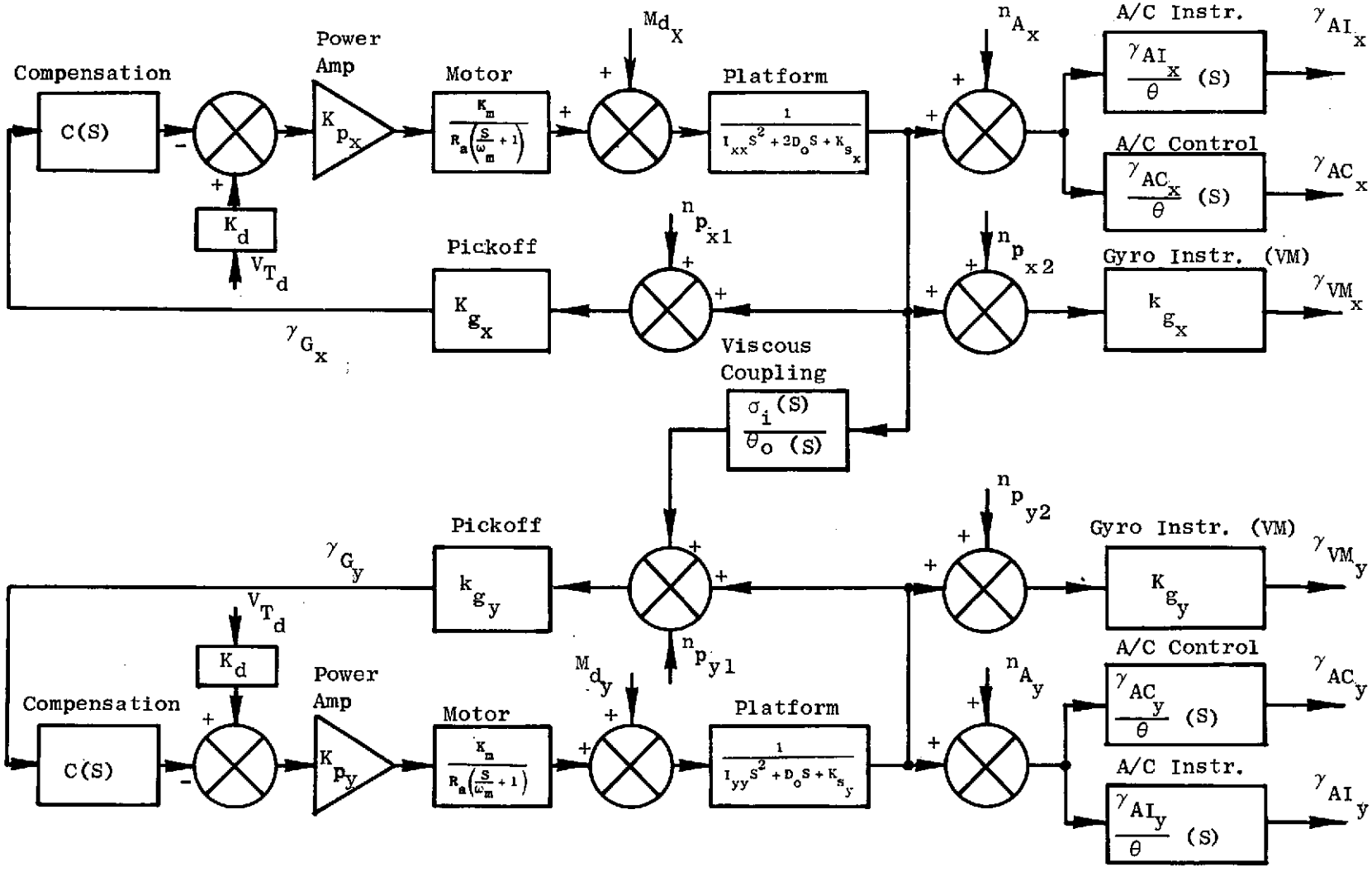

Fig. 27. X-Y AXES GYRO STABILIZATION LOOPS. Only at low frequencies is the viscous cross-axis coupling important.

consequently are not tabulated here. They may be found by simple modification of Table 5, using the new values of the low frequency closed loop poles listed in Table 6.

Table 6

GYRO STABILIZATION LOW FREQUENCY CLOSED LOOP ROOTS

Parameter	X	Y	Units
$\bar{\omega}_{c_1}$	5	5	rad/sec
$\bar{\omega}_{c_4}$	160	160	rad/sec
$\bar{\omega}_p$	43	60	rad/sec
ζ_p	0.24	0.27	--

Again, only the primary X and Y axes are of later interest. The autocollimator filter poles appear only in the autocollimator output transfer functions and do not affect the closed loop roots.

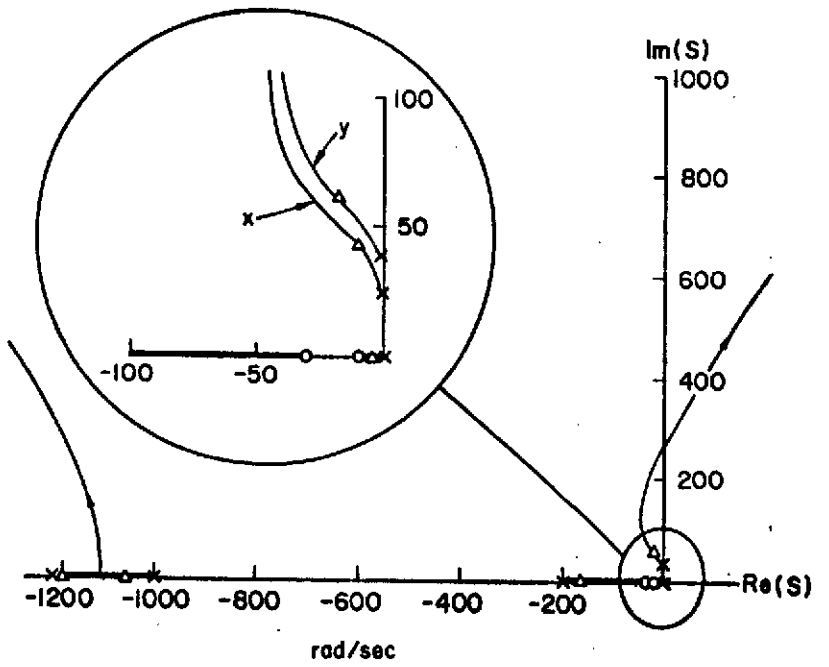

FIG. 28 X-Y AXES GYRO STABILIZATION LOOP ROOT LOCUS

Chapter IV

SPECTRAL ANALYSIS TECHNIQUES

A. Introduction

In evaluating the performance of precision instruments, the primary interest is in characterizing the errors present in the output signal. These errors can be categorized as systematic, random, or input dependent.

Systematic errors, those which can be described by an explicit model, are important to identify since they indicate error sources inherent in the design and those sensitive to the environment. Knowledge of the inherent error sources (e.g., gyro fixed drift) is necessary to verify that design specifications are being met, and may lead to performance improvement through compensation or design changes. It is also important to determine the errors due to the laboratory environment (e.g., gravity, temperature) to predict performance in the intended application of the instrument.

Random errors can only be described in terms of their statistics. These errors cannot be compensated directly; however, the statistical knowledge is often used to improve overall system performance through filtering or other means of noise rejection.

In addition to systematic and random errors, which are normally attributed to the instrument, a third source of error is uncertainty in knowledge of the input to the instrument. For example, case motion of a test gyro due to unknown seismic disturbances results in output signals which appear to be noise. This noise must be considered random since the disturbances cannot be predicted; however, the error could be compensated if the disturbance environment were known or measurable.

The immediate goals of testing are to separate systematic errors from random errors, to quantify the errors, and to reduce errors introduced by the test itself as far as possible. Analysis of the spectral content of signals provides considerable insight into noise mechanisms as will be shown subsequently. Correlation between signals to separate systematic from random errors can also be accomplished in the frequency domain.

A useful application of spectral analysis is in determining environmental effects such as vibration, temperature, and gravity. Most instruments designed to make these measurements are frequency independent only within a particular frequency band. For instance, bubble levels, used to measure the direction of gravity, indicate with fidelity only at low frequencies, whereas seismometers are insensitive at low frequency but provide good mid-frequency information. By comparing the measurements of such auxiliary devices with the instrument under test and relying on each auxiliary device only in its useful frequency band, accurate information about the instrument errors can be obtained across a wide range of frequencies.

The theory behind spectral analysis is well developed [W4], [J2]. However, noise is characteristic to each situation and must be analysed separately. Only recently has it been practical to use this theory to determine specific models, primarily through the development of high speed computers and efficient algorithms to compute the spectral functions. In Chapter V, the application of spectral analysis to the Fixed Base Simulator is discussed. To provide a background for this discussion, a brief review of spectral theory in a form suitable for digital computation is included here. Much of this material in greater detail can also be found in [B2] and [K2]. The major concepts are first discussed, and then examples provided to illustrate the concepts and demonstrate their utility.

B. Discrete Fourier Transform

The Fourier transform of a continuous function $x(t)$ is defined as

$$X(f) = \int_{-\infty}^{\infty} x(t)\, e^{-j2\pi ft}\, dt \,, \tag{4.1}$$

and, conversely, the inverse transform is defined as

$$x(t) = \int_{-\infty}^{\infty} X(f)\, e^{j2\pi ft}\, df \,. \tag{4.2}$$

Digital computation of these transforms require that the data appear as discrete points over a finite time interval T. Although uniform time spacing of the points is not necessary, the discrete points are assumed to be obtained by sampling the continuous signal $x(t)$ every $\Delta t = 1/f_s$ sec, where f_s is the sampling frequency in Hz. The number of data points generated is therefore $N = T/\Delta t$. With the data structured in this manner, a discrete approximation to the integral in (4.1) is

$$\hat{X}(f) = \Delta t \sum_{k=0}^{N-1} x(k\Delta t) e^{-j2\pi fk\Delta t} .$$

The overscript $(\hat{})$ is used to denote an approximate or estimated value. This function is periodic at the sampling frequency $f_s = 1/\Delta t$; i.e.

$$\hat{X}(f \pm if_s) = \hat{X}(f) \qquad i = 0, \pm 1, \pm 2 \ldots \tag{4.3}$$

For computational convenience, $\hat{X}(f)$ is computed only at integer multiples of the fundamental frequency, $\Delta f = 1/T$, of the truncated time signal; i.e.

$$\hat{X}(n\Delta f) = \Delta t \sum_{k=0}^{N-1} x(k\Delta t) e^{-j2\pi n\Delta fk\Delta t} . \tag{4.4}$$

Since $\Delta f = 1/N\Delta t$, (4.4) can be rewritten more simply as

$$\hat{X}(n) = \Delta t \sum_{k=0}^{N-1} x(k)\, W^{nk} , \tag{4.5}$$

where

$$W = e^{-j2\pi/N} . \tag{4.6}$$

An approximation to the inverse Fourier transform is

$$x(k) = \Delta f \sum_{n=0}^{N-1} \hat{X}(n)\ W^{-nk} \ . \qquad (4.7)$$

Both $\hat{X}(n)$ and $x(k)$ have period N due to the periodicity of W^i.

The discrete approximation (4.5) and (4.7) are related to the Discrete Fourier Transform (DFT) and the Inverse Discrete Fourier Transform (IDFT) treated extensively in [C1] by

$$DFT[x(t)] = \hat{X}(n)/N\Delta t$$

and

$$IDFT[\hat{X}(n)] = x(k)/\Delta t \ .$$

A more rigorous derivation of the DFT from the Fourier integral can be found in [C2].

C. Autocorrelation Functions

The autocorrelation function is useful in determining the dependence of a signal on itself displaced in time. It is defined as

$$R_{xx}(t,\tau) = E[x^*(t)\ \ x(t+\tau)] \ , \qquad (4.8)$$

where $x^*(t)$ is the complex conjugate of $x(t)$.

If, in addition, the process is wide-sense stationary, its mean is constant and the autocorrelation is dependent only on the relative time displacement τ,

$$R_{xx}(\tau) = E[x^*(t)\ \ x(t+\tau)] \ . \qquad (4.9)$$

Furthermore, if $x(t)$ is assumed ergodic, this expression is equivalent to

$$R_{xx}(\tau) = \lim_{T\to\infty} \frac{1}{2T} \int_{-T}^{T} x^*(t)\ x(t+\tau)\ dt \ . \qquad (4.10)$$

Note that $R_{xx}(0) = \bar{x}^2 + \sigma_x^2$ where $\bar{x} = E(x)$, $\sigma_x^2 = E(x-\bar{x})^2$.

One discrete approximation is found directly by assuming again uniform time spacing of the data over an interval T.

$$\hat{R}_{xx}(m) = \frac{1}{N-m} \sum_{k=0}^{N-1-m} x^*(k) \quad x(k+m) \qquad m = 0,1, \ldots, N-1$$

$$= 0 \qquad\qquad m < 0, \quad m \geq N \ , \tag{4.11}$$

where $m\Delta t = \tau$, and the time spacing Δt has been omitted from the indices for simplicity. An indirect method of computing the autocorrelation function will be described after a discussion of power spectral density functions.

D. Power Spectral Density Functions

The power spectral density function* of a stationary random process $x(t)$ is defined as the Fourier transform of the autocorrelation function

$$P_{xx}(f) = \int_{-\infty}^{\infty} R_{xx}(\tau)\ e^{-j2\pi f\tau}\ d\tau \ . \tag{4.12}$$

Alternatively, the power spectrum can be expressed as a time average of the spectrally decomposed power in the process $x(t)$,**

$$P_{xx}(f) = \lim_{T\to\infty} E\left[\frac{1}{2T}\left|\int_{-T}^{T} x(t)\ e^{-j2\pi ft}\ dt\right|^2\right] \ . \tag{4.13}$$

---

*The terms "power spectrum" and "PSD" are also used. The use of the adjective "power" is not generally descriptive but is included as a matter of convention.

**Although the expected value operator in (4.13) is often omitted in engineering texts, it is essential that it be included. This is because $(1/2T)\left|\int_{-T}^{T} x(t)\ e^{-j2\pi ft}\ dt\right|^2$ is not a consistent estimator of $P_{xx}(f)$; i.e. its variance does not go to zero as time tends to infinity. (See [B2] p. 82 and [P1] p. 343, also Appendix A).

This function is an indication of the frequency distribution of power in the signal $x(t)$. If the signal is considered to be the superposition of an infinite number of sinusoids of varying amplitude and phase, then $P(f)\Delta f$ is the power contributed by the sinusoids in the infinitesimal frequency band Δf centered at frequency f. No phase information about $x(t)$ exists in the power spectrum since the autocorrelation function is independent of shifts in the time origin.

By using the Fourier inversion formula, a transform pair between the power spectrum and autocorrelation function results,

$$R_{xx}(\tau) = \int_{-\infty}^{\infty} P_{xx}(f)\ e^{j2\pi f\tau}\ df \quad . \tag{4.14}$$

Setting $\tau = 0$, (4.14) yields the total power in the signal

$$R_{xx}(0) = \int_{-\infty}^{\infty} P_{xx}(f)\ df = E[x(t)^2] = \bar{x}^2 + \sigma_x^2 \quad . \tag{4.15}$$

Similarly, integrating the power spectrum over a finite frequency range yields the power in that band.

A discrete power spectrum can be computed directly by approximating (4.13) using (4.5)

$$\hat{P}_{xx}(n) = \frac{\Delta t}{N} \left| \sum_{k=0}^{N-1} x(k)\ W^{nk} \right|^2 , \tag{4.16}$$

$$= \Delta f \left| \hat{X}(n) \right|^2 \quad . \tag{4.17}$$

The power spectrum estimate, divided by Δf, is also the least-squares estimate of the squared magnitude of the n^{th} complex coefficient in a truncated Fourier series representation of x. To show this, assume x can be represented by a truncated Fourier series

$$x(k) = \sum_{n=0}^{N-1} a_n \, e^{j2\pi nk/N} \quad . \tag{4.18}$$

It is well known that if a set of measurements x are related to a set of parameters a by

$$\overset{n\times 1}{x} = \overset{n\times p}{A} \; \overset{p\times 1}{a} \quad , \qquad n \geq p, \quad \text{rank} \quad A = p \quad , \tag{4.19}$$

where the dimensions of the matrices are indicated as overscripts, that the estimate $\hat{a}$ which minimizes the mean squared error $(x-A\hat{a})^T (x-A\hat{a})$ satisfies the relationship

$$\hat{a} = (A^{*T}A)^{-1} \, A^{*T}x \quad . \tag{4.20}$$

Let

$$x = (x_1 \; x_2 \; \ldots \; x_N)^T \quad , \qquad a = [a_1 \; a_2 \; \ldots \; a_N]^T \quad ,$$

and

$$A = \begin{bmatrix} 1 & 1 & \cdots & 1 \\ 1 & e^{j2\pi/N} & \cdots & e^{j2\pi(N-1)/N} \\ \vdots & \vdots & & \vdots \\ 1 & e^{j2\pi(N-1)/N} & \cdots & e^{j2\pi(N-1)^2/N} \end{bmatrix} \quad .$$

We have, by the periodicity of $e^{j2\pi kn/N}$, that the columns and rows of A are orthogonal, resulting in

$$A^{*T}A = NI \quad ,$$

where I is the identity matrix. Therefore from (4.19)

$$\hat{a} = \frac{1}{N} A^{*T} x \quad , \tag{4.21}$$

or

$$\hat{a} = \sum_{k=0}^{N-1} x(k)\ e^{-j2\pi kn/N} \quad . \tag{4.22}$$

Finally,

$$|\hat{a}_n|^2 = \left| \sum_{k=0}^{N-1} x(k)\ e^{-j2\pi kn/N} \right|^2 \quad , \tag{4.23}$$

or

$$|\hat{a}_n|^2 = \hat{P}_{xx}(n)/\Delta f \quad , \tag{4.24}$$

as was to be shown.

An indirect method of computing a discrete autocorrelation function, alluded to in the previous section, is to approximate (4.14) using (4.17) and (4.7).

$$\hat{R}^c_{xx}(m) = \Delta f^2 \sum_{n=0}^{N-1} |\hat{X}(n)|^2\ W^{-nm} \quad . \tag{4.25}$$

It is often more efficient to compute autocorrelation functions using (4.25) rather than using (4.11) directly, due to time savings afforded by the efficient DFT algorithms. However, the results obtained by the two methods are not identical. The autocorrelation function computed using (4.25) is a circular* correlation related to the direct autocorrelation function (4.11) by

*$\hat{R}^c_{xx}(m) = \frac{1}{N} \sum_{n=0}^{N-1} x^*(n)\ x(n+m)$. Values of the indices falling outside the summation interval are shifted into the other end of the interval; hence, the term "circular." (See [S3])

$$\hat{R}^{c}_{xx}(m) = \frac{N-m}{N}\,\hat{R}_{xx}(m) + \frac{m}{N}\,\hat{R}_{xx}(N-1-m) \quad , \tag{4.26}$$

as can be verified by direct substitution. Only for the case $\hat{R}_{xx}(m) = 0$, $m \geq (N-1)/2$ are the two discrete autocorrelations equal. However, for autocorrelations which go to zero rapidly with increasing values of the lag index m, the difference is small. In practice, the overlap in (4.26) can be eliminated by appending zeroes to the original data or blanking out the last half of the data sequence, (see [B2]).

E. Cross-Correlation Functions

The time dependence of two stationary random processes $x(t)$ and $y(t)$ can be determined through use of the cross-correlation function

$$R_{xy}(\tau) = E[x^{*}(t)\; y(t+\tau)] \quad , \tag{4.27}$$

or, alternatively,

$$R_{xy}(\tau) = \lim_{T\to\infty} E\left[\frac{1}{2T}\int_{-T}^{T} x^{*}(t)\; y(t+\tau)\; dt\right] \quad . \tag{4.28}$$

By a simple change of variables,

$$R_{xy}(\tau) = R^{*}_{yx}(-\tau) \quad . \tag{4.29}$$

If $R_{xy}(\tau) = \bar{x}\,\bar{y}$ for all τ, where $\bar{x} = E[x(t)]$ and $\bar{y} = E[y(t)]$, $x(t)$ and $y(t)$ are uncorrelated. The stronger condition of statistical independence of $x(t)$ and $y(t)$ implies uncorrelation. However, the converse, that uncorrelation implies independence is not generally true, except for Gaussian processes.

An important application of the cross-correlation function occurs in the study of linear systems. Let $x(t)$ be a scalar input to a linear system with an impulse response $h(t)$, and let $y(t)$ be the output. Then,

$$y(t) = \int_{-\infty}^{\infty} x(t-\sigma)\; h(\sigma)\; d\sigma \quad . \tag{4.30}$$

Instead of working with the signals directly, it is often more desirable to use only their statistical properties. Multiplying both sides of (4.30) by $x(t-\tau)$ and taking the expected value yields

$$R_{xy}(\tau) = \int_{-\infty}^{\infty} R_{xx}(\tau-\sigma)\ h(\sigma)\ d\sigma\ . \tag{4.31}$$

Given the cross-correlation and autocorrelation functions $R_{xy}(\tau)$ and $R_{xx}(\tau)$, the impulse response of a linear system is determined by (4.31) The solution is easily expressed in terms of the cross-spectral density function discussed in the next section.

A discrete approximation to the cross-correlation function can be represented similarly to the discrete autocorrelation function (4.11)

$$\begin{aligned} \hat{R}_{xy}(m) &= \frac{1}{N-m} \sum_{k=0}^{N-1-m} x^*(k)\ y(k+m) \qquad m = 0,1,\ \ldots,\ N-1 \\ &= 0 \qquad\qquad\qquad\qquad\qquad\qquad\quad m \geq N,\quad m < 0\ . \end{aligned} \tag{4.32}$$

Discrete Fourier Transforms can also be used to compute a circular cross-correlation function analogous to (4.25). This technique is based on the relationship between the cross-correlation function and the cross-spectral density function.

F. Cross-Spectral Density Functions

The cross-spectral density function is defined as the Fourier transform of the cross-correlation function

$$P_{xy}(f) = \int_{-\infty}^{\infty} R_{xy}(\tau)\ e^{-j2\pi f\tau}\ d\tau\ , \tag{4.33}$$

and, conversely,

$$R_{xy}(f) = \int_{-\infty}^{\infty} P_{xy}(f)\ e^{j2\pi f\tau}\ dt\ . \tag{4.34}$$

Note that if x and y are uncorrelated, $R_{xy}(\tau) = 0$, which implies from (4.33) that $P_{xy}(f) = 0$.

For ergodic processes, the cross-spectrum can also be expressed as

$$P_{xy}(f) = \lim_{T\to\infty} \frac{1}{2T}\left[\int_{-T}^{T} \int_{-T}^{T} x^*(\sigma)\, y(\gamma)\, e^{-j2\pi f(\gamma-\sigma)}\, d\sigma\, d\gamma \right] . \quad (4.35)$$

The cross-spectrum is useful in determining the linear relationships between $x(t)$ and $y(t)$. In particular, for a linear system with single input $x(t)$ and output $y(t)$,

$$P_{xy}(f) = H(f)\, P_{xx}(f) , \quad (4.36)$$

where $H(f)$ is the Fourier transform of the system impulse response. From (4.36) it can be seen that

$$|H(f)| = \frac{|P_{xy}(f)|}{P_{xx}(f)} , \quad (4.37)$$

and that

$$\angle H(f) = \angle P_{xy}(f) . \quad (4.38)$$

A further relationship between the output power spectrum and the cross-spectrum is

$$P_{yy}(f) = P_{xy}(f)\, H^*(f) . \quad (4.39)$$

Combining (4.36) and (4.39) results in the well known equality

$$P_{yy}(f) = |H(f)|^2\, P_{xx}(f) . \quad (4.40)$$

It is evident that computing only the input and output power spectra yields only magnitude information about $H(f)$. The phase relationship between x and y as a function of frequency can only be obtained from the cross-spectrum.

A discrete approximation to the cross-spectrum can be made by applying the DFT to (4.35)

$$\hat{P}_{xy}(n) = \Delta f\ \hat{X}^*(n)\ \hat{Y}(n) \qquad n = 0,\ 1,\ \ldots,\ N-1\ . \tag{4.41}$$

Directly analogous to the circular autocorrelation function (4.25), a circular cross-correlation function can be computed by taking the IDFT of (4.41)

$$\hat{R}^c_{xy}(m) = \Delta f \sum_{n=0}^{N-1} \hat{P}_{xy}(n)\ W^{-nm} \qquad m = 0,\ 1,\ \ldots,\ N-1\ . \tag{4.42}$$

This circular cross-correlation is related to the lagged product cross-correlation (4.32) by

$$\hat{R}^c_{xy}(m) = \frac{N-m}{N}\ \hat{R}_{xy}(m) + \frac{m}{N}\ \hat{R}^*_{yx}(N-m) \qquad m = 0,\ 1,\ \ldots,\ N-1. \tag{4.43}$$

Again, this formula can be verified by substitution.

G. Coherence Function

In the study of linear systems, it is important to have a measure of how much of the output is due to the known input. An appropriate spectral function to provide this information is the coherence function, defined by

$$\gamma^2_{xy}(f) = \frac{|P_{xy}(f)|^2}{P_{xx}(f)\ P_{yy}(f)}\ . \tag{4.44}$$

Since

$$|P_{xy}(f)|^2 \leq P_{xx}(f)\ P_{yy}(f)\ ,$$

$$0 \leq \gamma^2_{xy}(f) \leq 1\ .$$

Consider the linear system in Fig. 29.

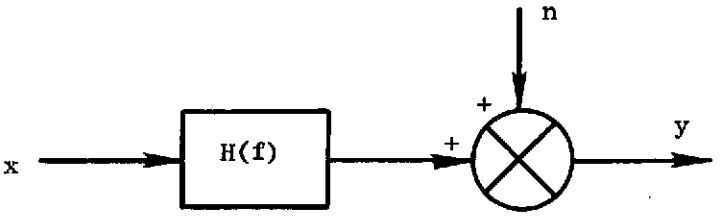

Fig. 29. LINEAR SYSTEM WITH MEASUREMENT NOISE.

Assume the measurement noise n is uncorrelated with the input x. In this case, the spectral functions of interest are

$$P_{yy}(f) = P_{nn}(f) + |H(f)|^2 P_{xx} = P_{nn}(f) + P_{ss}(f) \quad , \tag{4.45}$$

$$P_{xy}(f) = H(f) P_{xx}(f) \, . \tag{4.46}$$

Forming the coherence function,

$$\gamma^2_{xy}(f) = \frac{|H(f)|^2 P^2_{xx}(f)}{P_{xx}(f)\left[|H(f)|^2 P_{xx}(f) + P_{nn}(f)\right]} \quad , \tag{4.47}$$

or

$$\gamma^2_{xy}(f) = \frac{1}{1 + P_{nn}(f)/P_{ss}(f)} \quad . \tag{4.48}$$

The value of the coherence function is therefore controlled by the ratio of the noise power spectrum to the signal power spectrum. For a low signal to noise ratio $P_{ss}/P_{nn} \ll 1$, $\gamma^2_{xy}(f) \cong 0$, and the output is said to be incoherent with the input. For $P_{ss}/P_{nn} \gg 1$, $\gamma^2_{xy}(f) \cong 1$, and the input and output are nearly coherent. Note also that with $P_{nn} \neq 0$, the two values of $|H(f)|^2$ obtained from (4.37) and (4.40) are not equal. The result using the cross-spectrum, (4.37), is unbiased for no unknown noise at the input, whereas (4.40) is always biased except when $\gamma^2_{xy} = 1$. The former expression generally introduces less bias in the estimate of the transfer function.

A discrete approximation to the coherence function (4.44) can be computed directly from the discrete version of the cross-spectrum and the power spectra, (4.41) and (4.17) respectively ,

$$\hat{\gamma}^2_{xy}(n) = \frac{|\hat{P}_{xy}(n)|^2}{\hat{P}_{xx}(n)\ \hat{P}_{yy}(n)} \quad . \tag{4.49}$$

An interesting property of the coherence function estimate can be demonstrated for the case when the cross-spectrum and power spectra estimates are based on just one record of data. Then,

$$\gamma^2_{xy}(n) = \frac{\Delta f^2 \hat{X}^*(n)\hat{Y}(n)\hat{X}(n)\hat{Y}^*(n)}{\Delta f^2 \hat{X}^*(n)\hat{X}(n)\hat{Y}^*(n)\hat{Y}(n)} \equiv 1 \quad , \tag{4.50}$$

independent of the length of the data record. Therefore, to obtain a meaningful estimate of the coherence function, it is necessary to estimate the cross-spectrum and the power spectral independently. This can be accomplished by averaging the estimates from several data records before dividing as in (4.49) or by averaging the estimates over nearby frequency estimates. Other considerations which must be made in order to obtain reliable estimates of the various spectral and correlation functions from finite sampled data are treated in the Appendix.

H. Relationship of Spectral Analysis to Linear Estimation

The concepts introduced in the previous sections have an important application in the area of linear estimation and filter theory. The problem is: given measurements, y, of a signal, x, with additive noise, n,

$$y(t) = x(t) + n(t) \quad , \tag{4.51}$$

determine the linear filter $h(t,\tau)$ such that the estimate of the signal in the form

$$\hat{x}_o(t) = \int_{T_i}^{T_f} h(t,\tau)\, y(\tau)\, d\tau \qquad T_i < t < T_f \ , \tag{4.52}$$

minimizes the mean-square error. In other words, for any other linear estimate $\hat{x}$,

$$E\left|(\hat{x}_o - x)\right|^2 \leq E\left|(\hat{x} - x)\right|^2 \ . \tag{4.53}$$

By the projection theorem, the filter can be shown to satisfy the generalized Wiener-Hopf equation

$$R_{yx}(t,\sigma) = \int_{t_o}^{t_f} h(t,\tau)\, R_{yy}(\tau,\sigma)\, d\tau \ . \tag{4.54}$$

The optimum linear filter can therefore be derived knowing only R_{yx} and R_{yy}. No other information is necessary.

Wiener first solved this problem [W4] using spectral techniques by considering only stationary processes and developed a causal (realizable) filter. To develop a relationship between the optimal filter and the coherence function, consider an optimum non-causal filter by letting the limits of integration in (4.52) go to infinity. Assuming stationarity of the processes.

$$\hat{x}(t) = \int_{-\infty}^{\infty} h(\tau)\, y(t-\tau)\, d\tau \qquad -\infty < t < \infty \ , \tag{4.55}$$

and

$$R_{yx}(\sigma) = \int_{-\infty}^{\infty} h(\tau)\, R_{yy}(\sigma-\tau)\, d\tau \qquad -\infty < \sigma < \infty \ . \tag{4.56}$$

The solution to (4.56) is found by simply taking the Fourier transform of both sides

$$H(f) = \frac{P_{yx}(f)}{P_{yy}(f)} \ . \tag{4.57}$$

The mean square error $\Sigma = E\left|\hat{x}-x\right|^2$ is found from

$$\Sigma = E\left|x - \int_{-\infty}^{\infty} h(\tau)\ y(t-\tau)\ d\tau\right|^2 \tag{4.58}$$

to be

$$\Sigma = R_{xx}(0) - \int_{-\infty}^{\infty} h(\tau)\ R_{yx}(\tau)\ d\tau \quad . \tag{4.59}$$

Application of Parseval's Theorem to (4.59) yields

$$\Sigma = \int_{-\infty}^{\infty} \left[P_{xx}(f) - H(f)\ P_{yx}^{*}(f)\right]\ df \ . \tag{4.60}$$

Substituting (4.57) into (4.60) further results in

$$\Sigma = \int_{-\infty}^{\infty} P_{xx}(f)\left[1 - \frac{\left|P_{yx}\right|^2}{P_{xx}P_{yy}}\right]\ df \ ; \tag{4.61}$$

which, from (4.44), can finally be expressed as

$$\Sigma = \int_{-\infty}^{\infty} P_{xx}(f)\left[1 - \gamma_{yx}^2\right]\ df \ . \tag{4.62}$$

Equation (4.62) therefore relates the mean-square error to the signal power spectrum and to the coherency of the measurement. When the signal and measurement are fully coherent ($\gamma_{yx}^2 = 1$), the mean-square error is zero. Conversely, when the noise completely dominates ($\gamma_{yx} = 0$), the optimum filter and hence the estimate are approximately zero, implying from (4.62) that the mean-square error is the total power in the signal itself.

The mean-square error computed by (4.62) is the minimum value attainable from any linear filter, and can be used in determining the amount of

data and complexity of filter required in specific applications. Furthermore, if the signal and noise processes are both Gaussian, this error is the minimum for any filter, nonlinear or linear.

Solution of (4.56) for a causal filter (i.e. $h(\tau) = 0,\ \tau < 0$) using Wiener's techniques is generally practical only when the power spectrum of the measurement, P_{yy}, is rational. In this case a more heuristic solution of the causal filter than that given by Wiener can be found in [B6] and [V1].

Kalman and Bucy [K1] advanced the theory of linear estimation by finding a solution to the Wiener-Hopf equation (4.54) for finite time interval, nonstationary processes. The formulation of the filter requires certain assumptions which have proven to be valid for a wide variety of practical problems. The requirement in Wiener theory for knowledge of the multivariable cross-correlation functions between the measurements and signals is replaced in the Kalman-Bucy equations by a finite dimensional model of the signal processes of the form

$$x(t) = C(t)\ z(t) \tag{4.63}$$

$$\dot{z}(t) = F(t)\ z(t) + G(t)\ w(t) \tag{4.64}$$

$$y(t) = x(t) + n(t)\ , \tag{4.65}$$

where

$$E[z(t_o)] = E[w(t)] = E[n(t)] = 0$$

$$E\begin{bmatrix} w(t) \\ n(t) \end{bmatrix} [w^T(\tau)\ \ n^T(\tau)] = \begin{bmatrix} Q(t) & T(t) \\ T^T(t) & R(t) \end{bmatrix} \delta(t-\tau)$$

$$E\left[z(t_o)\ z^T(t_o)\right] = \Sigma_o,\ E\left[z(t_o)\ w^T(t)\right] = E\left[z(t_o)\ n^T(t)\right] = 0\ .$$

Instead of determining the optimum filter using spectral techniques, the Kalman-Bucy theory expresses the filter as the solution to a set of ordinary time differential equations.

$$\dot{\hat{z}} = F\hat{z} + K(y - C\hat{z}) \quad , \qquad \hat{z}(t_o) = 0 \tag{4.66}$$

$$K = \left(\Sigma C^T + GT\right)R^{-1} \tag{4.67}$$

$$\dot{\Sigma} = F\Sigma + \Sigma F^T - KRK^T + GQG^T \quad , \qquad \Sigma(t_o) = \Sigma_o \; . \tag{4.68}$$

Bryson and Ho have shown the relationship between the two filters [B10]. As a particular case, if F, G, C, R, and Q are constant matrices and w(t) and n(t) are stationary processes, the filter gain K may reach a steady-state value K_{ss}. Equation (4.66) may then be written as

$$\dot{\hat{z}} = [F - K_{ss}C]\hat{z} + K_{ss}y \; . \tag{4.69}$$

Laplace transforming (4.69),

$$\hat{z} = [SI - (F - K_{ss}C)]^{-1}K_{ss}y(S), \tag{4.70}$$

where I is the identity matrix. Defining

$$\Phi(t) = \mathcal{L}^{-1}[SI - (F - K_{ss}C)]^{-1} \quad , \tag{4.71}$$

the solution to (4.69) may be expressed as

$$\hat{z}(t) = \int_0^t \Phi(t-\tau)\, K_{ss}y(\tau)\, d\tau \tag{4.72}$$

Therefore, as t becomes large, the effects of the initial conditions diminish so that (4.72) can be written as

$$\hat{z}(t) = \int_{-\infty}^t \Phi(t-\tau)\, K_{ss}y(\tau)\, d\tau \tag{4.73}$$

Comparing (4.73) with (4.52) and (4.55), it can be seen that

$$h(\tau) = \Phi(\tau)\ K_{ss} \tag{4.74}$$

is the causal Wiener filter.

I. Illustration

As an example of the utility of spectral techniques in determining systematic errors, the situation shown in Fig. 30 was digitally simulated.

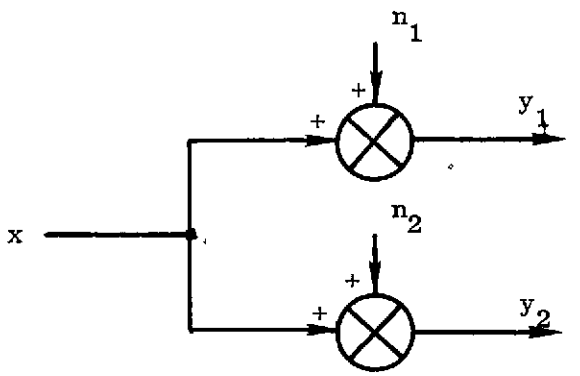

Fig. 30. MULTIPLE SIGNAL MEASUREMENTS WITH INDEPENDENT NOISE.

The two random noise sources n_1 and n_2 were generated independently and are sampled versions of white noise sharply bandlimited at 25.6 Hz. Sampling frequency corresponds to 51.2 Hz. The variance of each noise source was 51.2 which results in a power spectral density of 1, $0 \leq f \leq 25.6$. A small sinusoid at 10 Hz of amplitude 1 was taken to be the signal (or systematic error). Forty data records each 10 seconds long ($\Delta f = 0.1$ Hz) were processed and averaged for both measurements y_1 and y_2. Figure 31a is a typical time history of the measurements.

The power spectra of the two measurements are shown in Fig. 31b and 31c. A spike in the power spectra is apparent at 10 Hz. However, the statistical variability of the rest of the spectrum places some uncertainty in interpreting the spike at 10 Hz as a true component. The cross-spectrum between the two measurements Fig. 31d shows the independence of the noise, since the level of the noise is attenuated by an average factor of 6.3 while the systematic peak at 10 Hz is only slightly attenuated--mainly due to statistical variability.

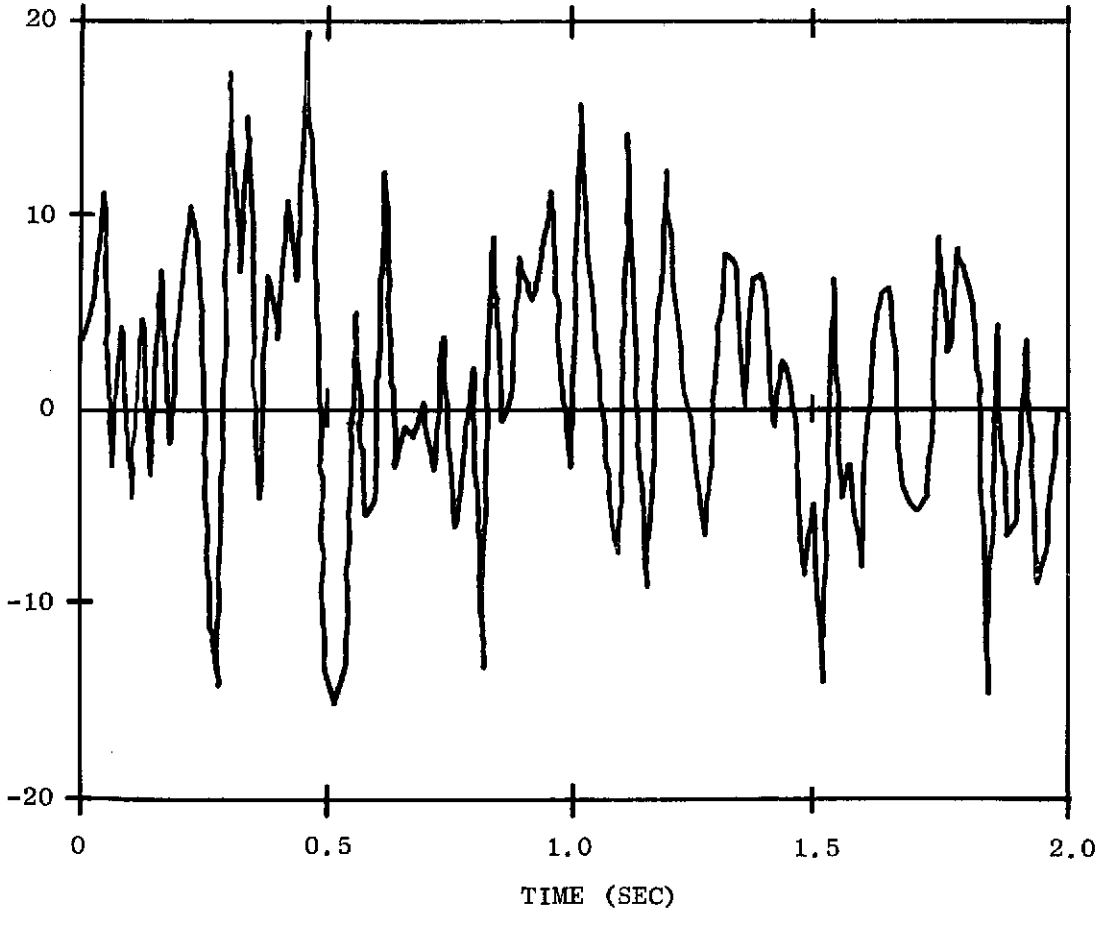

Fig. 31a. TYPICAL MEASUREMENT TIME HISTORY. The small 10 Hz systematic component is not evident.

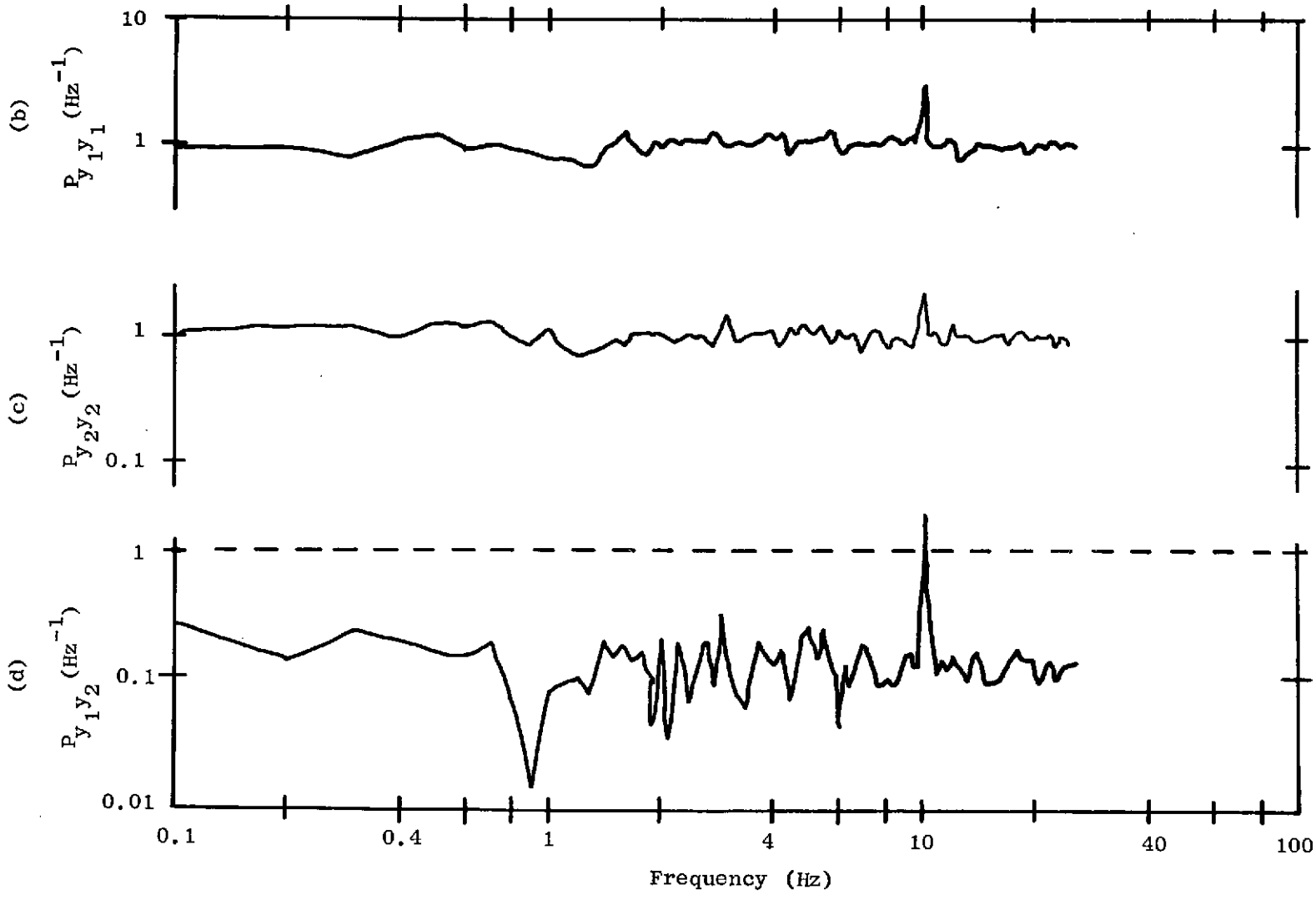

Fig. 31. POWER SPECTRA AND CROSS-SPECTRA OF MULTIPLE SIGNAL MEASUREMENTS. Computing the cross-spectrum between a signal and itself displaced in time can uncover the presence of a systematic components having relatively long correlation times.

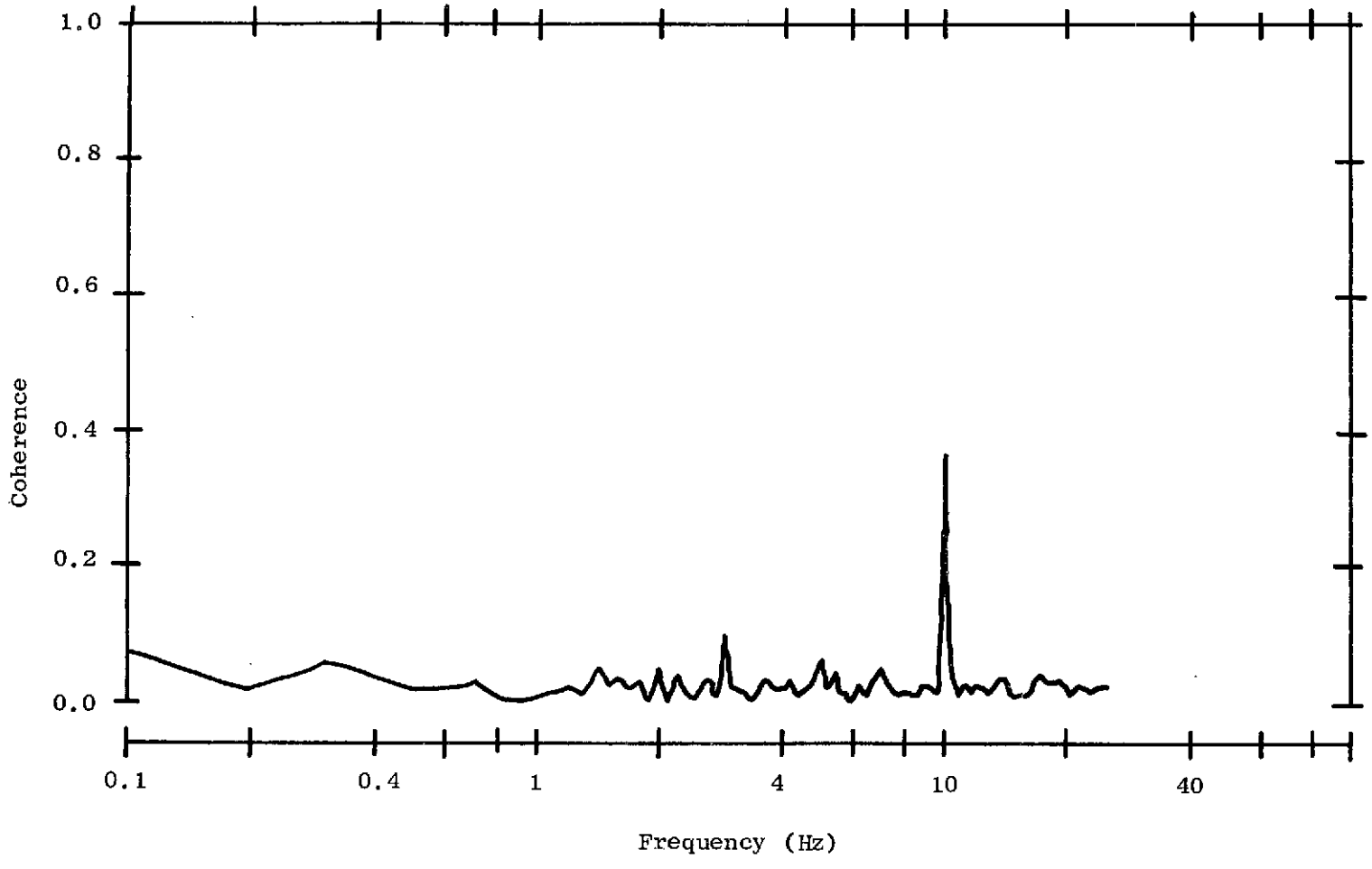

Fig. 31e. COHERENCE OF MULTIPLE SIGNAL MEASUREMENTS. The relatively high level of coherence at 10 Hz indicates that a common sinusoidal source is present in both measurements. The small spike at 3 Hz is due to statistical variability.

The coherence function Fig. 31e is theoretically equal to 1 at 10 Hz and zero elsewhere. However, due to the finite record length, leakage, and variability in the estimates of the cross-spectrum and power spectra, it only has a value of 0.35 at 10 Hz and near zero elsewhere. Therefore some judgment has to be used in interpreting the results. Bendat and Piersol [B2] discuss these practical considerations and give measures for the expected variation in the spectra and coherence function. Appendix A also contains a brief discussion.

The conclusions that may be drawn from these spectral plots are 1) the measurements are uncorrelated at all frequencies except at 10 Hz; 2) a common sinusoid at 10 Hz exists in both measurements; and 3) the two measurements are moderately coherent at 10 Hz. Further investigation into the statistical properties and computational aspects of the estimate must be made before attributing the lack of coherency to variability or to other effects introduced by finite record length.

Chapter V

EXPERIMENTAL RESULTS

A. Introduction

An application of spectral theory to the modeling of orientation sensors is described in this chapter. To demonstrate the application realistically, spectra obtained from the gyros, autocollimators, and other components of the Fixed Base Simulator are studied. Thus, the experimental results presented are primarily intended to demonstrate the spectral approach to modeling instrument errors rather than to evaluate the performance of the simulator. They present a guide to how spectral theory will be useful in the evaluation of the Stanford gyro test of relativity.

It is assumed that the system must be controlled or pointed actively to keep the sensor outputs within a representative range. Also, it is assumed that the orientation sensors have greater accuracy than available laboratory references, and, consequently, must be used to maintain their own orientation. As a result, the sensors become active elements of the pointing loops, with their output characteristics altered by the system dynamics. To properly evaluate the inherent instrument errors, system effects must be distinguished. This can be accomplished directly through measurements with a more accurate reference, or indirectly by modeling the system. These two approaches are discussed in turn.

A reference sufficiently accurate to test the orientation sensors, if available, must necessarily be derived from the sensors themselves, since other laboratory references are inadequate. For example, if the optical reference is known to have much less error than the gyro at low frequencies, then the difference in outputs can be attributed to errors in the gyro at these frequencies. Conversely, at high frequencies, gyros often have less noise than optical references, implying that differences in output are optical errors. This concept of using complementary sensors, each providing the reference at frequencies where its errors are small, could not be exploited in the present research since the autocollimator had superior accuracy throughout the frequency band considered (0.1 Hz to 200 Hz). Consequently, the indirect modeling approach was used.

The concept of modeling has many interpretations, several of which should be distinguished.

- Writing a set of differential equations from an a priori understanding of the system.
- Deducing a set of equation coefficients from empirical data, with or without knowledge of the structure of the equations.
- Determining a set of equations and coefficients, given an output time history and known input.
- Selecting a set of transfer functions which best match observed frequency responses of the system.
- Making plausibility arguments about system driving noise, given the output and knowledge of the system structure.
- Refining a priori models based on output data and plausible models of input noise, and developing descriptors both numerical and physical to explain model differences.

In Chapter III, the first two interpretations were used to gain a basic understanding of the simulator. The next two fall under the general classification of parameter identification, an area which has recently attracted widespread interest. The final two senses of modeling are those employed in analyzing the experimental results of this chapter.

B. Open Loop Sensor Measurements

The power spectra of signals from the primary autocollimator and gyro pickoffs with the sensors operating open loop are first presented in Fig. 32 and Fig. 33 as the "true" basic spectra of the instruments. The test setups used in obtaining the spectra were sufficiently quiet that base motion contributions to the signals are negligible. These spectra will be used later as bases of comparison for closed loop results.

1. Test Setup

The autocollimator spectra were computed from signals recorded while the primary autocollimator was separated from the simulator and positioned on a massive marble slab. Relative motion between the autocollimator and mirror at frequencies of interest was estimated to be several orders of magnitude less than the noise equivalent angle of the autocollimator. The autocollimator output signals are therefore interpreted as being entirely due to inherent instrument errors.

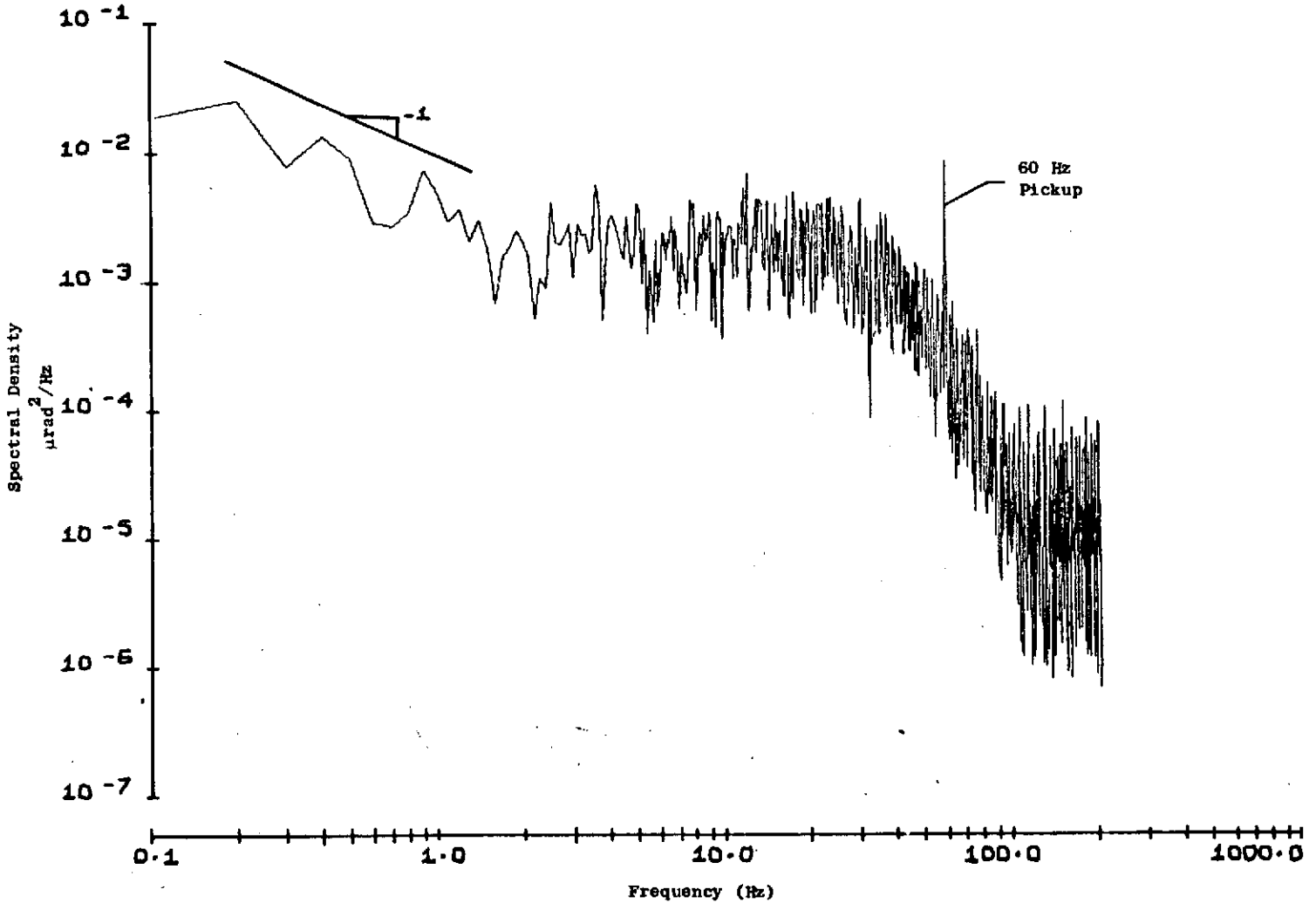

Fig. 32a. OPEN-LOOP POWER SPECTRUM OF THE PRIMARY AUTOCOLLIMATOR X-AXIS CONTROL CHANNEL. With the autocollimator resting on a massive marble slab, the effects of base motion are negligibly small.

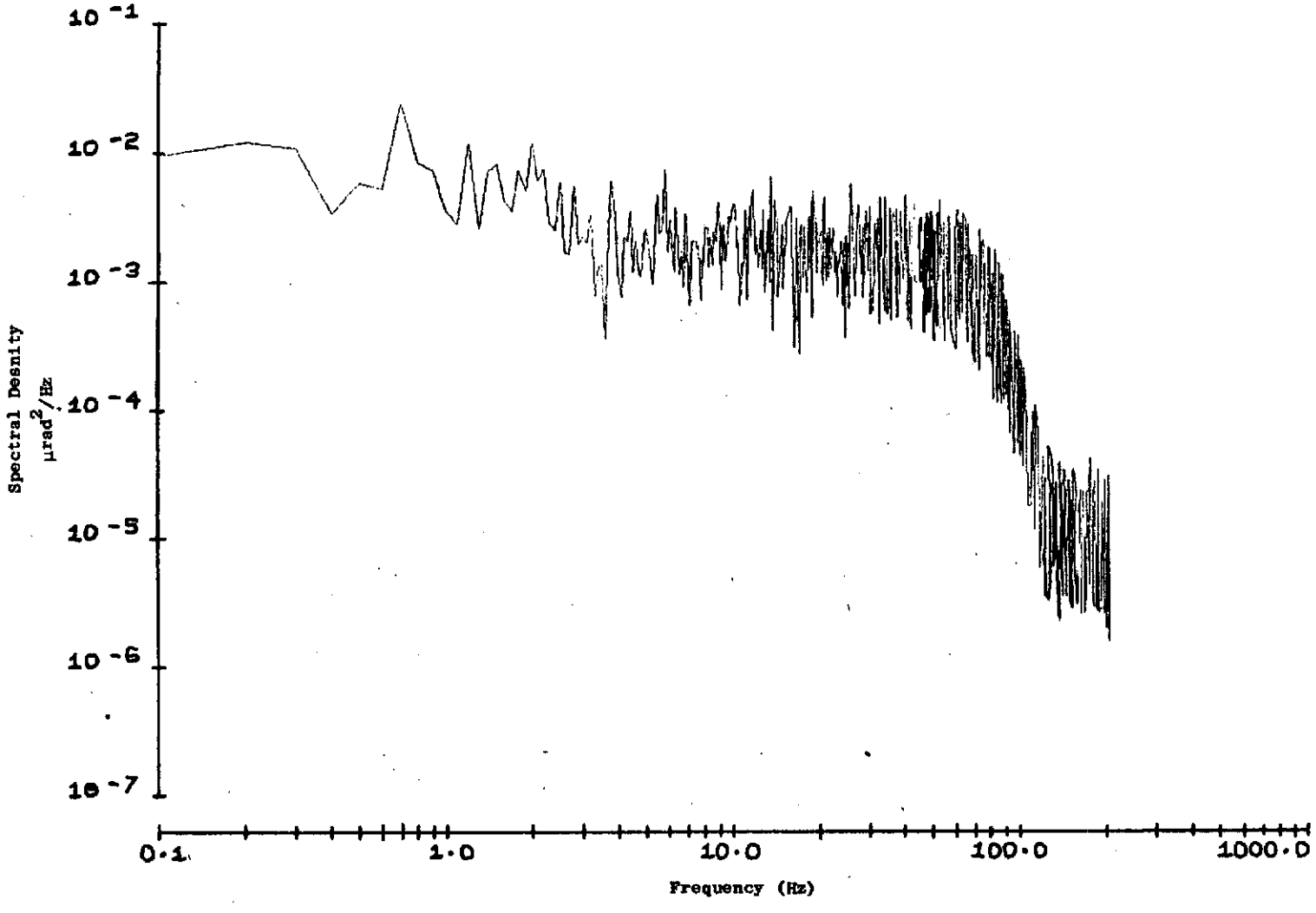

Fig. 32b. OPEN-LOOP POWER SPECTRUM OF THE PRIMARY AUTOCOLLIMATOR X-AXIS INSTRUMENTATION CHANNEL. The primary difference between this spectrum and the previous one is the filtering of noise above 40 Hz in the control channel.

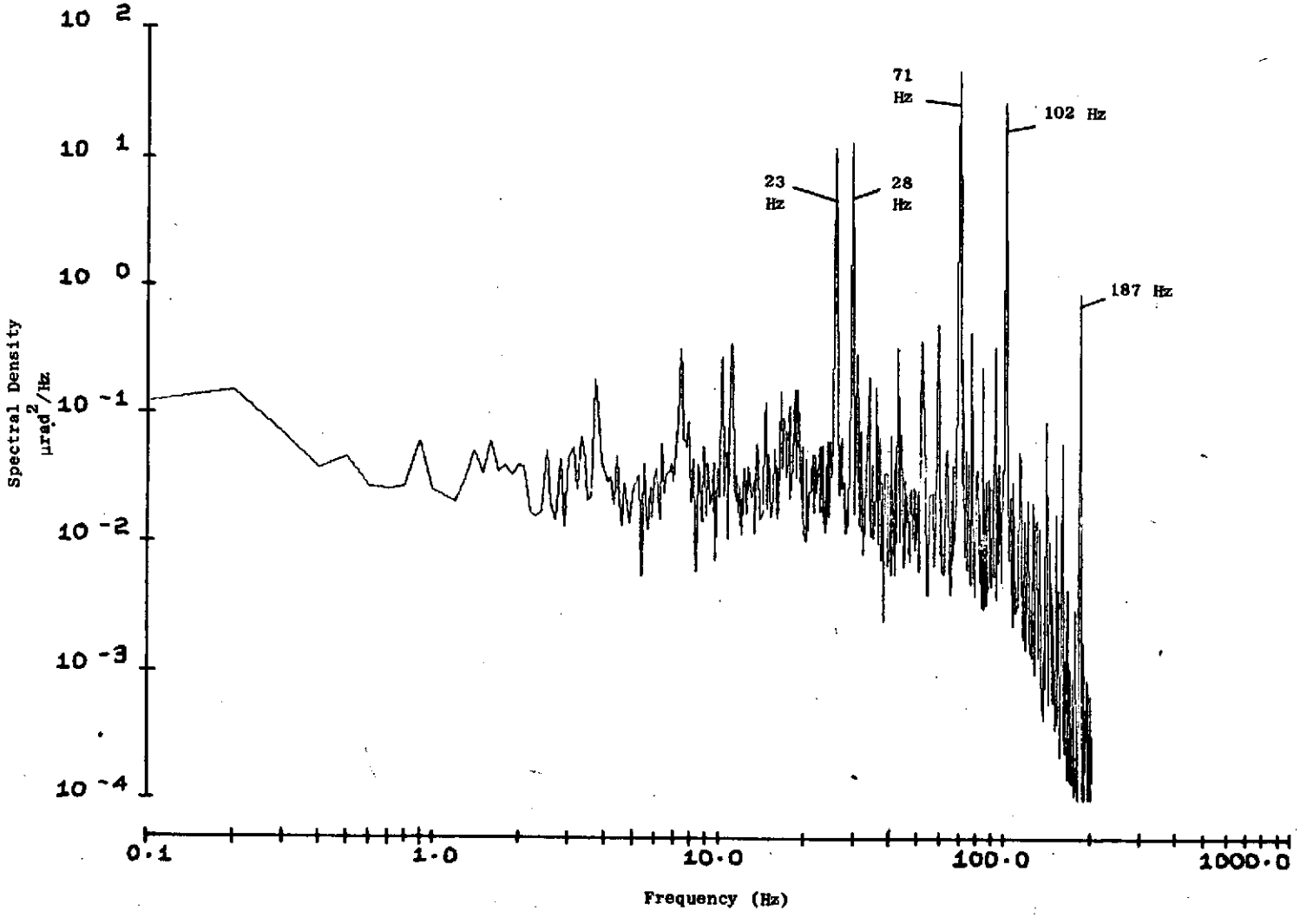

Fig. 33a. POWER SPECTRUM OF THE X-AXIS INSTRUMENTATION CHANNEL OF X-Y GYRO WITH PLATFORM CLAMPED. The concentration of power at discrete frequencies is characteristic of ball bearing gyros.

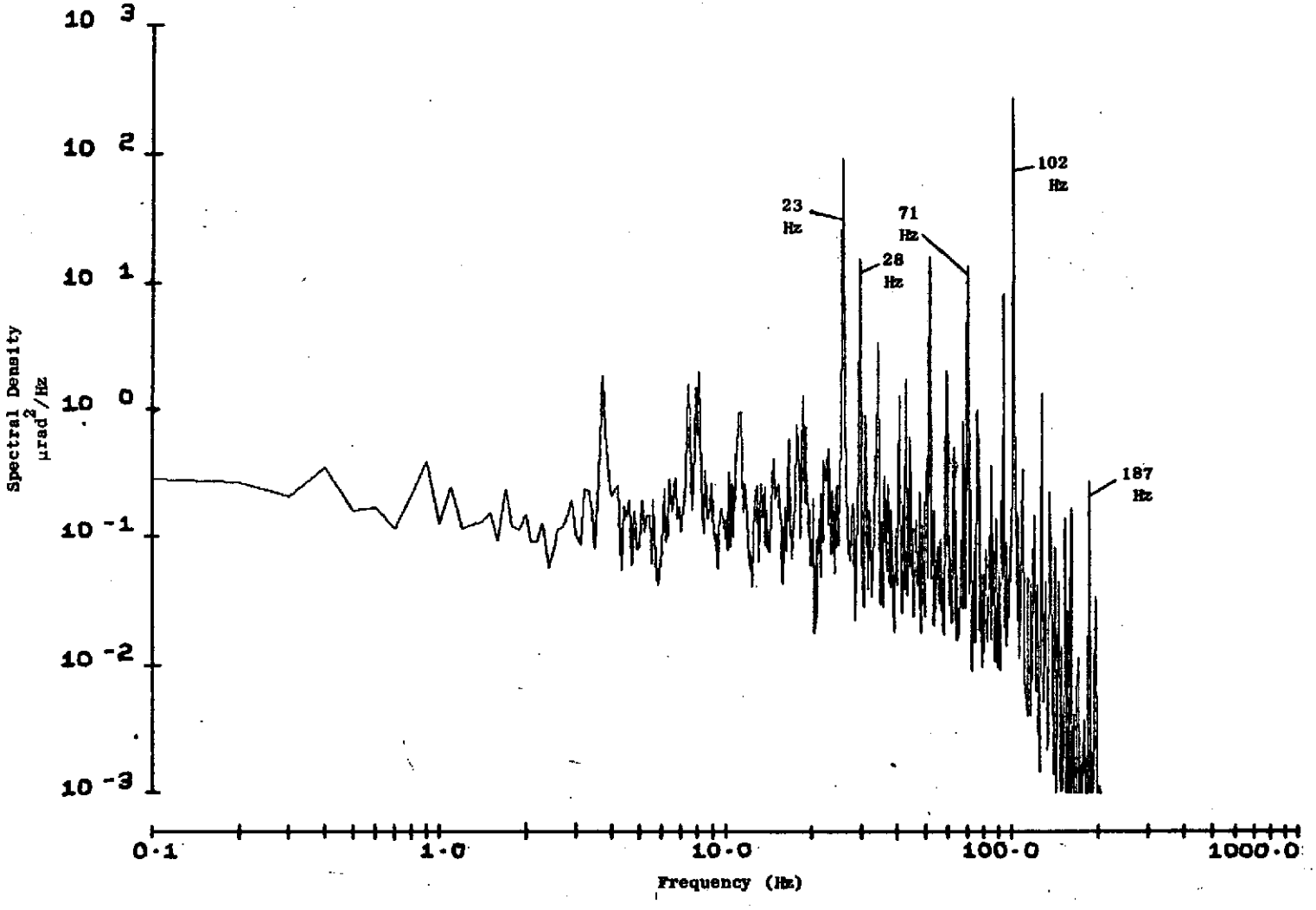

Fig. 33b. POWER SPECTRUM OF THE Y-AXIS INSTRUMENTATION CHANNEL OF X-Y GYRO WITH PLATFORM CLAMPED. Several of the spikes are also present in the X-axis, indicating a common source.

The gyro power spectra were obtained with the gyro mounted on the platform, but with the stabilization loops disabled and the platform rigidly clamped to the rotary table. With this rigid arrangement, any motion sensed by the gyro is due primarily to microseisms. Bradner and Reichle [B7] state that for an average test site the acceleration power spectrum in the range 0.5 to 50 Hz is approximately 0.001 g^2/Hz. Angular motion can be deduced from the linear acceleration knowing the soil shear propagation velocity and frequency of the underlying waves. A relation given in [F1] is

$$\alpha = \frac{5\ddot{y}}{Vf}$$

where

α = peak angle (μrad)

$\ddot{y}$ = peak vertical acceleration (μg)

V = soil shear propagation velocity (ft/sec)

f = wave frequency (Hz)

Using a value of V = 400 ft/sec, the angular power spectral density at 0.5 Hz is approximately 6×10^{-7} μrad^2/Hz and varies inversely with the square of frequency. This value is considerably below that observed in the gyro spectra. Gyro float motion due to mass unbalance and seismic accelerations are also negligibly small at frequencies above 0.1 Hz. Vibration induced by the gyro rotor bearings and electronic noise are the most probable sources of the pickoff noise.

2. Graphical Interpretation

Several general characteristics of these spectra should be noted. Firstly, the noisiness or jitter of the plots is due to insufficient averaging; only five estimates of each frequency point were averaged to obtain the values presented. Later spectral plots will appear smoother since the number of estimates in each average was increased. Secondly, frequency resolution of these spectra, as well as all other plots presented is approximately equal to the smallest frequency plotted. In the

present case, resolution is about 0.1 Hz. Thirdly, low-pass anti-aliasing filters with cutoff frequencies between 100 and 150 Hz were used to prevent spectral distortion below 100 Hz. Dramatic decreases in power above the cutoff frequency are evident in all the spectral plots. Finally, the spectral plots shown are two-sided, requiring the area under the curve to be doubled in computing the actual power in any particular frequency band.

3. Primary Autocollimator Spectra

The basic autocollimator spectra of Fig. 32, taken from the X-axis control and instrumentation channels, can be separated into three frequency bands. In the mid-frequency band, i.e. between 3 Hz and 35 Hz for the control channel and between 3 Hz and 80 Hz for the instrumentation channel, the spectra have constant spectral density, a characteristic of white noise. The level of noise in this band was predicted during design based on a shot noise model. The noise is almost entirely due to dark current in the autocollimator photodetector. Amplifier noise is negligibly small.

Below 3 Hz the power spectra vary inversely with frequency. Noise exhibiting this type of spectral behavior is often called $1/f$ or flicker noise [B3]. It can be generated electrically due to surface effects of solid state devices. However, since the autocollimator is an ac device, electronic $1/f$ noise is shifted to the 2.2 kHz switching frequency. Demodulation and filtering effectively eliminate this noise from the output. The $1/f$ characteristic in the spectra is therefore not likely caused by the electronics. A more plausible source is distortion of the infra-red rays due to turbulence in the air between the autocollimator and the reference mirror. This explanation was not well established.

Above the mid-frequency band, the noise decreases due to filtering. The spectral curves in these high frequency bands correspond to the squared magnitude of the filter transfer functions multiplied by the constant spectral density of the white shot noise source. The response is that predicted from a deterministic analysis of the instrument. This observation is important since it demonstrates the validity of the statistical spectral approach. Here the coloration of the noise clearly suggests

a model of the instrument without having to inject external signals to determine its response.

The control channel break frequency of 40 Hz corresponds to the two-pole output filter in the autocollimator electronics, while the instrumentation channel attenuation is due primarily to the anti-alising filter. Flattening of the spectra above 100 Hz is caused by the equivalent noise generated by quantizing the analog signal in the analog-to-digital converter [W3]. The autocollimator rms noise equivalent angle is 0.55 μrad, found by taking the square root of twice the area under the instrumentation channel spectrum. Similar measurements were used in obtaining the autocollimator performance data presented in Table 1 in Chapter II.

4. Gyro Spectra

The spectra from both axes of the X-Y gyro, shown in Fig. 33, are characterized by a white background with numerous spikes at discrete frequencies. This type of spectrum is typical of ball bearing gyros. The discrete components at 23 and 28 Hz appearing in both X and Y axes are not consistently present in spectra taken at other times and are of unknown origin. Three other large spikes appear in both X and Y axes at 71, 102 and 187 Hz. The 187 Hz discrete component is due to vibration at the rotor spin frequency. The induction spin motor field rotates at 200 Hz and a 13 Hz rotor slip frequency produces the torque required to overcome frictional losses. A small spike in the spectra near 13 Hz possibly corresponds to this slip frequency. The rotation of the rotor bearing retainers is a potential source of a large discrete frequency component. Unfortunately, the configuration of the rotor bearings is not known so the rotation frequency of the retainers cannot be computed. It is known, however, from available gyro documentation that the rotor is actually composed of two flywheels. It is likely that the bearing retainers of these flywheels do not have exactly the same rotation frequency due to manufacturing tolerances. The apparent large spike at 71 Hz is actually composed of two large spikes separated by about 0.8 Hz. Beating in the gyro pickoff signal, which would result from two nearby frequency

components, was observed in strip chart recordings of early simulator runs, although this phenomenon was not apparent in later tests. The computed spectra, however, consistently show two distinct frequency components, strongly indicating that rotation of the bearing retainers is responsible for the concentration of signal power near 71 Hz. Another possible, though less likely, source is nutation of the float, which occurs at a natural frequency $h/I_{f_t} = 625$ rad/sec. Inaccuracies in the measurement of the float inertia I_{f_t} could account for the discrepancy in frequency. The low damping ratio ($\zeta = 0.07$) of the nutation mode would allow large increases in power near its natural frequency.

The very large spike at 102 Hz is of unknown origin. Nutation is a likely source because of the close agreement in frequency. However, the height of the spike implies that a nutation damping ratio less than 0.02 is required, which is substantially less than the 0.07 value estimated. Other possible sources are electronic noise, irregularities in the rotor bearings, or a mechanical resonance.

It should be observed at this point that the power spectra only suggest noise mechanisms, and that further experiments are usually necessary to verify any particular model. The explanation given above for the discrete concentrations of signal power need further substantiation; they are, however, plausible based on the available evidence.

5. Azimuth Autocollimator Spectra

The power spectrum of the azimuth (Z) reference autocollimator, Fig. 34, is a clear example of 1/f noise. The data were obtained from an experimental setup similar to that used for the primary autocollimator. The azimuth autocollimator is a dc device, and consequently is more sensitive to low frequency noise than the primary autocollimator. As evident in the spectrum, the output signal is composed entirely of 1/f noise, at least out to the anti-aliasing filter break frequency.

Modeling of 1/f noise is especially difficult since it cannot be described using a finite number of lumped parameters. In other words, a state variable model would require an infinite number of equations to specify the noise.

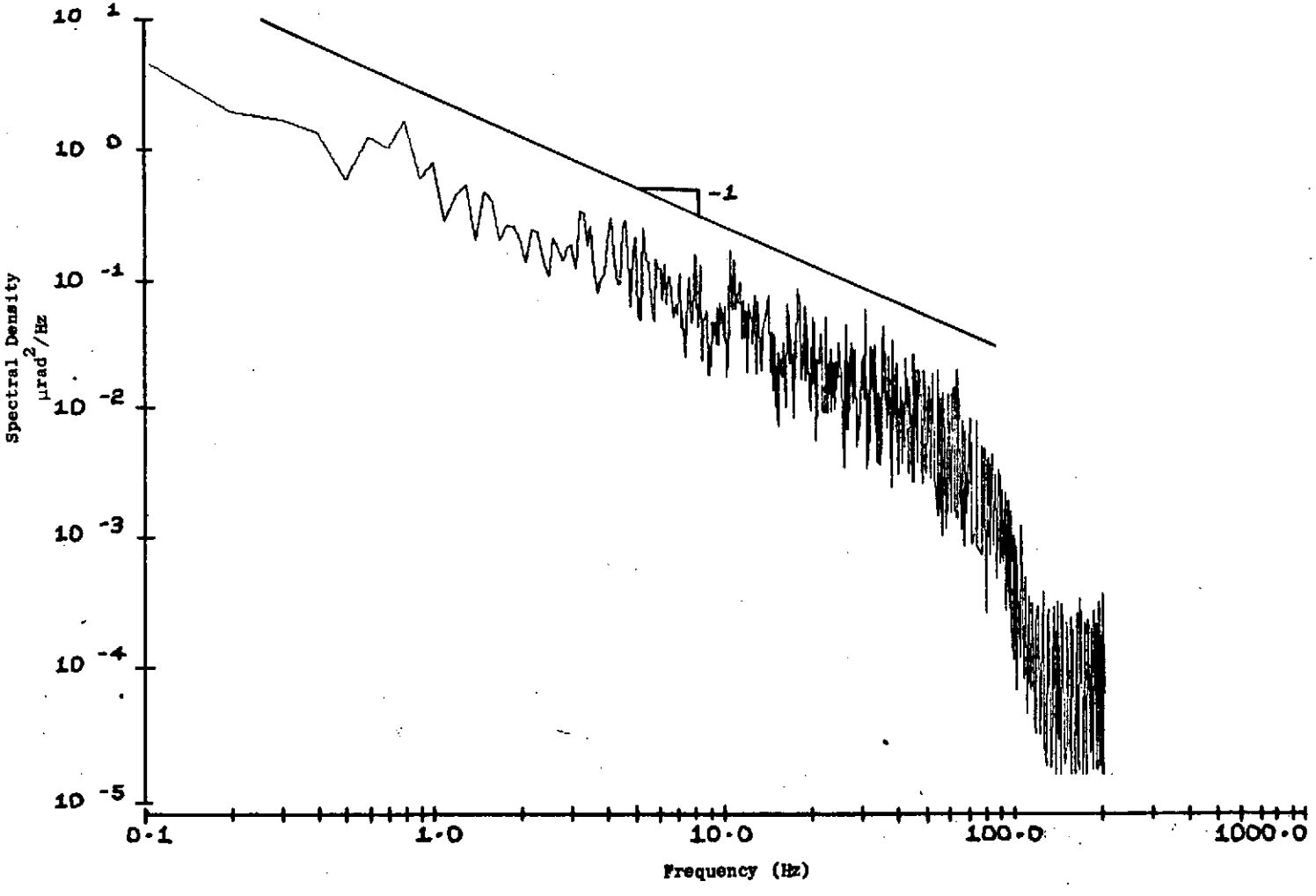

Fig. 34. OPEN-LOOP POWER SPECTRUM OF THE AZIMUTH REFERENCE AUTOCOLLIMATOR. Noise in the phototransistors is the most likely source of the 1/f spectrum.

An approximate time domain solution to this problem is given in [T1]. The noise is treated as the sum of outputs of first order lag networks driven by independent white noise sources. The lag time constants must be distributed throughout the frequency band of interest. Accuracy of this approximate model is determined by the number and distribution of networks.

C. Coherent Measurements

It is important to be able to distinguish platform motion from the inherent errors of the orientation sensors. With ideal instruments, corresponding channels should have the same output: that due to platform motion. The degree to which signals are different therefore depends on the amount of noise or instrument error present. As discussed in Chapter IV, an excellent measure of the amount of noise present in instrument outputs is the coherency function.

An experiment was conducted to demonstrate the use of this function. The intention was to raise the signal well above the noise in a particular frequency band. To do this, the platform gimbal torquers were excited by a low frequency white noise source band limited to 30 Hz while the simulator was autocollimator stabilized. Referring to Fig. 24, the excitation signal was introduced into the X axis as V_{T_d}. Its power spectrum is shown in Fig. 35; the total power corresponds to an rms excitation torque of 0.0078 N-m, which is "small" but larger than the noise. DC excitation and response were removed from the computation of the spectrum in the manner discussed in Appendix A.

The motion induced by the excitation torque was sensed by the gyro, and the output spectrum computed, Fig. 36. Angular rms amplitude is approximately 13 μrad. The coherence between the excitation voltage and the gyro signal is shown also in Fig. 37. Coherence is excellent up to and slightly beyond the stabilization loop bandwidth, approaching unity at these low frequencies. The gyro output below the servo bandwidth is therefore almost entirely due to the excitation. At very low frequencies, the coherence is not as high, indicating that gyro drift torques or other disturbances are influencing the gyro output. Above 20 Hz, the coherence

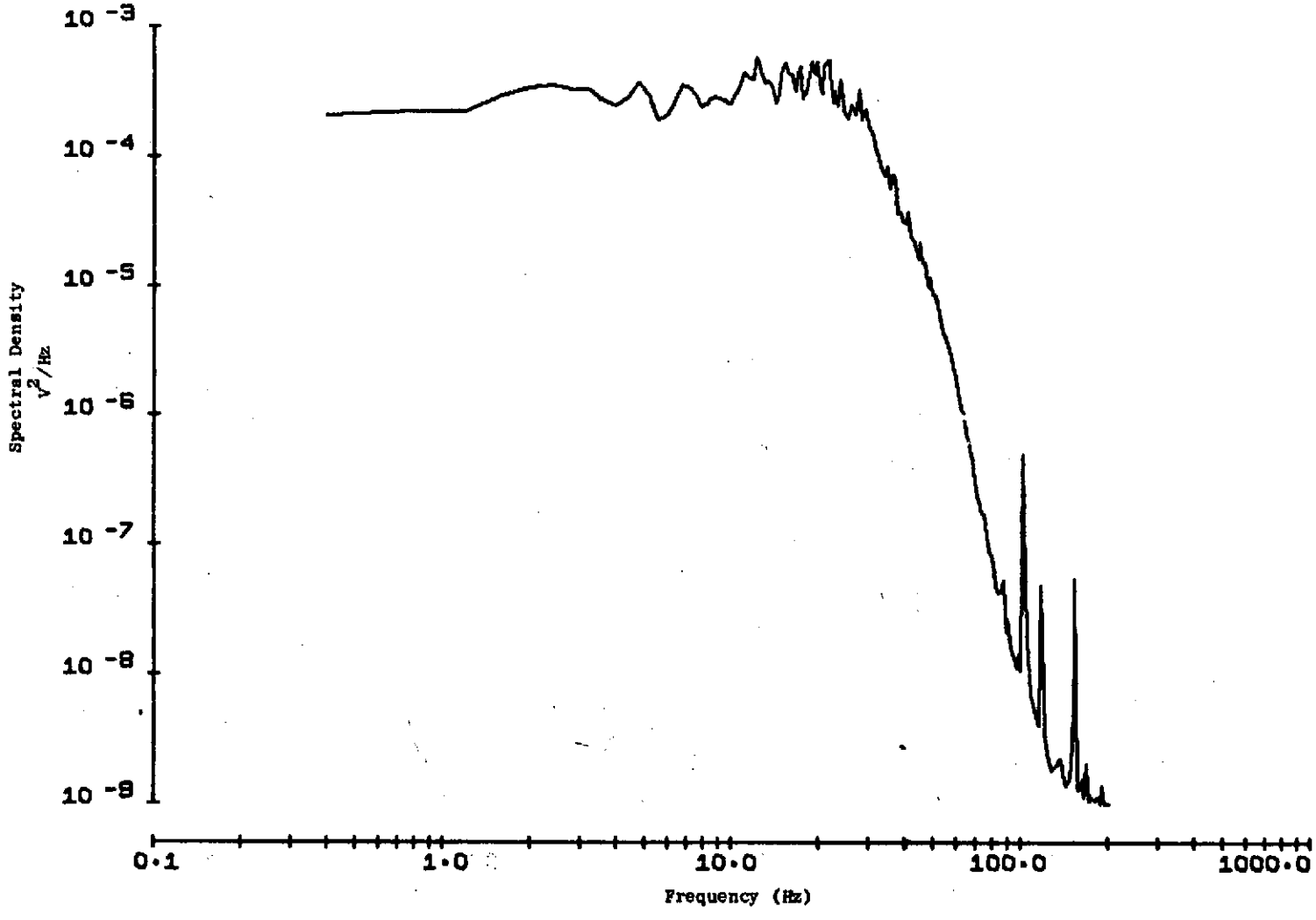

Fig. 35. POWER SPECTRUM OF EXCITATION SIGNAL V_{T_d} INTRODUCED INTO X-AXIS AUTOCOLLIMATOR STABILIZATION LOOP. Attenuation of the signal above 30 Hz is due to filtering in the low-frequency noise generator.

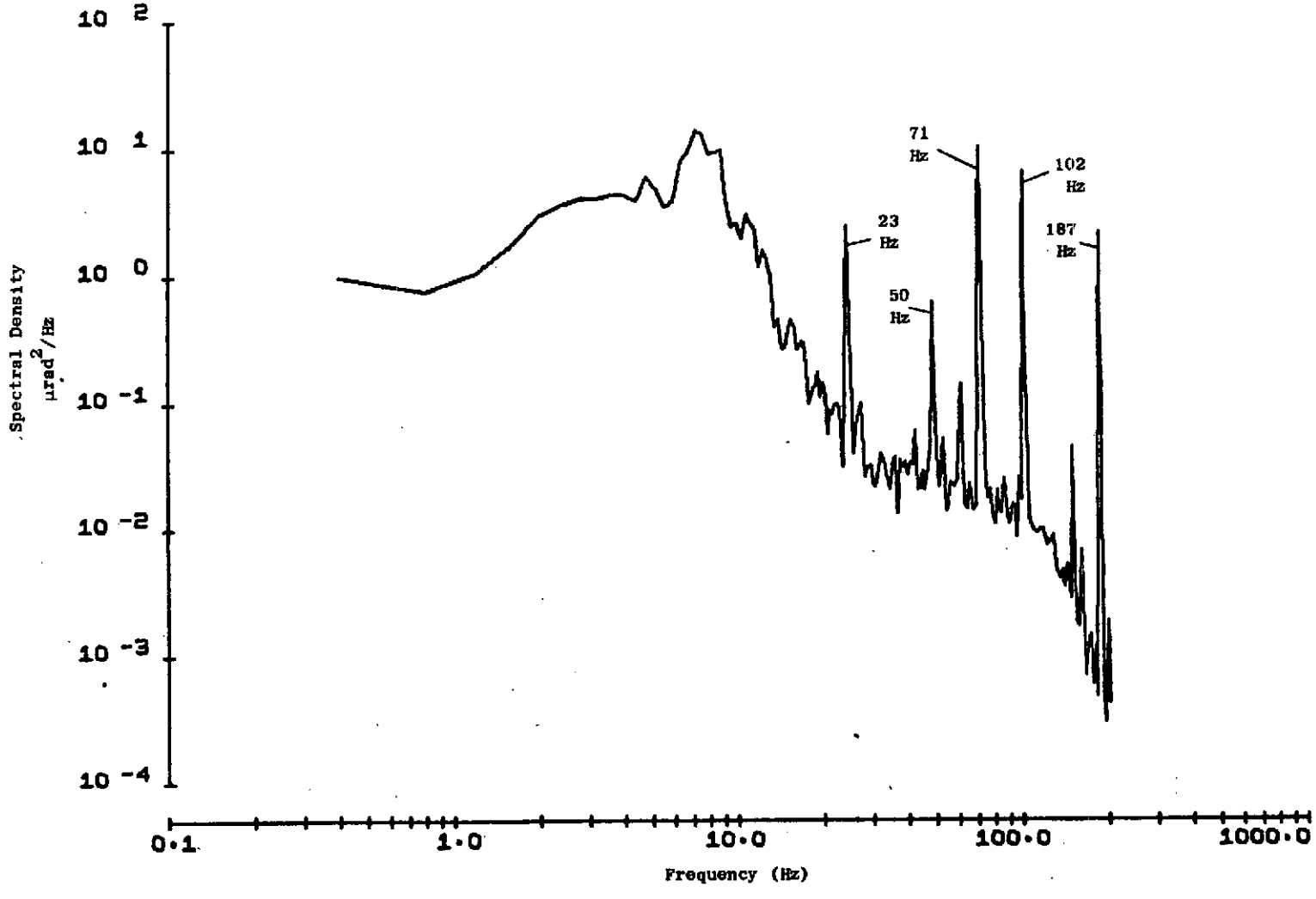

Fig. 36. POWER SPECTRUM OF THE GYRO X-AXIS DUE TO EXCITATION V_{T_d}. Power below 15 Hz is due to base motion while high frequency power is instrument error.

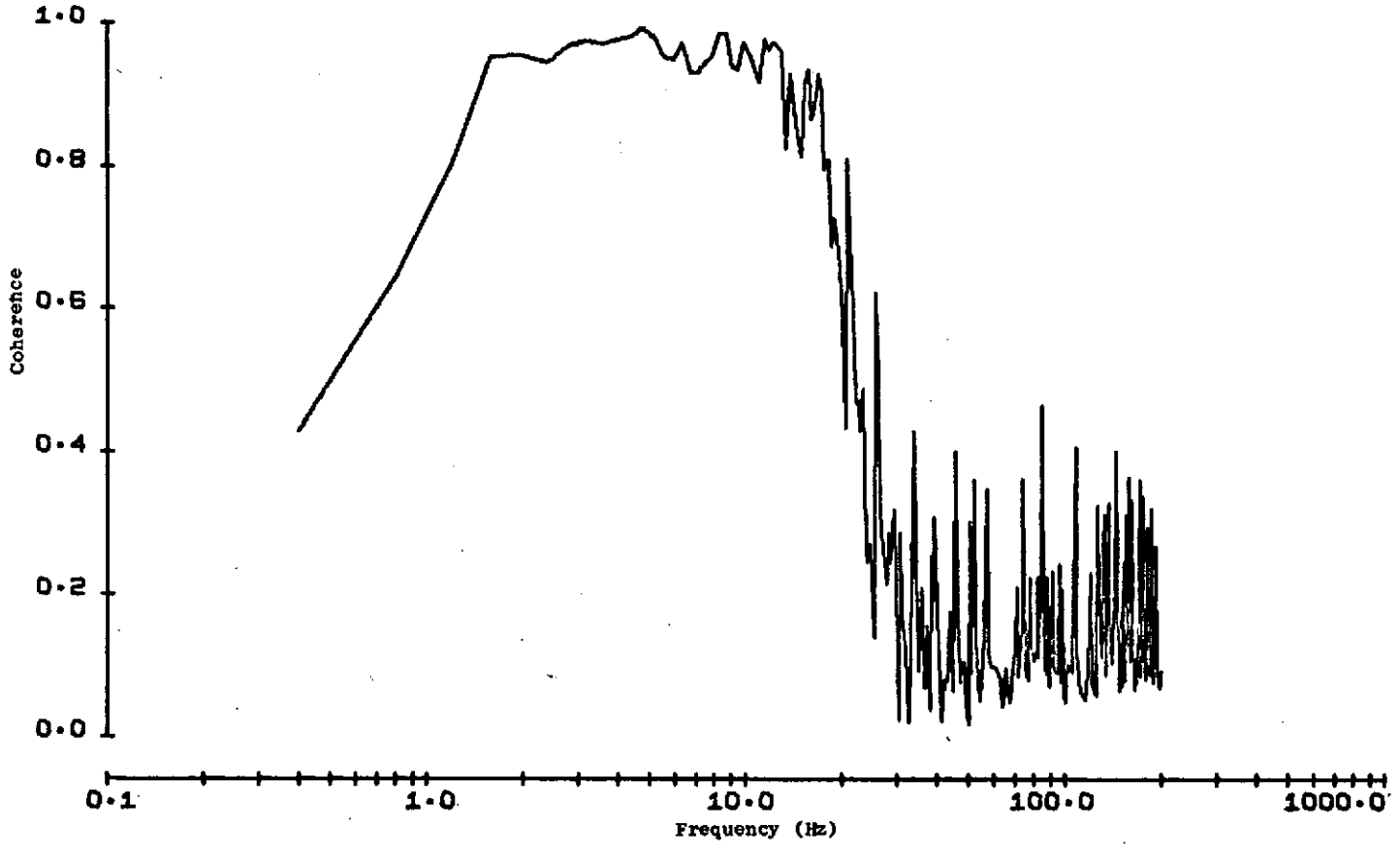

Fig. 37. COHERENCE OF EXCITATION V_{T_d} AND X GYRO RESPONSE. At the mid-frequencies, the coherence approaches the theoretical upper limit of unity.

is nearly zero, indicating that other gyro noise or disturbances are responsible for the output. This high frequency portion of the gyro spectrum is nearly identical to the open-loop gyro spectrum, Fig. 33a. The similarity implies that pickoff noise is the source of the high frequency power in both the open-loop and torquer-excited spectra.

In addition to determining the coherence between the input excitation and the output, a comparison of the outputs of the gyro and autocollimator was also made. Figure 38 is the power spectrum of the autocollimator. It is quite similar to the gyro spectrum except at high frequencies, a fact further substantiated by the coherence between the gyro and autocollimator, Fig. 39. The high coherence at low frequencies indicates that platform motion is primarily responsible for the output of the instruments. Instrument errors at these frequencies are negligible by comparison. The reduction in coherence below 1.5 Hz is similar to that seen in the previous coherence function, Fig. 37. At higher frequencies, gyro pickoff noise causes the two signals to be incoherent. The sharp reduction in coherence above the servo bandwidth is evidence of the high level of discrimination afforded by the coherence function.

D. Transfer Function Modeling

It is not always possible or desirable to excite a system in which precision orientation sensors are being evaluated. The sensors may be driven out of range, or the excitation magnitude may obscure small but important error sources. Furthermore, the excitation may actually alter the physical situation so that performance measurements are no longer valid. Consequently, it is desirable to model system transfer functions using only the noise inherent in the system. The transfer functions may then be used in determining the effects of the system on the sensors.

Figure 40 is the amplitude ratio of the transfer function of the X-axis compensation network computed from measurements of the network input and output. The simulator was autocollimator stabilized. No external excitation was used; the input to the network being the output of autocollimator control channel plus a small but unknown amount of electrical pickup noise. The transfer function derived in Chapter III by a network analysis, Fig. 22, is superposed for comparison. These two methods of

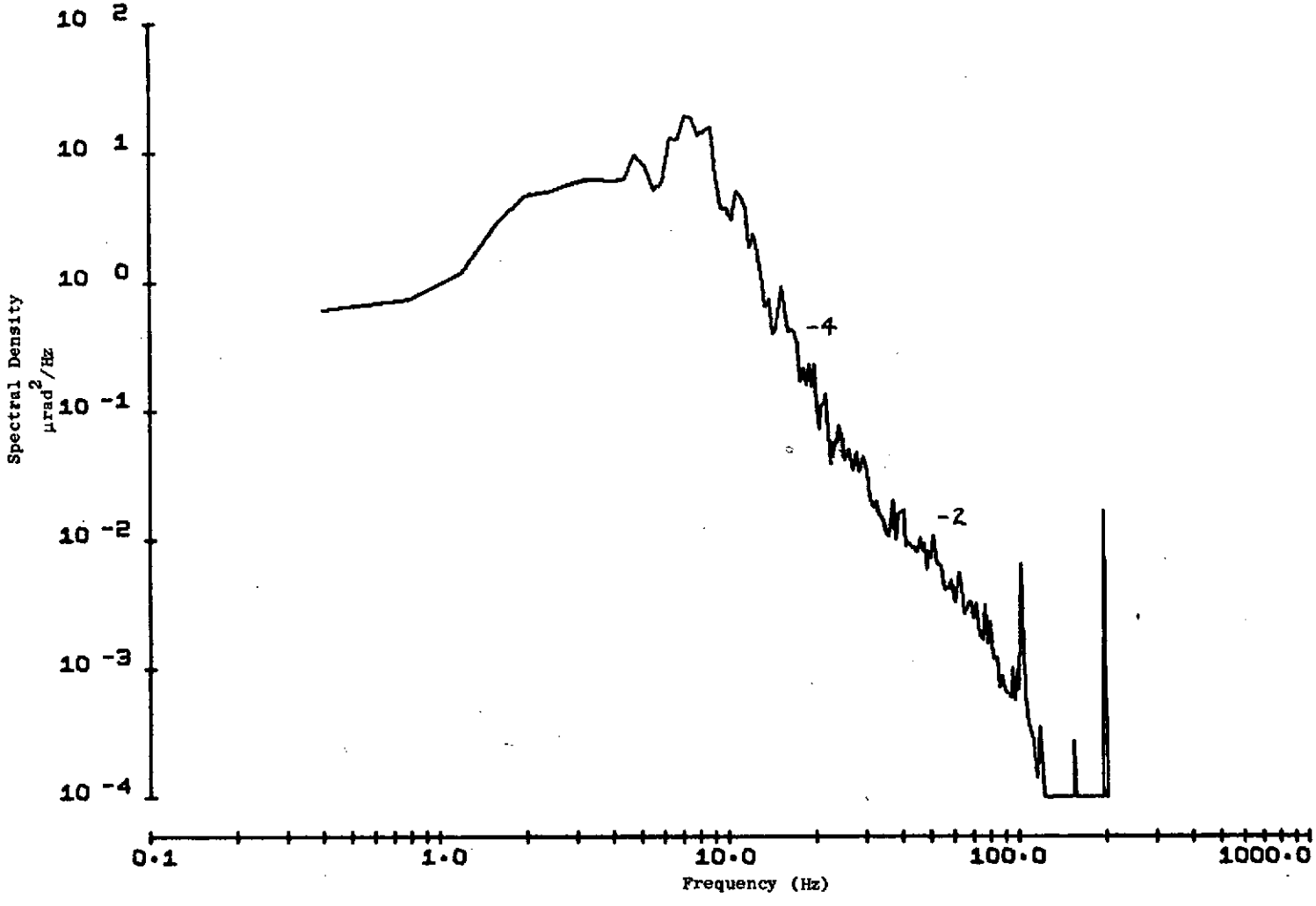

Fig. 38. POWER SPECTRUM OF THE AUTOCOLLIMATOR X CONTROL CHANNEL DUE TO EXCITATION V_{Td}. Low-frequency attenuation is due to the integral control feedback of the compensation network, while high frequency attenuation results from platform inertia and electronic filtering.

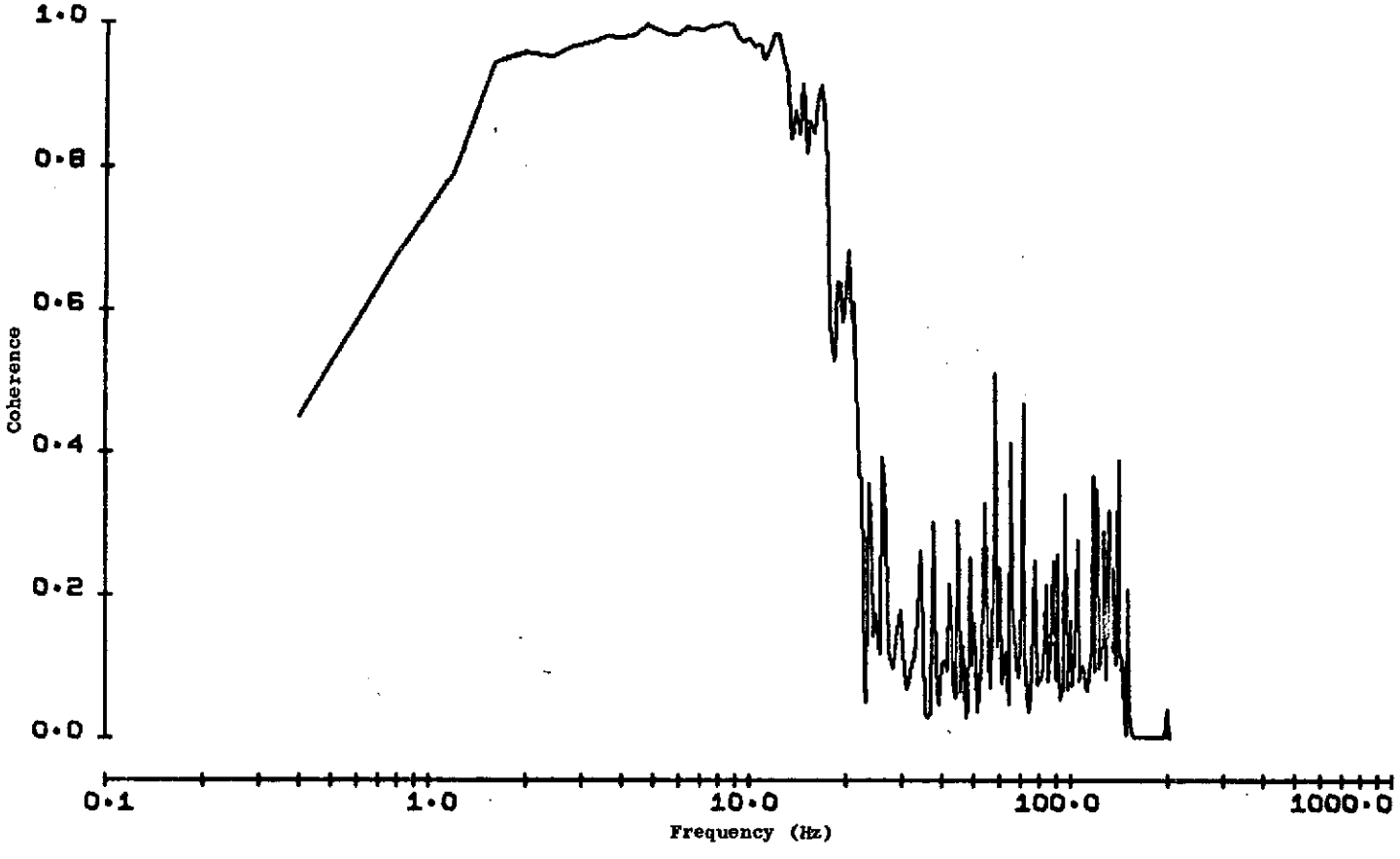

Fig. 39. COHERENCE OF GYRO AND AUTOCOLLIMATOR RESPONSES TO EXCITATION V_{Td}. Both the autocollimator and gyro provide accurate angle sensing when base motion exceeds the inherent noise.

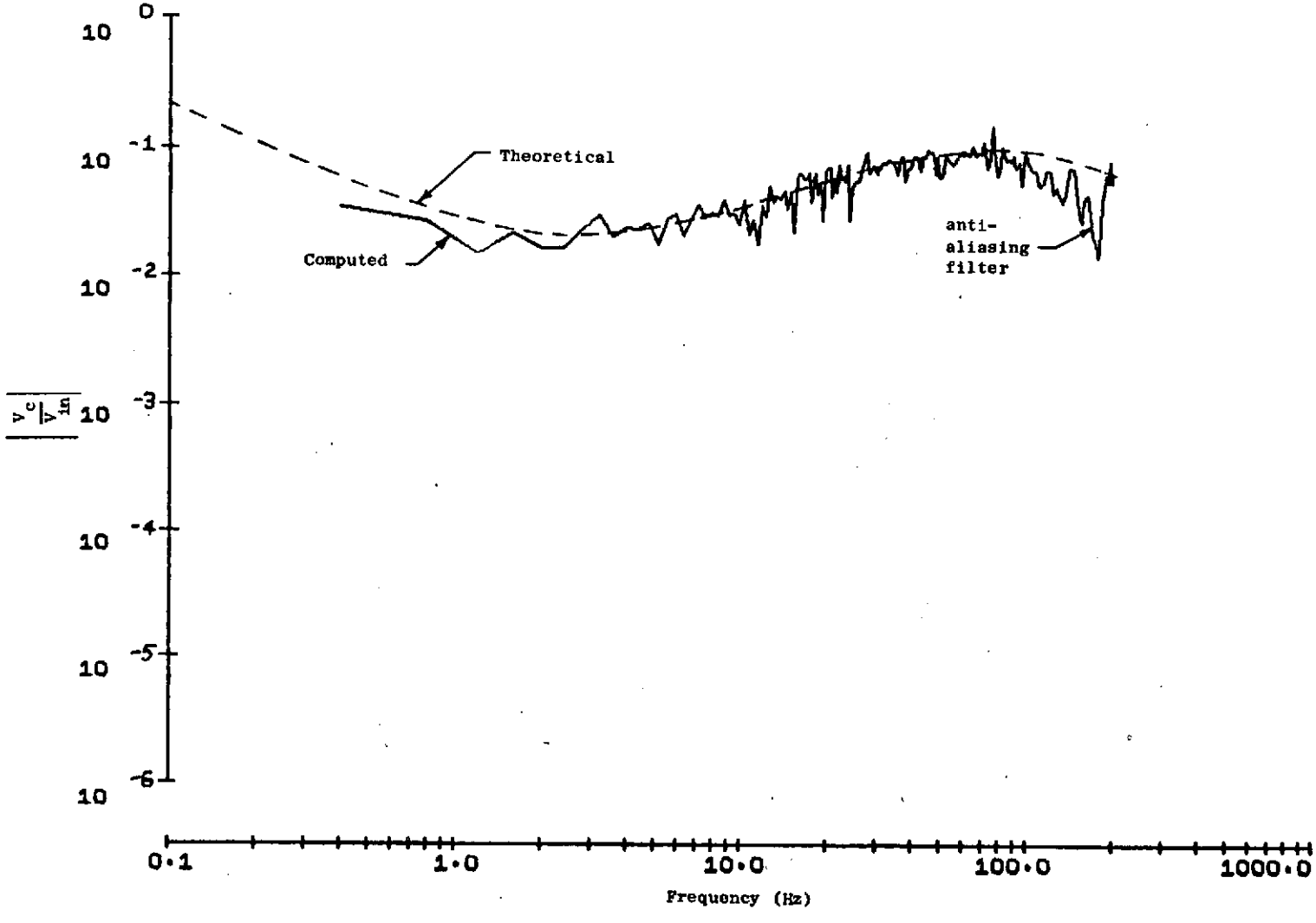

Fig. 40. COMPARISON OF EXPERIMENTAL AND DESIGN COMPENSATION NETWORK TRANSFER FUNCTIONS.

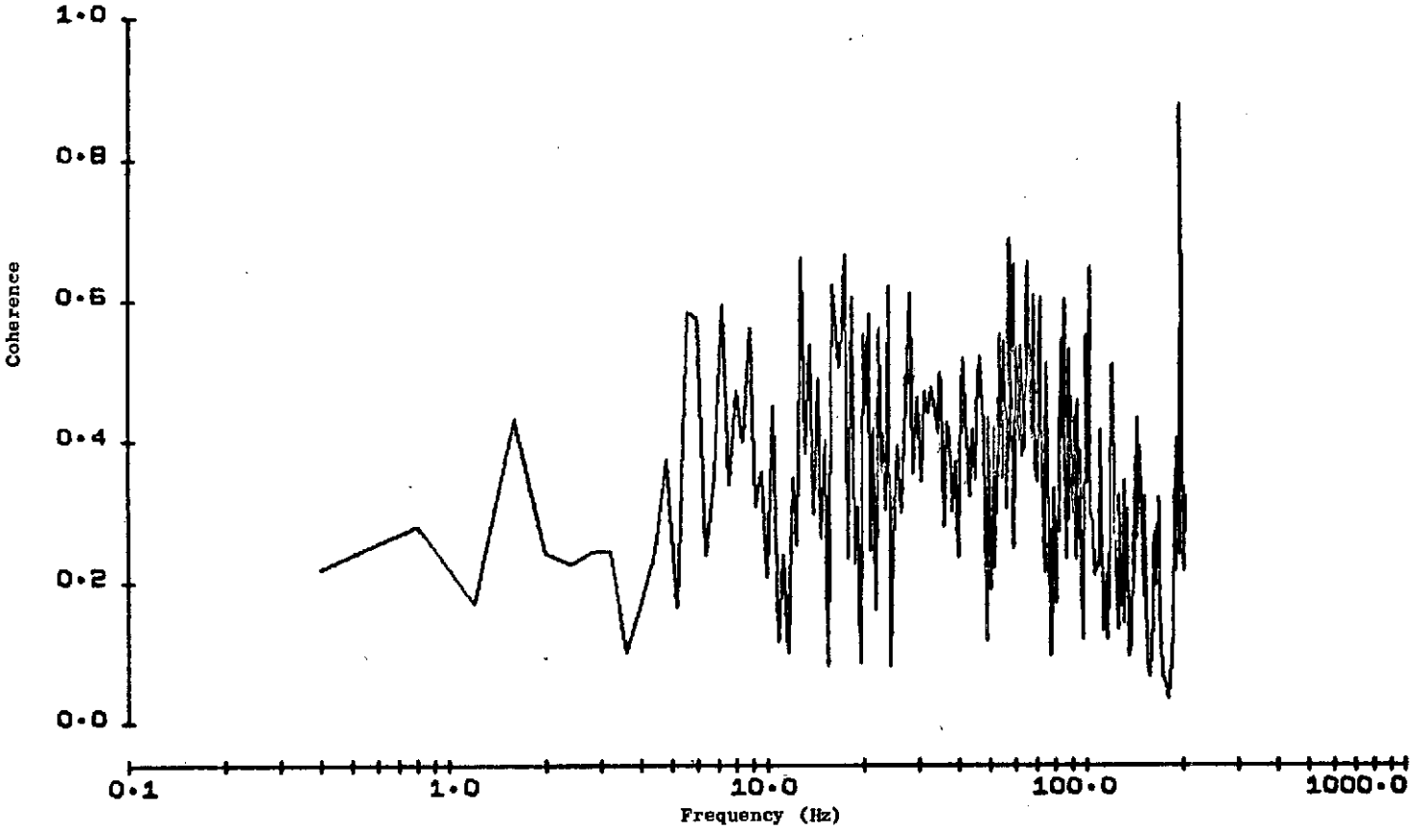

Fig. 41. COHERENCE OF COMPENSATION NETWORK INPUT AND OUTPUT. A probable source of the coherent components at 200 Hz is electrical pickup from the gyro spin motor drive electronics.

obtaining the transfer function agree to within a factor of two. This is considered good agreement for the amount of data processed and the amount of internal noise picked up from surrounding circuits. The moderate level of coherence in the coherence function, Fig. 41, indicates the presence of a significant amount of pickup noise.

This example of computing transfer functions was selected since the actual transfer function was accurately known and could be used as a basis of comparison. The technique, however, is applicable in determining input-output relationships throughout the system.

E. Closed Loop Sensor Measurements

The power spectra of the sensors, mounted on the simulator and operating as integral parts of the stabilization loops were calculated. Comparing these spectra, shown in Figs. 42 and 43, with the open loop spectra of Figs. 32 and 33 clearly demonstrates the need for an accurate system model in order to deduce sensor performance from closed loop data.

1. Autocollimator

The power spectrum of the autocollimator X control channel, Fig. 42, was computed from data taken with the simulator in Mode 3 (autocollimator stabilization). This spectrum is to be compared with the open loop spectrum, Fig. 32a. Only above 40 Hz, where the attenuation of the output filter is evident, are the spectra comparable in form. In this band the level of the closed loop plot is ten times greater than that of the open loop. The increased level of noise over the open loop measurement is most likely due to electrical pickup noise in the much harsher simulator electrical environment. Below 40 Hz almost no similarity exists because the operating conditions are completely different. Differences in the two plots must be explained by considering overall system behavior. In order to do this, the simulator model developed in Chapter III is used.

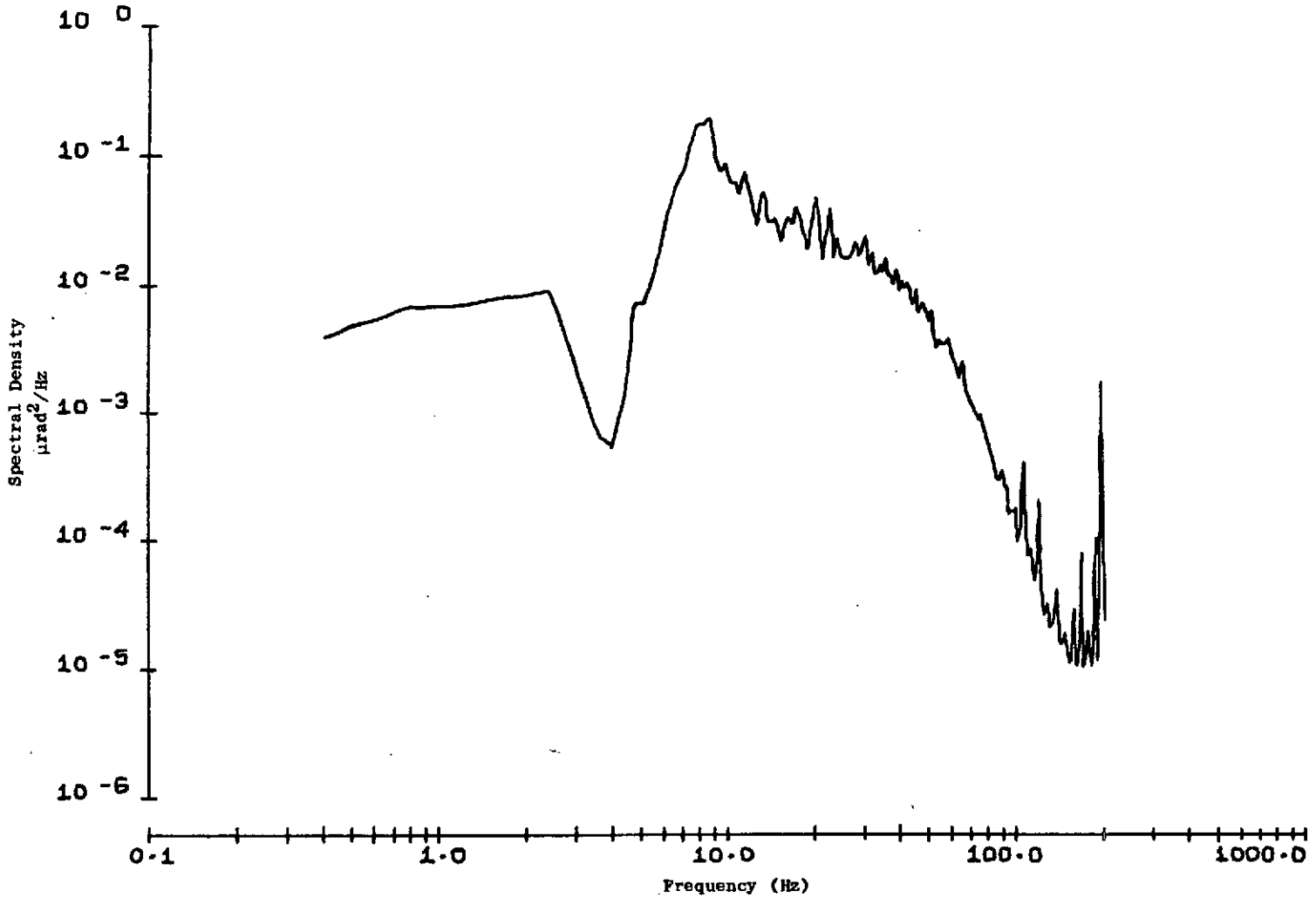

Fig. 42. POWER SPECTRUM OF THE X-AXIS CONTROL CHANNEL OF THE PRIMARY AUTOCOLLIMATOR IN MODE 3 (AUTOCOLLIMATOR STABILIZATION).

Referring to the autocollimator stabilization loop block diagram, Fig. 24, it can be seen that numerous paths exist between the various disturbance inputs and the sensor output. Assuming the simulator is adequately described by the model, each output is a combined response to all the disturbances. The responses have been evaluated previously in Table 5 in terms of the closed loop transfer functions. Since the system was not commanded ($\gamma_c = V_{T_d} = 0$), the most likely causes of the autocollimator spectrum are the autocollimator error n_A, disturbance torques M_d, or amplifier noise, also considered as a disturbance torque. Mechanical vibration is another possible source.

As a starting point in developing a model which explains the autocollimator spectrum, the pronounced decrease in power at 3.5 Hz is first noted. An explanation of this dip follows.

Within the bandwidth of the system (15 Hz) the closed loop transfer function between an input and the output is approximately $1/H(s)$, where $H(s)$ is the transfer function of the feedback path. A dip in the transfer function within the system bandwidth must therefore be caused by a peak in $H(s)$. Although resonant peaks can arise from several sources (e.g. gyro, reference mirror mount, autocollimator mount, flexible modes), the most likely source is a platform gimbal bearing resonance. Other resonances tend to be much higher in frequency than the observed 3.5 Hz, while a soft elastic restraint in the platform gimbal bearings coupled with the large gimbal inertia could produce the low frequency resonance. Referring to Fig. 24, the only noise input which has this potential source in the feedback path is the autocollimator noise n_A.

Based on this observation, an investigation of bearing behavior was undertaken. The study is described in Section F of this chapter. The main result, already accounted for in the simulator model of Chapter III, is that the bearings act like springs for small motion.

Using this model, the closed loop transfer function between n_A and the autocollimator control channel output, γ_{AC}, is expressed in Table 5 of Chapter III as $(1/K_{AC})(\gamma_{AC}/n_A)$. The observed spectrum is similar in form to the magnitude plot of this transfer function shown in Fig. 26a; the only differences occuring at low frequencies where the observed spectrum is higher and decreases only slightly with decreasing frequency.

Therefore, with a high level of confidence, the decrease in power at 3.5 Hz can be attributed to a platform gimbal bearing resonance, and the entire autocollimator spectrum attributed to the response of the stabilization loop to the autocollimator noise spectrum of Fig. 32a.

2. Gyro

The spectrum computed from the simultaneously recorded X-axis gyro pickoff signal, Fig. 43, is also consistent with these results. The model response of the gyro to white autocollimator noise has been shown previously in Fig. 26c. Above 15 Hz the gyro spectrum is essentially the same as the open-loop results obtained with the platform clamped. Below 15 Hz the closed-loop spectrum is a combination of pickoff noise and platform response to autocollimator noise. In the band around 9 Hz, coherence exists between the gyro and autocollimator signals. This can be seen in Fig. 44. Platform motion is significantly larger than the autocollimator noise equivalent angle near 9 Hz due to peaking of the lightly damped stabilization loop. The signal to noise ratio in both sensors is therefore increased, a condition reflected by the relatively high level of coherence. The signals are also moderately coherent at low frequencies for unknown reasons.

The gyro spectrum can also be used to deduce the level of motion of the platform. Again from Fig. 26c, the gyro (and platform) do not respond significantly to autocollimator noise above 15 Hz. Since the gyro spectrum below 15 Hz is primarily due to platform motion induced by autocollimator noise, the total power in this band is a reasonable estimate of the variance of the platform angle. This excludes any motion of the reference mirror at frequencies less than 0.4 Hz, which should be small due to the rigidity of the autocollimator reference mirror mount. The computed rms platform angle at frequencies greater than 0.4 Hz is approximately 1.6 μrad. Although no data were obtained below 0.4 Hz, very low frequency motion due to autocollimator noise should not be significant because of the excellent null stability of the autocollimator. Mechanical creep and thermally induced distortions are more likely sources of low frequency error.

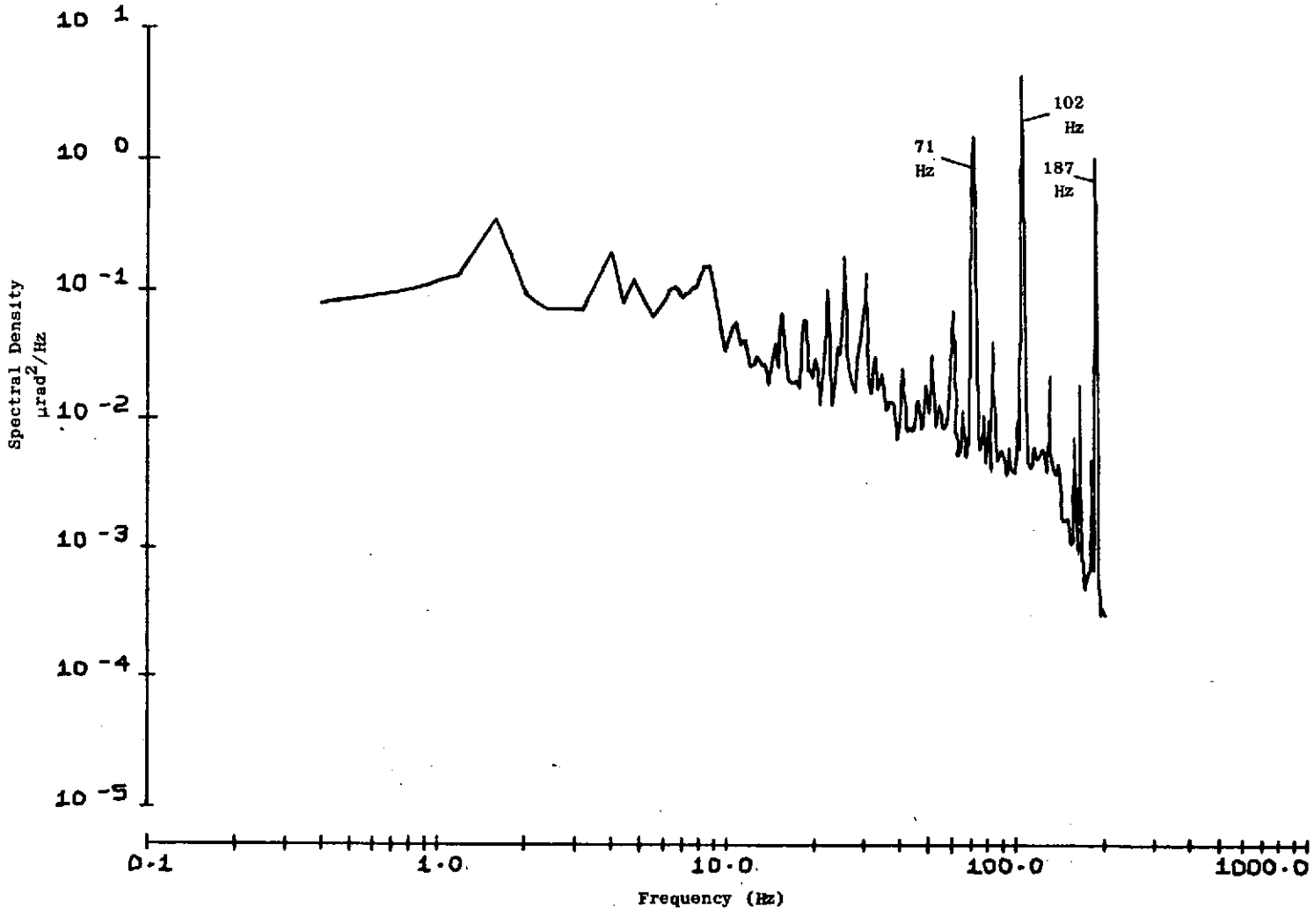

Fig. 43. SPECTRUM OF THE X-AXIS INSTRUMENTATION CHANNEL OF THE X-Y GYRO IN MODE 3.

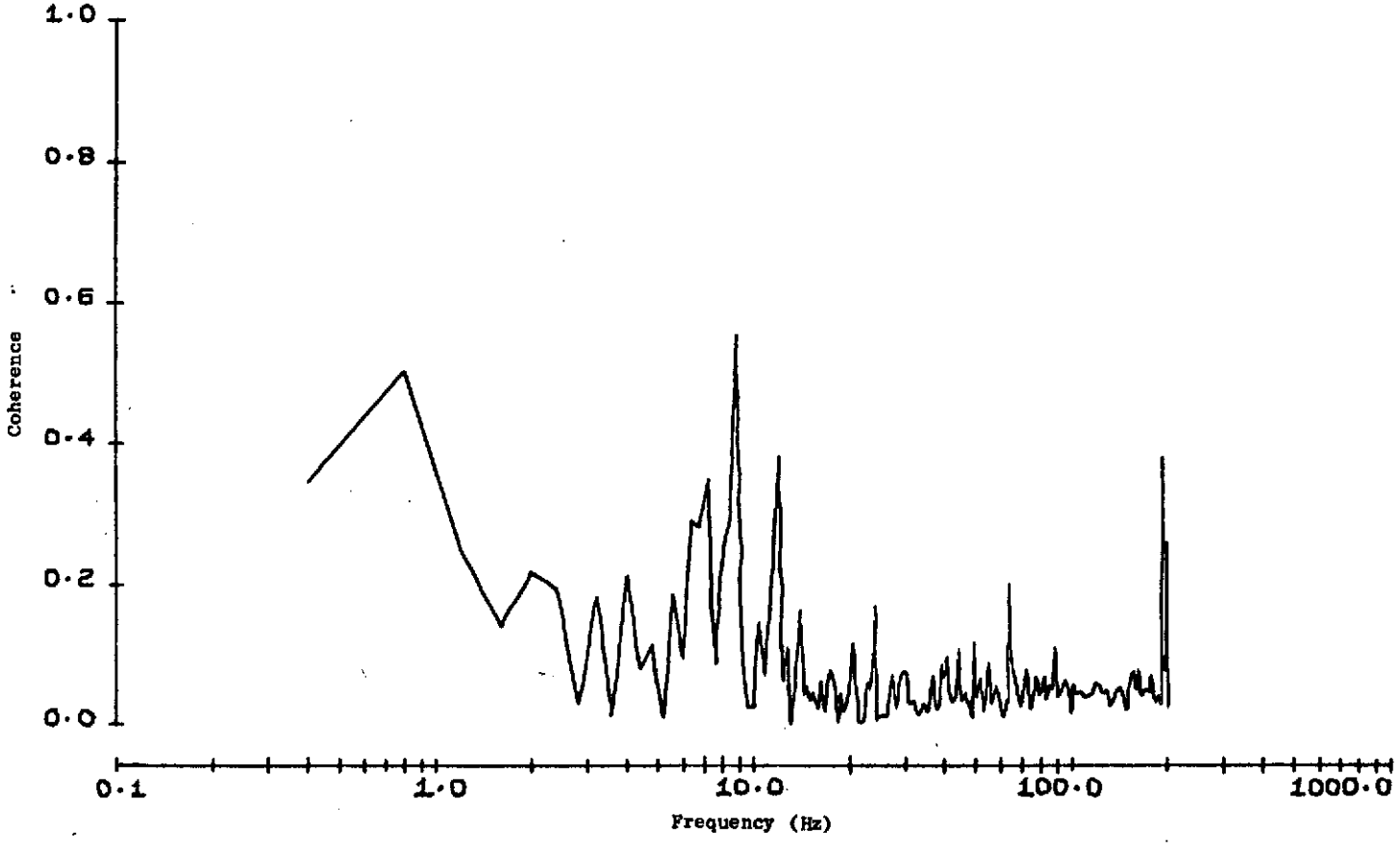

Fig. 44. COHERENCE OF THE X-AXIS AUTOCOLLIMATOR CONTROL AND GYRO INSTRUMENTATION CHANNELS.

Corresponding Mode 3 plots for the Y axis are shown in Figs. 45, 46, and 47. The behavior is similar to the X axis, the most notable differences being the general shift toward higher frequencies of the main features, and the broader band of the dip in the autocollimator spectrum. The large spike at 200 Hz in the autocollimator spectrum is probably due to interference at the gyro spin motor drive frequency. The results are otherwise consistent with the simulator model developed independently in Chapter III. The computed rms platform angle is 3.6 μrad.

3. Cross-Axis Coherence

The coherence between the X and Y autocollimator control channels was computed and is shown in Fig. 48. The high level of coherence above the stabilization loop bandwidth of 15 Hz indicates that the two channels have a common noise source. As discussed previously, this source is the dark current in the photodetector. At low frequencies the stabilization loops reduce the response to the noise to a sufficiently low level that other noise sources become important. Consequently, the coherence is also small.

The analogous coherence function of the two X-Y gyro instrumentation channels is shown in Fig. 49. The two channels are nearly incoherent everywhere except at a few discrete frequencies. This indicates that most of the noise arises in the separate pickoff electronics rather than from a common signal generator excitation noise or a platform motion about an axis skewed with respect to both X and Y.

F. Platform Gimbal Bearing Restraint

The decrease in power in the 3.5 - 10 Hz band consistently observed in the closed-loop autocollimator spectra was not anticipated. An original model for the platform gimbal dynamics consisted of the gimbal inertia and a small amount of bearing friction. For the small platform motion present, it was not known whether a viscous or coulomb (velocity independent) friction model was appropriate. Using a viscous model, the observed decrease in power could not be predicted. On the other hand, it was not

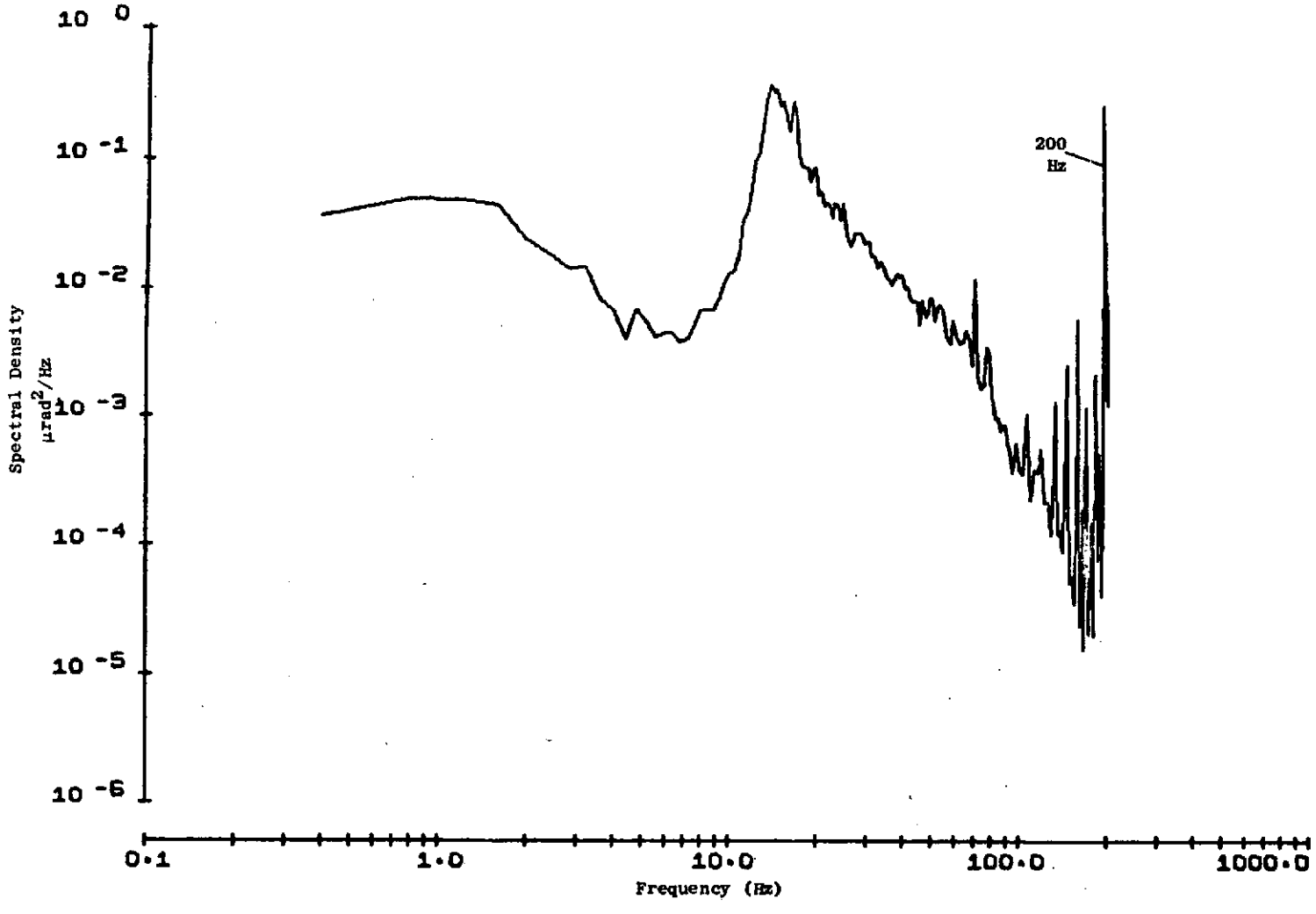

Fig. 45. POWER SPECTRUM OF THE Y-AXIS CONTROL CHANNEL OF THE PRIMARY AUTOCOLLIMATOR IN MODE 3. The broadening of the dip around 6 Hz over that predicted indicates that a simple linear spring model of the bearings is inadequate.

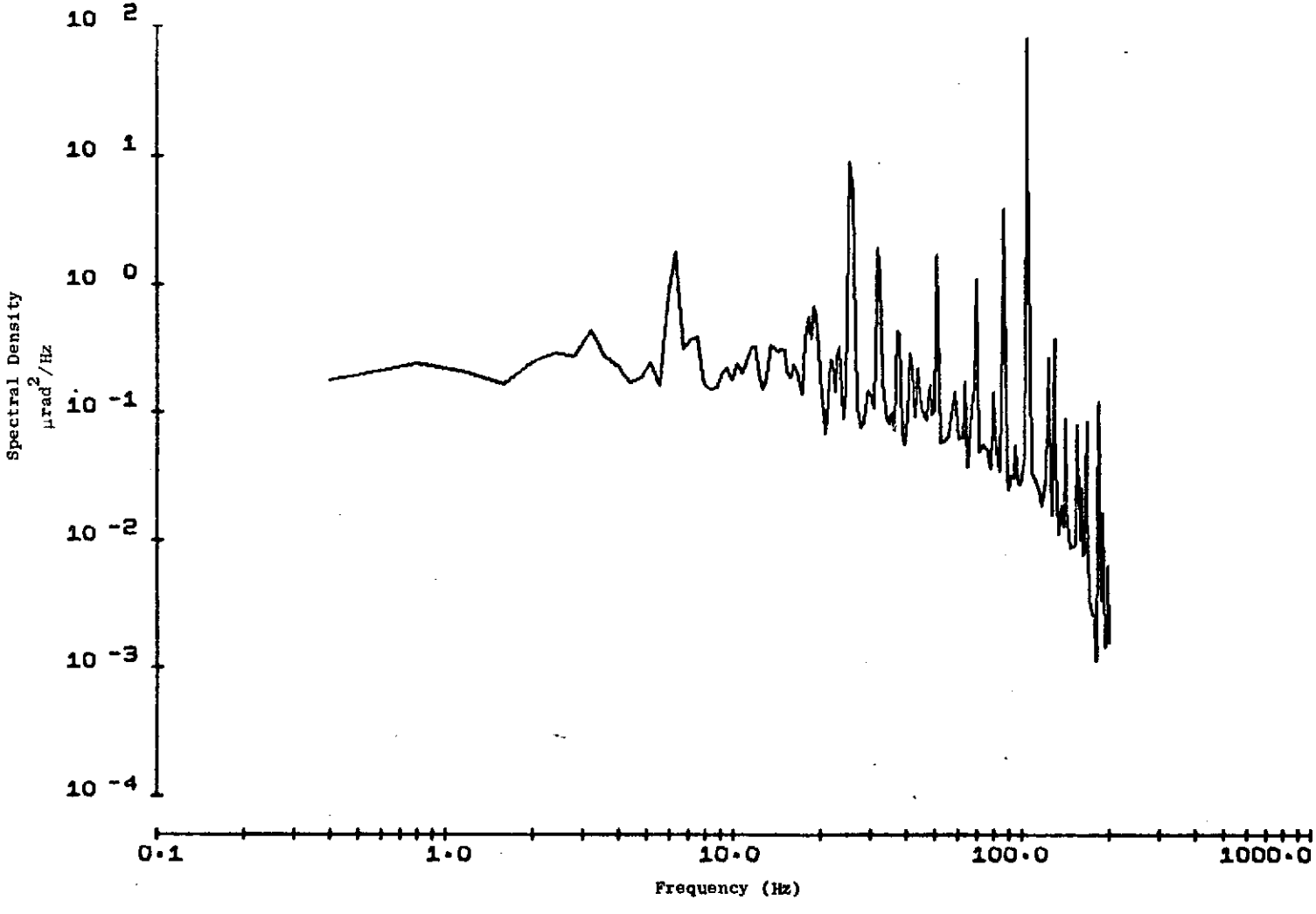

Fig. 46. POWER SPECTRUM OF THE Y-AXIS INSTRUMENTATION CHANNEL OF THE X-Y GYRO IN MODE 3.

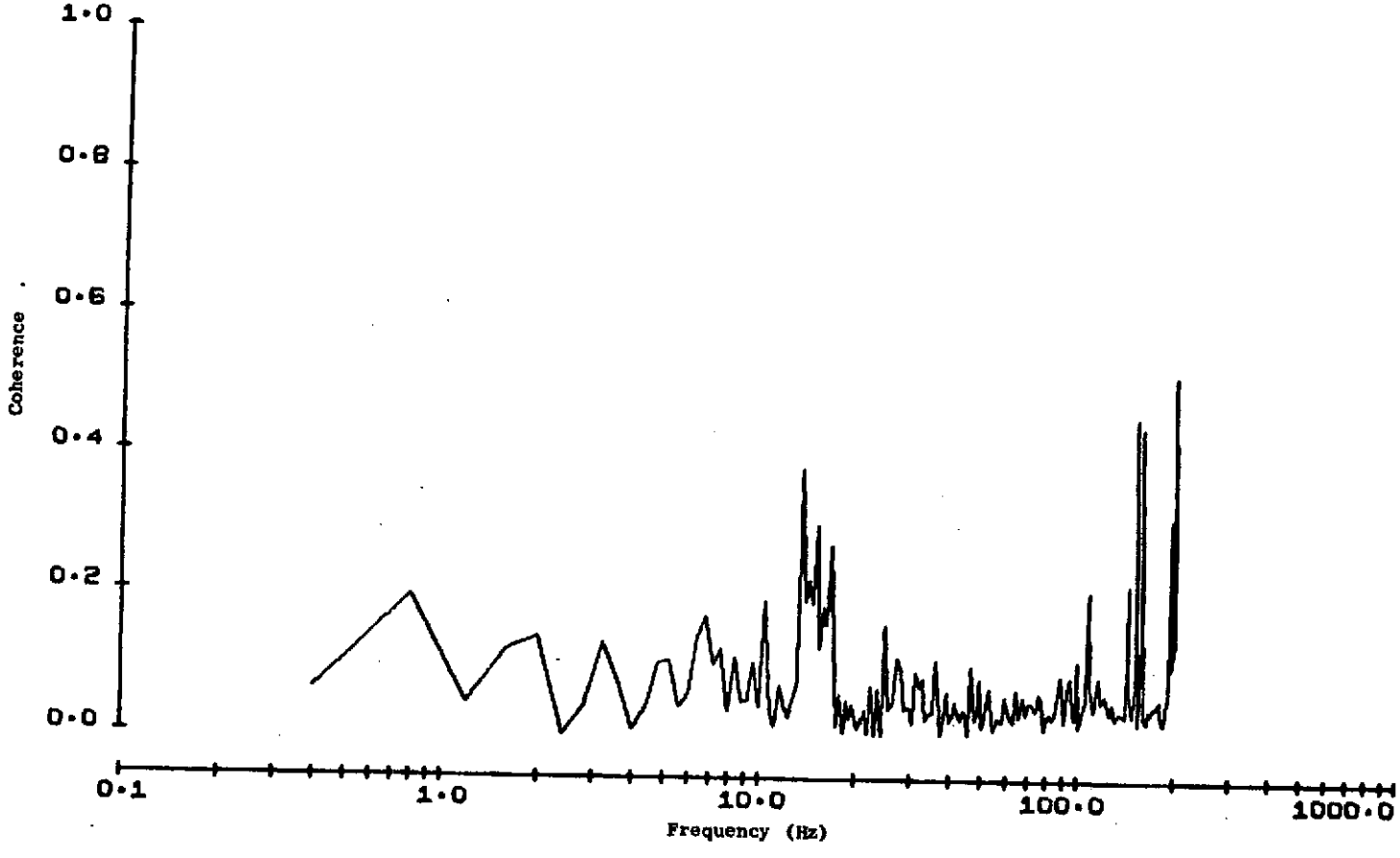

Fig. 47. COHERENCE OF THE Y-AXIS AUTOCOLLIMATOR CONTROL AND GYRO INSTRUMENTATION CHANNELS. Increased base motion near the 15 Hz stabilization loop cross-over frequency is sensed by both instruments.

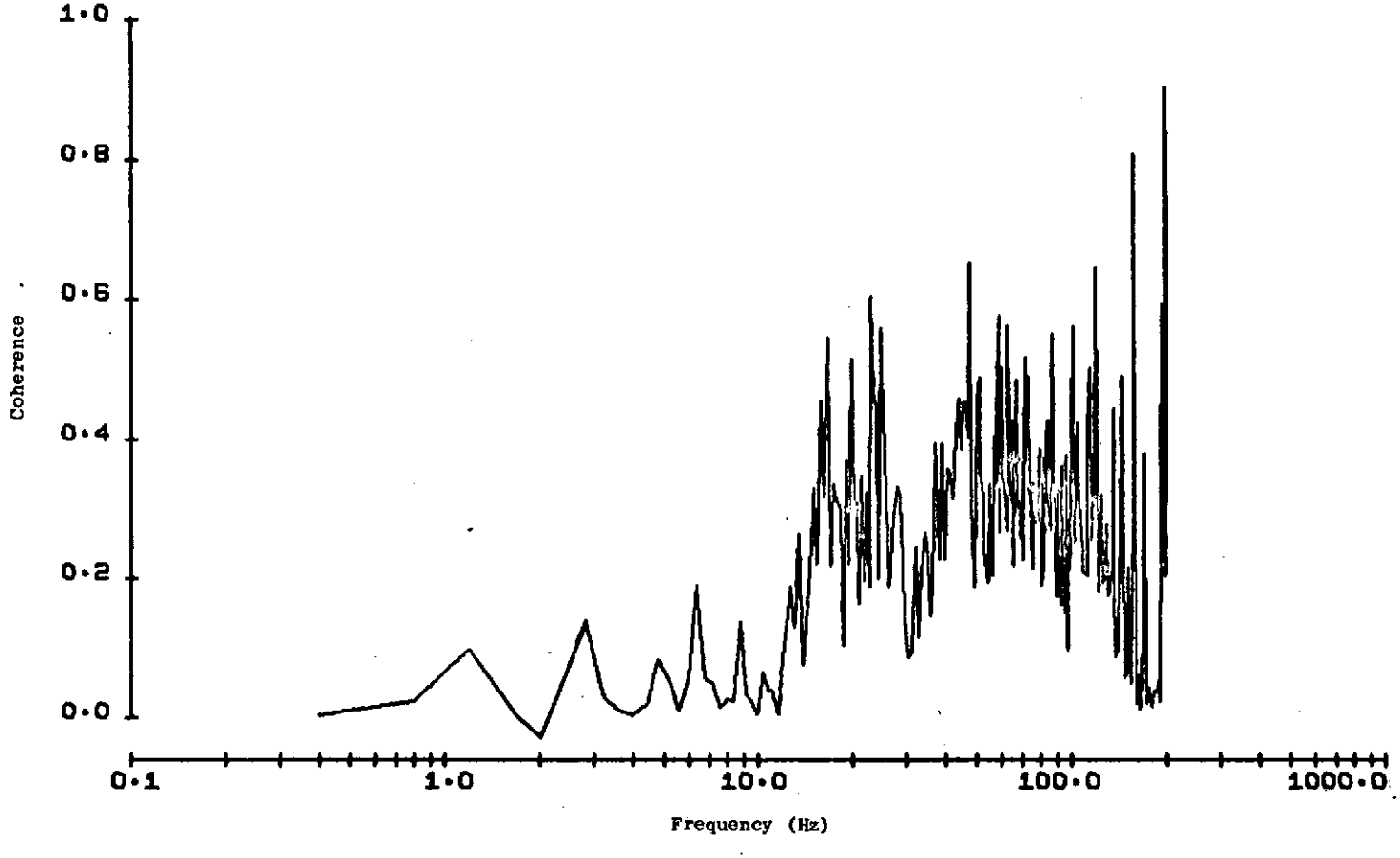

Fig. 48. COHERENCE OF X AND Y AUTOCOLLIMATOR CONTROL CHANNELS IN MODE 3.

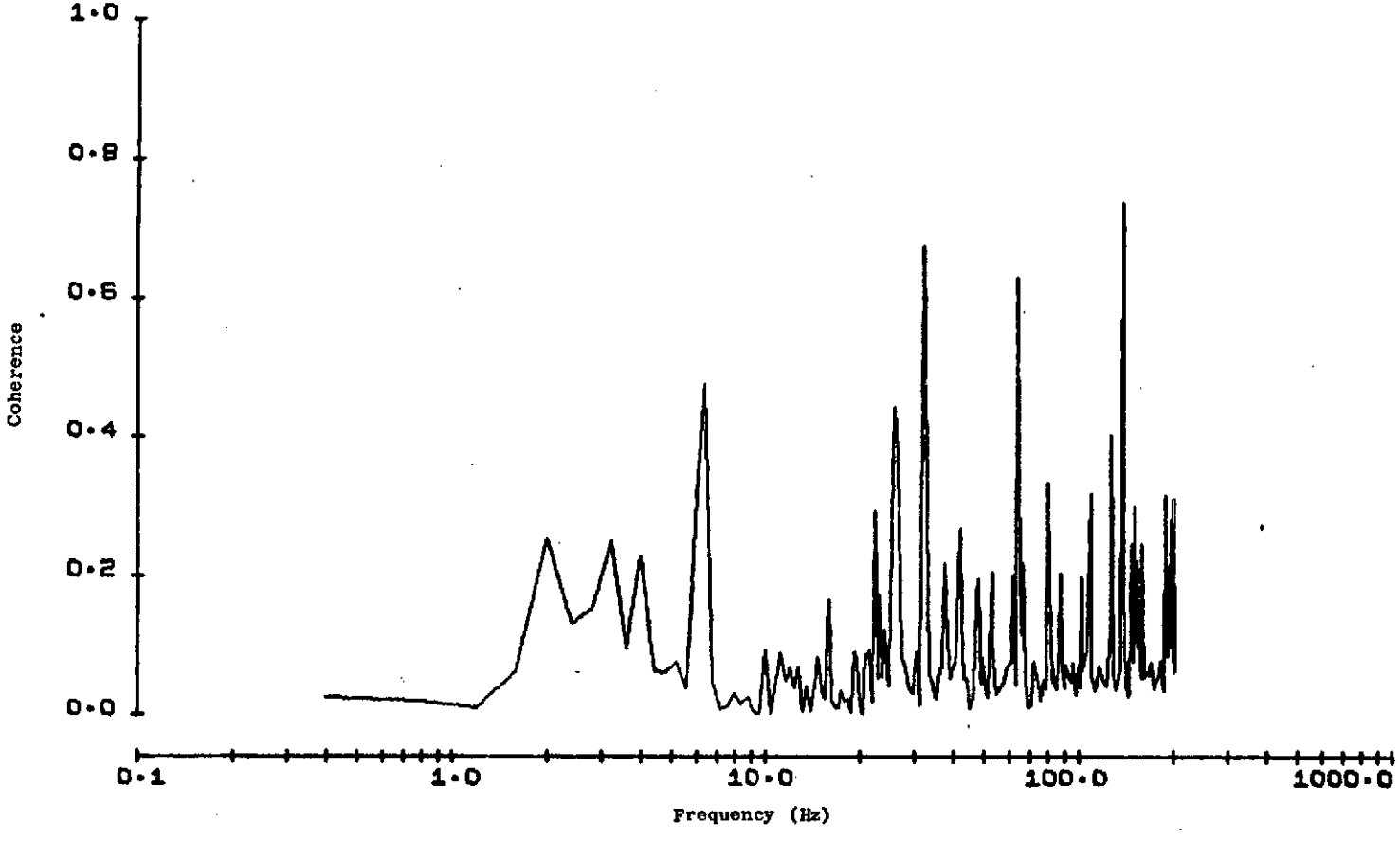

Fig. 49. COHERENCE OF X AND Y GYRO INSTRUMENTATION CHANNELS OPERATING IN MODE 3.

known how coulomb friction would manifest itself in the sensor power spectrum. A further indication that the initial platform model was not adequate was the increase in frequencies of the observed spectral peaks over those predicted from the linear model.

1. Identification and Measurement

In order to isolate the mechanism by which power is apparently absorbed, a study of the transfer functions of the individual system components was made. Transfer functions were determined using the spectral techniques already described, and also by inserting sinusoidal voltages from a function generator into the autocollimator and power amplifier command inputs. All computed transfer functions except the platform dynamics agreed well with the previously established model.

The platform response was determined by commanding the gimbals to oscillate sinusoidally at a very low frequency and simultaneously recording the autocollimator instrumentation output, the power amplifier input, and the voltage across the gimbal motor armature. The gimbal motor armature voltages are proportional to the motor current, and thereby the torque, since back EMF of the gimbal motor is negligibly small. The command was summed into the autocollimator control channel output with the simulator in Mode 3. The instrumentation channel indicated the actual gimbal angle. Figure 50 is a representative low frequency time history of the recorded signals. It can be seen that as the gimbal angle reaches its maximum displacement and starts returning to null, the applied torque unloads rapidly and then steadily increases until the velocity of the gimbal again changes polarity.

A cross plot of platform angle and torque taken at low frequency (0.4 Hz), Fig. 51, illustrates the hysteresis characteristic of coulomb friction. Identical behavior was observed at lower frequencies. The power amplifier input was used as the measurement of applied torque since it is quieter than the motor voltage. A large amplitude oscillation, 1000 μrad peak to peak, was used to increase the signal-to-noise ratio. The amplitude of motion (500 μrad) is more than two orders of magnitude greater than that experienced during normal simulator operation, and is not representative of small motion behavior.

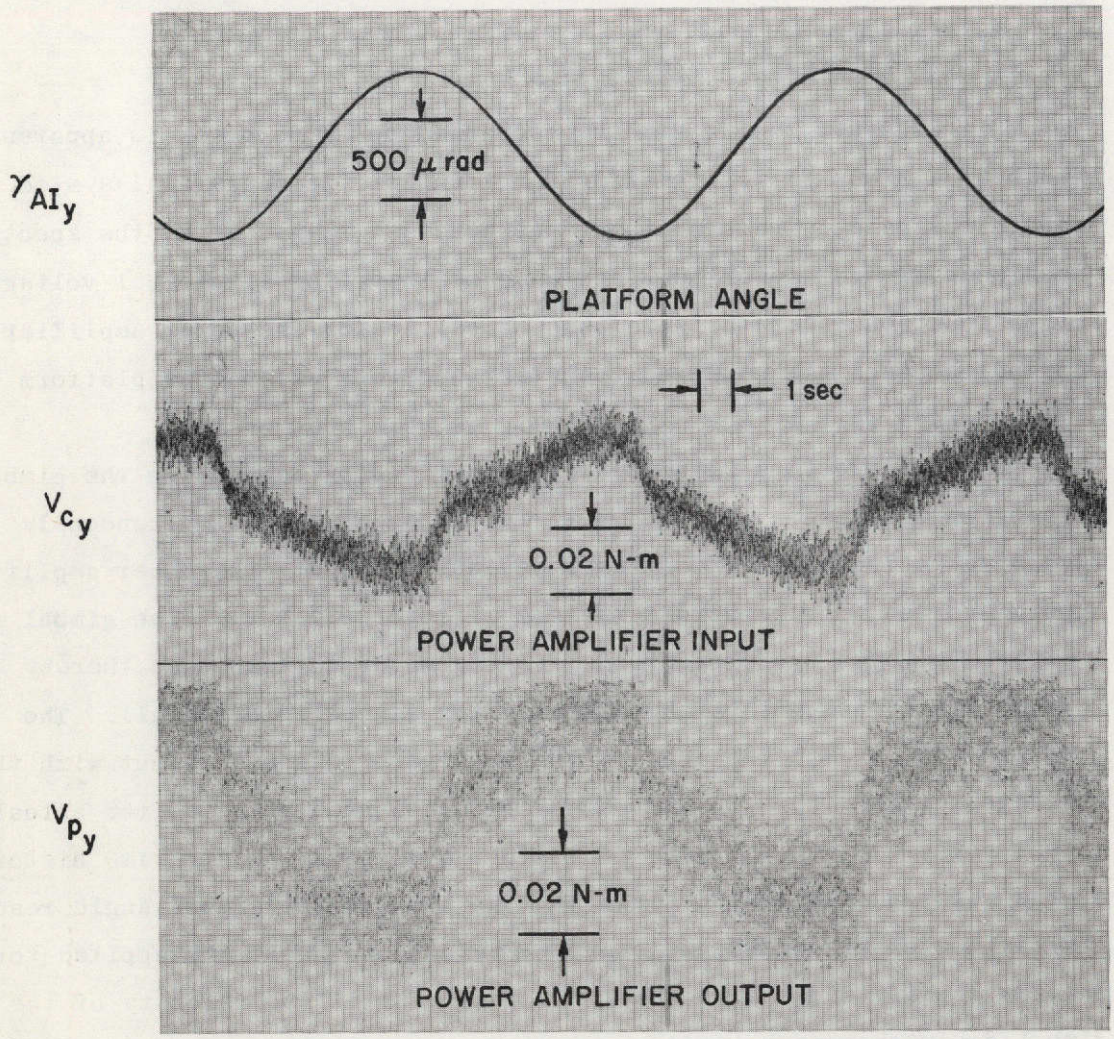

Fig. 50. REPRESENTATIVE LOW FREQUENCY TORQUE--ANGLE TIME HISTORIES.

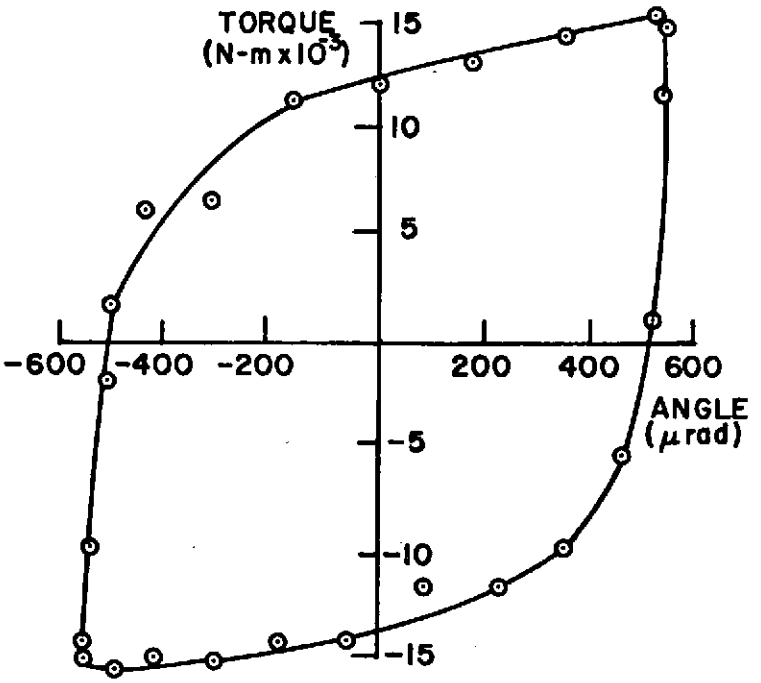

Fig. 51. LARGE AMPLITUDE, LOW-FREQUENCY BEARING TORQUE-DISPLACEMENT RELATIONSHIP.

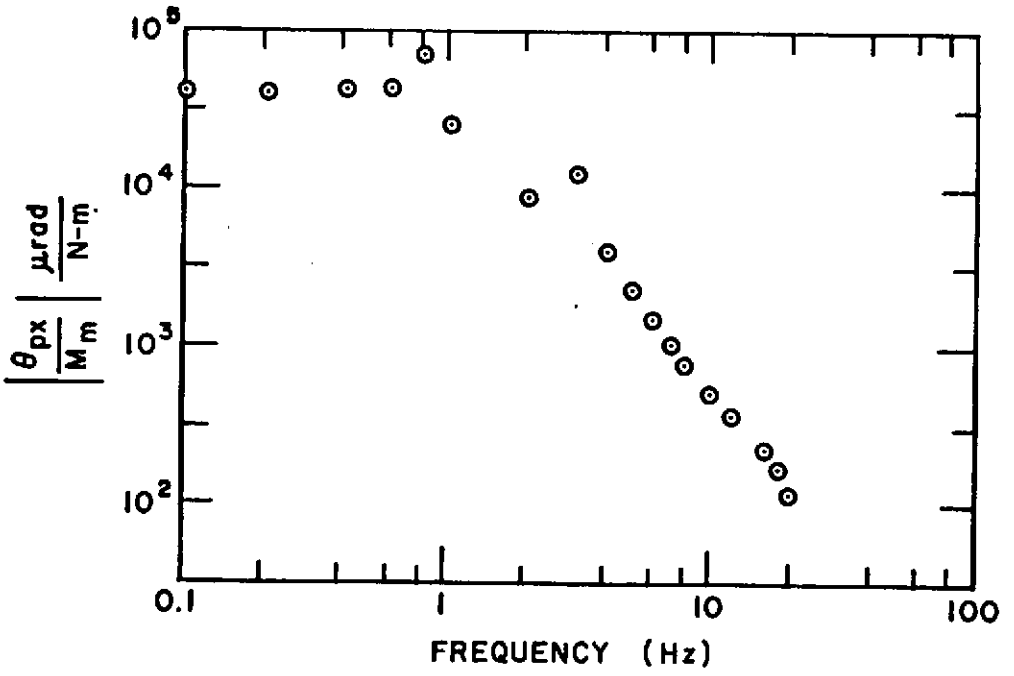

Fig. 52. FREQUENCY DEPENDENCE OF RESPONSE OF PLATFORM GIMBAL ANGLE TO MOTOR TORQUE.

The ratio of large amplitude motion to the peak applied torque taken at different frequencies, plotted in Fig. 52, is typical of a spring-mass system. However, the constant ratio at low frequencies can also be explained by coulomb friction. The ratio is amplitude dependent and not frequency dependent. At high frequencies where the inertia of the gimbal dominates, the ratio decreases as the square of frequency. Signals recorded in the transition region between 1 and 3 Hz were erratic in form, with time histories a combination of those observed at both low and high frequencies.

Two other low frequency torque-angle cross plots were obtained: one at moderate amplitude, the other at very low amplitude, Fig. 53 and Fig. 54. In both plots the overall behavior has changed from primarily hysteresis to one better described as a spring. Hysteresis is still present, but to a much less extent. Data obtained at very low amplitude were heavily corrupted by noise and jitter, and some visual averaging was necessary to read the values plotted. Results in this case were consistent, however, as were those at all amplitude levels.

2. Related Experiments

The behavior just described can be attributed to the platform gimbalbearings. Similar results have been obtained in tests conducted by Aerospace Corporation [D1] and Ball Brother Research Corporation (BBRC) [C7] under different conditions and with larger ball bearings. Aerospace considered three spherical bearings on a flat surface loaded by another plate. Dynamical response to small displacements was observed. BBRC developed a fixture in which the outer bearing race is attached to a worn wheel driven by a geared dc motor. Displacement of the inner race is measured by a linear variable differential transformer (LVDT). Variable bearing preloads can be established by suspending weights from the inner race. The inner race is driven by a precision dc motor. With the outer race fixed, calibrated torques can be applied by the precision motor and the inner race displacement recorded to obtain static friction measurements. Alternatively, running friction is measured with the outer race driven at a known rate and the LVDT output fed back to the motor through servo electronics to hold the inner race at null. The motor torque

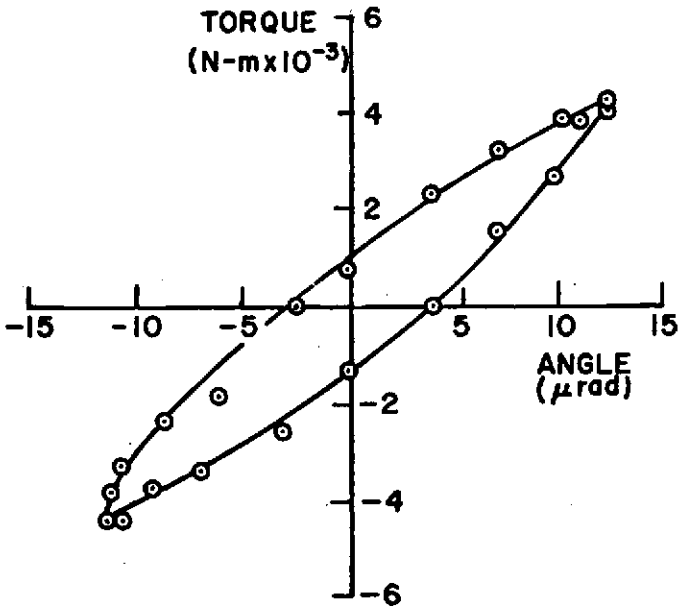

Fig. 53. MEDIUM AMPLITUDE BEARING TORQUE-DISPLACEMENT RELATIONSHIP.

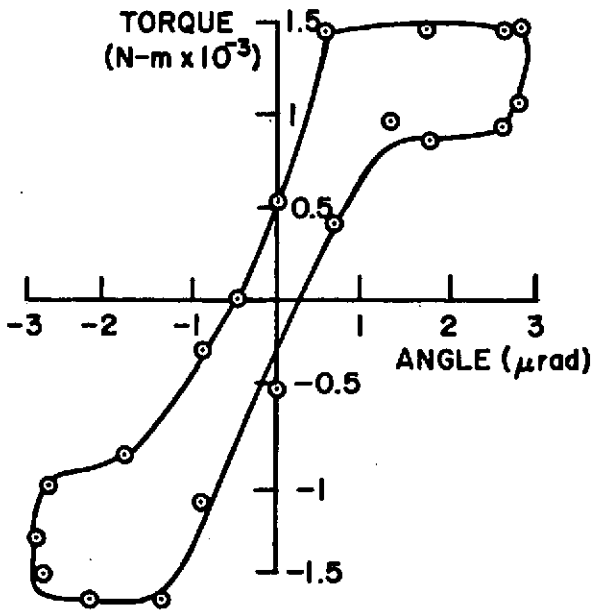

Fig. 54. SMALL AMPLITUDE BEARING TORQUE-DISPLACEMENT RELATIONSHIP.

required is then just equal to the friction.

Primary results of the BBRC tests were:

1. Displacement is proportional to torque at low torque levels.

2. The bearings do not completely return to their original position after torque is applied and then removed. This is indicative of losses due to coulomb friction.

3. Displacement increases indefinitely with time above a certain minimum torque level.

4. The minimum breakaway torque level increases with increasing preload.

3. Physical Interpretation

Dahl [D1] has developed a solid (or coulomb) friction model which has been used in a simulation to predict bearing behavior accurately. A summary of Dahl's physical explanation of bearing behavior is given below.

Bonds are formed between the bearings and their races, with the strength of the bond increasing with preload. As torque is applied, the bearings tend to rotate, placing the bonds in tension in the rear contact area and in compression in the leading contact area. Figure 55 illustrates this concept.

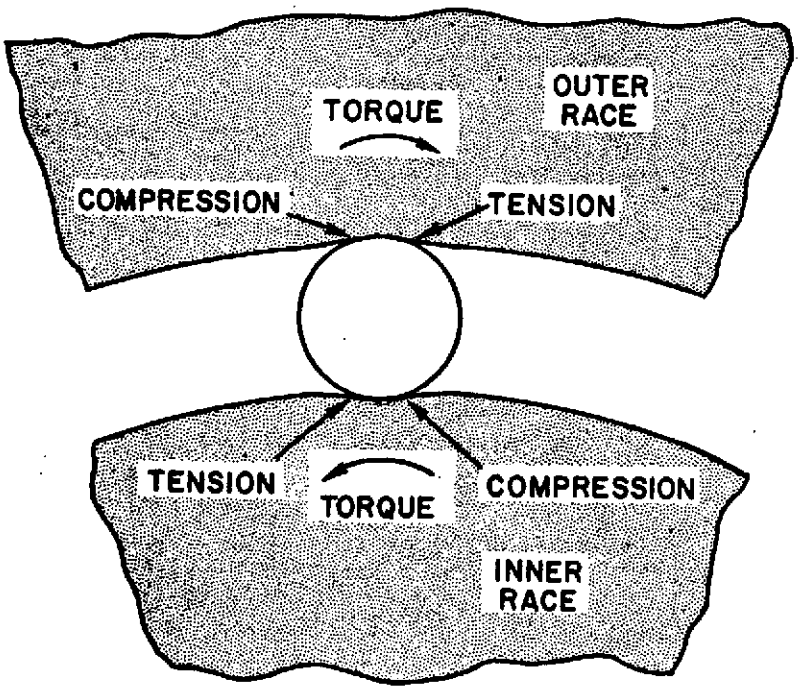

Fig. 55. BEARING STRESSES UNDER APPLIED TORQUE.

For sufficiently low torque levels, the contact stresses are proportional to displacement and to the applied torque. As torque is increased, permanent deformation of the interface first occurs, followed at higher levels by rupturing of the trailing edge of the contact area. Depending on geometry and surface properties, at some point the maximum restoring torque of the bearing is reached. Further increases in torque tend to accelerate the bearing.

4. Mathematical Model

In developing a mathematical model of rolling friction, Dahl first expressed the friction as the solution of the differential equation

$$\frac{dT}{dt} = \frac{dT}{d\theta}\,\dot{\theta} \tag{5.1}$$

Therefore, with known initial conditions, and a model of the relationship between torque and angular displacement, $dT/d\theta$, the frictional torque can be specified. Based on data obtained in the Aerospace study discussed above, a model was postulated,

$$\frac{dT}{d\theta} = \eta(T-T_o)^2 \qquad (\dot{\theta} > 0) \tag{5.2a}$$

$$\frac{dT}{d\theta} = \eta(T+T_o)^2 \qquad (\dot{\theta} < 0) \tag{5.2b}$$

where η is a constant, and T_o is the maximum frictional torque that can be produced (running friction). Excellent agreement between computed and experimental values of friction was obtained by employing this square-law model in a computer simulation.

To compare the model with the results obtained from the Fixed Base Simulator, (5.2a) and (5.2b) are solved:

$$\theta + c_1 = \frac{1}{\eta T_o(1-T/T_o)} \qquad (\dot{\theta} > 0) \tag{5.3a}$$

$$\theta + c_2 = \frac{-1}{\eta T_o (1+T/T_o)} \qquad (\dot{\theta} < 0) \qquad (5.3b)$$

where c_1 and c_2 are constants.

For small motion, $T \ll T_o$, which starts at $\theta = 0$ and $T = 0$, both Eqs. (5.3a) and (5.3b) can be expanded to yield, approximately,

$$T = \eta T_o^2 \theta \ .$$

This relationship is characteristic of a spring with elastic coefficient, ηT_o^2. For large motion, $\theta \gg \frac{1}{\eta T_o}$, the magnitude of friction approaches the constant value T_o, characteristic of coulomb friction.

Equations (5.3), normalized as discussed subsequently, are plotted in Fig. 56. The angle is varied sinusoidally so that the model plots can be compared with the experimental frictional torque data of Figs. 51, 53, and 54. Several amplitudes of motion are displayed to show the strong amplitude dependence of the frictional torque. The location of the origin is not of interest in displaying the amplitude dependence, so the constants of integration, c_1 and c_2, were selected to keep the figure centered.

The two constants and the maximum frictional torque, T_m, developed for any particular amplitude, θ_o, can be found by simultaneous solution of the three equations

$$-\theta_o + c_1 = \frac{1}{\eta T_o \left[1 - \left(\frac{-T_m}{T_o}\right)\right]} \qquad (5.4a)$$

$$\theta_o + c_1 = \frac{1}{\eta T_o \left[1 - \frac{T_m}{T_o}\right]} \qquad (5.4b)$$

$$-\theta_o + c_2 = \frac{1}{\eta T_o \left[1 + \left(\frac{-T_m}{T_o}\right)\right]} \qquad (5.4c)$$

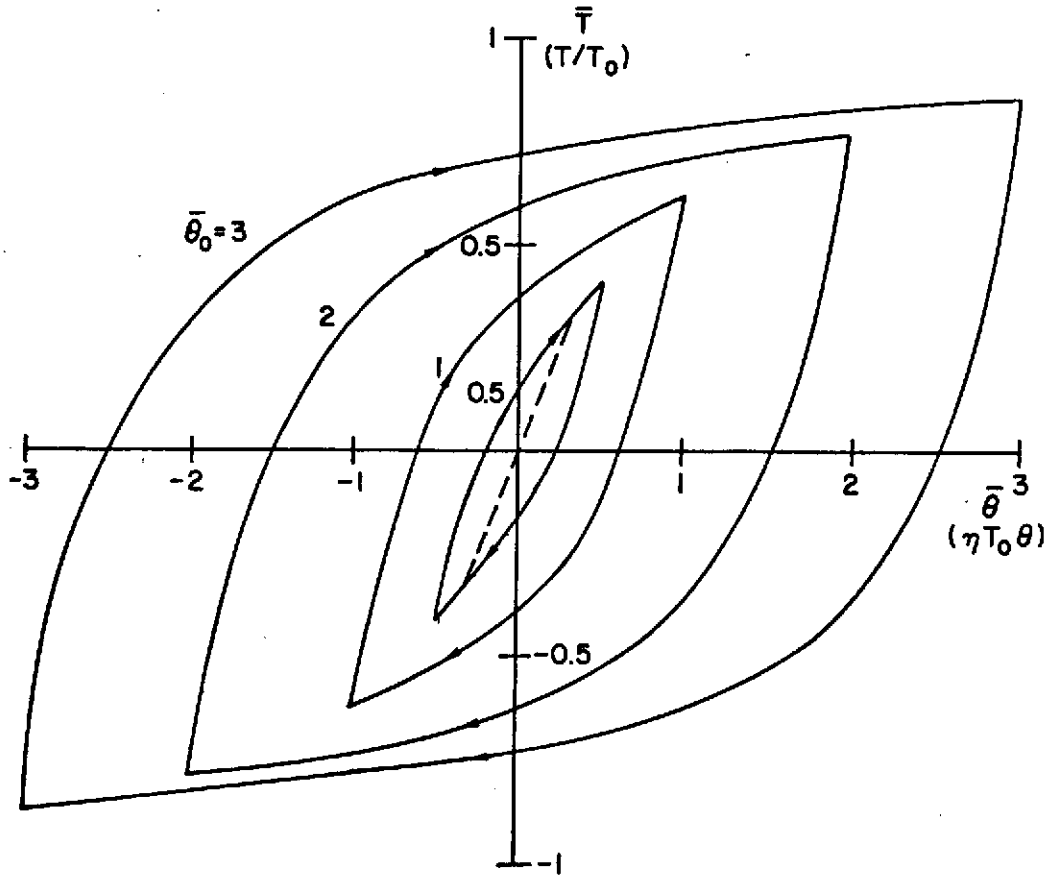

Fig. 56. SQUARE-LAW MODEL RELATING BEARING FRICTION TORQUE TO ROTATIONAL DISPLACEMENT.

The solutions are

$$\frac{T_m}{T_o} = \frac{1}{2\eta T_o \theta_o}\left[\sqrt{1 + (2\eta_o T_o \theta_o)^2} - 1\right] \tag{5.5a}$$

$$c_1 = \frac{2}{\eta T_o\left[1 - \left(\frac{T_m}{T_o}\right)^2\right]} \tag{5.5b}$$

$$c_2 = -c_1 \tag{5.5c}$$

It is convenient to normalize the angle with respect to the non-dimensinal parameter ηT_o; i.e.

$$\bar{\theta} = \eta T_o \theta \tag{5.6a}$$

$$\bar{\theta}_o = \eta T_o \theta_o \ , \tag{5.6b}$$

and to normalize the frictional torque with respect to the maximum possible or running torque T_o;

$$\bar{T} = \frac{T}{T_o} \tag{5.7a}$$

$$\bar{T}_m = \frac{T_m}{T_o} \tag{5.7b}$$

This particular normalization does not affect the shape of Figure 56. The normalized solutions to Eqs. (5.3a) and (5.3b) then become

$$\bar{T} = \frac{\bar{T}_m^2 + (1-\bar{T}_m^2)\bar{\theta}}{1 + (1-\bar{T}_m^2)\bar{\theta}} \qquad \dot{\bar{\theta}} > 0 \tag{5.8a}$$

$$\bar{T} = -\frac{\bar{T}_m^2 - (1-\bar{T}_m^2)\bar{\theta}}{1 - (1-\bar{T}_m^2)\bar{\theta}} \qquad \dot{\bar{\theta}} < 0 \tag{5.8b}$$

where

$$\bar{T}_m = \frac{1}{2\bar{\theta}_o}\left[\sqrt{1 + 4\bar{\theta}_o^2} - 1\right] \tag{5.9}$$

The basic parameters determined by fitting the model to the experimental data of Figs. 51, 53, and 54, are

$$T_o = 0.016 \text{ N-m}$$

$$\eta = 1.6 \times 10^6 \text{ (N-m)}^{-1}$$

5. Describing Function

A sinusoidal input describing function [G2] for the nonlinear torque has been derived from Dahl's model. Using the symmetry indicated in Fig. 56, the in-phase and out-of-phase components of the describing functions are calculated from

$$\bar{T}_D \cos \phi = \frac{2}{\pi}\int_{\pi}^{2\pi} \frac{\bar{T}_m^2 + (1-\bar{T}_m^2)\bar{\theta}_o \cos \psi}{1 + (1-\bar{T}_m^2)\bar{\theta}_o \cos \psi} \cos \psi \, d\psi \tag{5.10}$$

and

$$\bar{T}_o \sin \varphi = \frac{2}{\pi}\int_{\pi}^{2\pi} \frac{\bar{T}_m^2 + (1-\bar{T}_m^2)\bar{\theta}_o \sin \psi}{1 + (1-\bar{T}_m^2)\bar{\theta}_o \sin \psi} \sin \psi \, d\psi \tag{5.11}$$

where $\bar{T}_D = T_D/T_o$ is the amplitude, and φ is the phase angle of the describing function. Straightforward evaluation of (5.10) and (5.11) leads to

$$\frac{\bar{T}_D}{\bar{\theta}_o} e^{j\phi} = \frac{1}{\bar{\theta}_o}\left\{\frac{2}{\bar{\theta}_o}\left[\frac{1}{\sqrt{1 - \left[(1-\bar{T}_m)^2 \bar{\theta}_o\right]}} - 1\right] + j\left[\frac{4}{\pi} - \frac{2}{\pi\bar{\theta}_o} \ell n\left(\frac{1 + (1-\bar{T}_m^2)\bar{\theta}_o}{1 - (1-\bar{T}_m^2)\bar{\theta}_o}\right)\right]\right\} \tag{5.12}$$

This describing function is displayed in Fig. 57.

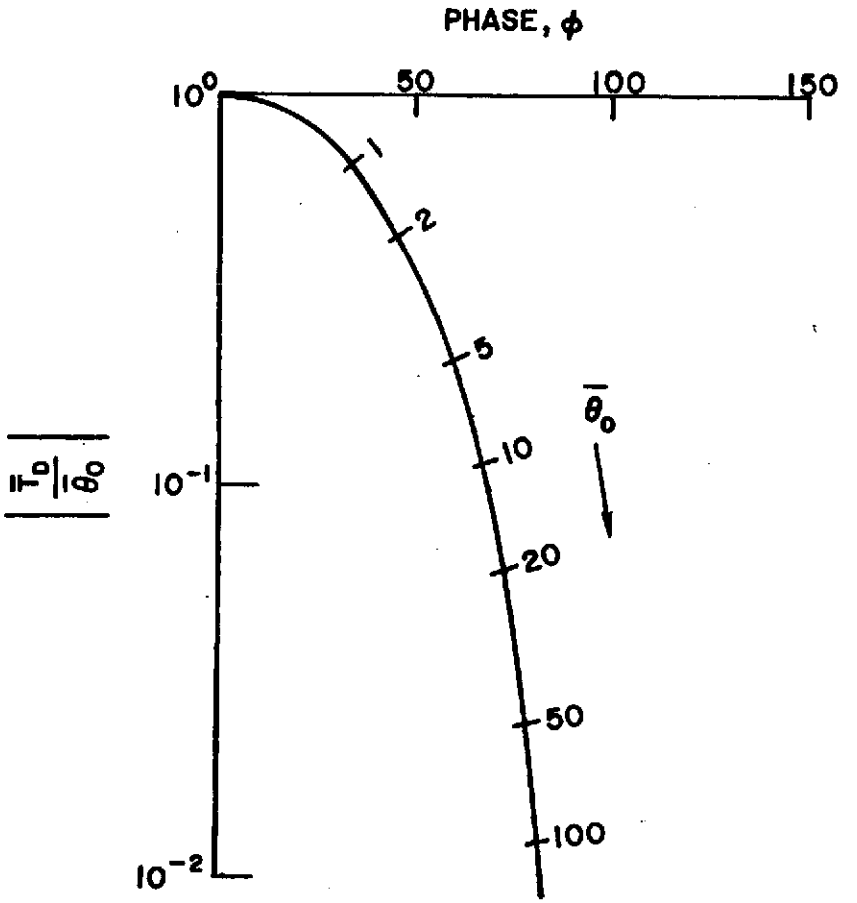

Fig. 57. SINUSOIDAL INPUT DESCRIBING FUNCTION OF A SQUARE-LAW BEARING FRICTION MODEL.

For $\bar{\theta}_o \ll 1$, (5.12) can be simplified to

$$\frac{\bar{T}_D}{\bar{\theta}_o} e^{j\phi} \cong 1 \qquad \text{(spring)}$$

Likewise, for $\bar{\theta}_o \gg 1$,

$$\frac{\bar{T}_D}{\bar{\theta}_o} e^{j\phi} \cong j \frac{4}{\pi\bar{\theta}_o} \qquad \text{(coulomb)}$$

Chapter VI
CONCLUSION

A. Summary

Analyzing the signals from precise orientation sensors using modern digital spectral techniques is an effective means of identifying error sources and modeling their effects. However, there are numerous considerations in converting raw spectral information into meaningful interpretations of instrument errors. The dynamical behavior of the system in which the sensors are operating can have a profound effect on the output spectra of the instruments. To interpret experimental results properly, it is essential to have an accurate model of the system, in terms of its natural behavior and disturbance environment. Operating the sensors as part of a closed stabilization loop requires that the paths through which instrument errors propagate before being measured be well understood.

Since instrument errors are created by both internal sources and by system disturbances, it is necessary to separate the sources to identify the inherent instrument errors. The coherence function was demonstrated to be useful in accomplishing this task. A further useful approach is to make plausible arguments about the disturbance spectra and compare the experimental results with those obtained by analysis of a system model. This technique was successful in discovering the presence of the unanticipated elastic restraint properties of the simulator platform gimbal bearings.

Once discovered, further direct measurements of the bearing behavior were made. Elastic restraint coefficients of approximately 400 N-m/rad were observed, with coulomb friction becoming dominant at rotation displacements greater than 100 μrad. The relationship between frictional torque and angular motion agreed well with a square-law model of rolling friction discussed in Chapter V. The model predicts spring-like behavior with low amplitude motion and coulomb friction at large amplitudes. A sinusoidal-input describing function of the frictional torque, derived from the model, indicates the strong amplitude

dependence and frequency independence of bearing friction.

The pointing accuracy of the Fixed Base Simulator, developed as an analog to the proposed laboratory test of the Stanford Relativity Experiment satellite, is limited primarily by the noise in the orientation sensors. Other disturbances are negligible by comparison. The observed spectra of the sensors operating as integral parts of the stabilization loops can be attributed to sensor noise as modified by the loop dynamics. Platform pointing errors in the band 0.4 to 200 Hz with the primary autocollimator serving as the controlling sensor are approximately 1.6 and 3.6 μrad rms for the X and Y axes, respectively.

Noise from the Atlas missile gyros is characterized by numerous discrete frequency components on top of a generally white noise background. The discrete power spikes are peculiar to ball bearing gyros. The discrete components contribute over 85 percent of the overall gyro rms noise level of 6.2 μrad in the X axis, and 12.4 μrad in the Y axis. Several of the discrete components arise from sources related to the wheel spin frequency. In particular, a strong 71 Hz component appears to be related to the rotation frequency of the rotor spin bearing retainers.

The primary autocollimator noise spectrum is essentially white, and is due to shot noise created in the photodetector. The rms noise equivalent angle in the frequency band 0.1 to 100 Hz is 0.5 μrad. In contrast to the white primary autocollimator noise, the azimuth reference autocollimator has primarily 1/f noise. The rms noise equivalent angle is 2.8 μrad.

B. Application to Relativity Experiment

It is likely that a test of the actual relativity experiment sensors will require active pointing of the experiment package to keep signals within the range of intended operation. Consequently, spectra obtained will be dependent on pointing loop dynamics, and proper interpretation will require a system model similar to the one developed for the Fixed Base Simulator. The same computer programs developed to compute the spectral functions of simulator signals will be directly applicable to

the new system. The present data acquisition system is cumbersome, and it is recommended that a direct digital acquisition system be considered.

With the increased precision of the relativity sensors, it is likely that base motion will contribute a much larger portion of the sensor output signals. The relative amount of base motion can be determined by using the coherence function

The large spikes observed in the simulator gyro spectra, caused by bearing irregularities, are not likely to be present in the relativity gyro signals. However, sinusoidal noise or systematic components produced either in the pickoff or the rotor will be detected. Care should be taken in determining the amplitude of such components from spectral estimates due to the effects of data windows, prewhitening, and other computational considerations discussed in Appendix A.

Appendix A

COMPUTING SPECTRAL FUNCTIONS

Straightforward application of the formulae of Chapter IV to estimate discrete spectral functions is generally neither efficient nor reliable in producing useful results. Several considerations must be made to minimize the computation required and to account for the finite length, relative power distribution, and randomness of the data. These considerations are outlined below. Three references [B5], [B2], and [K2] in particular are recommended for further reading in interpreting spectral plots and in avoiding numerous computational pitfalls.

1. Fast Fourier Transform

An initial inspection of the discrete Fourier transform formula (4.5) indicates that the number of computer operations required is proportional to N^2. However, as discussed in [C3] several algorithms have been developed which require a number proportional to $N \log_2 N$. The ratio of the number of operations or equivalently of the time required is $\log_2 N/N$. Dramatic reductions in computation time can therefore be achieved when N is large. As an example, when $N = 1024$, the new algorithms require only about 1/100 the time.

The most widely known and used algorithm is the Fast Fourier Transform (FFT) developed by Cooley and Tukey [C4]. A considerable body of literature exists on the FFT, including the entire June 1967 special issue of the IEEE Transactions of Audio and Electroacoustics. As a consequence, a description of the algorithm will not be given here. Intuitive developments and explanations of the FFT are given in [B8], [G1], [D3], and [G3].

2. Leakage

A consequence of finiteness of data is the loss of frequency resolution in the spectral functions. Consider a continuous finite length signal $x(t)$. This signal can be viewed as an infinitely long process multiplied by a time function, called a data window, which has unit value

over the finite signal length and is zero elsewhere

$$x_f(t) = d(t)\ x(t)$$

where

$x(t)$ = infinitely long signal

$$d(t) = \begin{cases} 0 & t < 0 \\ 1 & 0 < t < T \\ 0 & t > T \end{cases}$$

$x_f(t)$ = finite length record

T = record length

The effect of this time multiplication is the equivalent in the frequency domain of convolving the Fourier transform of $x(t)$ with the Fourier transform of $d(t)$. The latter transform is called a spectral window. The spectral window association with the rectangular data window $d(t)$ is easily shown to be of the form $\sin(af)/(af)$ where a is a constant. Because of the convolution, spectral estimates at a point are spread over neighboring frequencies. Using the rectangular data window, the contribution of a signal component at frequency $f = f_n + \Delta f$ to the power spectral estimate at f_n falls off as $1/|\Delta f|^2$. Conversely, a signal at f_n affects neighboring estimates as $1/|\Delta f|^2$. This phenomenon is known as leakage and can seriously affect the validity of power spectrum estimates.

Leakage also occurs in transforming discrete signals. Here, however, a signal component exactly at one of the discrete frequencies of the Discrete Fourier Transform (DFT) does not affect the estimate at any other frequency. On the other hand, signal components not at a discrete frequency of the DFT display leakage just as in the continuous case. Since most of the signals of interest do not fall at discrete frequencies of the DFT, it is necessary to reduce the effects of leakage by applying a different data window which will cause leakage to fall off at a rate greater than $1/|\Delta f|^2$ without broadening the main lobe of the spectral window excessively.

Blackman and Tukey, in their comprehensive book on computation of power spectra [B5], analyze several different windows. Selections widely

used are the "Hanning" window

$$d_m(t) = \begin{cases} 0.5(1 - \cos 2\pi t/T) & 0 < t < T \\ 0 & \text{otherwise} \end{cases}$$

and the "Hamming" window

$$d_n(t) = \begin{cases} 0.54 - 0.46 \cos 2\pi t/T & 0 < t < T \\ 0 & \text{otherwise} \end{cases}$$

Both data windows yield a spectral window with a narrow main lobe and small (1% - 2%) side lobes. However, hanning results in leakage falling off as $1/|\Delta f|^6$, for $T\Delta f \gg 1$, whereas hamming results in leakage attenuation of only approximately $1/|\Delta f|^2$ for $T\Delta f \gg 1$. The advantage of hamming is that the highest spectral window side lobe is one third as high as that of the hanning window. For spectra which do not rapidly change with frequency, that is where leakage is not of major concern, the lower peak side lobes of the hamming window can be more desirable than the increased leakage rolloff obtained from hanning.

A third window, called the Bartlett window, is described by

$$d_b(t) = 1 - \frac{|t-T/2|}{T} \qquad 0 < t < T$$

$$= 0 \qquad \text{otherwise}$$

The main advantage of this window is the ease of computation, since it requires no trigonometric functions. Leakage falls off as $1/|\Delta f|^4$.

Choice of an appropriate data window depends upon the form of the power spectrum. It should be noted, however, that any of the above windows will work satisfactorily in most applications where the spectrum changes slowly with frequency.

Multiplying the data by a window decreases the power in the estimate. Therefore, to maintain the proper amplitude in the power spectrum

estimate, it is necessary to normalize the estimate by the mean of the squared window. That is

$$\hat{P}_{xx}(n) = \frac{\Delta f}{u}\left| \sum_{k=0}^{N-1} x(k)\ d(k)\ W^{nk} \right|^2$$

where

$$u = \frac{1}{N}\sum_{j=0}^{N-1} d^2(j)$$

3. Prewhitening

As a result of leakage, significant errors can be introduced in the estimate when power is concentrated at a particular frequency. For example, test data almost always has some very low frequency noise including DC. This noise may come from instrument and data acquisition equipment biases and drifts or from analog to digital converter offsets. Due to leakage, the true values of the power spectrum at the low frequencies may be completely overcome by the relatively large side lobes of the spectrum at or near DC. It is desirable, therefore, to remove large amounts of noise at particular frequencies before computing the power spectrum. This procedure is known as prewhitening, since the resulting spectrum is more nearly white.

The prewhitening technique used in analyzing the Fixed Base Simulator consists of fitting a straight line and/or a sine wave to the data using unweighted least squares. The resulting fits are then subtracted from the data, and the sample mean and variance of the residual data computed. Since bad data points sometimes occur, all points greater than 4σ, where σ is the sample standard deviation, are output and then set equal to the mean of the residual data. This effectively eliminates bad data without significantly affecting the power spectrum. If any points are found to exceed 4σ, the entire prewhitening procedure is repeated with the bad points eliminated.

4. Randomness

The effects of data randomness must also be considered in addition to the frequency distortion due to finite data and strong frequency components. In Chapter IV, it was pointed out that forming spectral estimates from increasing amounts of data does not necessarily improve the estimate. In other words, the estimate of the spectrum may not converge to the true value no matter how much data is processed.

Take, for example, the case where the spectrum of the signal is white; i.e., it is constant for all frequencies. The estimate of the power at zero frequency is from (4.17),

$$\hat{P}(0) = \frac{\Delta t}{N}\left|\sum_{k=0}^{N-1} x(k)\right|^2$$

The $x(k)$ are assumed independent and Gaussian with zero mean and variance σ^2. Let $\Delta t = 1$, for convenience. The expected value of the estimate is

$$E[\hat{P}(0)] = \frac{1}{N} E\left|\sum_{k=0}^{N-1} x(k)\right|^2 = \sigma^2$$

The variance of $P(0)$ is

$$\text{Var } P(0) = E[P(0) - E[P(0)]]^2$$

or

$$\text{Var } P(0) = \frac{1}{N^2} E\left|\sum_{k=0}^{N-1} x(k)\right|^4 - \sigma^4 .$$

Application of the moment generating function of a normal process yields

$$\text{Var } P(0) = 2\sigma^4$$

The ratio of the standard deviation of $P(0)$ to its expected value is, then,

$$\frac{\sqrt{\text{Var } P(0)}}{E[P(0)]} = \sqrt{2} \ .$$

In other words, the rms error in estimating the actual $P(0)$ is greater than the expected value by a factor of $\sqrt{2}$, independent of record length N. Obviously, means of reducing such large uncertainties in the power spectrum have to be employed.

Although many approaches to the problem of reducing statistical variability have been discussed [B5], [B4], and [R2], the one selected for use is that published by Welch [W2]. This technique divides the entire data record into shorter, possibly overlapping subrecords, applies a data window to reduce leakage, computes a power spectrum for each subrecord, and averages the results point by point. Another approach is to convolve the spectrum obtained from one record with a spectral window. The convolution effectively forms a weighted average of the spectral estimates near the frequency of interest. The smoothed results obtained are achieved in this manner by a corresponding loss in frequency resolution.

The approach of Welch was selected since it most efficiently uses all of the data and yields finer resolution than the frequency convolution method. Improved resolution results not because of properties of the data, but because better use could be made of the limited storage capability of the XDS Sigma-5 computer on which the computations were made. The maximum number of positive frequency values which can be computed at one time on the Sigma-5 is 2049. Therefore, if a sufficient number of spectra of subrecords are averaged to achieve statistical stability, the resolution is $f_s/2048$, where f_s is the sampling frequency. To achieve the same resolution using the frequency convolution method, a spectrum containing $M \times 2048$ points would have to be initially computed, where M is the number of subrecord spectra computed. This is because the resolution of the average-over-frequency method is reduced by a factor about equal to the number of spectral estimates averaged. Since the maximum length of spectrum is specified by computer constraints, the

resolution available using average-over-frequency methods is $M\Delta f$, where Δf is the resolution of the average-over-time method.

How averaging several spectral estimates improves stability can be analyzed by noting that the spectral estimates $P(n)$ are normally distributed for normally distributed noise data. The average of several $P(n)$ therefore has a chi-square probability distribution, where

$$k = \frac{2E^2 \ P(n)}{\text{Var } P(n)}$$

is the equivalent number of degrees of freedom. Averaging over M non-overlapping subrecords gives $k = 2M$, or expressed differently,

$$\text{Var } \hat{P}(n) = \frac{E^2 \ \hat{P}(n)}{M}$$

For example, averaging 25 independent spectral estimates will yield a value within 20% of the true value with 67% confidence. This relationship holds only for normally distributed noise, but can be used as a rule of thumb for other distributions. Using this expression a tradeoff between relative stability and computation time can be made.

5. Sampling

Since the power spectra are computed digitally, it is necessary to digitize analog test data. The FFT algorithm assumes that the data points are equally spaced in time, and so it is convenient to sample at a fixed frequency. The act of sampling, however, can make spectral estimates meaningless unless noise at frequencies greater than half the sampling frequency is first rejected.

It is well known that the power spectrum of an ideally sampled signal is

$$P^*(f) = P(f - kf_s)$$

where $P(f)$ is the power spectrum of the original continuous signal, and f_s is the sampling frequency. This implies that high frequency

noise in $P(f)$ can appear as low freqeuncy noise in the sampled spectrum $P^*(f)$. If, for example, the signal is white noise bandlimited at ten times the sampling frequency, the resulting sampled spectrum at low frequencies is ten times greater than the actual.

Distortion of this nature, which is known as aliasing, is not present when $P(f) = 0$, $|f| > f_s/2$. For then $P^*(f) = P(f)$, $-f_s/2 < f < f_s/2$. Passing the signal through a low-pass analog filter with bandwidth less than $f_s/2$ therefore effectively eliminates aliasing.

The three figures A.1, A.2 and A.3, demonstrate the effectiveness of filtering. A 10 Hz square wave from a low-frequency function generator was passed directly into an analog-to-digital converter (ADC) sampling at 409.6 Hz. Ideally, the power spectrum should be composed of all the odd harmonics of the fundamental frequency with amplitudes falling off as $1/f^2$. This can be seen in Fig. A.1 which is the spectrum of a computer generated 5.12 Hz square wave. In practice even harmonics and noise will appear due to non-ideal aspects of the ADC, function generator, and signal transmission. The power spectrum of the unfiltered sampled signal is shown in Fig. A.2. The original analog signal was then passed through a 100 Hz low-pass filter before analog-to-digital conversion. The resulting spectrum is shown in Fig. A.3. Comparison of Figs. A.2 and A.3 shows the extensiveness of aliasing present in Fig. A.2. Except for the small even harmonics, the spectrum in A.3 is nearly ideal up to 100 Hz.

6. Digital Filtering

Once a signal has been sampled, there is no way to remove aliasing except by resampling the analog signal either at a higher frequency or after low-pass filtering. However, a low-passed analog signal sampled at one frequency can be sampled at a lower rate by first eliminating higher frequencies in the digitized information using a low-pass digital filter. The sampling rate is reduced by skipping points or averaging several points of the digitally filtered signal. Aliasing can still be introduced if the new sampling rate is less than twice the highest frequency present in the digitally filtered signal. Digital filtering is especially useful in obtaining low-frequency spectral information when the original analog signal is sampled at a high frequency.

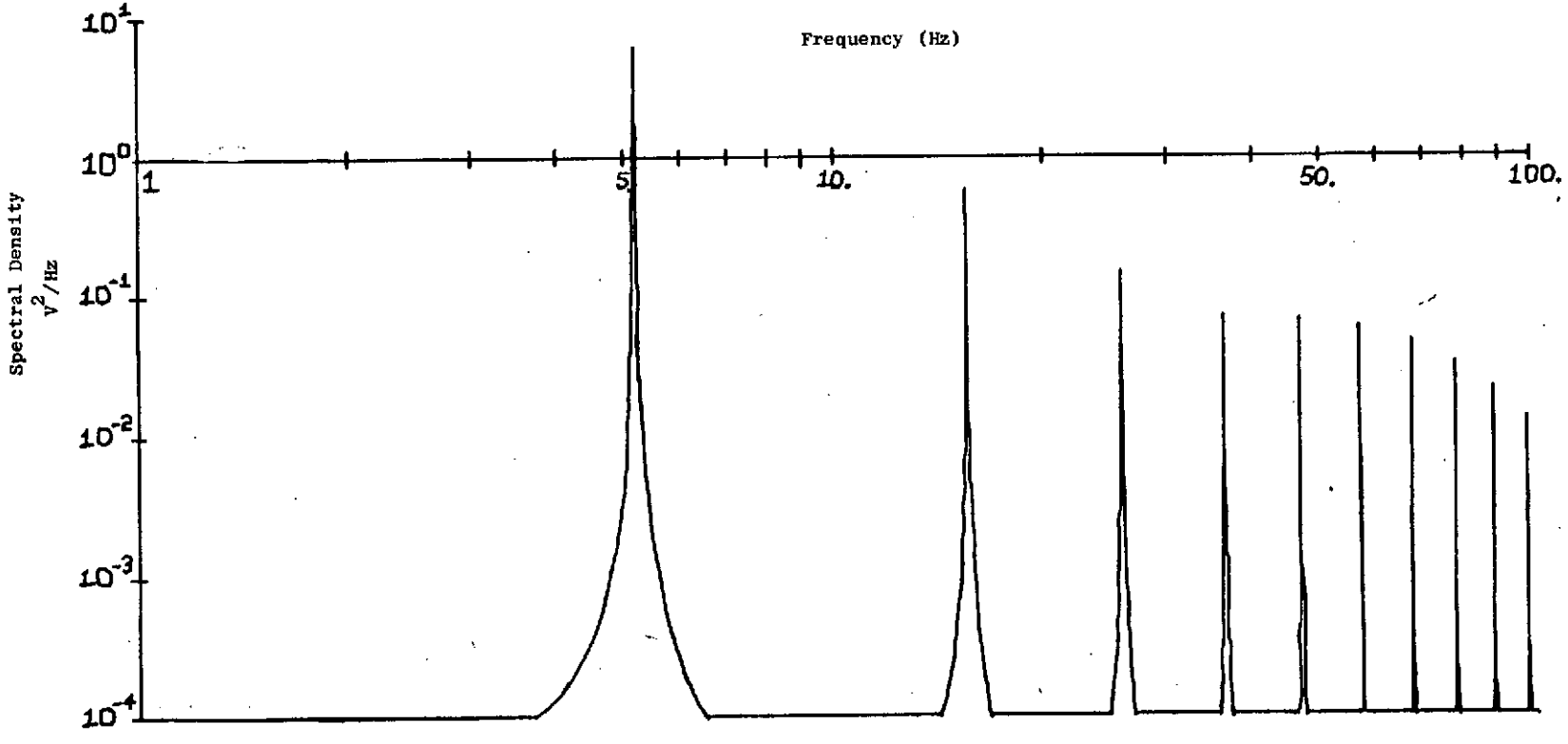

Fig. A.1. POWER SPECTRUM OF A COMPUTER GENERATED 5.12 Hz SQUARE WAVE.

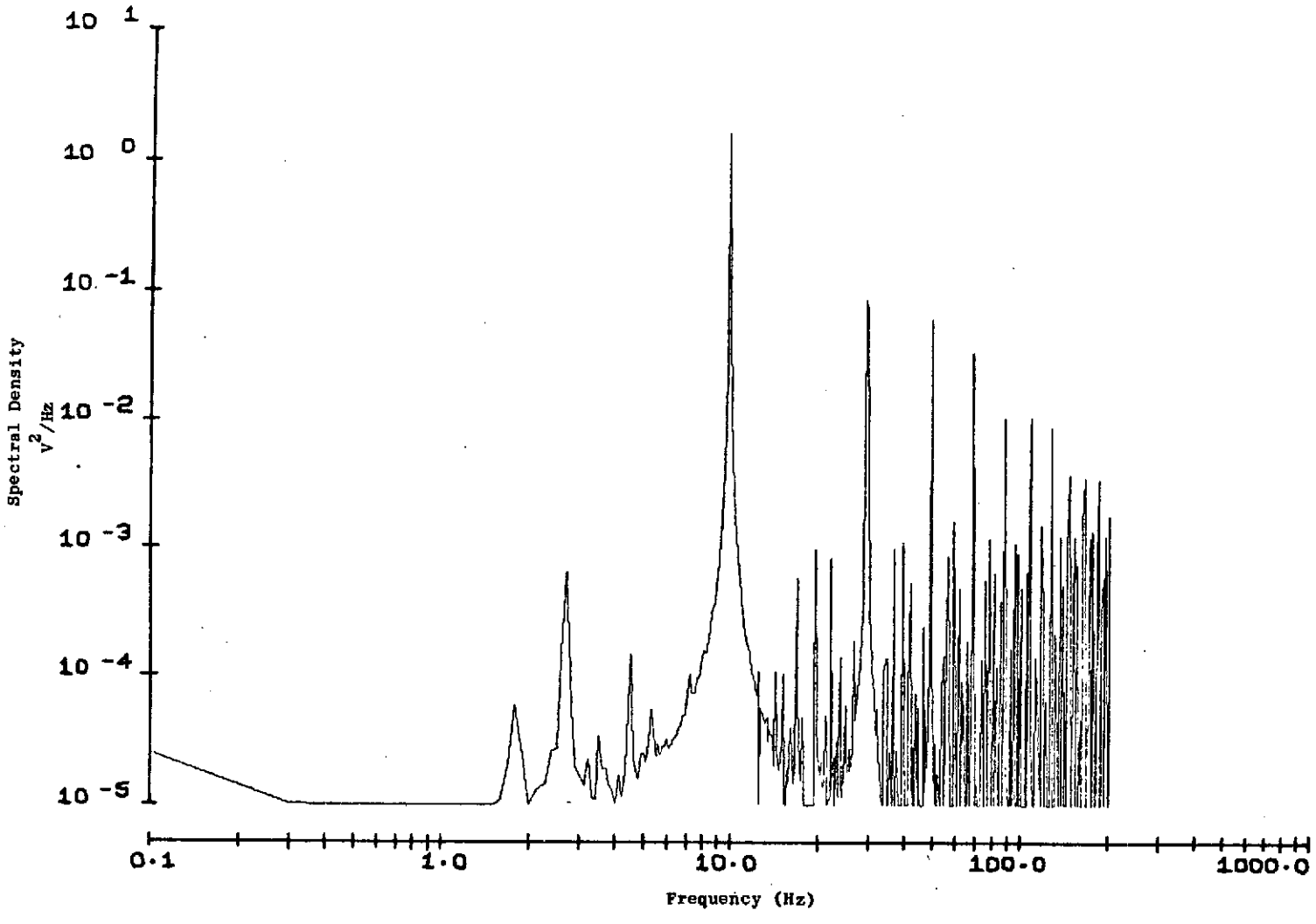

Fig. A.2. POWER SPECTRUM OF AN UNFILTERED SAMPLED 10 Hz SQUARE WAVE. The aliased spectrum appears folded about the 204.8 half-sampling frequency.

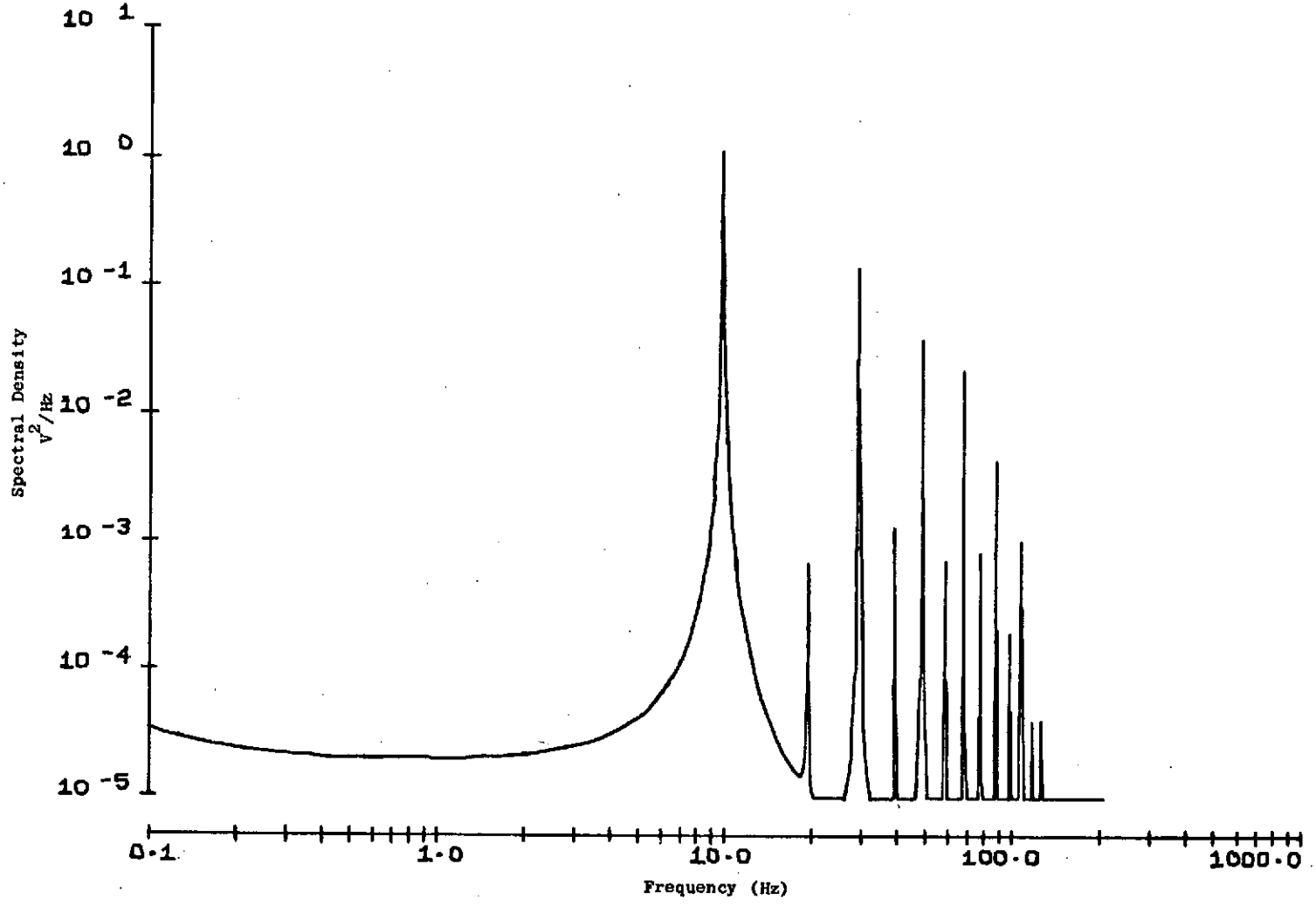

Fig. A.3. POWER SPECTRUM OF A SAMPLED 10 Hz SQUARE WAVE FILTERED ABOVE 100 Hz. Aliasing is substantially reduced by the filter.

7. Quantization

Another important aspect of sampling is the necessity of quantizing the data so that it can be represented as a digital word. In the A/D conversion process, the voltage level of the signal must be represented by one of 2^N possible numbers, where N is the number of bits per word. A roundoff error is therefore introduced into the digital data. Widrow [W3] has shown that this quantization error can be modeled as additive white noise, uniformly distributed between $-q/2$ and $q/2$ with zero mean and variance $q^2/12$, where q is the quantization level. Using this model, the contribution of quantization error to the power spectrum is

$$P(n) = q^2 \Delta t/12$$

Quantization error can be minimized by scaling the maximum signal level to the largest value which can be digitized.

8. Graphical Representation

A log-log plot of the spectral functions has been found to be the most useful presentation of the computed results. Most signal analysts are familiar with this form and can readily interpret the slopes of straight line segments and break frequencies in terms of their underlying physical mechanisms. The logarithmic scales also allow a wider range of data to be presented on the same plot.

One effect of logarithmic frequency scaling is the graphical compression of the equally spaced spectral estimates with increasing frequency. Since equal frequency resolution is normally not required across the entire spectrum, it has been suggested [K2] that only the average of several points in a frequency band be displayed, with more points averaged with increasing frequency. One convenient way to maintain an approximately constant fractional frequency resolution is to break up the spectrum into bands each twice as large as the next lower band and display only the average of the points in each band. Since more points are averaged at higher frequencies, greater smoothness results. A negative aspect is that a spike in the spectrum due to a discrete component can be lost due to the averaging.

As a compromise, the data is averaged as above, but any points greater than three times the average value are also plotted.

Page intentionally left blank

Appendix B

SCHEMATIC DIAGRAMS OF THE FIXED BASE SIMULATOR

Schematics of the electronic circuits developed for the Fixed Base Simulator are included in the following pages. Indicated card numbers correspond to those described in Chapter II and to the gyro and autocollimator preamplifiers mounted on the platform. Diagrams of the mode-switching relays and the meter panel are also included.

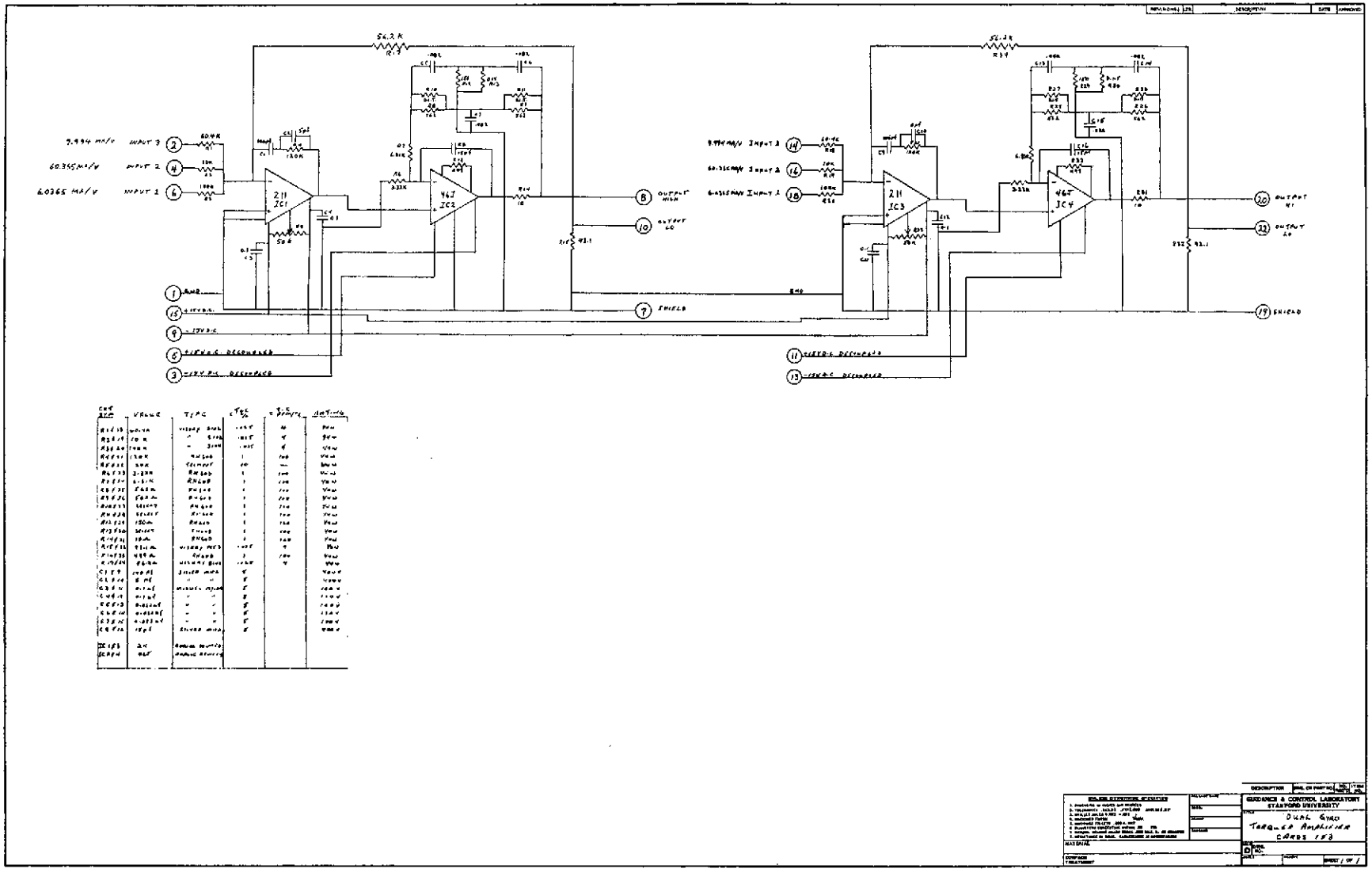

CARDS 1 & 3: GYRO TORQUER AMPLIFIER

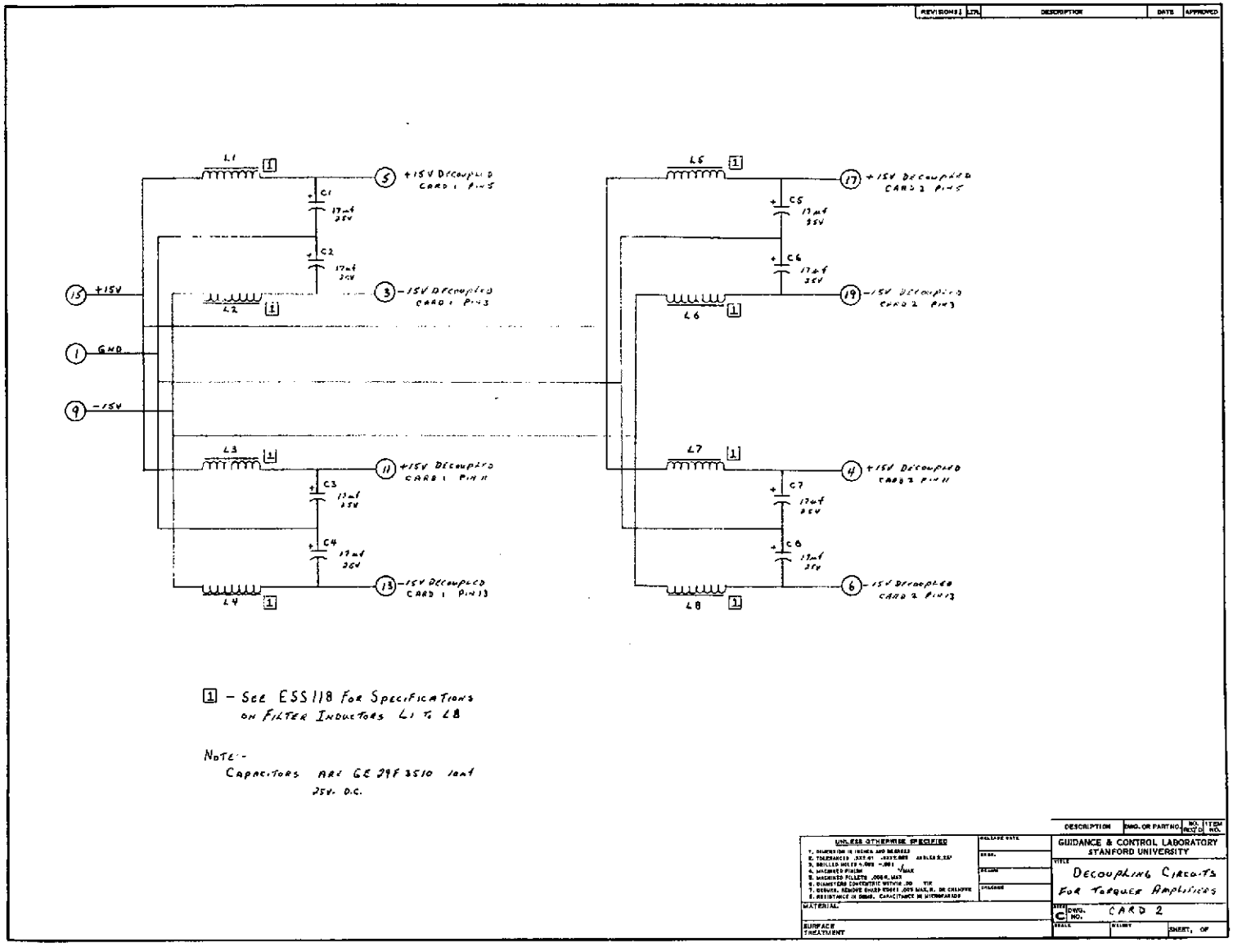

CARD 2: TORQUER AMPLIFIER DECOUPLING NETWORK

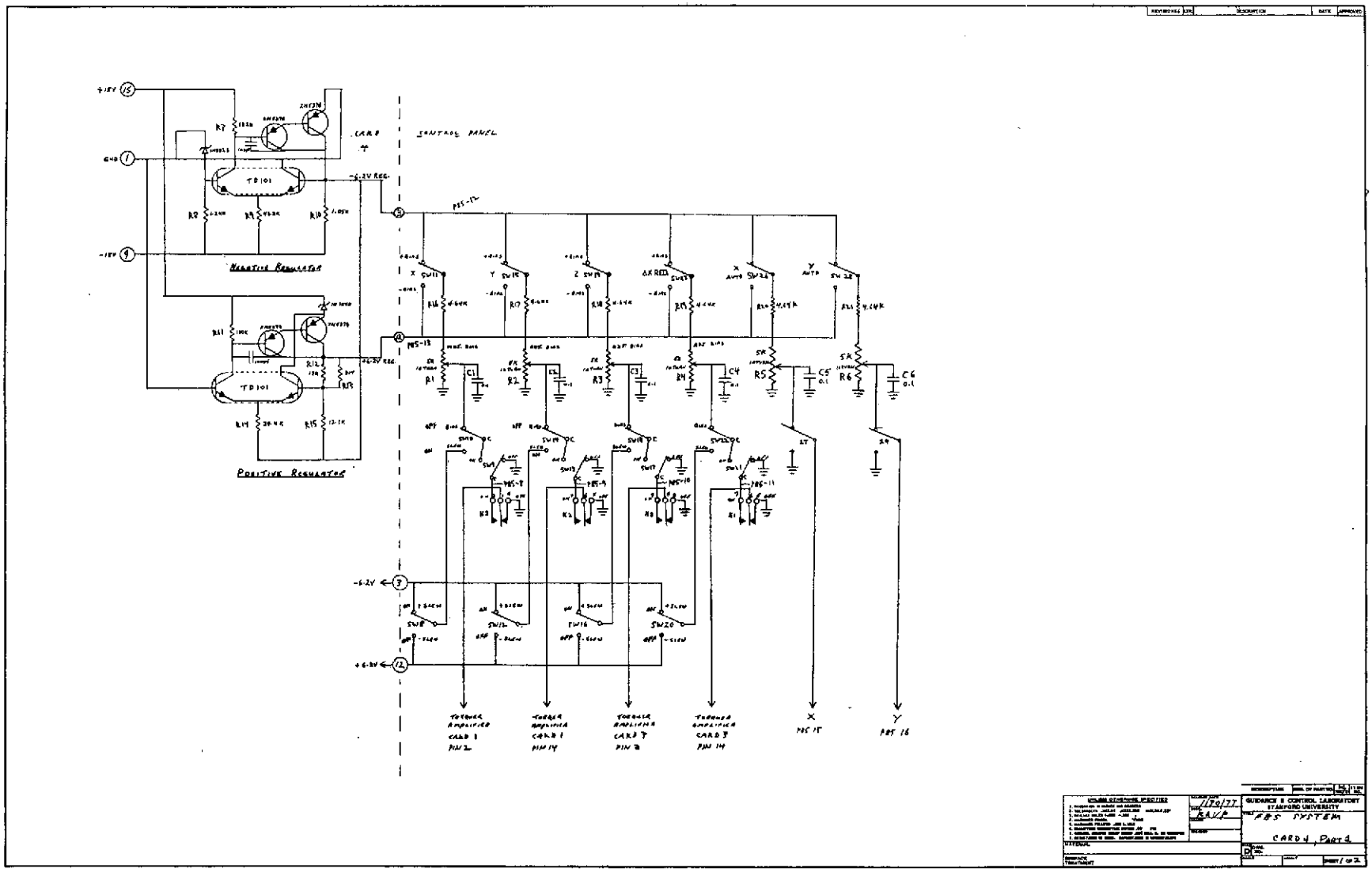

CARD 4: ± 6.2 VDC REGULATOR AND SENSOR BIASING NETWORK

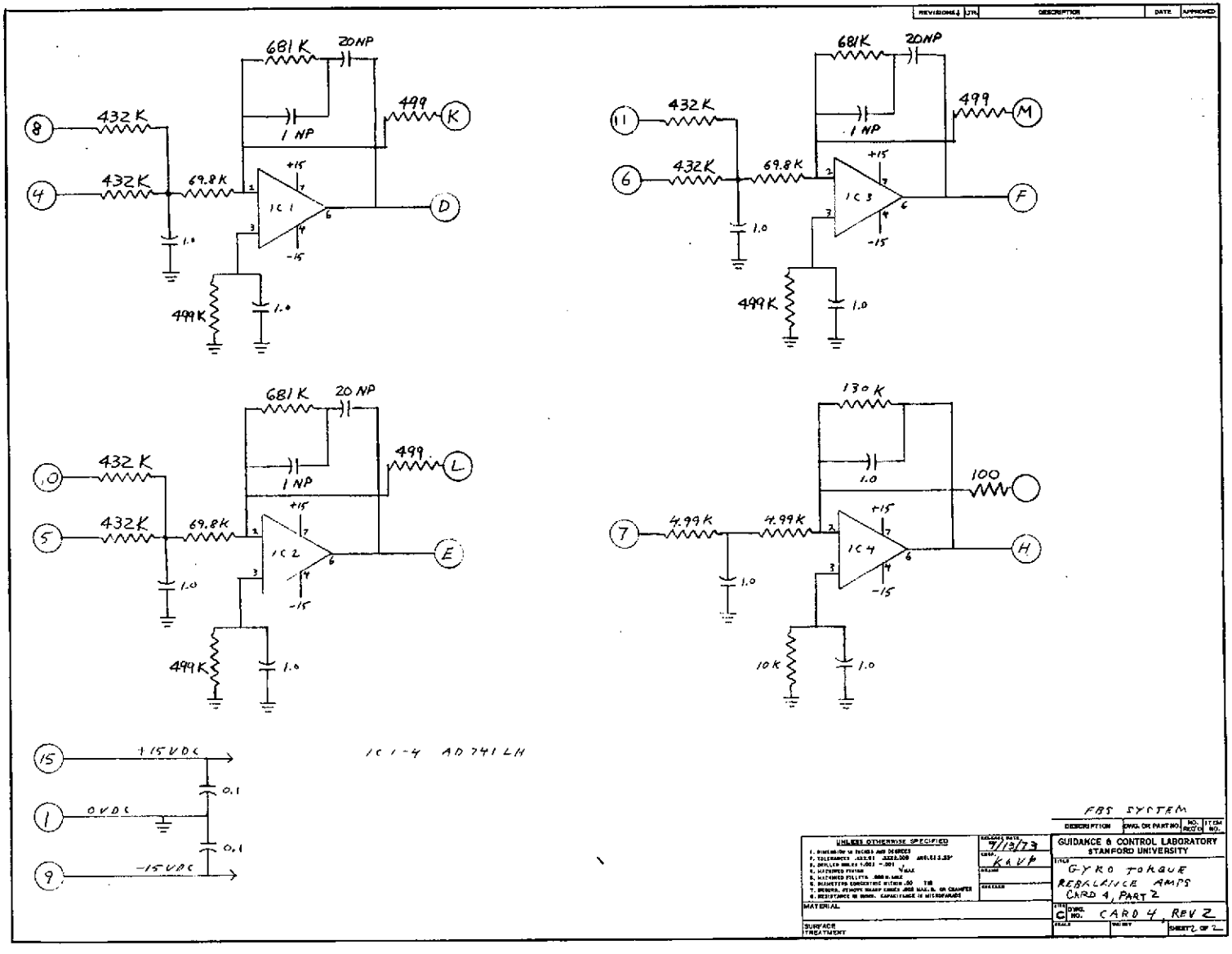

CARD 4: GYRO TORQUE REBALANCE (CAGING) AMPLIFIERS

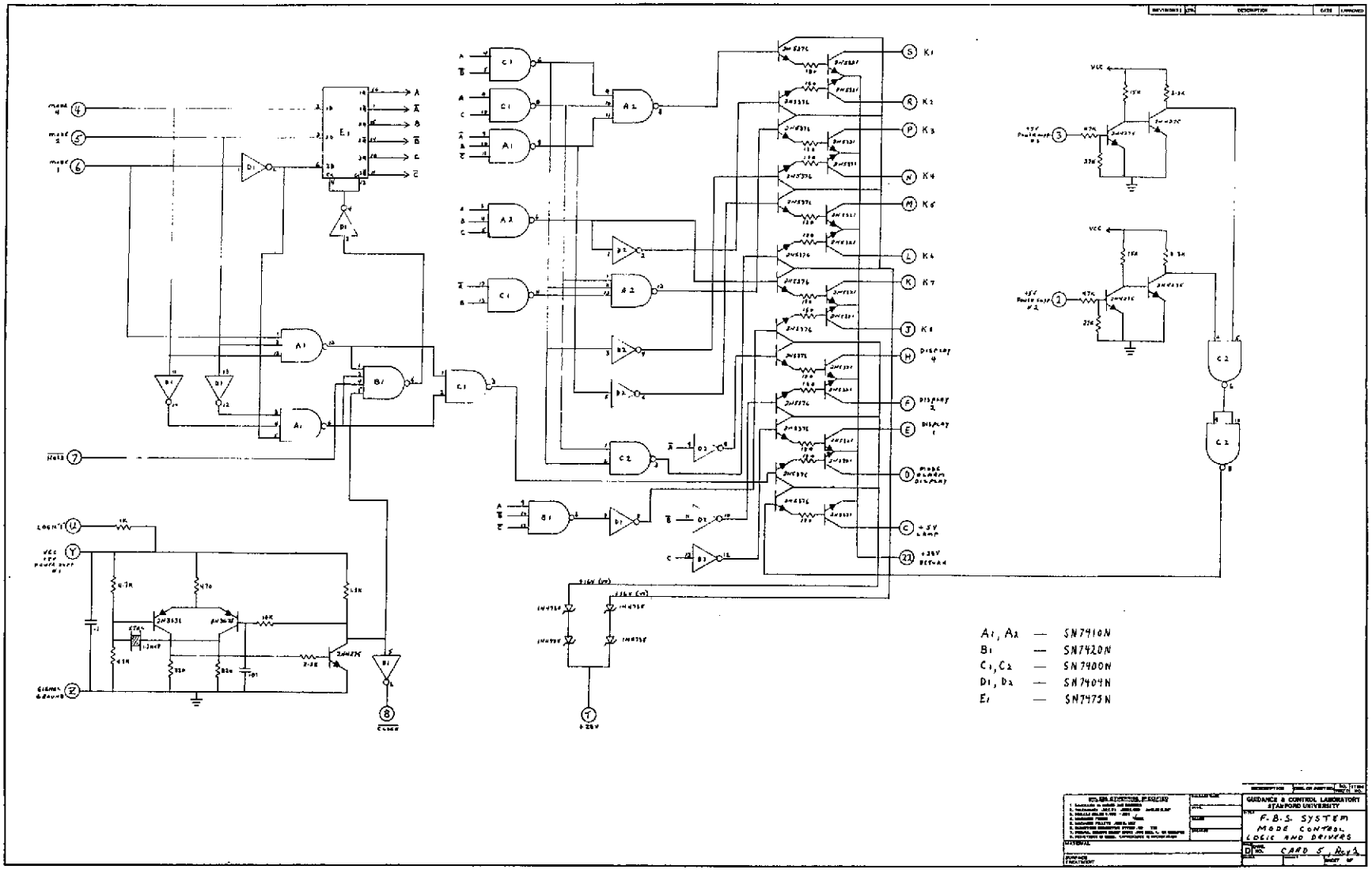

CARD 5: MODE CONTROL LOGIC AND DRIVERS

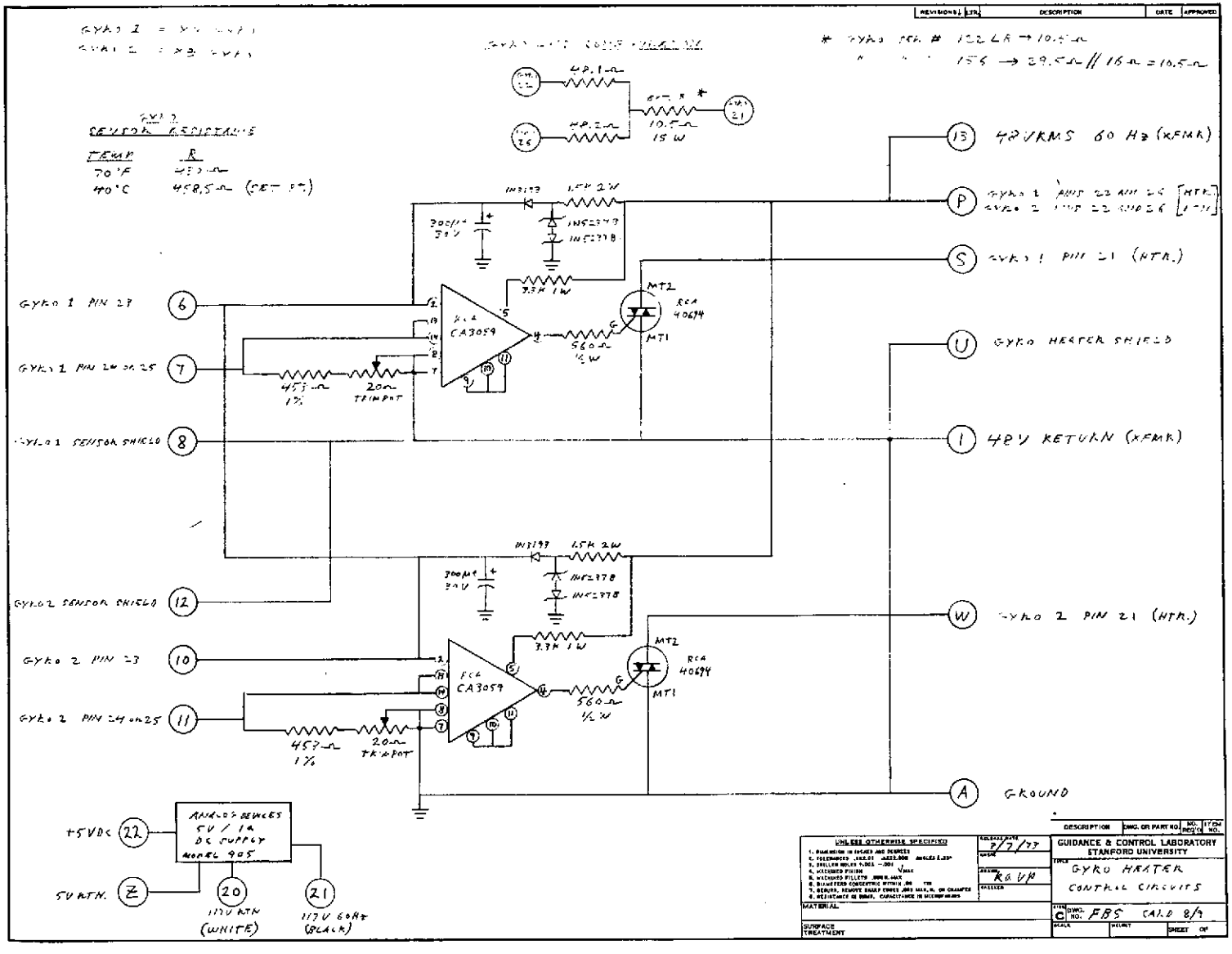

CARD 7: GYRO HEATER CONTROL

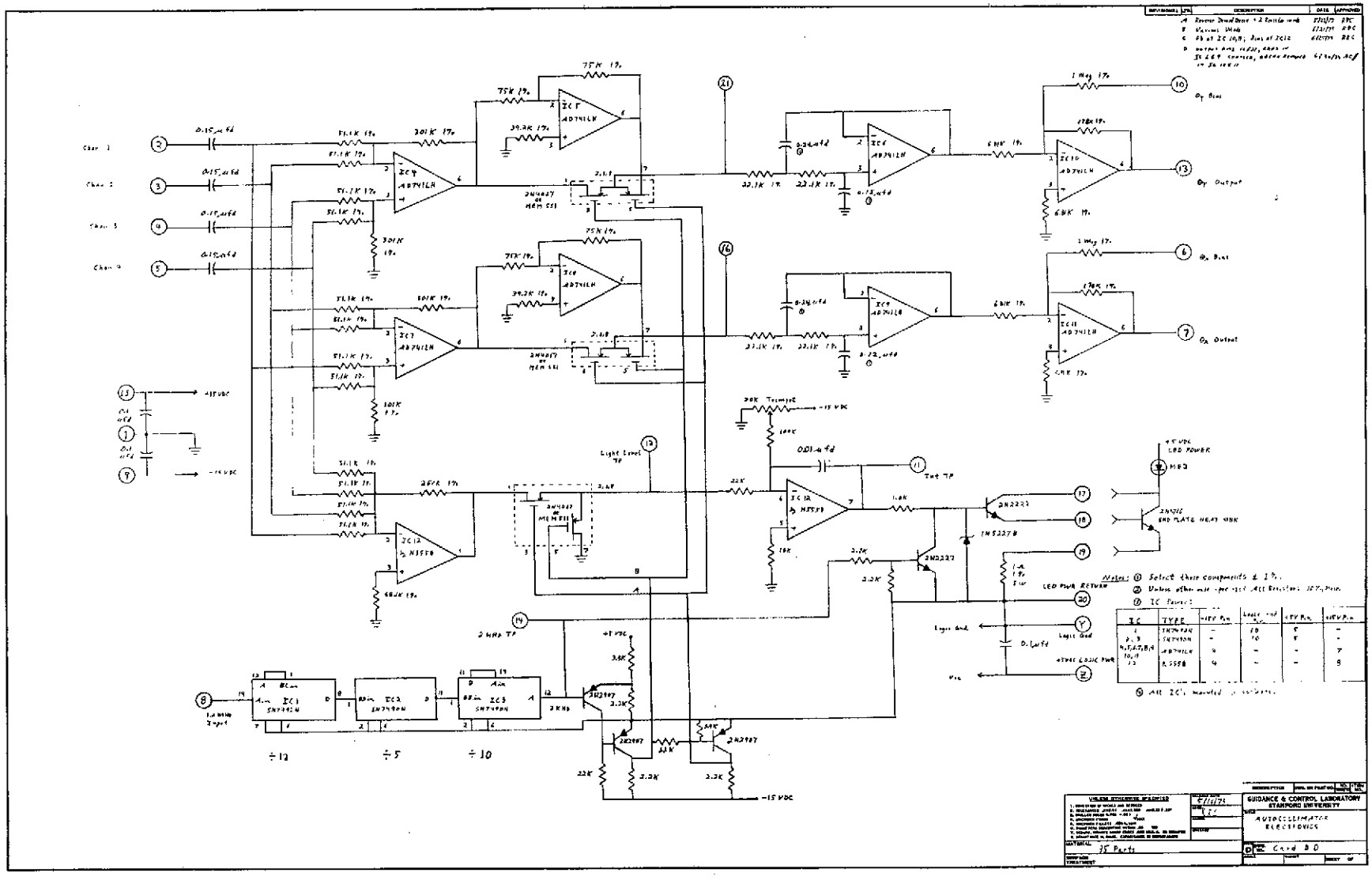

CARD 8: AUTOCOLLIMATOR ELECTRONICS

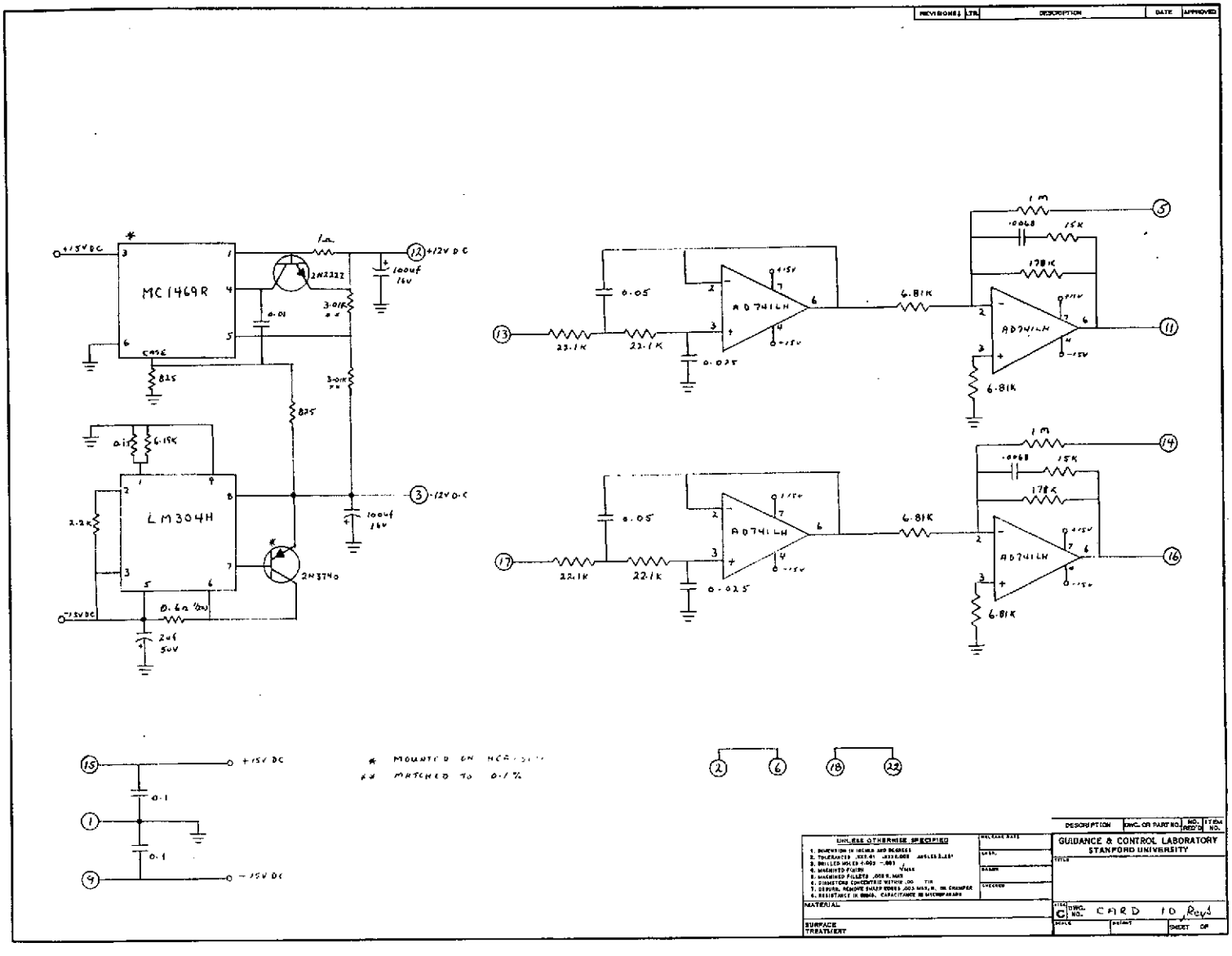

CARD 10: A/C INSTRUMENTATION FILTERS; ±12 VDC POWER SUPPLY

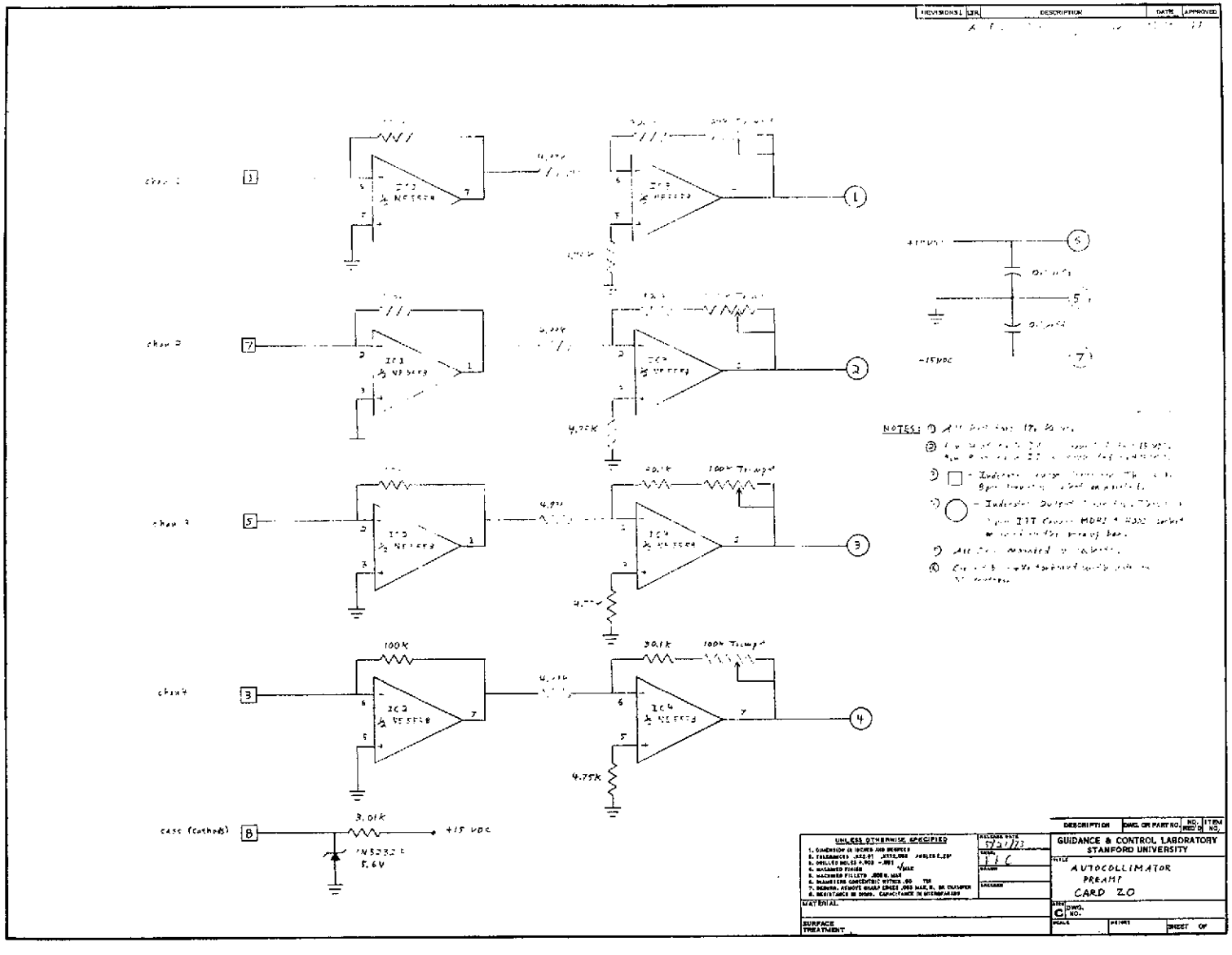

CARD 20: AUTOCOLLIMATOR PREAMPLIFIER

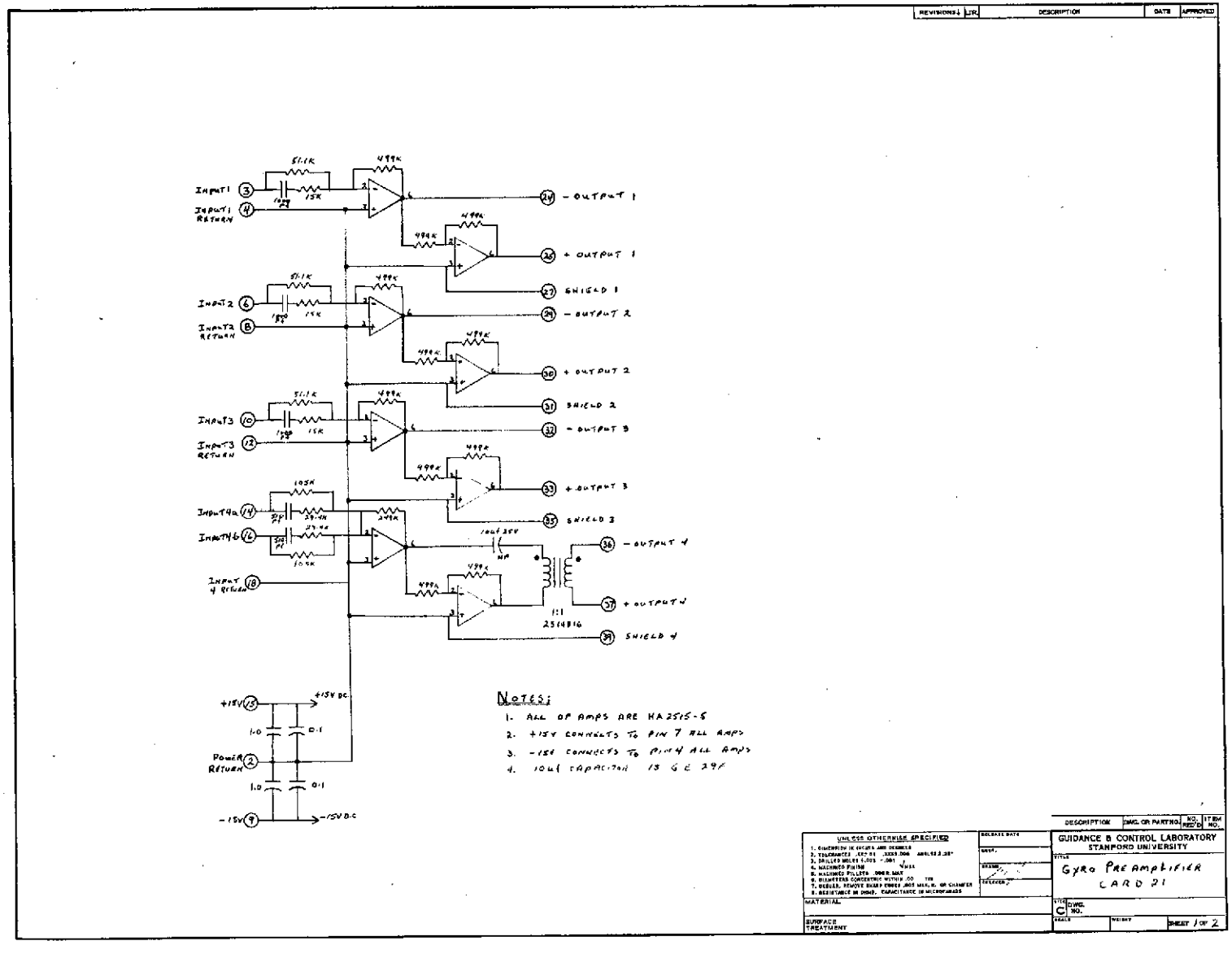

CARD 21: GYRO PREAMPLIFIERS

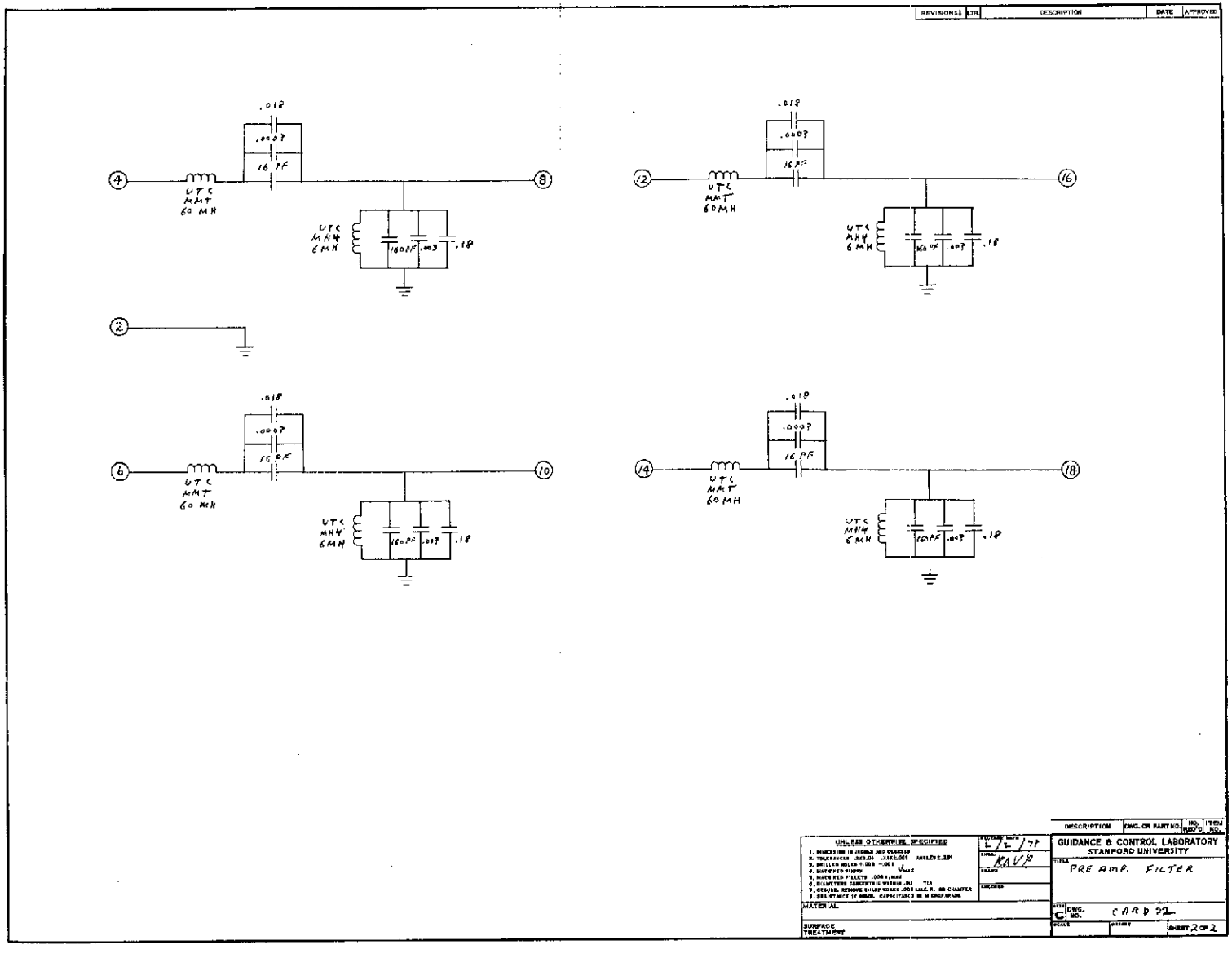

CARD 22: GYRO PREAMPLIFIER FILTER

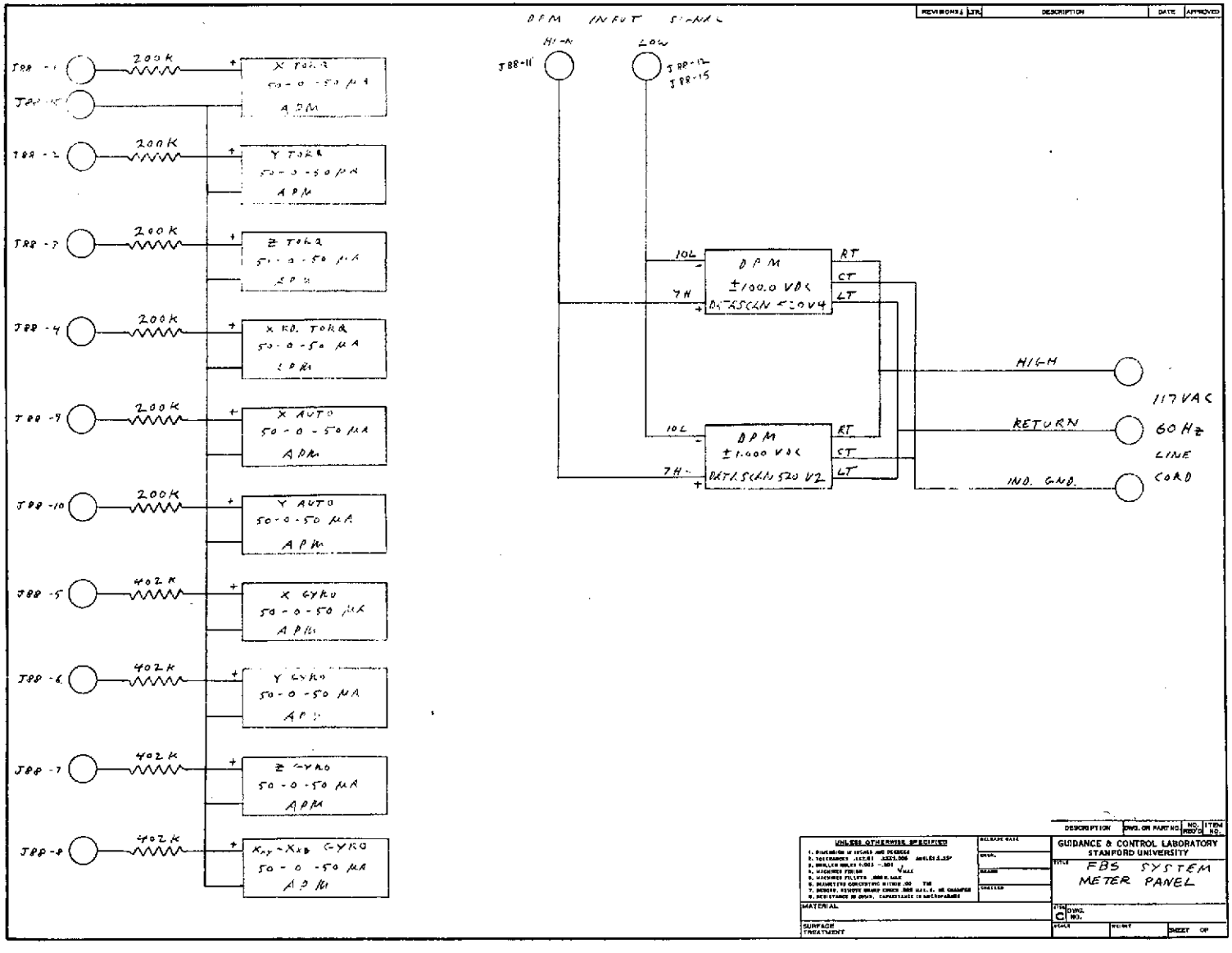
DPM INPUT SIGNAL
HIGH
LOW
J88-11
J88-17
J88-15
J88-1
J88-2
J88-3
J88-4
J88-9
J88-10
J88-5
J88-6
J88-7
J88-8
200K
402K
X TORQ
Y TORQ
Z TORQ
X RD. TORQ
X AUTO
Y AUTO
X GYRO
Y GYRO
Z GYRO
APM
LPM
50-0-50 μA
DPM
±100.0 VDC
±1.000 VDC
10L
7H
RT
CT
LT
HIGH
RETURN
IND. GND.
117 VAC
60 Hz
LINE
CORD
REVISIONS
LTR
DESCRIPTION
DATE
APPROVED
GUIDANCE & CONTROL LABORATORY
STANFORD UNIVERSITY
FBS SYSTEM
METER PANEL
MATERIAL
SURFACE TREATMENT
SIZE
DWG. NO.
SCALE
WEIGHT
SHEET OF

METER PANEL

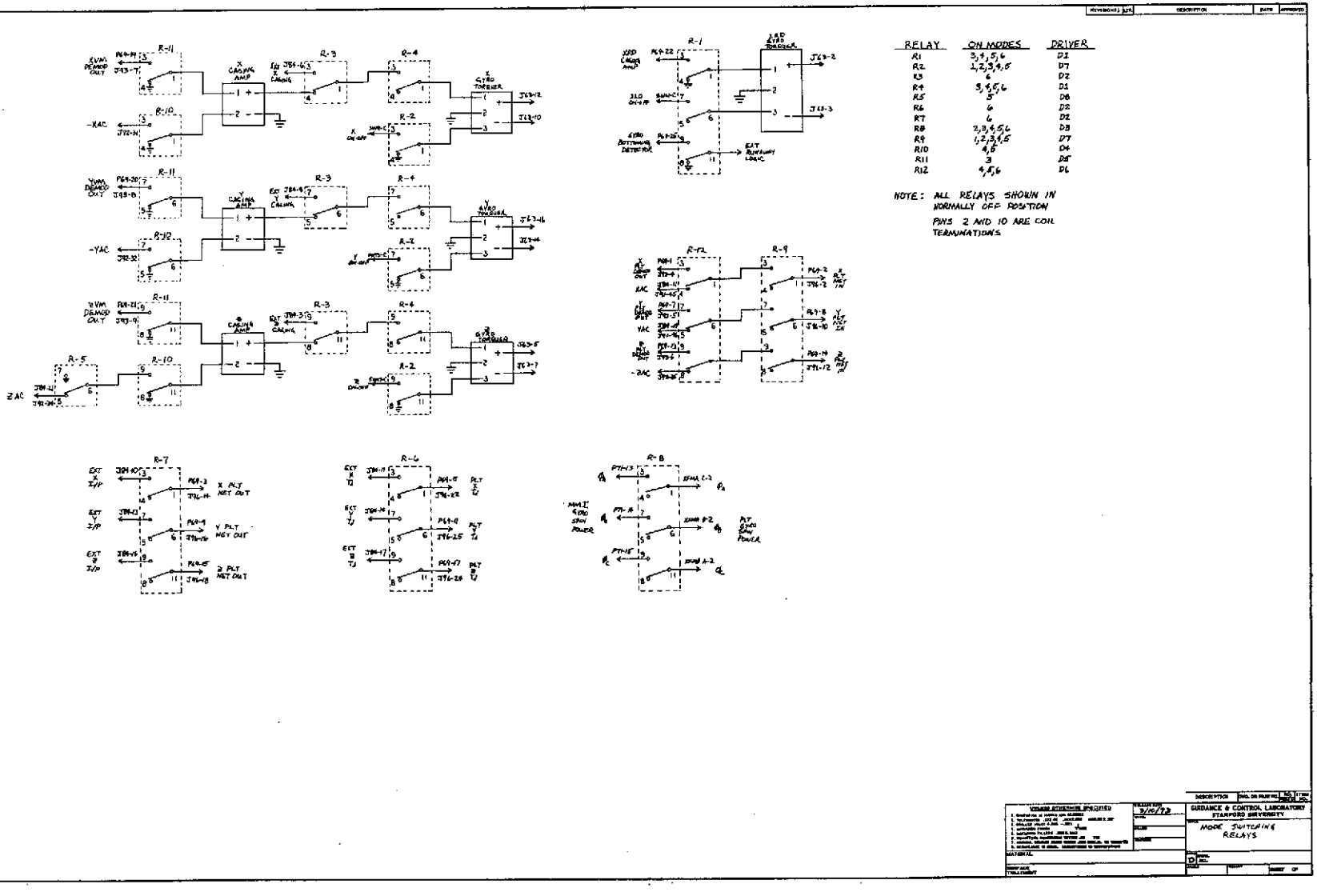

RELAY	ON MODES	DRIVER
R1	3,4,5,6	D1
R2	1,2,3,4,5	D7
R3	6	D2
R4	3,4,5,6	D1
R5	5	D6
R6	6	D2
R7	6	D2
R8	2,3,4,5,6	D3
R9	1,2,3,4,5	D7
R10	4,5	D4
R11	3	D5
R12	4,5,6	D1

NOTE: ALL RELAYS SHOWN IN NORMALLY OFF POSITION
PINS 2 AND 10 ARE COIL TERMINATIONS

MODE SWITCHING RELAYS – RELAY PANEL

REFERENCES

A1 Asseo, S. J., "Application of Optimal Control to 'Perfect' Model Following," Proceedings of the 1968 JACC, pp. 1056-1070.

B1 "Mission Feasibility for Stanford Relativity Experiment on Scout," Ball Brothers Research Corp. Final Report F73-03, Boulder, Colo., June 22, 1973.

B2 Bendat, J., and A. Piersol, Random Data: Analysis and Measurement Procedures, John Wiley & Sons, Inc., New York, 1971

B3 Bell, D. A., Electrical Noise, G. Van Nostrand Co., Princeton, N. J., 1960.

B4 Bingham, C., M. Godfrey, and J. Tukey, "Modern Techniques of Power Spectrum Estimation," IEEE Transaction on Audio and Electroacoustics, vol. AU-15, no. 2, June 1967.

B5 Blackman, R. B., and J. W. Tukey, The Measurement of Power Spectra, Dover Publications, New York, 1958.

B6 Bode, H. W., and C. E. Shannon, "A Simplified Derivation of Linear Least-Squares Smoothing and Prediction Theory," Proceedings of the IRE, vol. 38, 1950.

B7 Bradner, H. and M. Reichle, "On the Nature of Background Seismic Motions," AIAA Paper No. 72-819, August, 1972.

B8 Brigham, O., and O. Morrow, "The Fast Fourier Transform," IEEE Spectrum, December, 1967.

B9 Broxmeyer, C., Inertial Navigation Systems, McGraw-Hill Book Co., New York, 1964.

B10 Bryson, A., and Y. Ho, Applied Optimal Control, Blaisdell Publishing Co., Waltham, Mass., 1969.

B11 Bull, J. S., "Precise Attitude Control of the Stanford Relativity Satellite," SUDAAR 452, Department of Aeronautics and Astronautics, Stanford University, Stanford, Ca., March 1973.

B12 Bull, J. S., and D. B. DeBra, "Precision Pointing Thrustor," AIAA Paper No. 73-858, August, 1973

C1 Cooley, J., P. Lewis, and P. Welch, "The Finite Fourier Transform," IEEE Transactions on Audio and Electroacoustics, vol. AU-17, no. 2, June 1969.

C2 Cooley, J., P. Lewis, and P. Welch, "Application of the Fast Fourier Transform to Computation of Fourier Integrals, Fourier Series, and Convolution Integrals," IEEE Transactions on Audio and Electroacoustics, vol. AU-15, no. 2, June, 1967.

C3 Cooley, J., P. Lewis, and P. Welch, "Historical Notes on the Fast Fourier Transform," IEEE Transactions on Audio and Electroacoustics, vol. AU-15, no. 2, June, 1967.

C4 Cooley, J., and J. Tukey, "An Algorithm for the Machine Calculation of Complex Fourier Series," Mathematics of Computation, vol. 19, no. 90, 1965.

C5 Crowley, F. A., and H. A. Ossing, "An Analysis of the Vibration Environment with Applications to Single-Degree-of-Freedom Gyroscope Performance Tests," AIAA Paper no. 70-951, August, 1970.

C6 Curran, R. T., "Equicontrollability and the Model-Following Problem," Information Systems Laboratory Report 6303-2, Stanford University, July, 1971.

C7 Culver, R. C., "Evaluation of Concepts for a Laser Acquisition and Tracking System," Prepared for the Air Force Avionics Laboratory, Report AFAL-TR-73-180, June, 1973.

C8 Davis, W. R., and J. A. Miller, "SPARS--A Completely Strapdown Concept for Precise Determination of Satellite Vehicle Attitude," SAMSO Spacecraft Attitude Determination Symposium, October, 1969.

D1 Dahl, P. R., "A Solid Friction Model," Aerospace Corporation Report No. TOR-0158(3107-18)-1, El Segundo, Ca., May, 1968.

D2 DeBra, D. B., J. C. Mathiesen, and R. A. Van Patten, "A Precision, Active, Table-Leveling System," Journal of Spacecraft and Rockets, vol. 5, no. 9, September, 1968.

D3 Depeyrot, M., Fondements Algebriques de la Transformation de Fourier Rapide, Institute de Recherche D'Informatique et D'Automatique, 78-Rocquencourt, France, November, 1970.

E1 Erzberger, H., "Analysis and Design of Model Following Control Systems by State Space Techniques," Proceeding of the 1968 JACC, Ann Arbor, Mich., pp. 572-581.

E2 Everitt, C. W., W. M. Fairbank, and L. I. Schiff, "Theoretical Background and Present Status of the Stanford Relativity Satellite," Presented at ESRO Colloquium on the Significance of Space Research for Fundamental Physics, Interlaken, Switzerland, September 1969.

F1 Flack, M., and R. Dickie, "Building a Dynamic Test Complex Near an Inertial Test Facility and General Test Pad Considerations," AIAA Paper 73-827, August, 1973.

G1 "What is the Fast Fourier Transform," G-AE Subcommittee on Measurement Concepts, IEEE Transactions on Audio and Electroacoutics, vol. AU-15, no. 2, June, 1967.

G2 Gelb, A. and W. E. Vander Velde, Multiple-Input Describing Functions and Nonlinear System Design, McGraw-Hill Book Co., San Francisco, Ca., 1968.

G3 Gentleman, W. M., and G. Sande, "Fast Fourier Transforms--For Fun and Profit," 1966 Fall Joint Computer Conference, AFIPS Proceedings, vol. 29, Spartan Books, Washington, D.C., 1966.

H1 Hogan, J. J., and J. T. Welch, "A Real-Time Six-Degree-of-Freedom Hybrid Simulation Facility for Guidance System Testing," AIAA Paper No. 73-876, August, 1973.

H2 Hvoschinsky, V., and F. Y. Horiuchi, "Concepts and Mechanization for Evaluating SPARS in the Laboratory and in Orbit," SAMSO Spacecraft Attitude Determination Symposium, October, 1969.

J1 James, H., N. Nichols, and R. Phillips, Theory of Servomechanisms, Dover Publications, 1965.

J2 Jenkins, G. M., and D. G. Watts, Spectral Analysis and Its Applications, Holden-Day, San Francisco, 1968.

K1 Kalman, R. E., and R. S. Bucy, "New Results in Linear Filtering and Prediction Theory," Transaction ASME, Journal of Basic Engineering, ser. A., vol. 83, December, 1961.

K2 Koenigsberg, W. D., "Spectral Analysis of Random Signals--Techniques and Interpretation," C. S. Draper Laboratory Report E-2771, Cambridge, Mass., June, 1973.

L1 Lorell, K. R., and B. O. Lange, "Precision Attitude Control of Symmetric Bodies," SUDAAR 422, Department of Aeronautics and Astronautics, Stanford University, Stanford, Ca., April, 1971.

L2 Lorenzini, D. A., "Active Control of a Pneumatic Isolation System," AIAA Paper 72-843, August, 1972.

M1 Mathis, L. O., J. R. Stephens, and S. C. Wright, "The Design and Construction of an Inertial Test Facility," AIAA Guidance and Control Conference, Minneapolis, Minn., August, 1965.

N1 Newton, G., L. Gould, and J. Kaiser, Analytical Design of Linear Feedback Controls, John Wiley & Sons, Inc., New York, 1957.

P1 Papoulis, A., Probability, Random Variables, and Stochastic Processes, McGraw-Hill Book Co., New York, 1965.

P2 Pepi, J., and R. Cavanaugh, "Performance Characteristics of an Automatic Platform Tilt Stabilization and Vibration Isolation System," AIAA Paper No. 67-548, August, 1967.

P3 Preskitt, S., and J. Fix, "Six-Degree-of-Freedom Test Podium at the United States Air Force Standards Calibration Laboratory," AIAA Geokinetics Subcommittee, August, 1963.

R1 Reinel, K., "Motion Simulation Facility for the Satellite SYMPHONIE," Journal of the British Interplanetary Society, vol. 25, 1972.

R2 Richards, P. I., "Computing Reliable Power Spectra," IEEE Spectrum, January, 1967.

S1 Schiff, L. I., Proceedings of the National Academy of Science, vol. 46, 1960, p. 871.

S2 Singleton, P., and T. Poulter, "Spectral Analysis of the Call of the Male Killer Whale," IEEE Transactions on Audio and Electroacoustics, vol. AU-15, no. 2, June, 1967.

S3 Stockham, T. G., Jr., "High Speed Convolution and Correlation," Digital Signal Processing, IEEE Press, New York, 1972.

T1 Truncale, A., W. Koenigsberg, and R. Harris, "Spectral Density Measurements of Gyro Noise," C. S. Draper Laboratory E-2641, Cambridge, Mass., February, 1972.

T2 Tsutsumi, K., "Review of Geokinetics," AIAA Paper No. 72-893, August, 1972.

T3 Tsutsumi, K., "A Ground Tilt Isolation Platform," C.S. Draper Laboratory Report E-1508, Cambridge, Mass., January, 1964.

T4 Tyler, J. S., Jr., "The Characteristics of Model-Following Systems as Synthesized by Optimal Control," IEEE Transactions on Automatic Control, vol. AC-9, October, 1964.

V1 Van Trees, H. L., Detection, Estimation, and Modulation Theory, vol. 1, John Wiley & Sons, Inc., New York, 1968.

W1 Weinstock, H., "Design of a Precision Tilt and Rotational Vibration Isolation System for Inertial Sensor Testing," AIAA Paper No. 68-894, August, 1968.

W2 Welch, P., "The Use of Fast Fourier Transforms for the Estimation of Power Spectra: A Method Based on Time Averaging Over Short Modified Periodograms," IEEE Transactions on Audio and Electroacoustics, vol. AU-15, no. 2, June, 1967.

W3 Widrow, B., "Statistical Analysis of Amplitude Quantized Sampled-Data Systems," IEEE Applications and Industry, January, 1961.

W4 Wiener, N., Extrapolation, Interpolation, and Smoothing of Stationary Time Series, John Wiley & Sons, New York, 1949.

W5 Winsor, C. A., and R. J. Roy, "The Application of Specific Optimal Control to the Design of Desensitized Model Following Control Systems," IEEE Transactions on Automatic Control, vol. AC-15, no. 3, June, 1970.

W6 Wittry, J. P., "Description of an Inertial Test Facility Incorporating a Passively Isolated and Actively Stabilized Platform," AIAA Paper No. 69-893, August, 1969.

W7 Wrigley, W., W. Hollister, and W. Denhard, Gyroscopic Theory, Design, and Instrumentation, MIT Press, Cambridge, Mass., 1969.